Multiscale lung ventilation modeling in health and disease

Nicolas Pozin

MULTISCALE LUNG VENTILATION MODELING IN HEALTH AND DISEASE

THÈSE DE DOCTORAT

Présentée par

Nicolas POZIN

pour obtenir le grade de

DOCTEUR DE
L'UNIVERSITÉ PIERRE ET MARIE CURIE – Paris VI

Spécialité : MATHÉMATIQUES APPLIQUÉES

Soutenue publiquement le 06/10/2017 devant le jury composé de :

Mme Céline Grandmont	Directrice de thèse
M. Frédéric Hecht	Examinateur
M. Oliver Jensen	Rapporteur
M. Ira Katz	Examinateur
M. Benjamin Mauroy	Rapporteur
M. Bertrand Maury	Examinateur
Mme Stéphanie Salmon	Examinatrice
Mme Irène Vignon-Clementel	Directrice de thèse

Après avis favorable des rapporteurs :

Oliver Jensen et Benjamin Mauroy

Thèse préparée au sein de l'équipe-projet REO
Laboratoire Jacques-Louis Lions
Université Pierre et Marie Curie – Paris 6
et **Centre de Recherche Inria de Paris**
2 rue Simone Iff
75589 Paris Cedex 12

Abstract

The lung is an organ of the respiratory system. It supplies the organism with oxygen, which is necessary to the metabolism, and ensures carbon dioxide release. Humans have two lungs. The latter contain a tree, referred to as *tracheo-bronchial*, through which the air flows. It supplies a porous region, the parenchyma, where gas exchanges with the blood take place. Some pathologies affect the tree structure or the parenchyma integrity. They can induce ventilation defects or increased respiratory efforts. In vivo-studies are complex and mathematical modeling can provide some insights on the lung behavior, the pathologies' impacts or the efficiency of treatments.

In the first part of this thesis, we propose a ventilation model of the lung based on a mechanical description. A $0D$ model of the tracheo-bronchial tree is strongly coupled to a continuous $3D$ model of the parenchyma. An efficient implementation is proposed. We numerically show the influence of chosen boundary conditions as well as tree or parenchyma alterations on the ventilation distribution. Results are compared with those provided by a model, often used in the literature, in which the parenchyma is described as a set of mechanically independent compartments. Significant differences are obtained, in particular in pathological cases.

In a second part, we use the $0D$ tree-$3D$ parenchyma coupled model to investigate how breathing gas mixtures less dense than air would reduce efforts and ensure a better ventilation. To that end, we build an asthmatic tree model based on a literature review. We propose lines of thoughts on why, as observed in clinical trials, helium-oxygen mixtures have varying efficiency. The broncho-constriction distribution, i.e. the position and severity of constrictions, is a major explaining factor.

In the next part, we develop an approach to get insights on severe constrictions distribution based on the analysis of dynamic lung ventilation images. To do so, the $0D$ tree-$3D$ parenchyma coupled model is used along with a machine learning technique.

Finally, two prospective works are presented. First, we propose extensions to the ventilation models introduced in the first part as a step towards spirometry modeling, a standard test to assess respiratory pathologies. The last study is part of a global perspective that aims at getting insights on the lung geometry based on simple measurements on the patient's body. The final objective is to determine, in a simple way, with little effort, input data for the ventilation models.

Résumé

Le poumon est un organe de l'appareil respiratoire. Il a pour fonction d'assurer l'approvisionnement de l'organisme en oxygène, nécessaire au métabolisme, et l'évacuation du dioxyde de carbone. L'homme possède deux poumons. Ils sont constitués d'un arbre dit trachéo-bronchique par lequel circule l'air et qui alimente le parenchyme où ont lieu les échanges gazeux avec le sang. Certaines pathologies affectent la structure de l'arbre ou l'intégrité du parenchyme induisant notamment des défauts dans l'approvisionnement en air ou des efforts respiratoires accrus. Etudier l'organe in-vivo est complexe. Dans ce cadre, la modélisation mathématique peut apporter un éclairage utile sur le fonctionnement du poumon, les effets associés aux pathologies qui le touchent, et la pertinence des traitements proposés.

Dans la première partie de cette thèse, nous proposons un modèle mécanique de ventilation pulmonaire. Un arbre $0D$ des bronches est couplé de manière forte à un modèle continu de parenchyme $3D$. Une implémentation efficace est mise en œuvre. On met numériquement en évidence l'impact sur la distribution de ventilation des conditions aux limites appliquées et d'altérations de l'arbre ou du parenchyme. Le comportement de ce modèle est comparé à celui d'un modèle plus simple, couramment utilisé dans la littérature, dans lequel le parenchyme est décrit comme un ensemble de compartiments mécaniquement indépendants. Des différences significatives sont obtenues dans des cas pathologiques.

Dans une deuxième partie, on utilise le modèle couplé arbre $0D$-parenchyme $3D$ pour étudier dans quelle mesure respirer un gaz moins dense que l'air permet de diminuer les efforts et de réduire les défauts de ventilation observés chez des patients asthmatiques. A cette fin, on propose un modèle d'arbre asthmatique construit à partir d'une revue bibliographique. On conclut sur des pistes d'explication à l'efficacité variable observée pour les traitements à base de mixtures peu denses d'hélium et d'oxygène. La distribution des constrictions dans l'arbre respiratoire, i.e. leur position et sévérité, est un facteur primordial.

Dans la partie suivante, on propose une approche permettant de déterminer la distribution des constrictions bronchiques les plus sévères à partir de données d'imagerie dynamique de ventilation. Notre démarche s'appuie sur l'utilisation du modèle couplé arbre $0D$-parenchyme $3D$ présenté dans la première partie, enrichie par une technique d'apprentissage statistique.

On présente finalement deux études prospectives. La première étend les modèles de ventilation introduits précédemment avec pour objectif final de modéliser la spirométrie ; un test usuel de diagnostique de pathologies respiratoires. La deuxième s'inscrit dans une perspective visant à déterminer la géométrie du poumon à partir de mesures simples prises sur le corps du patient. L'objectif final étant de déterminer par des moyens simples et non coûteux les données d'entrées des modèles de ventilation.

Remerciements

Merci à Benjamin Mauroy et Oliver Jensen d'avoir rapporté cette thèse. Et merci à Frédéric Hecht, Bertrand Maury, Stéphanie Salmon, Ira Katz d'avoir accepté de faire partie de mon jury.
La thèse est une page de vie, elle apporte son lot de sourires et de difficultés. Plus peut-être que nos humbles découvertes pulmonaires, je retiendrai ces belles rencontres : elles m'ont marqué, appris et fait grandir.
Merci à mes directrices. A Céline pour ta passion, ton sens du partage et ton humanité. On apprécie parfois mieux les conseils avec le recul du temps, je retiendrai tes leçons de rigueur et d'abnégation. Merci à Irène pour ton sens de l'organisation, tes conseils réguliers et ton soutien floral. Vous m'avez beaucoup appris.
Je remercie également l'équipe physique respiratoire. Georges pour ta gentillesse et ta hauteur de vue. Cécile pour ton enthousiasme, tes sourires et ton soutien. Spyros et Ira pour vos conseils scientifiques et pour nos longues discussions, elles me manqueront. Marine pour ton aide.
J'ai aussi eu l'occasion de travailler avec de sympathiques chercheurs. Qu'ils soient ici remerciés. Xavier et Hongchen pour nos plans élastographiques de validation, je reste optimiste. Catalin pour ton aide en segmentation.
Se retourner sur ces années de thèse, c'est penser à toutes ces personnes que j'ai eu le bonheur de côtoyer. Merci aux chercheurs de Reo. Jean-Frédéric, j'ai beaucoup apprécié nos quelques discussions, ton recul et ta gentillesse. Marina, j'ai aimé t'écouter le matin devant mon thé. Damiano, cela a été un plaisir d'échanger. Merci Miguel pour ces discussions fort intéressantes devant les viennoiseries gratos. Et merci à toi Maryse pour ton aide régulière et souriante.
Je pense aussi à tous ces thésards, post-docs et stagiaires qui, au gré des discussions, pintes et baskets sont devenus des amis. Chloé, partager ton bureau a été un petit bonheur, merci pour ton écoute, tes conseils, ta bonne humeur et ton orchidée. Fabien, je garderai en tête ta générosité, ton aide, ta sérénité et toutes ces discussions… tu es un chic type. Noémie, tu redonnerais le sourire à une huître desséchée, merci d'être ce boute-en-train qui nous a tous aidé. Merci à mes amis Italiens, Matteo, Lara, Alberto, je suis heureux de vous connaître, un giorno parleremo italiano insieme. Merci à Eliott pour les innombrables choses que tu nous as apprises. Matthieu, L comme… (no offense). Ludo, je suis ému de t'avoir vu grandir. Je n'oublie pas les inconditionnels du playground ou de la course : Olivier, Sebastien, Hussam, Dena, Simplice, Jan. Et merci à tous les autres d'avoir parsemé cette thèse de si jolis moments : Nora, Léa, Yi, Alex, Florian, Gauthier. Et les anciens : Mikel, Benoit, Faysal, Gaetan le kid, Michele, Rodolfo (tantos recuerdos), Valentin, Ange. Il y aurait tant à dire…
Je n'oublie pas non plus toutes les belles rencontres du CRCD : FLORIAN BRUN (mon cher patron, ton nom a sa place ici, parsemé de majuscules), Sam tu as ton spot au panthéon des bros. Merci à Rodrigue, Quian, Mario, Alaeddine, Thomas, Ryckilelle, Florian S. Merci Moussa pour ces douces conversations matinales, et merci à toi chère dame de la cantine, je garderai le souvenir de ta gentillesse.
Je pense aussi ici à ceux qui m'ont donné le goût des sciences. A Mme Devanz, Mme Martin-Christol, et M. Boisson.
Au-delà du labo, des systèmes linéaires et des ping-pongs, la vie a continué. Ces trois années ont déroulé leurs joies et leurs tristesses. Merci à ceux qui comptent tant. Amar, Werner, Lolo, depuis bien longtemps vous êtes plus que des amis. Je pense à Anouar, Loic, Vincent, Cloclo, Cécile, Adé, Khadidia, que de beaux souvenirs je partage avec vous. A tous ceux dont je tais le nom, sans rancune, je vous aime aussi.
Aurélia, je n'oublie rien de ces années…
A mes chères cousines, mon oncle et ma tante à qui je tiens tant et sur qui j'ai si souvent compté.
Papa, merci d'être là… merci pour ton éducation, ta présence, ton soutien. S'il m'est parfois arrivé d'avoir des réussites, je te les dois beaucoup.
Ma belle petite maman, aujourd'hui tu aurais été fière. Tu peuples mes souvenirs et mon cœur. Le printemps s'est levé et la vie continue. Pour toi merci ne suffit pas.

A mon père, à ma mère…

Content

CHAPTER I- Introduction

The lung is a complex multi-scale and multi-physics system. Its function is to transfer oxygen from the atmosphere to the blood circulation. In this thesis we focus on lung ventilation, i.e. the distribution of gas within the organ. This work is carried out under the ANR Tecsan OxHealease which aims at investigating the use a low density helium-oxygen mixtures in the treatment of some respiratory diseases. This is a CIFRE thesis, result of a collaboration between INRIA and Air Liquide Santé International.

In this chapter the role and the physiology of lung ventilation in health and disease are described. In-vivo measurements are complex and the organ behavior in some pathological configurations is not well understood. In this context, mathematical modeling can bring relevant insights. A state of the art on modeling approaches is presented as well as the contributions and perspectives brought by this thesis.

1. Lung ventilation physiology

The human respiratory system is made of two lungs irrigated with fresh air through a dyadic structure called the tracheo-bronchial tree. Lungs are surrounded by respiratory muscles. In normal breathing, these muscles contract during inspiration generating lung expansion, and relax at expiration allowing lung deflation. This mechanism called respiration is responsible for air flow in the tree.
In this section, the role of the lung as well as its components are described both in healthy cases and when affected by some respiratory diseases. The interested reader could refer to [**1**], [**2**] and [**3**] for more details concerning lung physiology and mathematical modeling of ventilation.

1.1. Role of the lung

The lung supplies the organism with fresh air rich in dioxygen (O_2). The gas is carried trough the tree down to functional units where exchange takes place with the vascularization. The dioxygen is dissolved into the blood which then supplies body tissues. Concomitantly, carbon dioxide leaves the blood circulation, passing into the air and is exhaled out of the body by the respiratory system.

1.2. Human lung architecture

The human respiratory system is inserted in the thoracic cage which is itself surrounded by the sternum in the front, the spinal column in the back and laterally by twelve pairs of ribs. Both lungs are located on either side of the mediastinum, the central compartment of the thoracic cage containing the heart, the esophagus and the trachea. Lungs are in conical shape, with a narrow rounded apex at the top.

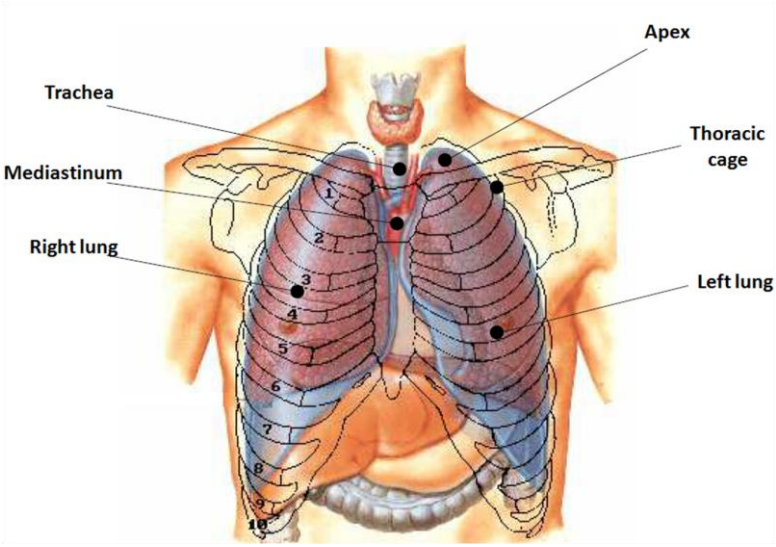

Figure 1: schematic of the thoracic cage. Modified from [4].

Air flows through the tracheo-bronchial tree which is inserted in a medium called pulmonary parenchyma.

Tracheo-bronchial tree:
The human tracheo-bronchial tree is a non-symmetric dyadic branching structure. It starts from the trachea, that gives birth to two airways irrigating the right and left lungs. It contains approximately 24 generations [**5**], from upper airways with centimetric diameter referred to as *proximal* down to

networks of millimeter size airways referred to as *distal* (see Figure 2 and Figure 3). Typical airway dimensions in the human lungs are indicated in Table 1. Along the first seventeen generations, the air flow is convective while in lower branches of the tree, called respiratory units or acini, Reynolds numbers are low and the flow regime is diffusive. Human lungs contain about 30000 acini, which are dyadic terminal sub-trees. They end in alveolar sacs (see Figure 4) where gas exchange takes place. There are about three hundred millions alveoli representing an exchange surface of about 100 m^2 [**3**]. See Figure 3 for a synthesizing scheme.

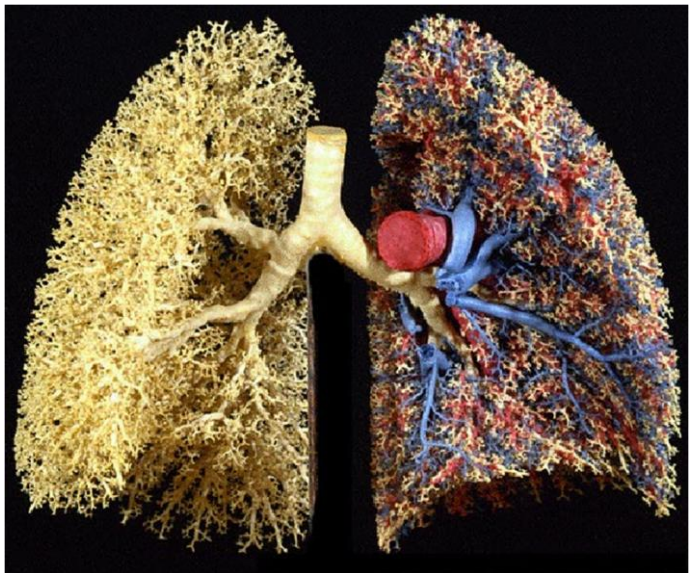

Figure 2: Cast of the lung tracheo-bronchial tree on the left, and blood vessels on the right. Colors of the vessels refer to the blood oxygenation, in red vessels flows oxygenated blood, in blue non-oxygenated blood. Taken from [6].

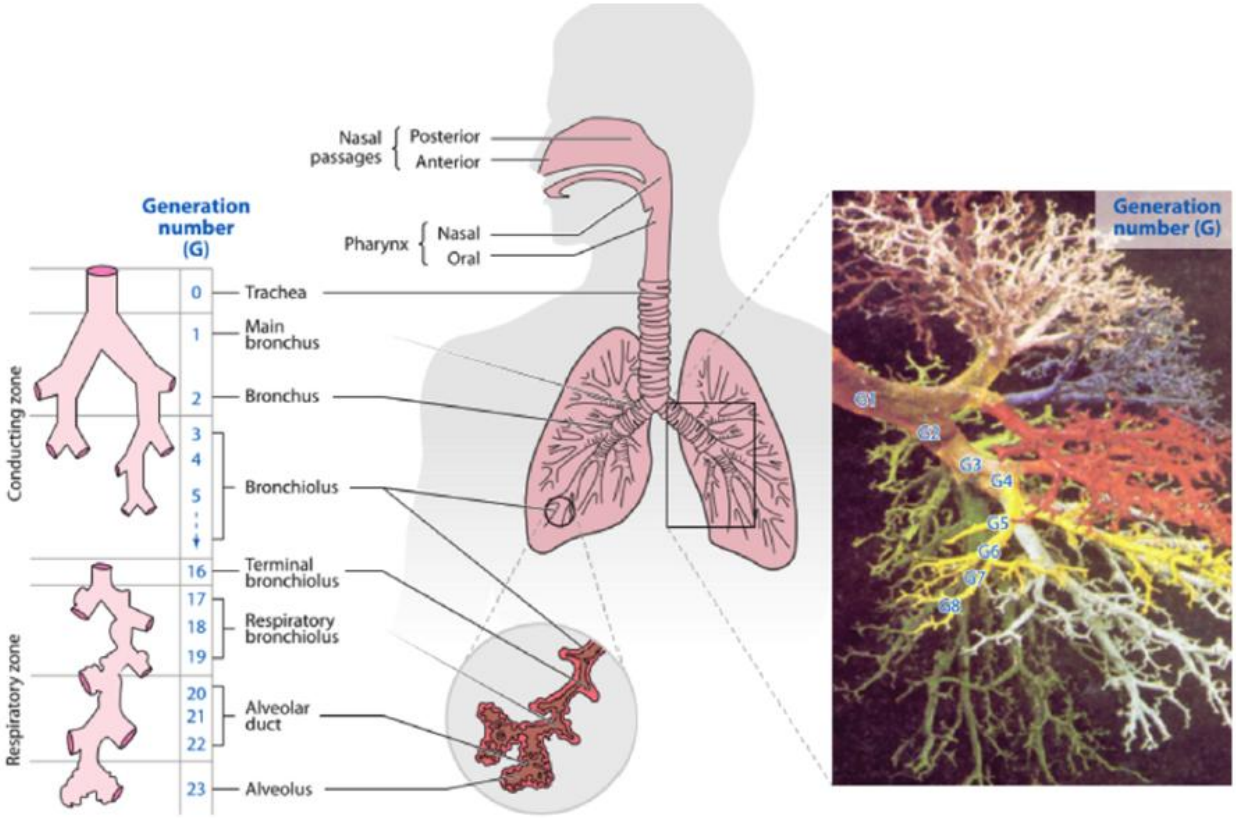

Figure 3: Schematic of the human respiratory system, from extra-thoracic components to alveoli, and cast of human airways. Taken from [7].

Generation	Number of branches	Diameter (cm)
0	1	1.800
1	2	1.220
2	4	0,830
3	8	0.560
4	16	0.450
5	32	0.350
6	64	0.280
7	128	0.230
8	256	0.186
9	512	0.154
10	1024	0.130
11	2048	0.109
12	4096	0.095
13	8192	0.082
14	16384	0.074
15	32768	0.066
16	65536	0.060
17	131072	0.054
18	262144	0.050
19	524288	0.047
20	1048576	0.045
21	2097152	0.043
22	4194304	0.041
23	8388608	0.041

Table 1 : Estimation of the number of airways and their diameter as a function of the generation. Taken from [5].

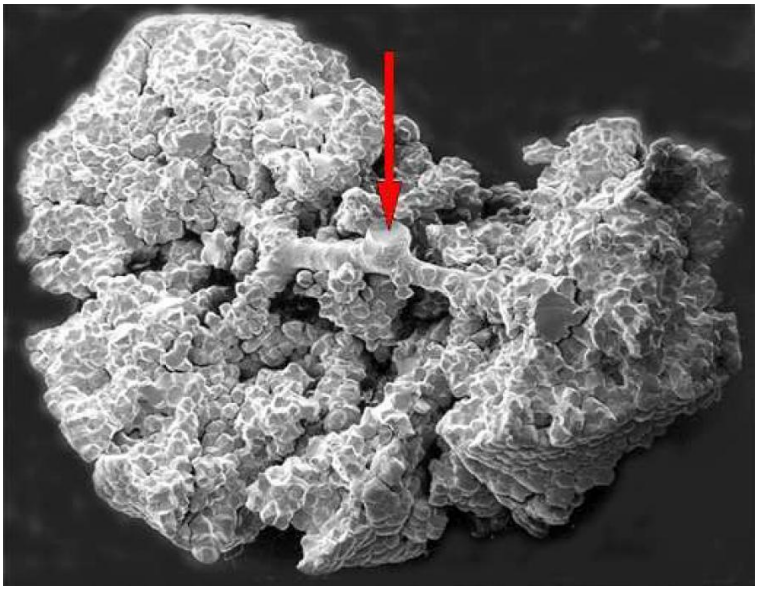

Figure 4: Pulmonary acinus, so-called respiratory unit. The red arrow indicates the acinus entrance. Human lungs contain about 30000 acini. Taken from [8].

Parenchyma:

The tree is inserted in a viscoelastic porous medium called the pulmonary parenchyma (see Figure 5). It is formed by the alveoli along with a dense network of blood capillaries. The membrane between alveoli and blood vessels contains elastic fibers that enable alveolar sacs expansions during inspiration. Lung viscoelasticity also stems from the presence of a thin surfactant layer in the alveoli which lowers the surface tension. Under normal quiet breathing, so-called *tidal regime*, the lung

volume difference from end inspiration to end expiration is called *tidal volume*. At end expiration, the lung is at functional residual capacity (FRC), this is its configuration at rest. It reaches the residual volume (RV) after full expiration while maximal inspiration leads to total lung capacity (TLC) volume (see Figure 6). The parenchyma has a linear behavior close to the FRC state and non linear hysteretic mechanical behavior as volume increases to broader ranges (see Figure 7).
At rest, tissues are extended due to gravity, and alveoli tend to shrink under elastic recoil and surface tension. On the contrary the thoracic cage would spontaneously be larger and exerts an opposing force. During the breathing cycle, activity of the muscles surrounding the parenchyma induces lung volume variations.
Lungs are divided into units called lobes that are not mechanically attached and can slide with respect to one another. The human left lung contains two lobes while the right one contains three lobes.

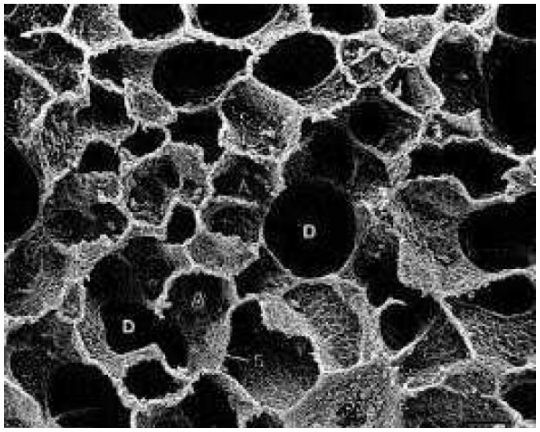

Figure 5: Pulmonary parenchyma, taken from [8].

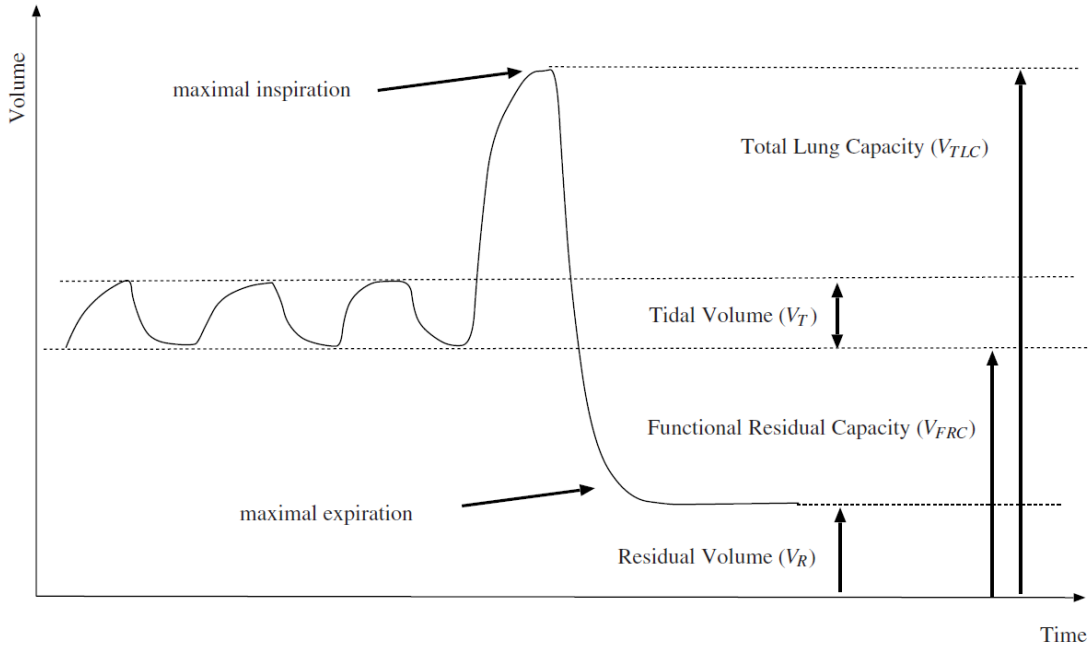

Figure 6: lung volumes nomenclature. Taken from [3].

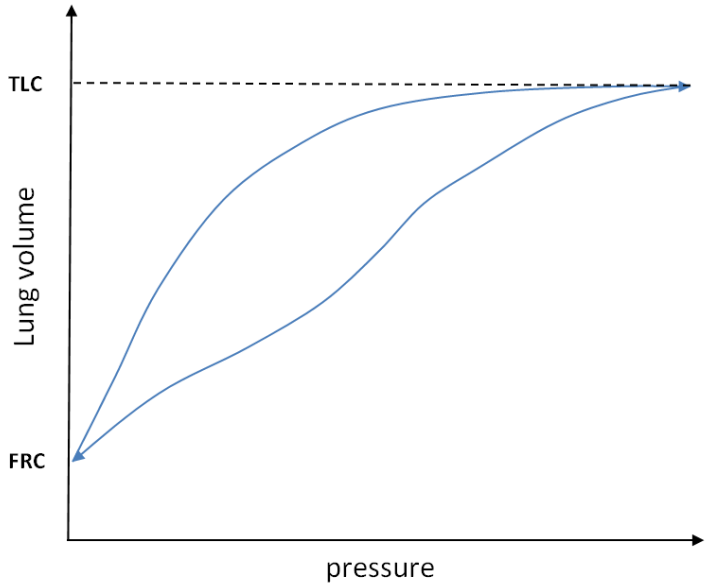

Figure 7: Typical shape of a lung pressure-volume loop. Due to its viscoelastic properties, the lung has a non linear hysteretic behavior.

1.3. Ventilation mechanism

Inspiration is mostly driven by the contraction of two groups of respiratory muscles: the diaphragm and intercostal muscles. The diaphragm is a thin dome-shaped muscle situated between the abdominal and the thoracic cavities. During inhalation, it contracts and its center moves downward generating lung expansion. Intercostal muscles are attached between the ribs. When they contract the rib cage rises, which assists the inhalation process (see Figure 8). Muscle efforts are transmitted to the lung through the pleural cavity, a few micrometers thick layer filled with a viscous fluid. The pressure inside this cavity is called the pleural pressure. It is lower than atmospheric pressure during inspiration inducing an expansion that draws air in the respiratory system. Under quiet breathing, expiration is passive: it is driven by the elastic recoil of the thoracic walls.

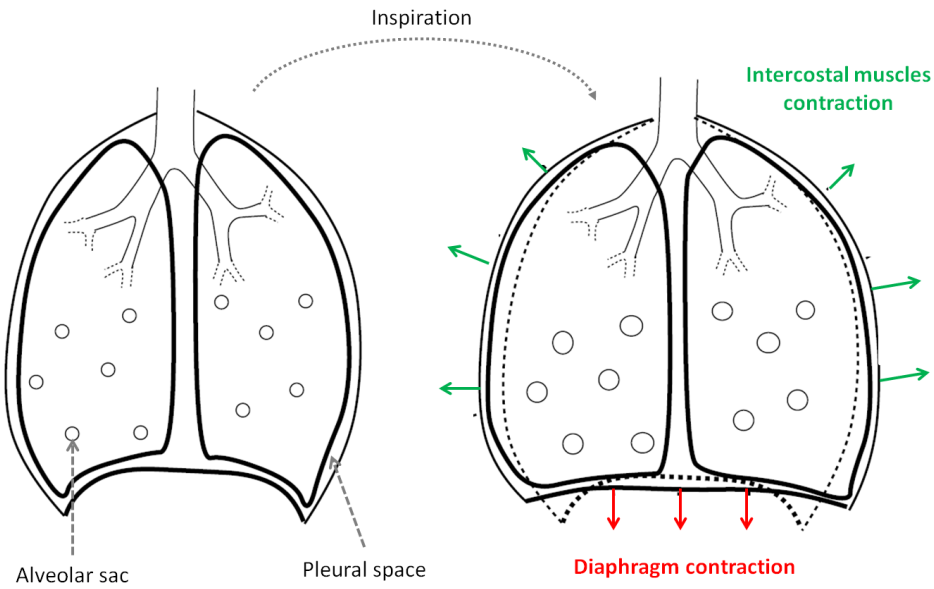

Figure 8: Lung motion and action of respiratory muscles during inspiration. Modified from [3].

1.4. Pathophysiology

Some pathologies affect the tree or the parenchyma structure. In this thesis we focus on asthma, chronic obstructive pulmonary diseases (COPD) and fibrosis.
Asthma is a common inflammatory disease characterized by airways narrowing. Constrictions can be due to smooth muscle contraction [**9**] or to mucus hypersecretion [**10**]. Asthma can induce permanent remodelling of some airways [**11**] which are then stenosed even out of crisis. As extensively described in subsection 15.2 this can go from frequent stenoses to some severe constrictions, both in upper large branches and small distal tree airways. There is no consensus on its causes. In 2015, 358 million people in the world had asthma, up from 183 million in 1990 [**12**], it causes several hundred of thousands deaths each year.
COPD is a type of obstructive lung disease characterized by long-term poor airflow. As in asthma the tree structure is affected. Parenchyma tissues integrity can be altered: in emphysema for instance connective alveolar walls are destroyed leading to poor airflow and eventually poor absorption and release of respiratory gases [**13**]. It can be caused in particular by continued inhalation of toxic particles, most often due to smoking. In 2015, COPD resulted in 3.2 million deaths, up from 2.4 million on 1990 [**14**].
Pulmonary Fibrosis is the accumulation of excess fibrous connective tissue leading to walls thickening and reduction in oxygen supply to the blood. As a consequence, patients suffer from perpetual shortness of breath. The parenchyma is made stiffer.

2. Lung properties, measured by in vivo and in vitro experiments

Some measurable quantities account for the lung properties. For instance, lung compliance assesses the parenchyma elasticity. When the lung mechanical properties are altered, compliance is changed. The respiratory tract resistance accounts for the energy dissipation within the tree, it can vary when pathological patterns affect the tree structure (see subsection 1.4). In this section, we give insights on those quantities and on various tools to assess them.

Assessing and measuring the resistance of the tree to airflow:
Because air is viscous, the respiratory tract resists to the flow passing through it. Let us consider an incompressible viscous flow q through a circular pipe. Viscous losses induce a pressure drop Δp through the pipe. When neglecting gravity and inertial effects, one can demonstrate that $\Delta p = R_{pois} q$ where the proportionality coefficient, called Poiseuille resistance, is defined by:

$$R_{pois} = \frac{8\mu L}{\pi r^4}.$$

Scalars r and L are respectively the pipe radius and length, μ is the fluid dynamic viscosity. Note that if the radius decreases as it may happen in asthma (see subsection 1.4) the airway resistance is rapidly increased. Note also that when considering high flows or more complex geometry, this formula is no longer valid. Airways are not straight circular pipes; they can be curved with varying section, and bifurcations can induce additional singular pressure drops [**15**]. The overall tree resistance includes those effects and can be experimentally measured. It is quantified by the airway resistance index R_{AW} defined analogously to Ohm's law as:

$$R_{AW} q = p_{atm} - p_{alv}$$

where p_{atm} is the atmospheric pressure, at the mouth, p_{alv} the alveolar pressure, and q the flow through the trachea. The higher the pressure drop required to induce a given flow, the higher the

resistance. When some airways are constricted as in asthma (see subsection 1.4), resistance can be dramatically increased [**16**]. This is a global measure, it does not account for possible heterogeneities in the tree structures. In particular, the alveolar pressure is not homogeneous throughout the lung. Note also that because of complex geometrical patterns within the tree or local flow increase due to constrictions, inertial effects can appear and resistance may be flow dependent (see for instance the Pedley resistance model [**17**] in subsection 8.1).
Plethysmography is the gold standard technique to measure R_{AW}. The patient is placed in a sealed box in which pressure variations are measured. From there the alveolar pressure can be inferred using thermodynamical laws. More details can be found in [**1**].

Assessing and measuring the lung elasticity:
The lung compliance is a measure of its ability to stretch or expand. It is non linear, see for instance Figure 7: as the parenchyma expands, its volume increase per pressure unit is reduced. Similarly, when the parenchyma contracts close to RV, it takes more strength to decrease its volume than around FRC. The lung compliance C is defined by:

$$C\Delta P_{tm} = \Delta V$$

where ΔV is the lung volume variation measured with a spirometer and ΔP_{tm} is the related transmural pressure variation. Transmural pressure is the difference between the alveolar pressure and the pleural pressure. A surrogate for alveolar pressure is the airway pressure measured during a breath-hold; a surrogate for pleural pressure is the so-called esophageal pressure measured in the esophagus thanks to a balloon catheter. More details can be found in [**18**]. Note that no-non invasive in-vivo technique enables to get a spatio-temporal distribution of the pleural pressure. An invasive procedure described in [**1**] is to place alveolar capsules just under the pleural surface to measure local alveolar pressures on open-chest animals.
Lung compliance is increased when the elasticity recoil is poor, as in emphysema [**19**] and low when tissues are more rigid as in fibrosis. Histology, the study of microscopic anatomy, is an invasive mean to study the parenchyma structure. It can be performed on lung cuts or biopsies. Though, for some pathologies such as fibrosis, modern non-invasive imaging techniques may provide insights of comparable quality [**20**].

Assessing the tree structure:
One can get precise insights on the tree structure through computed tomography (CT) or sub-millimetric high resolution computed tomography (HRCT). X-ray images taken from different angles are gathered to provide a representation of the inner lung structure. The tree geometry can be determined with segmentation techniques [**21**], [**22**], [**23**] (see Figure 9). The number of segmented airways depends on the image resolution. With conventional HRCT, a 0.5 mm^3 resolution is typically obtained [**24**]. Airway segmentations can be performed up to around generation 5 or 6 and pathological airway patterns such as constrictions can be visualized (see Figure 10).
Note that histology is another mean to study the tree structure. It has been used to study constriction distributions in patients who died from status asthmaticus [**25**], [**26**] showing that some obstructions are observed both in upper and small airways.
To get knowledge on the parenchyma mechanical properties, some tensile tests have been performed on excised lungs with various results [**27**].

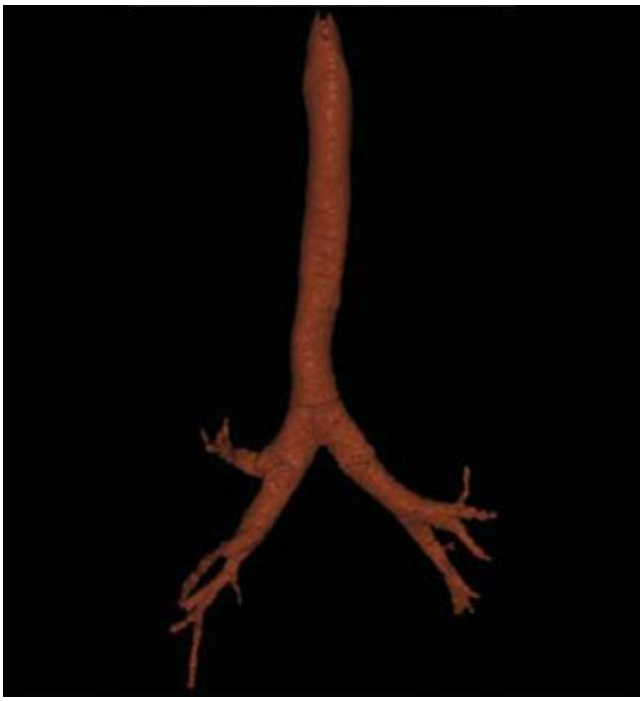

Figure 9: Human upper airways structure, segmented from a HRCT scan. Taken from [22**].**

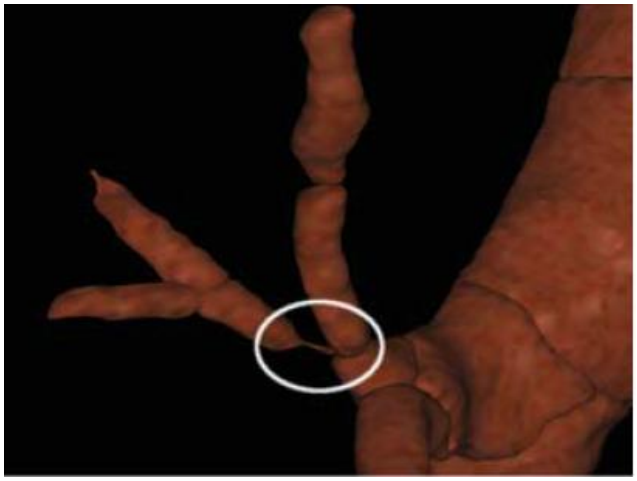

Figure 10: Constrictions segmented on a HRCT scan of an asthmatic patient. Taken from [22**].**

Measuring the lung ventilation:

Lung ventilation distribution refers to the gas repartition within the lung along the respiration. It can be studied from CT images at breath-hold. The parenchyma local density, which is linked to the local concentration of gas, can be deduced from voxels intensity [**28**], [**29**] (see Figure 11). Magnetic resonance imaging (MRI) measures the reaction of free proton spins under a time varying magnetic field gradient. As the lung is rich in air and poor in hydrogen, the signal is low, though it can be enhanced when breathing hyperpolarized gas such as ^{3}He or ^{129}Xe [**30**]. Their distribution can then be studied. Both CT and MRI can be implemented with a real-time modality. The resulting 4D-CT [**31**] and 4D-MRI [**32**], [**33**] images provide dynamical ventilation maps. Depending on the device, dynamic imaging techniques lead to various spatial and temporal resolutions [**34**], [**35**], [**36**]. Typically, spatial and temporal resolutions are 4 mm^3 isotropic and 0.4 s respectively.

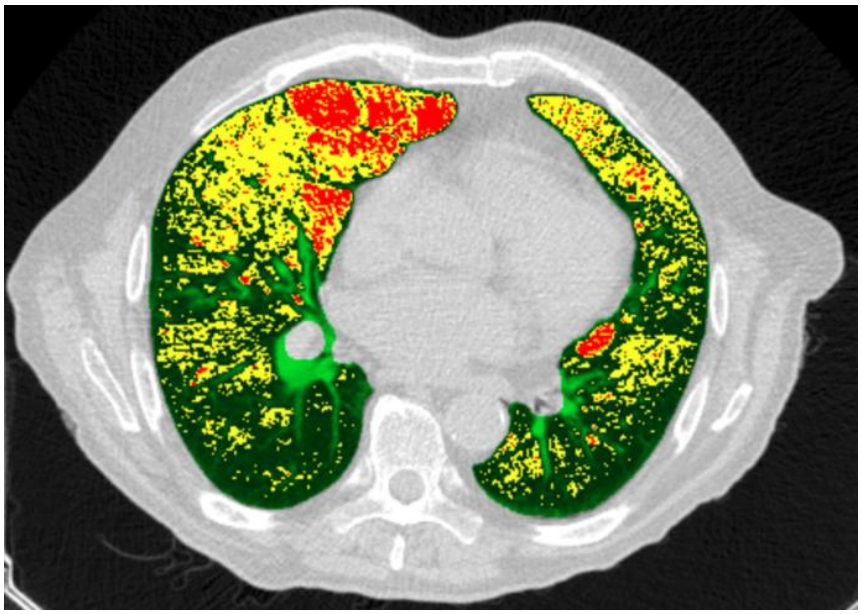

Figure 11: Density map on a lung cut from a CT scan on an emphysematous patient. Red regions have pathological low density, whereas green and yellow regions are in normal ranges. Data taken from [37].

Spirometry, a tool to assess diseases:

Imaging techniques are costly. A common accessible test to assess pulmonary pathologies is spirometry. It consists in a full inspiration and a forced expiration. Inspired and expired flows are measured with a spirometer. The shape of the resulting flow volume curves gives insights on pathologies that possibly affect the lung. In obstructive diseases such as asthma and emphysema (see Figure 12), it is harder to expire and the peak flow reached at forced expiration is reduced compared to a healthy configuration. Also, the tree and parenchyma are not homogeneously affected, and some regions may empty normally while others do not. This creates phase shifts that appear in the form of curvature change in flow volume curves. Depending on whether both the tree and parenchyma are affected as in COPD, or only the tree as in asthma, curvature changes may be different.

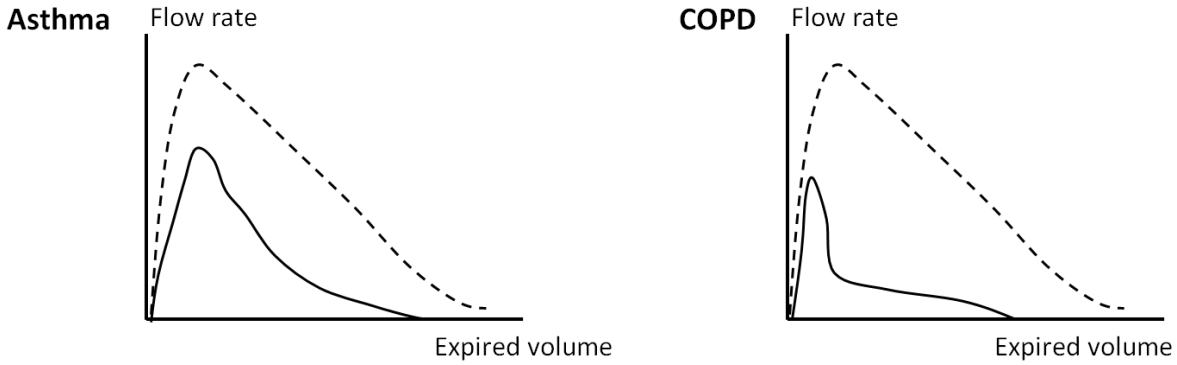

Figure 12: Typical flow volume spirometry curves in asthma (left), COPD (right) and healthy (dashed curve) cases. Modified from [38].

3. Motivations for lung ventilation modeling

As already stated lung is a complex multi-scale and multi-physics system. As described in section 2, in vivo or in vitro experiments enable to characterize some of its physiological properties and diagnose the underlying pathologies. Although they provide relevant insights, measurements are not

by themselves a prediction tool and they cannot be reproduced easily, in particular when the measurements require invasive procedures. Consequently, numerical experiments that can be referred to as *in silico* experiments, based on appropriate mathematical models, can provide useful tools to understand or predict the ventilation process in healthy or pathological situations. The mathematical models have to be simple but representative and their parameters shall be chosen based on the available measurements so that they can be easily fitted.
Mathematical modeling and numerical mehods can then be used either to:

- understand and reproduce a physical phenomenon or the effect of a pathology;
- investigate the efficiency of a therapy or a medical device;
- optimize a treatment.

In this thesis we will mostly focus on the two first issues but let us first illustrate these points by some examples.
A possible application of modeling is the understanding of pathological patterns effect on ventilation distribution. It is known from CT and MRI that bronchoconstrictions induce ventilation defects [**39**], [**40**], i.e. some regions of the parenchyma are not irrigated. The effect of constrictions on flow repartition as well as breathing efforts can be analyzed through modeling approaches [**41**]. Insights given by experiments on the distribution of stenoses (see section 2) can be used to build *in silico* asthma model and study how breathing efforts and ventilation are impacted by constrictions [**42**], [**43**] (and see CHAPTER III). Furthermore, modeling approaches enable to study how ventilation is affected depending on constriction severity or distality (see [**43**] and CHAPTER III).
Lung ventilation modeling can also be a tool to assess treatments efficiency. For instance it has been extensively used to predict aerosol deposition in the tree, [**44**], [**45**]. Upper airway geometry is acquired from CT/HRCT scans [**23**] or MRI [**45**] and Computational Fluid Dynamics (CFD) enables to simulate flows in this geometry. It has been observed experimentally with gamma-scintigraphy that while big particles get deposited in upper airways, small micrometric ones reach more distal regions [**46**]. Deposition highly depends on particle size, but also on airway geometry and breathing patterns. In this context, modeling can bring insights on respective contributions and may help optimizing therapies [**47**], [**48**].
Moreover, it has been advocated that breathing low-density gas mixtures instead of air can be mechanically easier and ensure a more homogeneous ventilation distribution for asthma and COPD patients. Several clinical trials have been conducted on the benefit of breathing helium-oxygen mixtures in case of obstructive lung diseases with no consensus on its efficiency [**49**]. In this context, modeling may help understanding why, when affected by a same disease, some patients respond to the treatment while others do not [**43**]. This is the object of CHAPTER III.
Another application for models is a better understanding of functional tests. For instance, spirometry tests (see section 2) provide a global flow measurement. Modeling may help to understand how tree and parenchyma pathological patterns influence the flow volume loop [**50**], [**51**], [**52**].
Finally, modeling can give insights on the use and impact of biomedical devices. In some cases such as acute lung injury, acute severe asthma or neurological diseases such as muscular dystrophy, spontaneous breathing can be inadequate to maintain life and respiration needs to be mechanically assisted. Though, this technique can be harmful [**53**] and some studies [**54**], [**55**] have focused on mechanical ventilation modeling in order to assess some of the associated risks and optimize the process.

4. State of the art on mathametical lung ventilation modeling

In this thesis we focus on lung ventilation modeling, i.e. the prediction of gas distribution within the tree, in health and disease. This has been addressed in numerous studies and a hierarchy of models is

proposed in the literature, from a two-parameter $0D$ lung description to tree-parenchyma coupled approaches with $3D$ geometries segmented from in-vivo imaging (see section 2). In this section, some of these models are described.

4.1. Mono-compartment zero-dimensional model

Here, we aim at describing the lung global volume evolution. In [**1**], a simple mono-compartment description of the lung is proposed. It is described as a single compartment, accounting for the parenchyma, irrigated with air through a single pipe that stands for the tracheo-bronchial tree (see Figure 13). Computed values are constant along the pipe, this is a $0D$ description. Elastic properties of the lung are modeled through a constant compliance C while a pipe resistance R_{AW} accounts for the energy it takes to induce flow through the tree. The actions of the diaphragm and chest wall appear though the application of a homogeneous time varying pleural pressure p_{pl}. The pressure inside the parenchyma is supposed homogeneous and equal to the alveolar pressure p_{alv}. The pressure at the mouth is p_{ext}. Let V_0 be the volume of the lung at rest, i.e. at FRC, and V its time dependent current volume along the breathing cycle. Following section 2, the lung compliance C is defined by:

$$C\left(p_{alv} - p_{pl}\right) = V - V_0, \tag{1}$$

and the pipe resistance R_{AW} is defined by:

$$R_{AW}\dot{V} = p_{ext} - p_{alv} \tag{2}$$

where $\dot{V}$ is the flow rate through the pipe. It is defined by $\dot{V} = \frac{dV}{dt}$. Denoting $\tilde{V} = V - V_0$ the inhaled volume and expressing the pressure difference between the mouth and the pleural space with (1) and (2) we get

$$R_{AW}\dot{\tilde{V}} + \frac{1}{C}\tilde{V} = p_{ext} - p_{pl}.$$

This is the governing equation of the system, its resolution provides lung ventilation. Assuming the pressure drop $p_{ext} - p_{pl}$ is known, one can deduce the parenchyma volume evolution and consequently have a global insight on the ventilation process. In order to investigate how pathologies impact ventilation, for a given pleural pressure, one can modify the various parameters: increasing R_{AW} to model asthma or decreasing C to model fibrosis. Nevertheless, as stated in section 2, the pleural pressure is not easily accessible. Reversely, from the knowledge of the volume evolution along with the lung compliance and the tree resistance, the pressure drop $p_{ext} - p_{pl}$ can be recovered. That is an indicator of the effort made by the patient to breath for a given scenario.
This model is too simple to capture for instance non linear effects or to describe the $3D$ flow or $3D$ parenchyma displacement. In particular the compliance is constant whereas, as seen in Figure 7 lung parenchyma has a non linear mechanical behavior when expanding above the FRC state. In [**56**] the authors propose to extend the model with a volume dependent compliance (see subsection 24.2.1). The resulting pressure-volume relation is no longer linear, and such compliance is thus referred to as *non-linear*. Another strong limitation is that this model does not account for heterogeneities: it provides global integrated values over the whole lung. To extend it, some multi-compartments descriptions have been proposed as explained in the next subsection. Note also that, as described in section 2, resistance can be flow dependant which is not accounted for here.

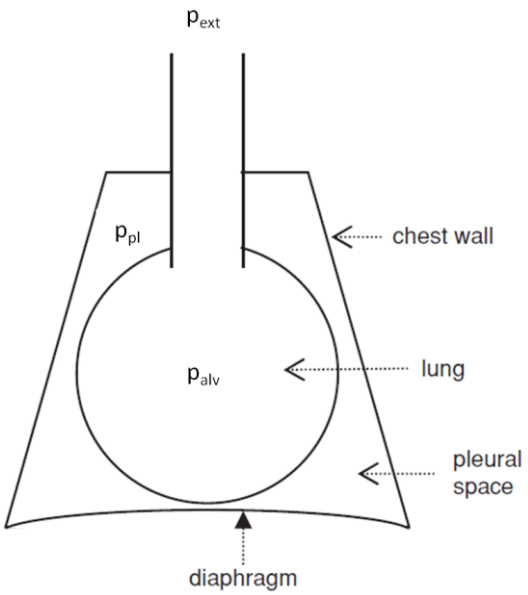

Figure 13: Illustration of a mono-compartment lung description. Modified from [1]. The whole lung is described as a single compartment irrigated by a pipe that accounts for the respiratory tree. Respiratory muscles induce variations of the pleural pressure (P_{pl}) around the lung in which the alveolar pressure is P_{alv}. Pressure at the mouth is P_{ext}.

4.2. Multi-compartment zero-dimensional model

In [**1**], as an extension to the mono-compartment description, a two-compartment lung model is proposed so as to account for regional differences in mechanical properties and ventilation distribution heterogeneity. In [**57**] and [**58**], going further, authors model the lung as a set of independent compartments standing for acinar units (see Figure 14), each one irrigated with gas by a terminal branch of the tracheo-bronchial tree. This description will be referred to as *multi-compartment* or *exit-compartment* model. The tree is described as a set of $0D$ resistive tubular branches and built thanks to a space-filling propagation model [**59**]. Both linear (i.e resistance is constant and pressure drop is thus a linear function of the flow) and flow-dependent resistance models can be considered. Various laws are used in the literature to account for acinar units mechanical properties. In [**1**] a linear model is proposed. In [**57**] compliances are heterogeneous and computed from a non linear hyperelastic constitutive relation. In [**58**] a multi-parameter nonlinear lumped model is used to account for the parenchyma mechanical properties. In both studies, nonlinear resistance models in which the resistance depends on the flow are used to describe the $0D$ airways. While airways are assumed to be rigid in [**57**], they are compliant in [**58**]. In the frame of the exit-compartment model, the pleural pressure evolution is imposed as boundary condition. From there the ventilation distribution can be computed. In [**57**] for instance, a homogeneous pressure boundary condition is applied, and ventilation heterogeneity stems from the heterogeneous distribution of compliance which is itself linked to gravity: upper regions of the lung are pre-extended by the weight of lower parenchyma areas and thus expand less over the breathing cycle.

Two main limitations can be emphasized for the exit-compartment model. First, as for the mono-compartment model, the pleural pressure has to be imposed as boundary condition. However, as noted in section 2, no in-vivo measurement enables to access its spatio-temporal distribution. The esophageal pressure (see section 2) is often taken as a surrogate but it does not account for possible spatial heterogeneities. In some studies, flow boundary conditions extracted from imaging are imposed (see details in subsection 4.3).

Another limitation of the exit-compartment description is that terminal units are mechanically independent from one another while the parenchyma is a continuum, at a lobar level at least. To overcome this problem, authors of [**60**] propose to link acini through static equilibrium conditions.

Inertia is thus neglected but this model can account for mechanical interactions between regions. To go further in the mechanical description of the lung parenchyma, other studies consider $3D$ elastic or visco-elastic models (see details in subsections 4.3 and 4.4).
Note also that considering $0D$ tubular airways might be irrelevant. In particular most proximal branches are curved and their sections vary (see Figure 9). This approximation may influence the ventilation distribution. As described in [**61**], the pressure drops computed in $3D$ upper airway geometries can differ significantly from those computed with available resistance models. In addition, knowing the flow patterns can be necessary, for example to compute particle deposition. Thus, some authors propose to account for proximal airways $3D$ geometries in ventilation models (see next subsection).

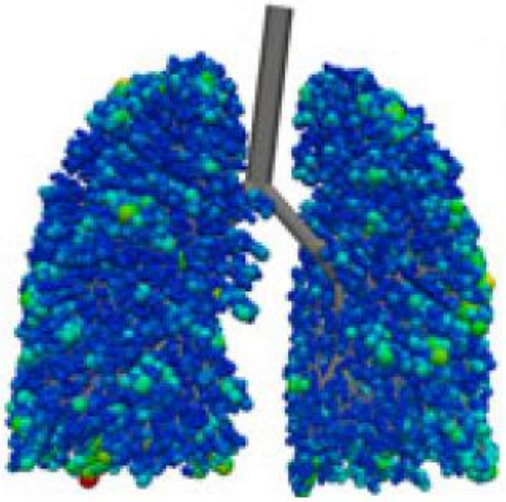

Figure 14: Illustration of a multi-compartment lung description. The tree is a set of tubular $0D$ airways. The parenchyma is modeled as a set of mechanically independent compartments (spheres). Here colors are relative to the ventilation distribution. Taken from [58**].**

4.3. Three-dimensional upper airways

As a $0D$ description of proximal airways can lead to errors on pressure drops and hence on flow distribution prediction, some authors propose a $3D$ description of proximal airways, possibly segmented from CT or MRI images [**62**], [**63**] or with idealized geometries [**64**]. The Navier-Stokes equations are numerically solved to compute the flow evolution within the respiratory tract. In this section we first present studies in which flow or pressure boundary conditions are directly imposed at the outlets of tree branches artificially defined as the tree exits. Then as extensions to the models presented in the previous subsection, we mention studies in which proximal $3D$ airways are coupled to exit compartments (see Figure 15).

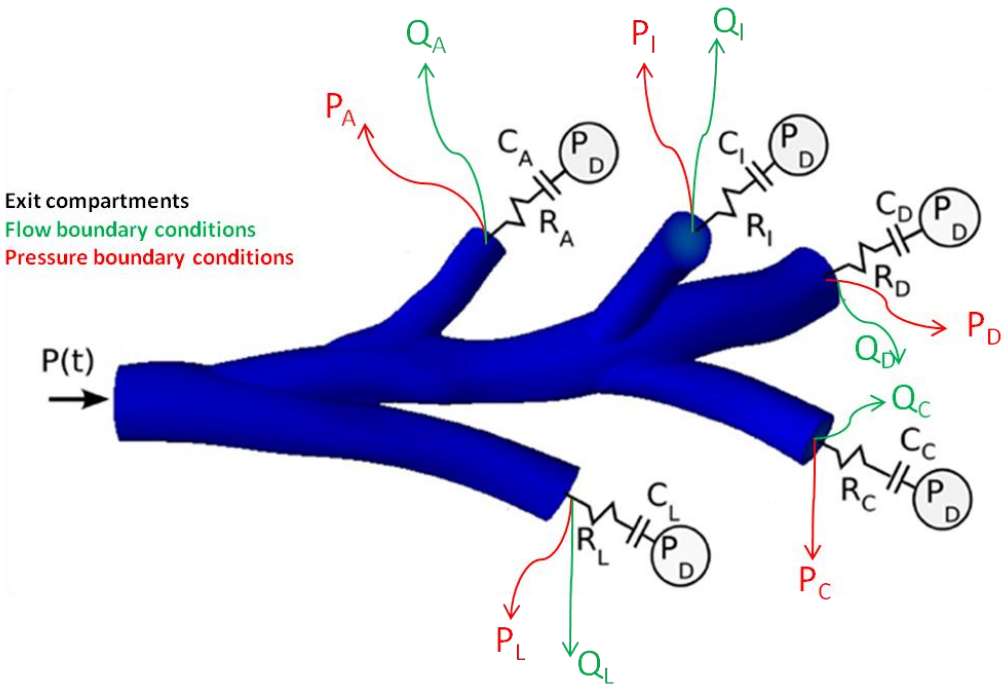

Figure 15: Illustration of $3D$ upper airways with various boundary conditions applied at the outlets artificially defined as tree exits. Modified from [63]. Upper airways are coupled to lumped compartments made of a resistance and a compliance (black), or pressure are imposed (red) at the outlets, or flows are imposed (red) at the outlets. A pressure is applied at the trachea entrance.

Three dimensional tree description with boundary conditions applied at the exits.

Various boundary conditions have been proposed to compute the flow distribution within the tree. In [**65**] for instance, authors choose to impose uniform pressure at the exits; such simplification does not enable to recover the true ventilation distribution [**66**]. In [**64**], pistons are set at airways exits and their motion is prescribed so as to impose a given breathing dynamics. In other studies [**61**], [**67**], flow boundary conditions are directly imposed at the tree outlets to ensure an arbitrary distribution or a uniform velocity.

Some studies propose to impose flows measured by imaging at the exits and deduce the ventilation distribution in the whole tree. In [**68**], local volume variations between two CT images of a patient at two different static lung inflation states are computed through a $3D$ registration method. Upper airways are segmented and from the registered evolution, flows are imposed at the tree exits. In [**69**] the same authors use this technique and compare the computed CFD lobar ventilation distribution with the ones obtained with the uniform pressure and uniform flow boundary conditions. Significant differences are observed which demonstrates the need to impose boundary conditions obtained from experimental measurements. In [**70**] the same type of analysis is performed and the lung hysteretic behavior is recovered. Although this approach generates faithful results in term of flow distribution, it is not predictive, in particular if some airways are constricted, one cannot determine how the distribution is affected. Local parenchyma volume evolution has to be coupled to the tree structure.

Three-dimensional tree description coupled to a reduced zero-dimensional parenchyma.

In [**62**], [**63**] upper $3D$ airways are coupled to $0D$ compartment models. The resulting system is the Navier-Stokes one with non standard boundary conditions at the outlets accounting for compartment models namely the distal subtree resistance and terminal compliance. In [**63**] for instance, proximal airways are coupled to lumped terminal compartments made of a resistance so as to model downstream sub-tree resistance and a constant compliance to describe the parenchyma behavior (see Figure 15). Zero pressure is applied to the compartments. The model is used to describe the ventilation distribution in a mechanical ventilation case: a pressure is imposed at the

trachea and respiratory muscles resistance to expansion is included in the compliance distribution. In [**71**] $3D$ upper airways are coupled to reduced $0D$ branches and impedance boundary conditions are applied at the exits.
Since the pressure around the parenchyma cannot be measured (see section 2), the relevance of applied boundary conditions remains a hard point. And as noted in previous section, neglecting mechanical interaction between compartments is a limitation of those models.

4.4. Zero-dimensional tree coupled to a three-dimensional parenchyma

In [**41**], the authors describe the parenchyma as a $3D$ porous medium irrigated by a space-filling $0D$ resistive tree. Energy dissipation within airways makes it harder to pull flow into the parenchyma. The tree and the parenchyma are coupled through the pressure exerted by the former on the latter and by ensuring a volume conservation constraint: under the gas incompressibility hypothesis, the gas volume entering or leaving a parenchyma region induces a corresponding volume variation of this region. The lung geometry is segmented from CT images. An arbitrary surface-displacement is imposed as boundary condition. With this model, the flow distribution within the tree can be studied along with the impact of resistance increase in a tree region or local elasticity change within the parenchyma.
Instead of imposing a volume constraint, the action of the tree on the parenchyma may be integrated into the parenchyma constitutive relation. Following [**72**], [**73**], this is the approach followed in this thesis (see CHAPTER II and [**74**]). Both pressure and surface displacement boundary conditions can be applied to the parenchyma. As the pleural pressure is not easily experimentally measurable, we propose to impose realistic Dirichlet boundary conditions extracted from lung images at different inflation states. The $3D$ parenchyma model could be further coupled to a full $3D$ flow model in the proximal part of the airway tree.

4.5. Full three-dimensional model

To our knowledge, [**75**] is the only study in which a $3D$ description of the airways is coupled to a $3D$ parenchyma model (see Figure 16). Upper airways geometry is segmented from a CT scan, and the flow within the tree is obtained from the resolution of Navier-Stokes equations. Unlike studies mentioned in subsection 4.3, airways are not assumed to be rigid, and fluid-structure interaction between the gas and the airway wall is taken into account. The parenchyma is described as a Neo-Hookean material. The coupling between the respiratory tract and the parenchyma is ensured by imposing volume conservation with Lagrange multipliers. This framework is used to mimic mechanical ventilation so as to investigate ventilator-associated lung injuries (see subsection 3). This fully $3D$ integrated model provides relevant ventilation and strain calculation results, though such a precise description is done at the price of time-consuming heavy computations.

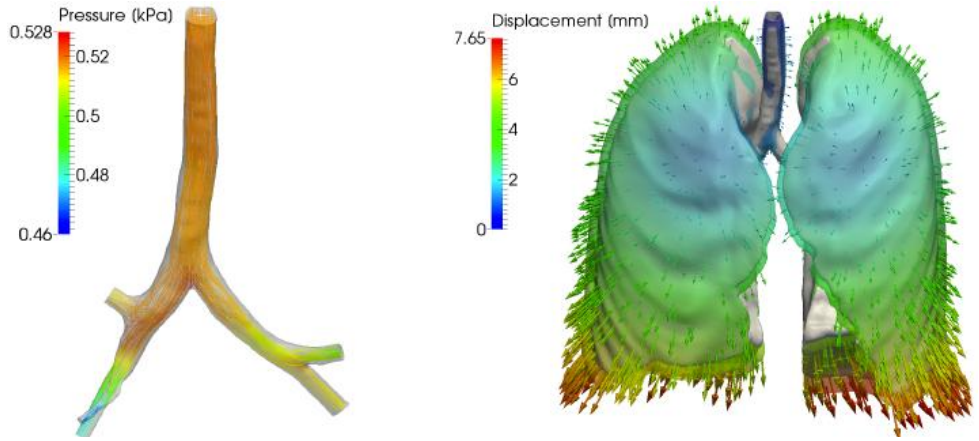

Figure 16: Lung ventilation model coupling $3D$ upper airways and the parenchyma. Geometries are segmented from CT scans. Surface displacement boundary conditions are applied to the parenchyma, this generates flow boundary conditions at the tree outlets for CFD calculations. Taken from [75].

4.6. A perspective on boundary conditions for lung ventilation modeling

As presented above, the various models require the knowledge of either the pleural pressure or the dynamic of the surface displacement of the parenchyma envelope. They correspond to the applied forces appearing as the right hand side of the 0D models for instance or as boundary conditions for the 3D parenchyma equations. Nevertheless pleural pressure cannot be measured in time and space around the lung, and assessing the parenchyma surface displacement requires heavy imaging techniques.
In [**76**], the authors propose an interesting method to recover the surface displacement from the knowledge of the skin motion only. The assessment of the parenchyma surface dynamics is based on the modeling of the rib cage motion and diaphragm action. More precisely, the thoracic cage outer skin displacement is first measured with captors and a kinematic model enables to deduce ribs motions. The action of the diaphragm is modeled based on the measured tracheal flow and sliding conditions are applied within the pleural cavity. Finally, the lung surface evolution is deduced from a mechanical model. This work has been further completed with models for the diaphragm [**77**] and for ribs kinematic [**78**].

As a conclusion to this section, we note that a large hierarchy of models has been proposed to describe lung ventilation. Depending on the needs, available data and numerical resources, one would rather use a fully reduced $0D$ description, a $3D$ tree-parenchyma coupled model or a model in between. In the next section, contributions to lung ventilation modeling brought by this thesis are presented.

5. Thesis organization and contributions

The main objective of this thesis is to provide a lung ventilation model and use it to study the organ behavior in a healthy case and when affected by airway obstructive diseases. In particular, we will investigate the impact of bronchoconstriction on ventilation distribution and breathing effort, and we will study the response of asthmatic patients to helium-oxygen treatments (see subsection 3). This model shall overcome limitations pointed out in the previous section, in particular we would like to:

- Apply realistic boundary conditions based on experimental measures
- Take into account the mechanical interaction between parenchyma regions.

To achieve these two goals, we first introduce the lung ventilation model presented in CHAPTER II. A space-filling $0D$ description of the tracheo-bronchial tree is adopted. Each branch is assumed to be rigid, and the pressure drop Δp along an airway is given by $\Delta p = Rq$ where R is the airway resistance and q the flow in the airway. The parenchyma is modeled as a $3D$ elastic continuum. As mentioned in section 4, the tree and parenchyma have to be coupled. Indeed, if for instance an airway is constricted, more energy is required to pull flow through it. Hence, parenchyma areas irrigated by stenosed branches are harder to contract or expand. The dynamics of a lung region are influenced by the resistance of the tree path through which it is irrigated.
Let Ω be the domain occupied by the parenchyma at the reference state. Each tree exit irrigates a region Ω_i (see Figure 17). The constitutive equations of the system are obtained by applying the least-action principle. The action of the tree on the parenchyma is similar as an apparent pressure exerted on each region. At least formally, we obtain the following strong formulation that describes the full coupled tree-parenchyma model:

$$div\left(\sigma_{mat} + \sigma_{coupling}\right) + \rho_{par}\boldsymbol{g} = \rho\ddot{\boldsymbol{u}}, \quad in\ \Omega.$$

where $\boldsymbol{u}$ is the parenchyma displacement field, ρ_{par} the parenchyma density, σ_{mat} the stress tensor of the parenchyma. The term $\sigma_{coupling}$ is the stress tensor associated to the tree-parenchyma coupling. As in the spirit of [**72**], [**73**], it is defined by:

$$\sigma_{coupling} = -p_{tree}I$$

where I is the identity operator, and p_{tree} is the piecewise constant function equals in region Ω_i to the pressure at tree exit irrigating Ω_i (see Figure 17). Note that here, the action of the tree is similar as a viscous term in the constitutive equations: the more the pressure drop along the path leading to Ω_i, the harder it is to induce volume variations of this region. In particular, the pressure p_{tree} can be further expressed thanks to the volume variations of the terminal region Ω_i and thus depends on the displacement velocity. As shown in CHAPTER II, we have:

$$p_{tree} = \sum_i \mathbb{1}(\Omega_i)\,[P_{trachea} - (AQ)_i]$$

where $\mathbb{1}$ is the characteristic function and $P_{trachea}$ is the pressure at the trachea entrance. Matrix A accounts for the tree resistance distribution, and the i^{th} component q_i of vector Q is the flow irrigating region Ω_i. The i^{th}component $(AQ)_i$ of AQ, is the pressure drop from the tree entrance to the i^{th} tree exit. The flow q_i is linked to the parenchyma displacement field through the linearized relation

$$q_i = \frac{d}{dt}\int_{\Omega_i} div(\boldsymbol{u}).$$

This global formulation, that integrates the action of the tree in the constitutive law, is an alternative to the approaches found in [**41**], [**75**] where the tree and the lung parenchyma are coupled thanks to volume conservation constraints.

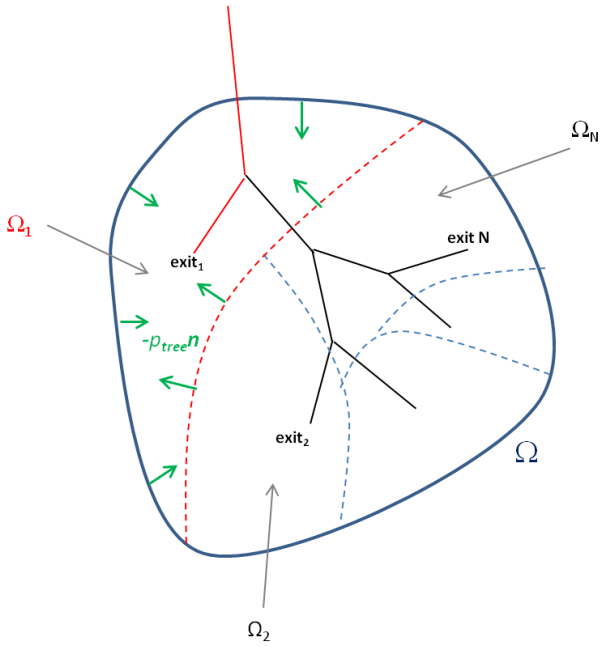

Figure 17: apparent pressure exerted on terminal regions. The domain Ω is occupied by the parenchyma and subdivided into non-intersecting regions Ω_i, each of which is fed in gas through the exit i. Green arrows represent the apparent pressure p_{tree} applied on terminal region Ω_1 when it expands due to the coupling with the tree, *n* is the normal vector to Ω_1 boundary.

Next, the variational form associated with the strong formulation is discretized in time, then in space in the finite element framework, and finally solved. With the chosen coupling formulation, the resulting system contains less degrees of freedom than with the approaches proposed in [**41**] and [**75**]. But the finite element matrix C associated to $\sigma_{coupling}$ is full: the tree couples all the degrees of freedom of the system. The strategy is thus to compute, efficiently and based on the problem structure, the product of C with a vector without assembling C. The resulting linear system associated to the discretized tree-parenchyma coupled model is then solved with an iterative method. Compared to [**41**] and [**75**], stored objects are lighter. We work on patient-specific tree and lung geometries segmented from HRCT images.

Both pressure and surface displacement boundary conditions can be applied. In this study, we propose to extract the parenchyma surface evolution from HRCT images. Contrarily to pleural pressure which cannot be measured, this a physiologically realistic boundary condition issued from in-vivo data. Both boundary conditions are compared in terms of the ventilation they induce. We also investigate the impact of the airway resistance model: a linear description and a non linear model proposed by Pedley [**17**] in which the resistance depends on the flow are compared. Significant differences are obtained in case of stenoses. The influence of bronchoconstrictions and parenchyma local stiffening on the ventilation distribution are studied. We also compare how the gas distributes in the frame of our tree-parenchyma coupled model and with the exit-compartment description (see subsections 4.2). The assumption of regional mechanical independence can thus be investigated showing that mechanical connections may have an impact on the ventilation distribution, in particular in pathological configurations.

In CHAPTER III, we take advantage of the tree-parenchyma coupled model to further investigate ventilation distribution and breathing effort for healthy and asthmatic cases, when changing the breathed gas. In particular we propose an asthma model: bronchoconstrictions are stochastically generated within the tree following statistical laws chosen based on histological studies and HRCT images of pathological trees. In the frame of Pedley model, airway resistance accounts for inertial effects and depends and the gas density. Low density gas induce smaller pressure drops and are thus easier to breathe. As mentioned in section 3, clinical trials were conducted to study the benefit of helium-oxygen (Heliox) mixtures on asthma and COPD patients [**49**]. Results were contradictory or inconclusive. For instance, some asthmatic patients respond while others do not. In this chapter we

investigate how helium-oxygen mixtures influence the effort and ventilation compared to air. We conclude that the treatment may be efficient in case of proximal rather than distal constrictions, and in diaphragmatic regions where the lung expands more rather than around the apex where flows are reduced. We also study how the respiratory frequency influences breathing efforts.
To model asthma, and predict responsiveness to helium-oxygen mixtures as done in CHAPTER III, it is necessary to get insights on the constriction distribution. Constrictions also influence aerosol deposition [**79**] and knowing their localization may help predicting the efficiency of inhaled therapies. Imaging techniques such as HRCT enable to visualize stenoses in proximal generations (see section 2). However, to the best of our knowledge, no in-vivo technique gives insights on the constriction distribution in more distal generations. The tree-parenchyma coupled model developed in this thesis indicates that severe constrictions strongly influence the ventilation distribution. Dynamic imaging techniques such as 4D-CT [**80**] or 4D-MRI [**81**] provide ventilation maps that shall thus correlate to the constriction distribution. In CHAPTER IV we propose to use those dynamic maps to get insights on the tree pathological patterns. More precisely, we investigate how the airways radii and hence their constrictions can be inferred from the parenchyma displacement field. In the frame of this study, we suppose that the tree topology and the parenchyma mechanical properties are known. We also suppose the parenchyma displacement field can be extracted from the 4D images. From the tree-parenchyma coupled model and using imaging data, we compute exit tree pressures as the solution of a minimization problem. Then, based on the ventilation model described in CHAPTER II, we show that if the tree contains $2N-1$ airways, only less than N independent equations can be written, the unknowns being the airways radii. To choose which one shall be considered as unknowns, a machine learning process that predicts branch constriction likeliness based on the ventilation maps is proposed. The system is then inverted to identify which airways are severely constricted. Promising results are obtained.
The last chapter is devoted to some perspectives of the present work. As mentioned in section 2, a standard diagnostic tool is the spirometry test. In spirometry, expiratory flows are much higher than in tidal breathing. Inertial effects can be important and parenchyma deformations are large. To account for this complex physics, the exit-compartment model is extended with non-linear compliances so that it is harder to expand the lung when its volume gets close to TLC and inversely. For the tree-parenchyma coupled model, we propose a way to determine which surface force is equivalent to given Dirichlet boundary conditions and we investigate how the flow-volume loop is impacted by bronchoconstrictions. Many more developments shall be brought to those models in order to predict spirometry.
A second possible improvement is linked to the obtention of input data. Indeed, our tree-parenchyma coupled model requires complex data that are not available in routine practice: lung and tree geometry for instance. A daily use of this model is thus compromised. If input data could be determined from simple measurements on the patient outer body: bust height or thoracic cage perimeter for example, one could use the model on a broader scale. In this chapter, we focus on determining the proximal tree topology, i.e. nodes position, from the knowledge of lung surface. A machine learning technique is used to correlate the shape and the tree topology. As a preliminary, shape dimensionality is reduced with a principal component analysis technique. Encouraging results are obtained.
Part of these works have been published or will be submitted in the form of articles.

6. List of publications

A tree-parenchyma coupled model for lung ventilation simulation [published];
Int J numer Method Biomed Eng, 2017, Pozin N, Montesantos S, Katz I, Pichelin M, Vignon-Clementel I, Grandmont C.

Calculated ventilation and effort distribution as a measure of respiratory disease and Heliox effectiveness [accepted];
J Biomed, 2017, Pozin N, Montesantos S, Katz I, Pichelin M, Vignon-Clementel I, Grandmont C.

From 4D lung dynamic maps to plugs distribution in asthma – a diagnosis tool [to be submitted]

CHAPTER II-
A tree-parenchyma coupled model for lung ventilation simulation

In this chapter we develop a lung-ventilation model. The parenchyma is described as an elastic homogenized medium. It is irrigated by a space-filling dyadic resistive pipe network, which represents the tracheo-bronchial tree. The tree and the parenchyma are strongly coupled. The tree induces an extra viscous term in the system constitutive relation, which leads, in the finite element framework, to a full matrix. We consider an efficient algorithm that takes advantage of the tree structure to enable a fast matrix-vector product computation. This framework can be used to model both free and mechanically induced respiration, in health and disease. Patient-specific lung geometries acquired from HRCT scans are considered. Realistic Dirichlet boundary conditions can be deduced from surface registration on HRCT images. The model is compared to a more classical exit-compartment approach. Results illustrate the coupling between the tree and the parenchyma, at global and regional levels, and how conditions for the purely $0D$ model can be inferred. Different types of boundary conditions are tested, including a nonlinear Robin model of the surrounding lung structures.
The content of this chapter has been published in the form of an article [**74**].

7. Introduction

The lung is a complex multi-scale and multi-physics system. It supplies the organism with oxygen by carrying a flow of fresh air through the tracheo-bronchial airway tree. Gas exchange takes place in regions distal to the tree, in the alveoli, which are embedded in a viscoelastic tissue, called the lung parenchyma (see section 1). Common lung diseases can affect lung ventilation distribution [**82**], [**83**] and numerous studies have focused on lung ventilation modeling (see section 4).

In [**1**], the lung is modeled as a single viscoelastic compartment fed in gas by a resistive pipe. Although this model is able to recover appropriate tidal tracheal flow and lung volume evolution through the respiration cycle, it does not give insights on regional ventilation. In [**57**], [**58**] the single compartment model is extended to a multi-compartment description. The lung is seen as a $0D$ space-filling resistive branching network feeding independent compliant terminal regions. A possible limitation of this exit compartment model is that it is driven by a pressure forcing term, though no in-vivo experiment provides the spatio-temporal pressure field around the lung. Some studies [**69**], [**28**], [**70**] propose to impose flows determined from image registration as boundary conditions at the tree exits. Ventilation distribution is then computed along the tree. This approach may provide relevant results but it is not predictive. In particular, boundary conditions acquired in a healthy configuration cannot be used to simulate ventilation when airway remodeling occurs. Besides, to distribute the flow obtained from the surface displacement among the different tree exits is not obvious. Another possible limitation of the exit compartment model is that terminal units are mechanically independent from one another; this may not reflect the lobar-level-continuous nature of the parenchyma. Some studies [**84**], [**4**] treat the parenchyma as a continuous elastic material but do not consider the effect of the tree on the parenchyma dynamics, though in some pathological cases airway remodeling induces ventilation defects. In [**60**] an exit-compartment model in which compartments are mechanically linked through a static equilibrium relation is proposed.

In this work we treat the parenchyma as an elastic medium coupled, in the same spirit as [**41**], to a space-filling dyadic resistive tree. In [**41**], the tree is coupled to a poroelastic medium through applied pressures and volume preservation constraints. Here we consider a linear elastic medium. We derive the governing weak equations of the tree-coupled model by applying the least-action principle. It leads to the same type of coupling conditions as in [**41**]. Here, we take advantage of the fact that the action of the tree can be viewed as a damping term in the tree-parenchyma constitutive law, together with the tree structure, to propose a new efficient numerical scheme to treat the coupling between the airway tree and the lung tissue. To overcome the lack of knowledge on pleural pressure we propose to apply Dirichlet boundary conditions namely the surface displacement of the parenchyma, which can be registered from images at different lung inflation states. We work on physiologically realistic tree and lung geometries segmented from $3D$ computed tomography (CT) images. We study the influence of airway remodeling on ventilation heterogeneity. Finally, we also investigate the possible limitations of the exit compartment description through a comparison to the tree-parenchyma coupled model.

In Section 8, the theoretical background of the model is presented and the tree-parenchyma coupling governing equations are obtained. An exit compartment model designed for comparison is also described. It assumes alveolar regions are mechanically independent from one another. To enrich the comparison, we show how the tree-parenchyma coupled model can be used in order to compute a pressure forcing term that takes into account the mechanical interaction between alveolar regions and that is applicable to the exit-compartment model. In section 9, numerical methods used to solve equations of both models are presented. In section 10, we detail how the space-filling tree and the parenchyma mesh, along with its registered surface displacement are built. In section 11, some numerical examples are presented. We test the tree-parenchyma coupled model in spontaneous tidal breathing conditions with both linear and non-linear flow dissipation models and we study the effect of bronchoconstriction on lung ventilation. Then, we investigate the assumption of mechanical independence between the exit compartments in the eponym model. Based on parenchyma surface

image registration, we apply "realistic" Dirichlet boundary conditions and we study the impact of various boundary conditions on the ventilation distribution. Finally we simulate a pressure-controlled mechanical ventilation with boundary conditions that prevent the lung from expanding over total lung capacity.

8. Model

First we present two different ventilation models. Each of them takes into account the compliant behavior of the lung tissue. The first one - called here tree-parenchyma model - describes the parenchyma as an elastic continuous media. The second one, called hereafter the exit compartment model, treats the parenchyma as a set of independent compliant compartments, each of them characterized by a unique compliance coefficient. In both cases the lung tissue receives inhaled air through a branching network of pipes that represents the bronchial tree. We assume that the air flow in each branch of this dyadic tree is characterized by a resistance, modeling fluid dissipation. In this section, we thus present the resistive tree model, then the tree-parenchyma model and the exit compartment model. The last two models are finally compared and their links explained.

8.1. Tracheo-bronchial tree

The gas flows through a dyadic branching network (see Figure 18) and we assume its branches to be rigid during the respiration cycle. This assumption is reasonable under tidal breathing conditions as a first approximation and is supported by simulations performed in [**58**]. Moreover the fluid is assumed to be Newtonian and incompressible. The air incompressibility is justified since the Mach number is much lower than one [**3**]. We also neglect fluid inertance [**58**]. Consequently the air flow in each cylindrical branch of the tree can be characterized by a single resistance parameter denoted R and the pressure drop Δp along an airway is proportional to the flux q within the branch, namely

$$\Delta p = Rq.$$

In the case of Poiseuille flow in a circular branch we have

$$R_{pois} = \frac{8\mu L}{\pi r^4}, \tag{3}$$

where μ is the fluid dynamic viscosity, L and r are the pipe's length and radius, respectively. If only interconnected pipes in which the fluid flow is described by Poiseuille law are considered, one may fail to predict accurately the pressure drops due to bifurcations and to non-linear inertial effects, in particular in the upper airways [**61**]. In [**17**] Pedley proposes a non-linear resistance model designed to account for the pressure drop at symmetric bifurcations:

$$R_{ped} = \begin{cases} \gamma \left(Re \frac{2r}{L} \right)^{\frac{1}{2}} R_{pois}, & R_{ped} > R_{pois}, \\ R_{pois}, & R_{ped} < R_{pois}, \end{cases} \tag{4}$$

where $\gamma = 0.327$ and Re is the Reynolds number defined by $Re = \frac{2\rho|q|}{\mu\pi r}$ with ρ the fluid density. This model is designed to treat bifurcations with a branching angle θ=70°. However θ does not significantly impact the pressure drop as noted in [**85**], so R_{ped} will be used independently of the angle. Note that the Pedley model was designed for inspiration. Since the aim here is to model the tree-parenchyma coupling and to investigate the possible effects of resistance non-linearities, and

not to provide a precise description of pressure drops in the tree, (4) is also used for expiration. Other non-linear resistance laws in the literature [**61**], [**15**] could also be readily incorporated in the proposed model.

A human tracheo-bronchial tree contains on average 24 generations leading to 2^{23} exits [**5**]. To reduce the computational cost, starting at a given generation, we condense the subtrees into single equivalent branches, hereafter called tree exits. In distal regions, under tidal breathing, the Reynolds number is low. Flows are laminar and fully developped so that Poiseuille law holds true. We also assume that subtrees are symmetrical. As in [**5**] we assume distal airways resistances follow a geometrical progression with common ratio 1.63. Given those assumptions, a subtree equivalent resistance can be computed according to classical series/parallel resistance network formulas. This requires that outlet pressures within each subtree are uniform; which is usually valid when the subtree is small, i.e. when the tree exit generation is high. Note that, as shown in Appendix 13.1, pressure drops significantly decrease in distal regions compared to upper airways.

Now, following [**72**], [**86**], we describe how to link pressure drops between the trachea and the exits, and exit flows. Let Γ be a $0D$ dyadic tree structure with N terminal branches. Let vectors $\delta_{V\,tree} = \begin{pmatrix} P_{trachea} - P_{ex_1} \\ \vdots \\ P_{trachea} - P_{ex_N} \end{pmatrix}$ and $Q = \begin{pmatrix} Q_1 \\ \vdots \\ Q_N \end{pmatrix}$, where $P_{trachea}$ is the pressure at the trachea entrance, and P_{ex_i} and Q_i are the pressure and flow at the i^{th} exit, respectively. Let us denote T_i the set of indices (n,k) associated to airways going from the trachea down to the i^{th} exit (see Figure 19). Set T_i defines a unique path and it will be indistinctly referred to as *set* or *path*. Index n refers to the airway generation starting at zero. Index k orders the airways of a given generation. From a branch to its sister it has a unit increment. A tree is said to be complete if each path contains the same number of generations. On a complete tree, at a given generation n, index k runs through interval $[\![0; 2^n - 1]\!]$. From a complete tree one can extract a dyadic subtree as illustrated on Figure 19. We denote T_{ij} the intersection set between T_i and T_j (see Figure 18).

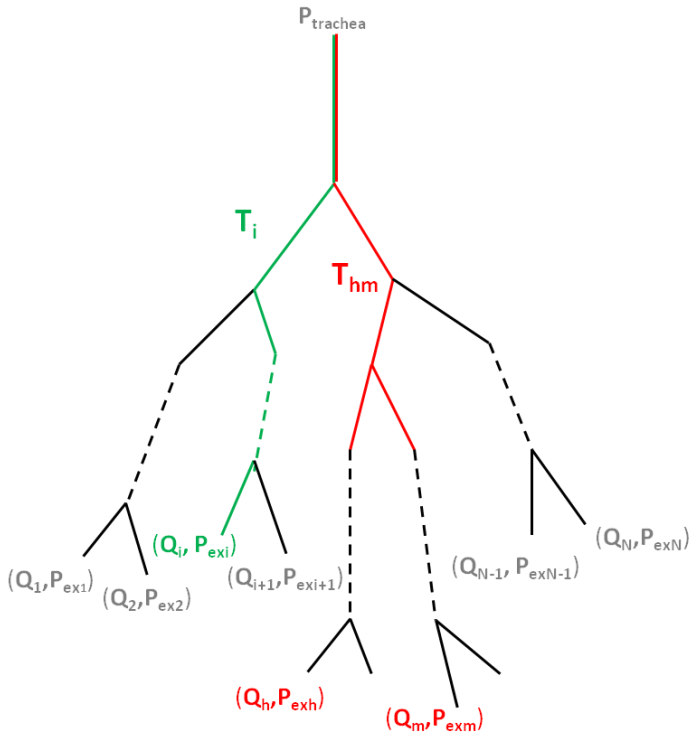

Figure 18: schematic tracheo-bronchial tree representation, from the trachea down to the N exits through each path T_i (example in green). T_{hm} (in red) contains the branches common to the paths T_h and T_m.

Since conducting airways are assumed rigid and gas flow is incompressible, the flow going through a

branch equals the sum of the flows going through its daughters (see Appendix 13.3). Under these conditions, it can be shown (see [**72**] and subsection 13.2) that $\delta_{V_{tree}}$ and Q are linked by a linear operator that accounts for the tree resistance:

$$\delta_{V_{tree}} = AQ, \tag{5}$$

where $A = \left[A_{ij}\right]_{ij}$ with $A_{ij} = \sum_{(n,k)\in T_{ij}} R_{n,k}$, $R_{n,k}$ being the resistance associated with branch (n,k) (see Figure 19). This formulation avoids computing the pressure at each tree node as in [**58**], [**41**] hence keeping the number of unknowns tractable. The power dissipated in the tree can be written as

$$\wp = {}^{T}QAQ \tag{6}$$

where ${}^{T}Q$ is the transposed vector to Q.

Remark 1: If one wants to take into account airway compliance using, for example, the model developed in [**58**], then the mother to daughter flow conservation does not hold anymore; and (5) is no longer valid. However, as shown in Appendix 13.2, by considering the model of [**58**], the flux loss due to compliant airways is negligible. Nevertheless, to take into account airway compliance, one can consider that the radii in (3) or (4) are given by a quasi-static elastic law; see for instance [**87**] where such models are described.

Pressure at the trachea is an external force applied to the system. If breathing is spontaneous and without considering the extra-thoracic part, this pressure is a known constant, the atmospheric pressure. The extra-thoracic part could be included as an extra resistance at the trachea level. In case of mechanical ventilation, air is pushed in by the ventilator resulting in an imposed pressure $P_{ventilator}(t)$ at the trachea, so $P_{trachea}(t) = P_{ventilator}(t)$. Exit tree pressures on the other hand are unknowns of the system. In the following we show how they can be determined and coupled to the parenchyma.

8.2. A tree-parenchyma coupled model

We assume that the lung parenchyma is an isotropic elastic media occupying a $3D$ domain denoted by Ω. Here, since our aim is to describe the tree-parenchyma coupling, we choose to consider a linearized behavior law and to neglect tissue viscosity. This assumption can be justified when considering normal breathing (see section 12). Let us denote the displacement of the parenchyma by $\boldsymbol{u}$ defined in Ω, taken as the reference state of the lung. The linearized stress tensor of the media is given by

$$\sigma_{mat}(\boldsymbol{u}) = 2\mu\varepsilon(\boldsymbol{u}) + \lambda tr\big(\varepsilon(\boldsymbol{u})\big)I,$$

where λ and μ are the Lamé parameters of the effective material, and ε the strain tensor defined by $\varepsilon(\boldsymbol{u}) = \frac{1}{2}(\nabla\boldsymbol{u} + {}^{T}\nabla\boldsymbol{u})$. Note that these effective macroscopic coefficients λ and μ may be obtained using a homogenization process as described in [**73**] and [**88**]. The latter takes into account the alveoli microstructure so that we may refer to the homogenized media when considering the lung tissue. In particular, when the alveoli are assumed to have a hexagonal shape and to be uniform in size then the isotropic behavior of the homogenized law can be derived [**73**].

As stated above, the lung parenchyma is supplied with gas that flows through a dyadic resistive tree. If an airway of the tracheo-bronchial tree is nearly closed (due to a stenosis for example) the related supplied region will require more effort to stretch, even if its elastic properties are not affected.

Hence the parenchyma and the tree models need to be mechanically coupled. Let us assume that $\Omega = \cup_{i=1}^{N} \Omega_i$ and $\forall i, j \; \Omega_i \cap \Omega_j = \emptyset$, for each of the subregions Ω_i corresponding to one tree exit (see Figure 19). Doing so we neglect the conductive tree volume which is of the order of 100mL [**3**] and which is indeed much smaller than the overall lung volume (around 5L). We denote $\Omega_i(t)$ the image of Ω_i through the transformation $I + \boldsymbol{u}(\boldsymbol{x}, \boldsymbol{t})$**.** Assuming that lung tissue at the microscopic level is incompressible and because of the fluid incompressibility, the volume variation of $\Omega_i(t)$ is equal to the associated fluid flux, namely

$$Q_i = \dot{V}_i$$

where V_i is the volume of $\Omega_i(t)$. So setting $\dot{\boldsymbol{u}}(x,t) = \frac{\partial \boldsymbol{u}}{\partial t}(\boldsymbol{x}, t)$, we have

$$Q_i = \frac{d}{dt}\int_{\Omega_i} \det(I + \nabla \boldsymbol{u}) = \int_{\partial\Omega_i} \dot{\boldsymbol{u}} \cdot \operatorname{cof}(I + \nabla \boldsymbol{u})\boldsymbol{n} = \int_{\partial\Omega_i(t)} \dot{\boldsymbol{u}} \cdot \boldsymbol{n}(t) \tag{7}$$

where $\partial\Omega_i$ is the boundary of Ω_i, $\boldsymbol{n}(t)$ is the unit normal vector along $\partial\Omega_i(t)$ and $\operatorname{cof}(\mathrm{A})$ the cofactor matrix of a matrix A. Under the hypothesis of small displacements around the reference state, which is assumed to be the initial position, we get

$$Q_i(\dot{\boldsymbol{u}}) \approx \int_{\partial\Omega_i} \dot{\boldsymbol{u}} \cdot \boldsymbol{n}\,. \tag{8}$$

Next, to derive the system of equations describing the time evolution of the coupled tree-parenchyma system, we apply the least-action principle. Since energy is lost in the resistive tree the system is dissipative. In case resistances do not depend on the flow, based on (6), the power lost to friction can be included in the Lagrangian with a Rayleigh dissipation function:

$$F = \frac{1}{2}{}^{T} Q(\dot{\boldsymbol{u}}) A Q(\dot{\boldsymbol{u}}). \tag{9}$$

where Q is the vector of elements defined by (8). Next the kinetic and potential energies of our system as well as the work of the external forces can be defined as follows. The kinetic energy of the system is

$$E_c = \frac{1}{2}\int_{\Omega} \rho_{par} \, |\dot{\boldsymbol{u}}|^2 \tag{10}$$

where ρ_{par} is the macroscopic lung parenchyma density. The potential energy of the system is

$$E_p = \frac{1}{2}\int_{\Omega} \sigma_{mat}(\boldsymbol{u}) : \varepsilon(\boldsymbol{u}) - \int_{\Omega} \rho_{par} \boldsymbol{g} \cdot \boldsymbol{u} \tag{11}$$

where the colon denotes the contraction operation between tensors. Depending on the respiration regime, the chest and diaphragm induce a surface force field, $\boldsymbol{f}$**,** on the parenchyma, generating or resisting the motion. The associated work is

$$H = \int_{\partial\Omega} \boldsymbol{f} \cdot \boldsymbol{u} + P_{trachea} \int_{\partial\Omega} \boldsymbol{n} \cdot \boldsymbol{u} \tag{12}$$

that includes the pressure at the trachea introduced previously. The Lagrangian of the tree-

parenchyma system S writes

$$L(\boldsymbol{u}, \dot{\boldsymbol{u}}) = E_C + H - E_p.$$

In case dissipative forces are applied to S, the Lagrange equation is

$$\frac{d}{dt}\left(\frac{\partial L}{\partial \dot{\boldsymbol{u}}}\right) - \frac{\partial L}{\partial \boldsymbol{u}} + \frac{\partial F}{\partial \dot{\boldsymbol{u}}} = 0. \tag{13}$$

Its weak form reads

$$\int_0^\tau \left(\frac{\partial L}{\partial \dot{\boldsymbol{u}}}(\boldsymbol{u}, \dot{\boldsymbol{u}}).\dot{\boldsymbol{w}} + \frac{\partial L}{\partial \boldsymbol{u}}(\boldsymbol{u}, \dot{\boldsymbol{u}}).\boldsymbol{w} - \frac{\partial F}{\partial \dot{\boldsymbol{u}}}(\boldsymbol{u}, \dot{\boldsymbol{u}}).\boldsymbol{w}\right) = 0, \tag{14}$$

$\forall \tau > 0$ and $\forall \boldsymbol{w}$ sufficiently smooth such that $\boldsymbol{w}(., t = 0) = \boldsymbol{w}(., t = \tau) = 0$ and $\dot{\boldsymbol{w}}(., t = 0) = \dot{\boldsymbol{w}}(., t = \tau) = 0$.
From (9) we easily have:

$$\frac{\partial F}{\partial \dot{\mathbf{u}}}.\boldsymbol{w} = {}^tQ(\boldsymbol{w})AQ(\dot{\boldsymbol{u}}) = \delta_{tree}(\dot{\boldsymbol{u}}) \int_\Omega div(\boldsymbol{w}) = \int_\Omega \delta_{tree} I : \varepsilon(\boldsymbol{w}),$$

where δ_{tree} is the piecewise-constant function defined by

$$\delta_{tree}(\dot{\boldsymbol{u}}) = (AQ)_i \ \ in\ \Omega_i\ . \tag{15}$$

From (10) we derive

$$\frac{\partial E_c}{\partial \boldsymbol{u}} = 0 \text{ and } \frac{\partial E_c}{\partial \dot{\boldsymbol{u}}}.\dot{\boldsymbol{w}} = \int_\Omega \rho_{par}\ \dot{\boldsymbol{u}} \cdot \dot{\boldsymbol{w}}.$$

From (11) we have

$$\frac{\partial E_p}{\partial \boldsymbol{u}}.\boldsymbol{w} = \int_\Omega \sigma_{mat}(\boldsymbol{u}) : \varepsilon(\boldsymbol{w}) - \int_\Omega \rho_{par}\ \boldsymbol{g} \cdot \boldsymbol{w} \text{ and } \frac{\partial E_p}{\partial \dot{\boldsymbol{u}}} = 0.$$

From (12) we get

$$\frac{\partial H}{\partial \boldsymbol{u}}.\boldsymbol{w} = \int_{\partial\Omega} \boldsymbol{f} \cdot \boldsymbol{w} + P_{trachea} \int_{\partial\Omega} \boldsymbol{w} \cdot \boldsymbol{n} \text{ and } \frac{\partial H}{\partial \dot{\boldsymbol{u}}} = 0.$$

So (14) reads

$$\int_0^\tau \left(-\int_\Omega \rho_{par}\ \ddot{\boldsymbol{u}} \cdot \boldsymbol{w} + \int_{\partial\Omega} \boldsymbol{f} \cdot \boldsymbol{w} + P_{trachea} \int_{\partial\Omega} \boldsymbol{w} \cdot \boldsymbol{n} + \int_\Omega \rho_{par}\ \boldsymbol{g} \cdot \boldsymbol{w} - \int_\Omega \sigma_{mat}(\boldsymbol{u}) : \varepsilon(\boldsymbol{w}) - \int_\Omega (\delta_{tree}(\dot{\boldsymbol{u}}))I : \varepsilon(\boldsymbol{w})\right) = 0$$

from which we deduce the weak formulation of the equations satisfied by $\boldsymbol{u}$: $\forall \boldsymbol{w}$ being sufficiently smooth

$$\rho_{par} \int_\Omega \ddot{\boldsymbol{u}} \cdot \boldsymbol{w} + \int_\Omega \sigma_{mat}(\boldsymbol{u}) : \varepsilon(\boldsymbol{w}) + \int_\Omega \delta_{tree}(\dot{\boldsymbol{u}}) I : \varepsilon(\boldsymbol{w}) - \int_\Omega \rho_{par}\ \boldsymbol{g} \cdot \boldsymbol{w} - \int_{\partial\Omega} \boldsymbol{f} \cdot \boldsymbol{w} - P_{trachea} \int_{\partial\Omega} \boldsymbol{w} \cdot \boldsymbol{n} = 0\ . \tag{16}$$

The associated strong formulation then reads:

$$div(\sigma_{mat}(\boldsymbol{u}) + \delta_{tree}(\dot{\boldsymbol{u}})I) + \rho_{par}\boldsymbol{g} = \rho_{par}\ddot{\boldsymbol{u}}, \quad in\ \Omega.$$

It is associated with the following Neumann boundary conditions:

$$\sigma_{mat}(\boldsymbol{u})\boldsymbol{n} + \delta_{tree}(\dot{\boldsymbol{u}})\boldsymbol{n} = \boldsymbol{f} + P_{trachea}\boldsymbol{n} \quad on\ \partial\Omega.$$

Let p_{tree} be the piecewise constant function defined by

$$p_{tree}(\dot{\boldsymbol{u}}) = P_{trachea} - \delta_{tree}(\dot{\boldsymbol{u}})\,, \tag{17}$$

which is the pressure felt by the parenchyma material. Equation (16) then writes:

$$\rho_{par}\int_{\Omega}\ddot{\boldsymbol{u}}\cdot\boldsymbol{w} + \int_{\Omega}\sigma_{mat}(\boldsymbol{u}):\varepsilon(\boldsymbol{w}) - \int_{\Omega}p_{tree}(\dot{\boldsymbol{u}})I:\varepsilon(\boldsymbol{w}) - \int_{\Omega}\rho_{par}\,\boldsymbol{g}\cdot\boldsymbol{w} - \int_{\partial\Omega}\boldsymbol{f}\cdot\boldsymbol{w} = 0\,. \tag{18}$$

The associated strong formulation is:

$$div\left(\sigma_{mat}(\boldsymbol{u}) + \sigma_{coupling}(\dot{\boldsymbol{u}})\right) + \rho_{par}\boldsymbol{g} = \rho_{par}\ddot{\boldsymbol{u}}, \quad in\ \Omega. \tag{19}$$

It is associated with the following Neumann boundary conditions:

$$\sigma_{mat}(\boldsymbol{u})\boldsymbol{n} + \sigma_{coupling}(\dot{\boldsymbol{u}})\boldsymbol{n} = \boldsymbol{f}, \quad on\ \partial\Omega \tag{20}$$

where $\sigma_{coupling}$ is the stress tensor associated with the action of the tree on the parenchyma

$$\sigma_{coupling}(\dot{\boldsymbol{u}}) = -p_{tree}(\dot{\boldsymbol{u}})I. \tag{21}$$

With such a coupling, the displacement field is the only unknown. Note that the approach introduced in [**75**] to impose the flux conservation (8) uses a Lagrange multiplier, thus introducing new variables. This is not the case here since we have a global formulation describing the fully coupled system. The tree-parenchyma coupling reduces to an apparent piecewise-constant pressure that depends on the flow. The associated volume force is

$$\boldsymbol{f}_{coupling} = \boldsymbol{\nabla}p_{tree}. \tag{22}$$

The function p_{tree} is defined by (17). Equation (22) is only defined at the distribution level since it is a Dirac on the terminal regions boundaries. The effect of the tree is analog to an apparent pressure exerted on terminal regions boundaries (see Figure 19). Flow dissipation in the tree induces an extra viscous component to the parenchyma constitutive relation: $\int_{\Omega}\delta_{tree}(\dot{\boldsymbol{u}})I:\varepsilon(\boldsymbol{w})$. From the mechanical point of view it makes it harder to expand the effective material during inspiration and to contract it during expiration. Higher flow means more power is required to induce motion. Note that (22) remains valid when A depends on the flow, p_{tree} still being given by (17). This generalizes the approach to any airway resistance law, e.g for non-linear models.

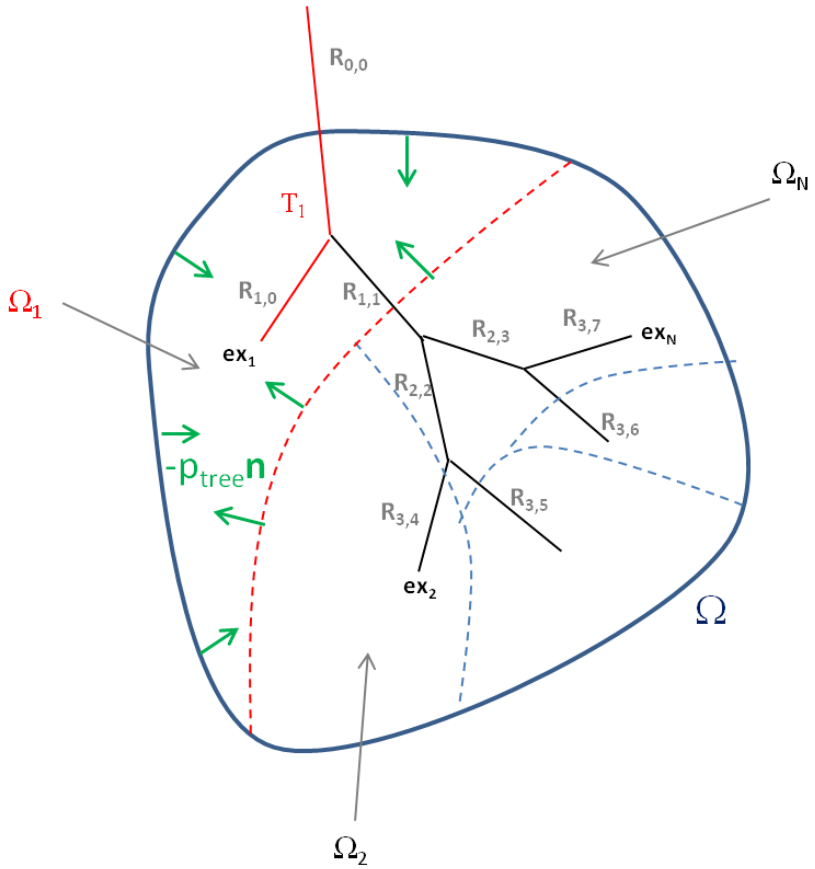

Figure 19: apparent pressure exerted on terminal regions. The domain Ω is occupied by the parenchyma and subdivided into non-intersecting regions Ω_i, each of which is supplied gas through the path T_i. Each airway (n,k) has a resistance $R_{n,k}$. Green arrows represent the apparent pressure p_{tree} applied on terminal region Ω_1 when it expands due to the coupling with the tree.

The derivation has been performed, as an illustration, for a Neumann boundary condition (20). In the case where a pressure field is applied around the parenchyma, $\boldsymbol{f}$ is

$$\boldsymbol{f} = -P\boldsymbol{n}, on\ \partial\Omega,$$

where P corresponds to the pleural pressure field around the parenchyma. However, there is no consensus on the spatio-temporal distribution [**89**] of this pressure. To our knowledge, non-invasive in-vivo measurements cannot be performed. Other boundary conditions can be applied; in particular we can impose Dirichlet boundary conditions by prescribing the spatio-temporal displacement field of the parenchyma surface:

$$\boldsymbol{u} = \boldsymbol{u_D}, on\ \partial\Omega,$$

where $\boldsymbol{u_D}$ may be provided by imaging data as we will see in section 11.4. The variational formulation of the problem is given by:

$$\rho_{par}\int_\Omega \ddot{\boldsymbol{u}}\cdot\boldsymbol{w} + \int_\Omega \sigma_{mat}(\boldsymbol{u}):\varepsilon(\boldsymbol{w}) + \int_\Omega \delta_{tree}(\dot{\boldsymbol{u}})I:\varepsilon(\boldsymbol{w}) - \int_\Omega \rho_{par}\boldsymbol{g}\cdot\boldsymbol{w} = 0.$$

with $\boldsymbol{u} = \boldsymbol{u_D}$ on $\partial\Omega$, and $\boldsymbol{w}$ such that $\boldsymbol{w} = 0$ on $\partial\Omega$.

For mechanical ventilation or spirometric tests modeling, Robin boundary conditions can be applied to model the action of the surrounding tissue. Based on [**56**] we propose non-linear boundary conditions that take into account the chest and the diaphragm resistance to lung expansion. One can consider $\boldsymbol{f}$ given by

$$\boldsymbol{f} = -k(V)\boldsymbol{u} \; on \; \partial\Omega$$

where k is a lobar dependent function that can be for instance defined by

$$k(V) = k_i(V_i) = c_i \frac{(V_{tlc_i} - V_{frc_i})V_i}{V_{tlc_i} - V_{frc_i} - V_i}, \quad if \; \boldsymbol{x} \in \partial L_i \cap \partial\Omega \tag{23}$$

with ∂L_i the outer surface of lobe *i*, V_i , V_{frc_i} and V_{tlc_i} are the current inhaled volume in lobe *i*, its volume at functional residual capacity (FRC) and total lung capacity (TLC) respectively. Coefficient c_i is a constant. Its value should be chosen based on physiological considerations, that is to say the compliance of the lung surrounding media: rib cage, diaphragm. At a given volume inflation, function k is constant on each lobe: the constraint is assumed to be uniform at a lobar level.

A complete problem statement for this system (19) requires boundary conditions as well as initial conditions. We simulate respiration, which is a periodic phenomenon. This means here that initial conditions will not affect the behavior of the system after a transition period. The initial conditions used herein are simply $\boldsymbol{u}(\boldsymbol{x}, t = 0) = 0, in \; \Omega$ and $\dot{\boldsymbol{u}}(\boldsymbol{x}, t = 0) = 0, \quad in \; \Omega$.

Instead of considering the parenchyma as a continuum, some models (see [**1**], [**57**], [**58**], [**45**]) consider a set of mechanically independent compartments. In the following we present an exit-compartment model in the perspective of a comparative study between both descriptions.

8.3. An exit-compartment model

Here, the tracheo-bronchial tree feeds some “balloons” that represent groups of alveolar sacs. They are modeled through a $0D$ pressure-volume relationship that can incorporate viscous, elastic and inertial effects. This kind of model is based on an inherent assumption: exit compartments are mechanically independent although the lung parenchyma is a continuous media, at least at a lobar level. In this framework, spontaneous ventilation is driven by the pleural pressure evolution, which is, as stated before, challenging to measure. Both the mechanical independence assumption and the lack of knowledge on pleural pressure are possible limitations to the use of such model. In order to investigate these possible drawbacks, an exit-compartment model (see Figure 20) is defined and compared to the previous tree-parenchyma coupling description.

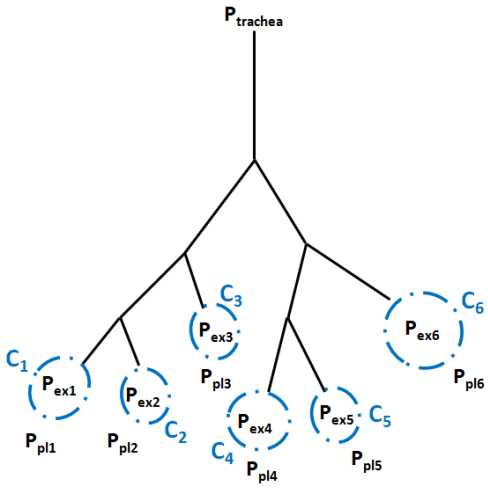

Figure 20: schematic of a 6-exit tree in the frame of the exit-compartment model. The tree spplies gas to independent terminal regions standing for groups of alveolar sacs. Elastic properties of those compartments are accounted for by compliances C_i. Inside each compartment is the alveolar region with pressure P_{exi}, while outside is the local pleural pressure P_{pli}.

To make a relevant comparison, the tree description remains unchanged, and as for the parenchyma (see subsection 8.2), terminal balloon dynamics is governed by a linear elastic law. The pressure P_{ex_i} in the i^{th} compartment is linked to the local pleural pressure around the parenchyma P_{pl_i} through

$$P_{ex_i} - P_{pl_i} = \frac{V_i - V_{0_i}}{C_i}$$

where V_i and V_{0_i} are respectively the current volume and the reference state configuration volume of the compartment. Coefficient C_i is the i^{th} balloon compliance and quantifies the stiffness of the region. Since compliance is an extensive variable, C_i can be chosen as $C_i = \frac{V_{0_i}}{V_0} C_{lung}$ where V_0 is the lung volume at the reference state and C_{lung} is the total static lung compliance. In a pathological case where lung tissue properties are locally affected, one can modify regional compliances accordingly.
The pressure drop along the tree according to (5) is

$$\begin{pmatrix} P_{trachea} - P_{ex_1} \\ \vdots \\ P_{trachea} - P_{ex_N} \end{pmatrix} = AQ. \tag{24}$$

The pressure drop in the alveolar region is

$$\begin{pmatrix} P_{ex_1} - P_{pl_1} \\ \vdots \\ P_{ex_N} - P_{pl_N} \end{pmatrix} = B_c(V - V_0) \tag{25}$$

where $V = \begin{pmatrix} V_1 \\ \vdots \\ V_N \end{pmatrix}$, $V_0 = \begin{pmatrix} V_{0_1} \\ \vdots \\ V_{0_N} \end{pmatrix}$ and B_c is the diagonal matrix with coefficient $\frac{1}{C_i}$ on the i^{th} diagonal element. Denoting $\tilde{V} = V - V_0$, and since $\dot{\tilde{V}} = Q$, summing up equations (24) and (25) leads to the following system of governing equations:

$$A\dot{\tilde{V}} + B_c\tilde{V} = P_{tr} - P_{pl} \tag{26}$$

where $P_{tr} = \begin{pmatrix} P_{trachea} \\ \vdots \\ P_{trachea} \end{pmatrix}$ and $P_{pl} = \begin{pmatrix} P_{pl_1} \\ \vdots \\ P_{pl_N} \end{pmatrix}$.

Remark 2: the balloons' compliance C_i could be chosen as current volume dependent in the same spirit as the Robin boundary conditions described in subsection 8.2. Doing so would take into account that the lung is harder to expand when its volume gets close to the total capacity and harder to contract when its volume gets close to the residual capacity, see [**56**].

In the following we show how the pleural pressure applied as a forcing term to this exit-compartment model can be computed from the tree-parenchyma coupled model.

8.4. From the tree-parenchyma coupled model to the exit-compartment model

In this section we compute the average pressure P_i^{eff} endured by terminal region Ω_i in the tree-parenchyma coupled model. This resulting pressure naturally includes the mechanical connection between alveolar regions and its evolution can be driven by "realistic" Dirichlet boundary conditions (see subsection 8.2). Then P_i^{eff} is applied as a driving force to the balloon i of the exit compartment model. Doing so accounts for mechanical interactions between compartments and avoids the need to know the pleural pressure distribution around the lung.
The pressure applied to the i^{th} terminal balloon of the exit-compartment model is

$$P_i^{eff}(t) = -\frac{1}{S_i}\int_{\partial\Omega_i} \sigma\, \boldsymbol{n}\cdot\boldsymbol{n}dS$$

where σ is the parenchyma stress tensor and $S_i = \int_{\partial\Omega_i} \boldsymbol{n}\cdot\boldsymbol{n}dS$. As tangential forces are not included in P_i^{eff}, energy spent to induce motion might be different in both models although ventilation is the same. We have:

$$P_i^{eff}(t) = -\frac{1}{S_i}\int_{\partial\Omega_i} (\sigma_{\,coupling} + \sigma_{parenchyma})\boldsymbol{n}\cdot\boldsymbol{n}dS\,.$$

The coupling term is easily computed following (17) and (21),

$$\tfrac{1}{S_i}\textstyle\int_{\partial\Omega_i} \sigma_{coupling}\, \boldsymbol{n}\cdot\boldsymbol{n}dS = (AQ)_i - P_{trachea}\,.$$

In the linear elasticity framework we assume

$$-\frac{1}{S_i}\int_{\partial\Omega_i} \sigma_{parenchyma}\boldsymbol{n}\cdot\boldsymbol{n}dS \;= \frac{\int_{\Omega_i} p_{elastic}(\boldsymbol{u})}{V_{0_i}}$$

where, when neglecting shear and inertia, the elastic pressure associated with the recoil of the material is

$$p_{elastic}(\boldsymbol{u}) = -Kdiv(\boldsymbol{u}) \tag{27}$$

with K the bulk modulus. It sets a correspondence between Lamé parameters and the local

compliance. For a given domain with reference volume V_0 we have:

$$K = \frac{E}{3(1-2\nu)} = -V_0 \frac{dp_{elastic}}{dV} = \frac{V_0}{C} \tag{28}$$

where, E is the Young modulus, ν is the Poisson ratio. Coefficients E and ν are linked to the Lamé parameters through $\lambda = \frac{\nu E}{(1+\nu)(1-2\nu)}$, $\mu = \frac{E}{2(1+\nu)}$.
Under the assumption that elastic pressure is null at equilibrium, it leads to

$$P_{elastic,i} = -\frac{1}{S_i}\int_{\partial\Omega_i} \sigma_{parenchyma}\boldsymbol{n}\cdot\boldsymbol{n}dS \ = \frac{\int_{\Omega_i} p_{elastic}(\boldsymbol{u})}{V_{0_i}} = -K\frac{V_i - V_{0_i}}{V_{0_i}}$$

where V_{0_i} is the reference equilibrium volume of region i. To account for a residual pressure at equilibrium a constant can simply be added. We finally end up with a similar equation as (26):

$$P_{pl_i}(t) - P_{trachea}(t) = P_i^{eff}(t) - P_{trachea} = -(AQ)_i - \frac{E}{3(1-2\nu)}\frac{V_i - V_{0_i}}{V_{0_i}}. \tag{29}$$

Next, to solve the governing equations presented in the current section, efficient numerical methods are developed.

9. Numerical methods

In this section we describe numerical methods used to solve constitutive equations of both models. The weak form of the equations governing the tree-parenchyma coupled model (see subsection 8.2) is discretized in time and space within the finite element framework. As described below, due to the tree the obtained linear system contains a full matrix. Consequently this can make a direct resolution inefficient. A decomposition of this operator enabling the use of a fast matrix-vector product is thus proposed. The system is then solved iteratively. Iterative methods are not commonly used in elasticity; however, it is possible here since the homogenized material is compressible, and even approaching incompressibility the system can still be solved. The linear system governing the exit-compartment model (26) is discretized in time and efficiently inverted following methods described in [**73**].

9.1. Tree-parenchyma coupled model

Let $\Delta t > 0$ be the time step. For any vector $\boldsymbol{h}$ we denote $\boldsymbol{h}^n$ its approximation at time $n\Delta t$. In the following, discretization is performed on the variational form relative to the Neumann pressure boundary conditions case (18). A similar treatment can be applied to other boundary conditions. As in [**73**] we apply the following time scheme:

$$\begin{cases} \boldsymbol{u}^{n+1} = \boldsymbol{u}^n + \Delta t\boldsymbol{k}_{\boldsymbol{u}}^{n+1} \\ \dot{\boldsymbol{u}}^{n+1} = \dot{\boldsymbol{u}}^n + \Delta t\boldsymbol{k}_{\boldsymbol{v}}^{n+1} \\ \boldsymbol{k}_{\boldsymbol{u}}^{n+1} = \dot{\boldsymbol{u}}^n + \Delta t\boldsymbol{k}_{\boldsymbol{v}}^{n+1} = \dot{\boldsymbol{u}}^{n+1} \end{cases} \tag{30}$$

and equation (18) discretized with (30) leads to

$$\int_\Omega \rho_{par} \boldsymbol{k_v^{n+1}}.\boldsymbol{w} = -\int_\Omega \sigma_{mat}(\boldsymbol{u}^n + \Delta t \boldsymbol{k_u^{n+1}}): \varepsilon(\boldsymbol{w}) - \int_\Omega \sigma^n{}_{coupling}(\boldsymbol{k_u^{n+1}}): \varepsilon(\boldsymbol{w}) - \int_{\partial\Omega} P^{n+1}\boldsymbol{w}\cdot\boldsymbol{n}$$

When considering non-linear resistances, they are treated explicitly; i.e. to solve the system at step $n+1$ the resistance matrix (see subsection 8.2) is computed with flows from step n. We get to solve $b(\boldsymbol{k_u^{n+1}}, \boldsymbol{w}) = L(\boldsymbol{w})$ where $L(\boldsymbol{w}) = \int_\Omega \rho_{par}\boldsymbol{v}^n \cdot \boldsymbol{w} - \Delta t \int_\Omega \sigma_{mat}(\boldsymbol{u}^n): \varepsilon(\boldsymbol{w}) - \Delta t \int_{\partial\Omega} P^{n+1}\boldsymbol{w}\cdot\boldsymbol{n}$ and $b(\boldsymbol{k_u}, \boldsymbol{w}) = \int_\Omega \rho_{par}\boldsymbol{k_u}\cdot\boldsymbol{w} + \Delta t^2 \int_\Omega \sigma_{mat}(\boldsymbol{k_u}): \varepsilon(\boldsymbol{w}) + \Delta t \int_\Omega \sigma^n{}_{coupling}(\boldsymbol{k_u}): \varepsilon(\boldsymbol{w})$.
Implementation is performed on our in-house finite element software FELIScE [**90**]. Lagrangian P1 finite elements are used for space discretization. Decomposition in the finite element basis leads to:

$$E\, X^{n+1} + C^n\, X^{n+1} = F^{n+1}_{pressure} \tag{31}$$

where X^{n+1} is the vector representation of $\boldsymbol{k_u^{n+1}}$ in the finite element method (FEM).
Matrix E stands for the mass and elastic term. It is the FEM matrix associated with the linear form $(\boldsymbol{k_u}, \boldsymbol{w}) \mapsto \int_\Omega [\rho \boldsymbol{k_u}\cdot\boldsymbol{w} + \Delta t^2 \sigma_{mat}(\boldsymbol{k_u}): \varepsilon(\boldsymbol{w})]$. In the linear elasticity framework we have:

$$E = \left[E_{ij}\right]_{ij} = \left[\int_\Omega \rho_{par}\boldsymbol{e_i}\cdot\boldsymbol{e_j} + \Delta t^2 \int_\Omega [2\mu\varepsilon(\boldsymbol{e_i}): \varepsilon(\boldsymbol{e_j}) + \lambda div(\boldsymbol{e_i}) div(\boldsymbol{e_j})]\right]_{ij} \tag{32}$$

where $\boldsymbol{e_l}$ is the l^{th} element of the finite element basis.
The matrix C^n represents the coupling term associated to following bilinear form:

$$(\boldsymbol{k_u}, \boldsymbol{w}) \mapsto \Delta t \int_\Omega (A^n Q) div(\boldsymbol{w}) = \Delta t \sum_m (A^n Q)_m \int_{\Omega_m} div(\boldsymbol{w})$$

where $(A^n Q)_m$ is the m^{th} component of vector $A^n Q$ and $Q_l = \int_{\Omega_l} div(\boldsymbol{k_u})$. So we have:

$$C^n \boldsymbol{k_u} = \left[\Delta t \sum_m \left(A^n \begin{pmatrix} \int_{\Omega_1} div(\boldsymbol{k_u}) \\ \cdots \\ \cdots \\ \int_{\Omega_N} div(\boldsymbol{k_u}) \end{pmatrix}\right)_m \int_{\Omega_m} div(\boldsymbol{e_l})\right]_l \tag{33}$$

and finally

$$C = \Delta t\, B^T A\, B \tag{34}$$

with $B = \left[\int_{\Omega_i} div(\boldsymbol{e_j})\right]_{ij}$. The decomposition given by (34) is a consequence of the tree structure. Note that C^n is a full matrix since the tree couples all the FEM degrees of freedom of the system.
Finally the right hand side of (31) writes:

$$F^{n+1}_{pressure} = \left[\int_\Omega \rho_{par}\boldsymbol{v}^n\cdot\boldsymbol{e_l} - \Delta t \int_\Omega \sigma_{mat}(\boldsymbol{u}^n): \varepsilon(\boldsymbol{e_l}) - \Delta t \int_{\partial\Omega} P^{n+1}\boldsymbol{e_l}\cdot\boldsymbol{n}\right]_l . \tag{35}$$

Equation (31) is solved through a conjugate gradient method with preconditioning. A Jacobi preconditioner is computed at the first time step and then reused to precondition the system at further time steps. Robustness of the resolution scheme is studied in Appendix 13.4. Operator C changes at each time step when resistances are non-linear. Assembling and storing C would be a highly memory demanding operation. Taking advantage of its decomposition (34) and noticing that B

is a sparse matrix and A is small compared to C (the size of A is the number of tree exits, which is much lower than the size of the finite element system), we do not assemble C and rather compute $Y = CX$ product through

$$\begin{bmatrix} Y \longleftarrow BX \\ Y \longleftarrow AY \\ Y \longleftarrow B^T Y \end{bmatrix}$$

enabling more efficient computation (see subsection 11.6). Note that in case A is a big matrix, i.e. the tree contains a high number of branches, product AX can be computed without storing A by taking advantage of the tree structure as described in [**73**].
When Dirichlet boundary conditions are applied, the right hand side of (31) is replaced by

$$\begin{aligned} F_{surface}^{n+1} = \Bigg[& \int_\Omega \rho_{par} \boldsymbol{v}^n . \boldsymbol{e_l} - \Delta t \int_\Omega \sigma_{mat}(\boldsymbol{u}^n) : \varepsilon(\boldsymbol{e_l}) + \int_\Omega \rho_{par} (\boldsymbol{v_D^n} - \boldsymbol{v_D^{n+1}}) . w \\ & - \Delta t \int_\Omega \sigma_{mat}(\boldsymbol{u_D^n}) : \varepsilon(\boldsymbol{w}) - \Delta t^2 \int_\Omega \sigma_{mat}(\boldsymbol{v_D^{n+1}}) : \varepsilon(\boldsymbol{w}) \\ & - \Delta t \int_\Omega \sigma_{coupling}(\boldsymbol{v_D^{n+1}}) : \varepsilon(\boldsymbol{w}) \Bigg]_l , \end{aligned} \tag{36}$$

where $\boldsymbol{u_D}$ and $\boldsymbol{v_D}$ are respectively liftings of the displacement and velocity of the parenchyma surface.
Discretizing the variational formulation associated to the Robin boundary condition leads to the following system:

$$E\ X^{n+1} + C\ X^{n+1} + R_{mecha}^{n+1} X^{n+1} = F_{mecha}^{n+1} \tag{37}$$

with

$$R_{mecha} = \left[\Delta t^2 \int_\Gamma k(V^{n+1}) \boldsymbol{e_i} \cdot \boldsymbol{e_j} \right]_{ij}$$

and

$$F_{mecha}^{n+1} = \left[\int_\Omega \rho_{par} \boldsymbol{v}^n \cdot \boldsymbol{e_l} - \Delta t \int_\Omega \sigma_{mat}(\boldsymbol{u}^n) : \varepsilon(\boldsymbol{e_l}) + \Delta t \int_{\partial\Omega} P_{vent}^{n+1}\ \boldsymbol{n} \cdot \boldsymbol{e_l} - \Delta t \int_{\partial\Omega} k(V^{n+1}) \boldsymbol{u}^n \cdot \boldsymbol{e_l} \right]_l$$

where P_{vent} is the trachea pressure for mechanical ventilation. The Robin boundary conditions are treated implicitly through a fixed-point algorithm with relaxation as illustrated by the following scheme:

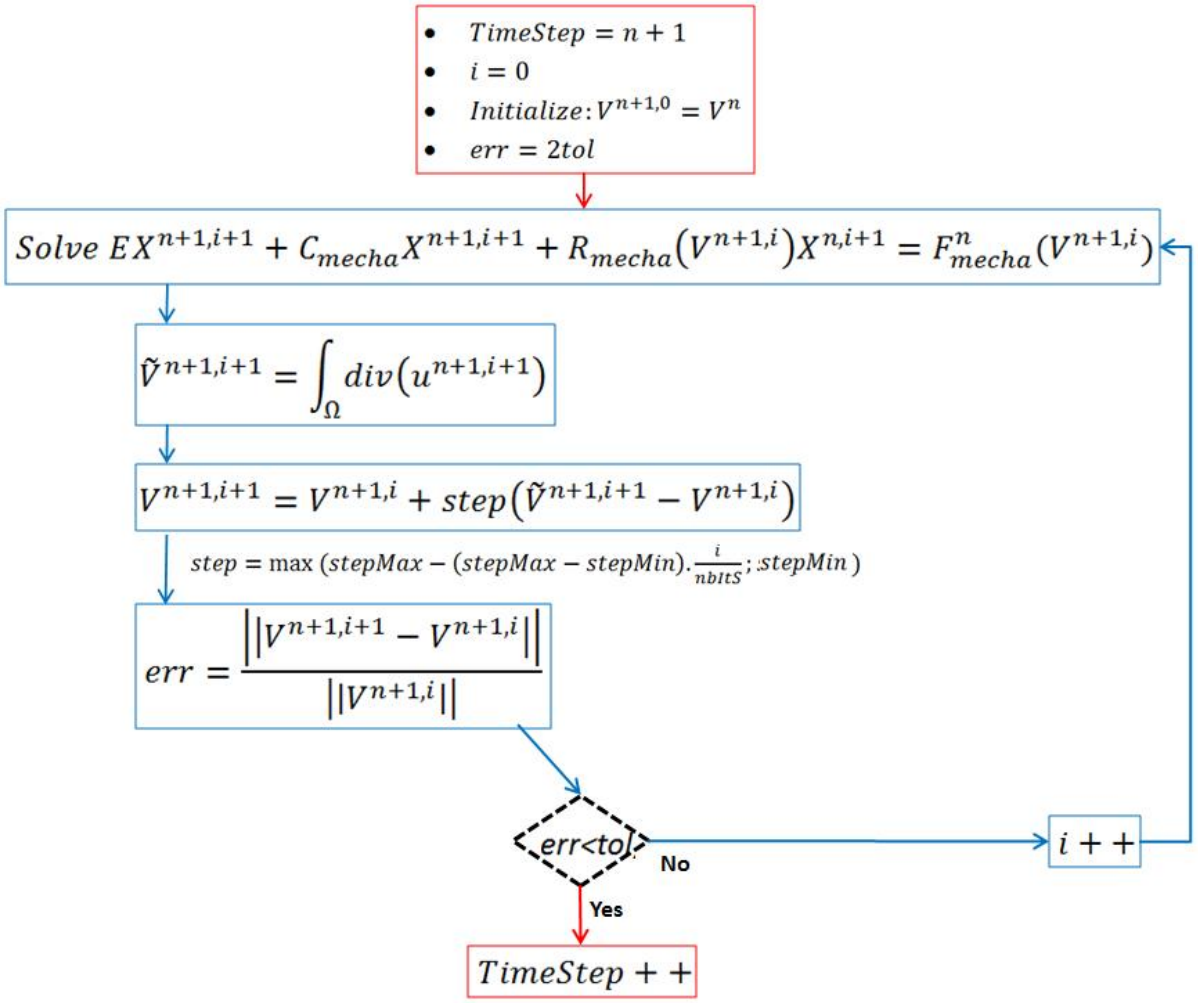

Figure 21: resolution scheme for non-linear Robin boundary conditions. Non-linearities in the boundary are treated through a fixed-point scheme (blue loop) with tolerance given by the coefficient tol and relaxation accounted by the coefficient step. Step is computed upon $stepMax$ and $stepMin$, positive real numbers fixing the amount of relaxation in the system and $nbItS$ is an integer determining at which pace relaxation is introduced.

Remark 3: To ensure numerical stability, rather than the continuous version of $k(V)$ given by (23) we consider the following approximation:

$$k_i(V_i) = \begin{cases} c_i \dfrac{(V_{tlc_i} - V_{frc_i})V_i}{V_{tlc_i} - V_{frc_i} - V_i}, & V < r(V_{tlc_i} - V_{frc_i}) = V_{M_i}, \\ a_i + b_i V_i, & V \geq r(V_{tlc_i} - V_{frc_i}) = V_{M_i}, \end{cases}$$

with r close to 1 and a_i, b_i chosen so that k_i is a $\mathbf{C^1}$ function: $\begin{cases} a_i = c_i \dfrac{(V_{tlc_i} - V_{frc_i})^2}{(V_{tlc_i} - V_{frc_i} - V_{M_i})^2}, \\ b_i = c_i \dfrac{(V_{tlc_i} - V_{frc_i})V_{M_i}}{V_{tlc_i} - V_{frc_i} - V_{M_i}} - aV_{M_i}. \end{cases}$,

With this choice of k_i, we ensure an increasing recoil when the lung expands, as shown in Figure 22.

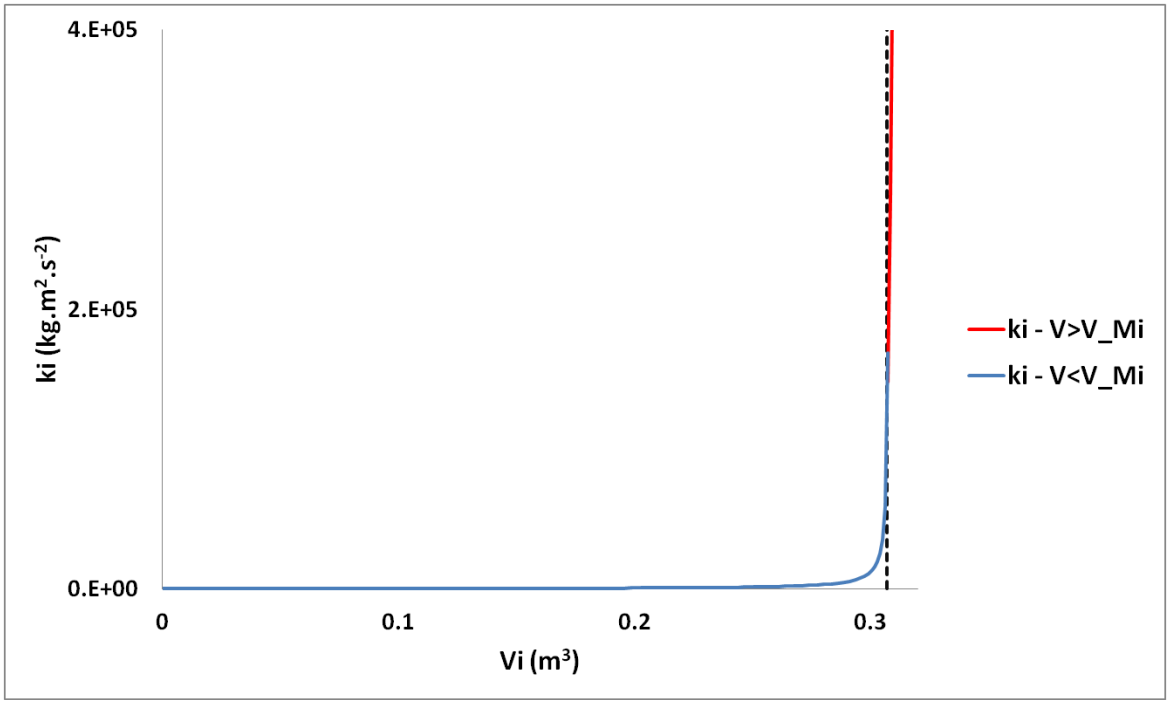

Figure 22: lobar recoil function. To ensure numerical stability, k_i is linearly extended for values above the TLC lobar volume. For this plot r=0.999 and $(V_{tlc_i} - V_{frc_i}) = 0.31L$.

9.2. Exit-compartment model

In order to solve (26) we introduce an Euler explicit time scheme:

$$(A^n + \Delta t {B_c}^n)\tilde{V}^{n+1} = A^n\tilde{V}^n + \Delta t\left(P_{tr} - P_{pl}\right)^{n+1}$$

It follows

$$\tilde{V}^{n+1} = (A^n + \Delta t {B_c}^n)^{-1}\left(A^n\tilde{V}^n + \Delta t\left(P_{tr} - P_{pl}\right)^{n+1}\right)$$

Matrix inversions and matrix vector products are computed in an efficient way without operator storage following algorithms introduced in [**73**]. This method takes advantage of the dyadic structure of the tree, and thus enables fast computation (see subsection 11.6).

10. Patient specific structural elements

In order to validate ventilation models through comparison to experiments, physiologically realistic geometries of the tree and the parenchyma are required. In the following section we detail how a tree model is constructed based on the first branches segmented from HRCT data. From images we also recover the parenchyma surface that is used to build a workable mesh for finite element simulations. From HRCT images taken at different lung inflations, we perform non-rigid surface registration to compute the displacement field of the parenchyma surface.

10.1. Tree geometry

The tree geometry is produced as a combination of medical image data [**91**] and mathematical modeling. The first few bronchial generations are segmented and measured from the HRCT images

using Pulmonary Workstation 2 (VIDA Diagnostics, IA, USA) software, along with the lung and lobar envelopes. The segmented data are then used as initial conditions for the implementation of a lobar space-filling algorithm, along the lines described in [**59**] and [**92**], thus producing a complete tree structure of the conductive part, from the trachea down to the most distal conductive airways (see Figure 23). Let us briefly explain this recursive algorithm. At each step a mother branch gives birth to two daughters that irrigate identified regions which will contain the related sub-trees. Mother to daughter radius ratios are set based on human lung physiology. The length of an airway is function of the distance between the barycenter of the region it irrigates and its mother downstream node. Stopping criteria are based on the airways size and irrigated volumes.

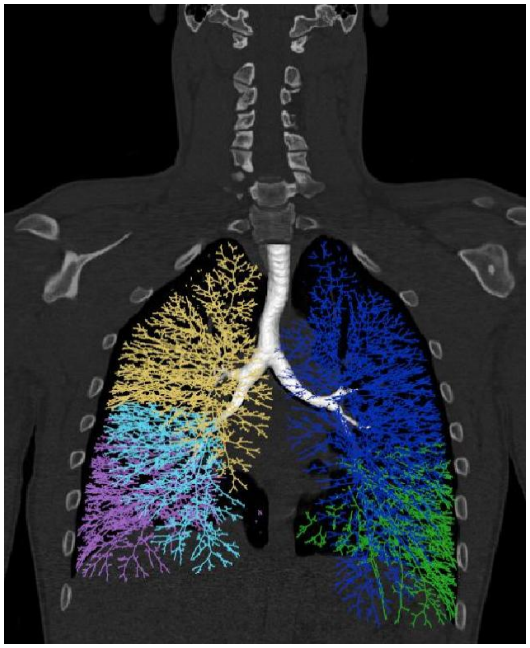

Figure 23: Space-filling tracheo-bronchial tree representation on a human lung. The tree is built by propagating the first segmented airways into the segmented lobes in order to fill their envelope. Constructed branches are modeled as pipes with radius and length determined by the algorithm depicted in [59]**. Note that in ventilation models presented above, every airways including proximal ones are modeled as $0D$ branches. Each of the five colors corresponds to a lobe.**

10.2. Mesh generation from HRCT images

To generate a mesh for the finite element solver, we use HRCT DICOM data from [**91**]. DICOM images are first treated with Matlab to generate a surface triangle mesh. This surface mesh is then processed with Meshlab software [**93**]. First we perform decimation to adjust the mesh size as desired, then smoothing through a Taubin filter [**94**] to improve mesh quality. We use Gmsh [**95**] to generate from the surface mesh a $3D$ tetrahedric volume mesh. Once the $3D$ mesh is built, each tetrahedron is assigned to one of the tree exits according to the algorithm described in Figure 24.
We denote by *m* a mother branch, Ω_m a region of the parenchyma fed by *m*, d_1 and d_2 the daughter branches of *m*, Ω_1 *and* Ω_2 the regions of the parenchyma fed respectively by d_1 and d_2, $\mathcal{C}_1$ and $\mathcal{C}_2$ the subsets of the tracheo-bronchial tree fed respectively by d_1 *and* d_2, *R* and *L* the daughters of the trachea and $\mathcal{L}$ the list of the chosen tree exit branches: $\mathcal{L}=\{ex_i\}$. So-called nodes are the bifurcation junctions' positions.

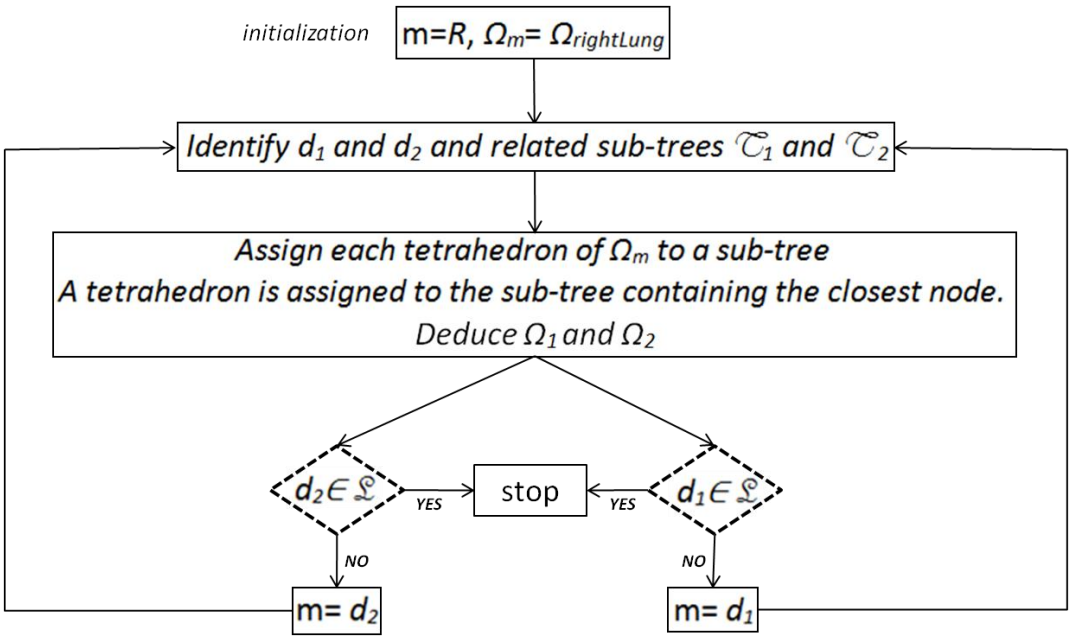

Figure 24: terminal region parenchyma division, illustration on the right lung. Each tetrahedron is associated to the closest subtree.

As stated in subsection 8.1, the chosen exits are not necessarily the conductive tree terminal branches. Figure 25 illustrates the process on a schematic tree with 3 chosen exits **ex**$_i$.

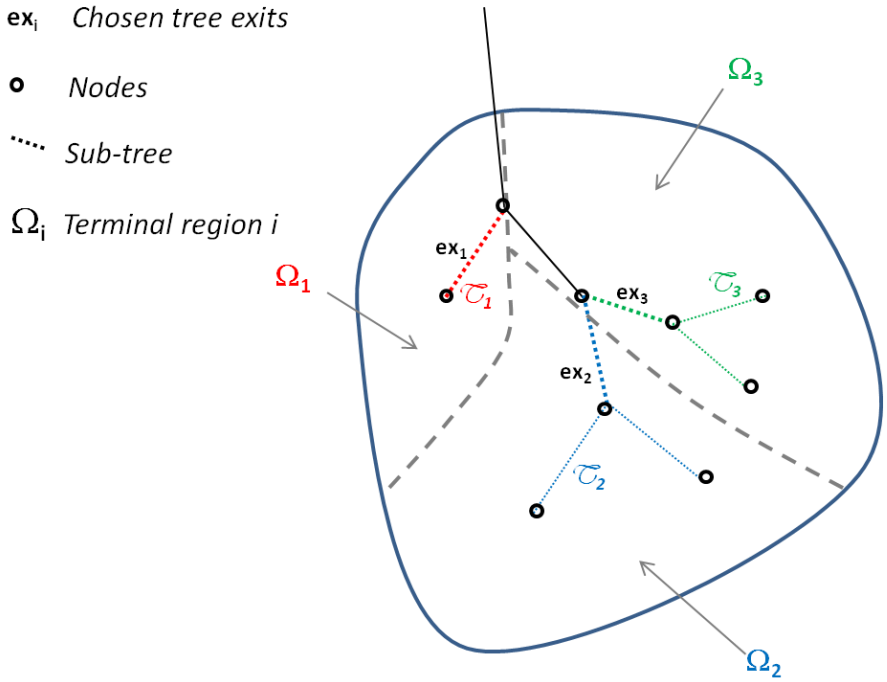

Figure 25: illustration of the subdivision process for a three exit tree defining three terminal regions. Each bifurcation gives birth to two subtrees. Each elementary volume of the domain is supplied by gas flowing through this bifurcation is assigned to the subtree containing the closest node.

Figure 26 illustrates a lobar subdivision on a physiological geometry. The subdivision is built upon a twelve-generation tree with 1633 exits.

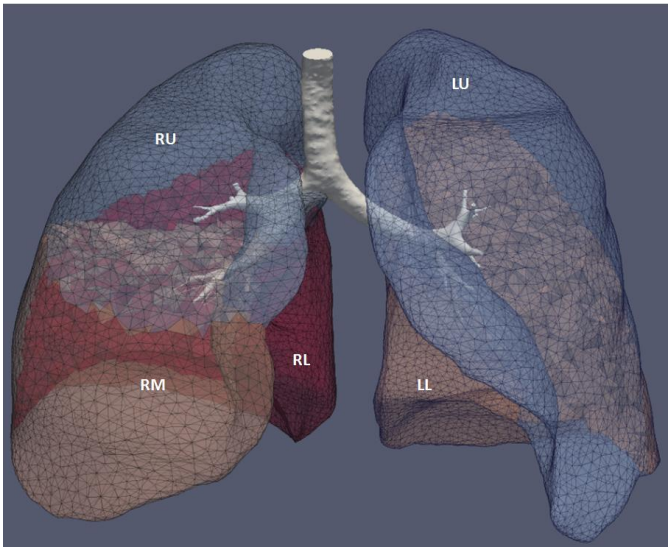

Figure 26: illustration of a lobar subdivision on a physiological geometry. Segmented upper airways are represented along with the lung mesh subdivided at the lobar level. Nomenclature for left lung lobes: LU=Left Upper lobe (in blue on the figure), LL=Left Lower lobe (in yellow on the figure), for right lung lobes: RU=Right Upper lobe (in blue on the figure), RM=Right Middle lobe (in yellow on the figure), RL=Right Lower lobe (in red on the figure)

In Figure 27 we compare lobar volumes obtained by segmentation on HRCT images with VIDA software and those given by the mesh subdivision technique process described in Figure 24. Results are similar.

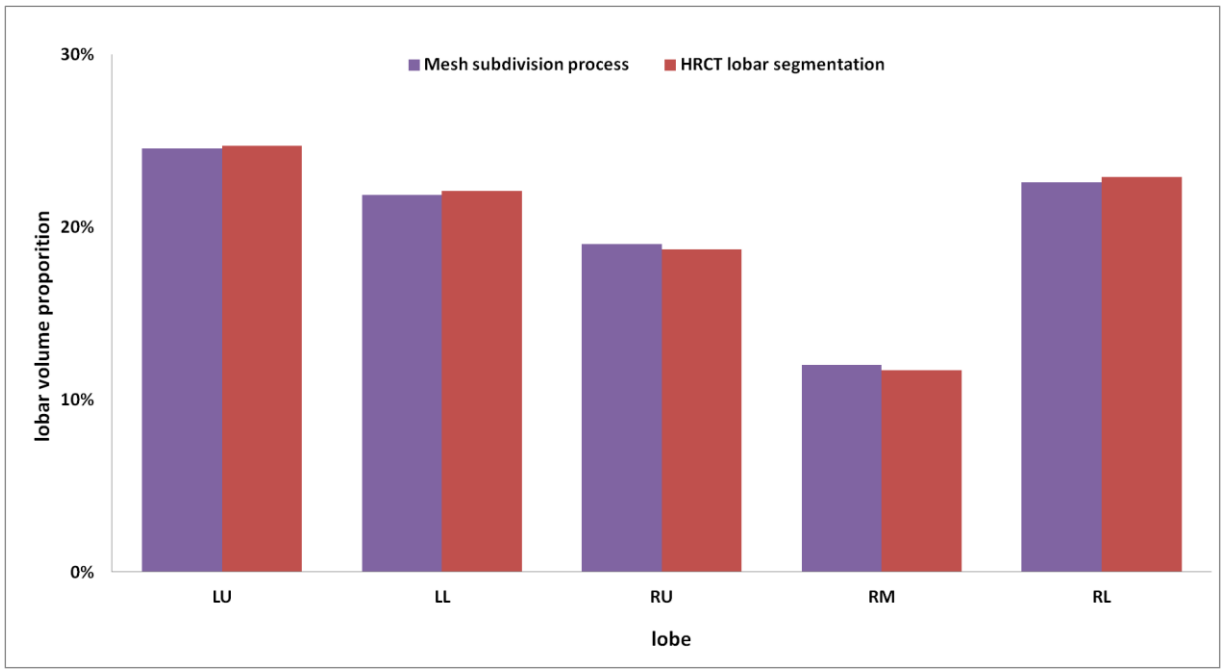

Figure 27: comparison of lobar volumes obtained by HRCT segmentation with the software VIDA, and with the mesh subdivision process, based on a ten-generation space-filling tree.

Figure 28 illustrates a subdivision of a left lung geometry into 477 terminal regions fed by terminal branches of a ten-generation tree.

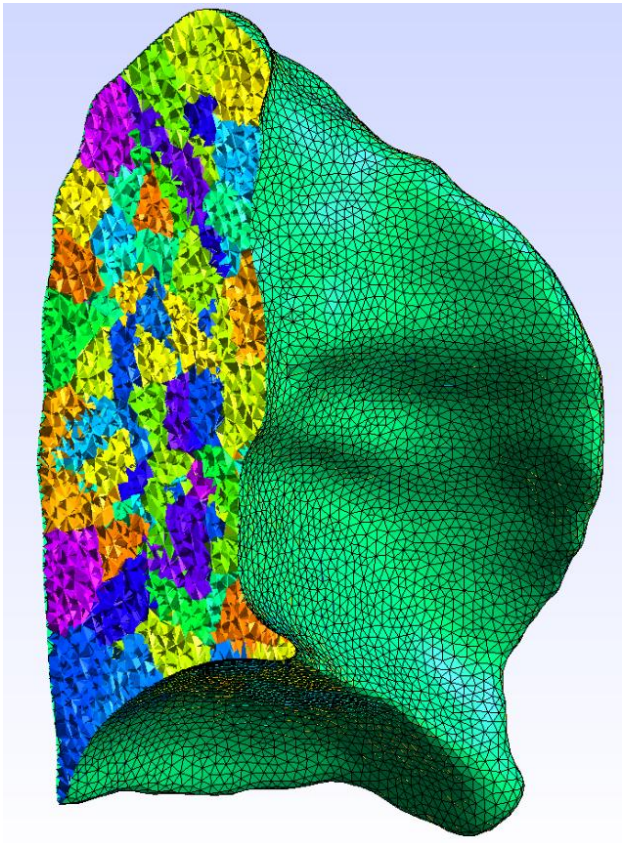

Figure 28: left lung mesh subdivision based on a ten-generations tree structure. The domain is divided into 477 terminal regions. Each color corresponds to a different region.

Remark 4: Code vectorization makes the process fast. On aZBook15, Intel®Core™ i7-4810MQ CPU@2.80GHz*8 it takes less than one minute to subdivide a 51495 tetrahedrons mesh for a 12 generation conductive tree with 1633 exits.

10.3. Surface displacement registration

To impose Dirichlet boundary conditions, we need to have the displacement field of the surface over time. To that end we used Deformetrica software [**96**] that performs non-linear surface registration on surface meshes via the Currents method [**97**]. This computed displacement is not physical in the sense that no mechanics is included in the underlying process. There is no uniqueness in surface points correspondence from one inflation state to another, this may lead to non-physiological evolution. Yet Deformetrica allows the addition of landmarks and curves correspondence to the process so that physiological patterns can be tracked along the breathing cycle. Doing so provides registration with a more physical basis.

In the following section results of simulations performed on the tree-parenchyma coupling and the exit compartment models are presented.

11. Simulations and results

Simulations have been performed using a human lung geometry acquired in the supine position [**91**]. In [**91**] MLV (Mean Lung Volume) HRCT scan of the parenchyma envelope are provided along with

lobar and upper airways segmentation. In what follows MLV is taken as the reference zero stress configuration. Applying processes described in subsection 10.1, we build a space-filling tree within the MLV geometry. For both right and left lungs at MLV we build $3D$ meshes sub-divided from the generation ten level (see subsection 10.2). The left lung mesh contains 51495 tetrahedrons (33990 degrees of freedom) distributed in 477 terminal regions. The right lung mesh contains 43395 tetrahedrons (32589 degrees of freedom) distributed in 752 terminal regions. Prior to resolution settings, a mesh and time convergence analysis has been led (see Appendix 13.5). Mechanical properties are assumed to be homogeneous. They are chosen following ranges provided in [**27**]: Young's modulus E=1.256.10^3Pa, Poisson ratio ν=0.4, parenchyma density ρ=100kg/m^3. MLV volume is 2.231L. Following (28) we compute the equivalent static compliance C=2.$10^{-6}$$m^3$/Pa. Gravity is neglected. Lobe nomenclature is: LU=Left Upper Lobe, LL=Left Lower, RU=Right Upper Lobe, RM=Right Middle Lobe, RL=Right Lower Lobe.

In the following we investigate the tree-parenchyma coupled model. The impact of using non-linear resistances vs. linear ones is studied in both healthy and pathological configurations. Then we test the mechanical independence assumptions associated with the exit-compartment model. Applying the process described in subsection 8.4, we show how the tree-parenchyma model can generate appropriate forcing terms for the exit compartment model. In a following section we compare experimental lobar ventilation with simulation results obtained when applying Dirichlet boundary conditions built from imaging. Results obtained with the Dirichlet boundary conditions and with homogeneous Neumann pressure boundary conditions are compared in order to investigate the effect of boundary conditions spatial heterogeneity on ventilation. Finally we present a pressure controlled mechanical ventilation simulation for which non-linear Robin boundary conditions (see subsection 9.1) are implemented.

In the following we usually display relative volume expansion from the reference state, displacement maps, and pressure maps where pressure is defined as:

$$p_{eff}(\dot{\boldsymbol{u}}) = -\delta_{tree}(\dot{\boldsymbol{u}}) - p_{elastic}(\boldsymbol{u}) \tag{38}$$

with notations defined in subsection 8.2 and 8.4.

11.1. Tree-parenchyma coupled model

In this section we investigate the tree-parenchyma coupled model described in subsection 9.1. We simulate spontaneous tidal breathing driven by Neumann homogeneous pressure boundary conditions, first in a healthy configuration, then in the case of a bronchoconstriction.

Linear (3) and non-linear (4) resistance models are compared. There is no consensus on the spatio-temporal pleural pressure profile during the breathing cycle [**89**]. In this section we impose an academic piecewise constant pressure pattern $P_{pl} - P_{trachea}$ with a physiological plateau of $-300\ Pa$ at inspiration [**89**] and $0\ Pa$ at expiration so as to simulate passive recoil. This approach isolates the effect of the tree resistance distribution by ensuring that simulated ventilation heterogeneities are not due to spatial heterogeneities in the boundary conditions.

In Figure 29 left lung lobar volumes are plotted. Branch resistances are computed with the Poiseuille resistance model. The time step is $\Delta t = 0.05\ s$.

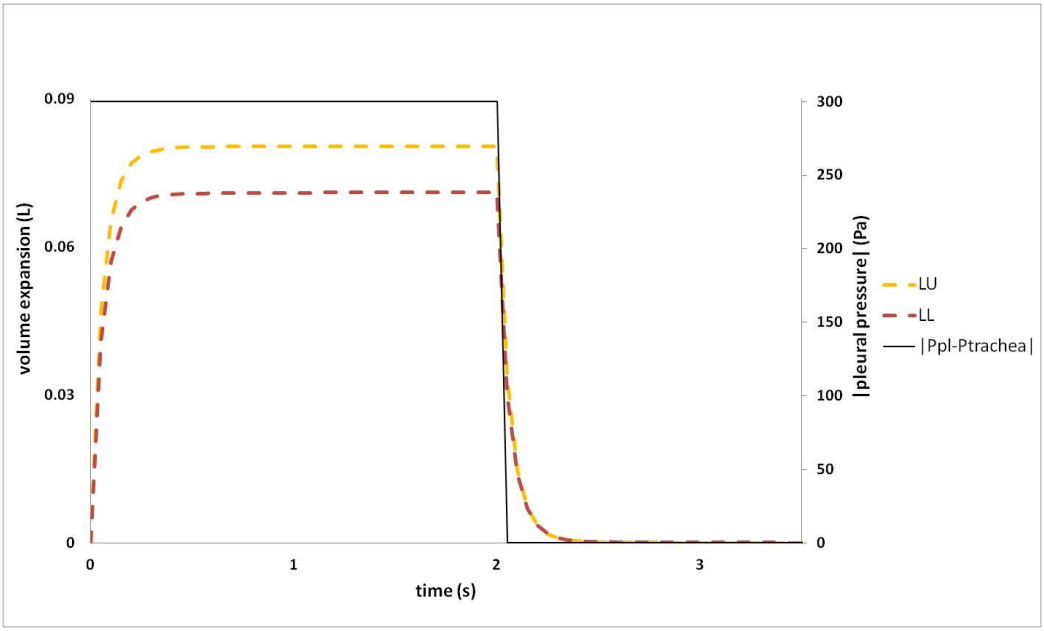

Figure 29: left lung lobar volume expansion evolution from the reference state in a healthy configuration. A piecewise constant in time, homogeneous pressure profile is imposed as boundary condition. Resistances are computed with the Poiseuille theory.

Let us first note that with a physiological pleural pressure amplitude, we obtain physiological volume amplitudes. In the frame of tidal breathing, linear elasticity thus seems to be a reasonable approximation. Both volume lobes evolve in phase with the applied pressure, and the tree resistance induces a time delay in the system's response. This has been noted in [**98**]. Ventilation distribution is proportional to the reference state lobar volumes. In Figure 30 we compare Poiseuille, Pedley and a zero resistance tree configuration.

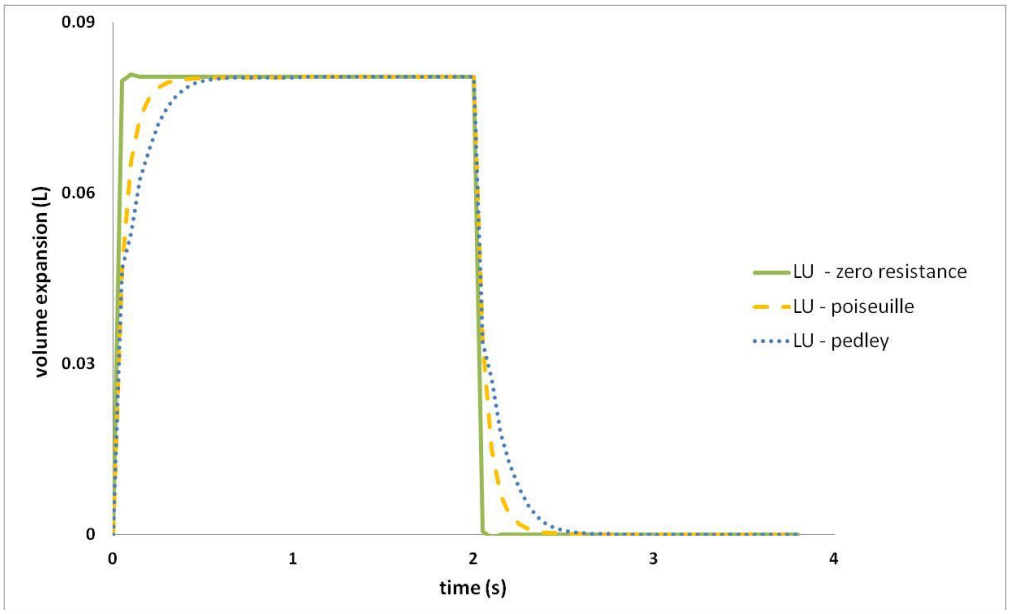

Figure 30: LU lobe volume expansion from the reference state in a healthy configuration. Comparison of Poiseuille, Pedley, and zero resistance models.

Since it takes into account pressure drops at bifurcations, the Pedley model results in higher resistances than the Poiseuille model. With higher resistance the dissipation within the system increases, in turn inducing a longer time delay. The higher the resistance, the higher the dissipation and consequently the lower the expansion generated for a given applied pressure. Here, the time delay is underestimated since tissue viscosity and the extra-thoracic contribution to the pressure

drops are not considered. Note also that measured airway resistances show a high variability among individual, from 0.5 to 2.5 $cmH_2O.L^{-1}.s^{-1}$ [**99**], inducing a variability of response times. The lung slice plot in Figure 31 shows the spatial distribution at time $t = 0.25\ s$ (inspiration) of the relative volume variation and the magnitude of the effective pressure field.

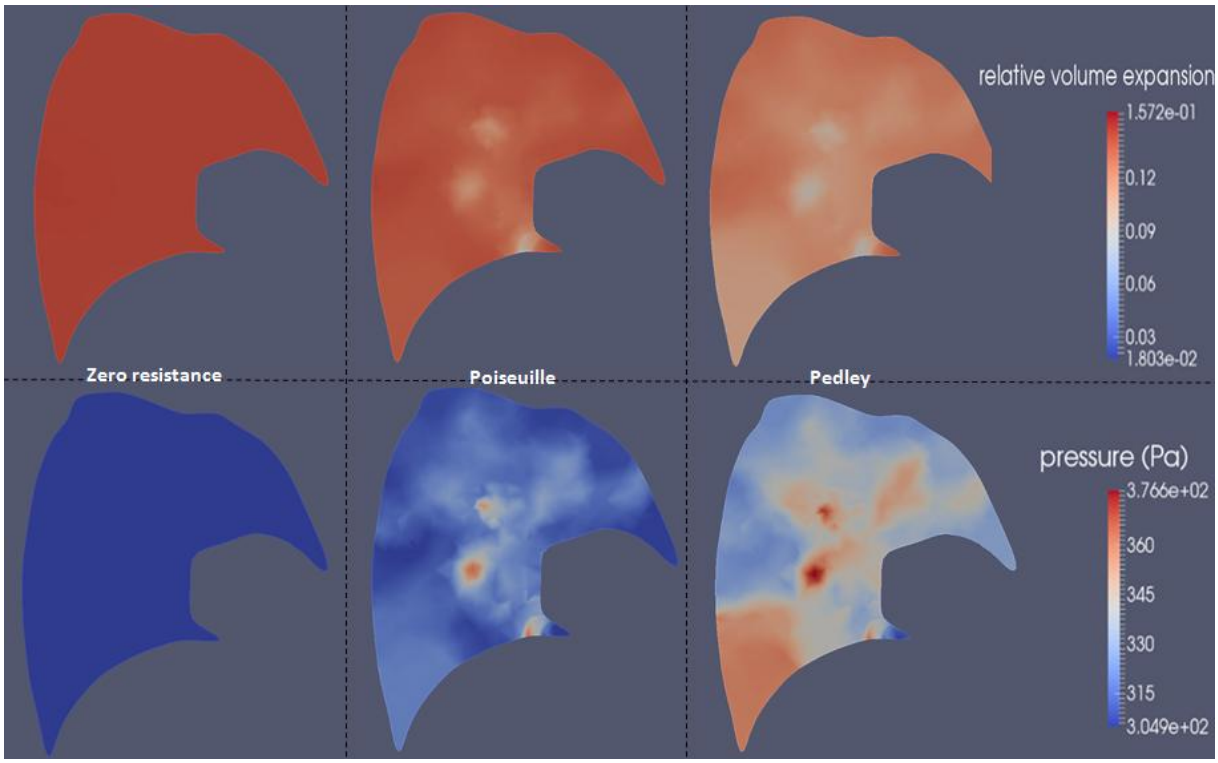

Figure 31: relative volume expansion from the reference state and effective pressure (38) magnitude maps on a left lung slice. The homogeneous constant piecewise pressure shown in Figure 30 is applied around the parenchyma. Comparison at time 0.25 s in a healthy configuration for different airway resistance models: zero resistance, Poiseuille and Pedley.

As described in subsection 8.4, the effective pressure field within the parenchyma is made of two components: the elastic pressure due to expansion and the pressure drop within the tree. The higher the pressure drop through this path, the higher $|\delta_{tree}(\dot{\boldsymbol{u}})|$ is in the region. The coupling pressure $\delta_{tree}(\dot{\boldsymbol{u}})$ opposes volume variations; thus regions fed by a path along which pressure drop is high, expand less during inspiration and contract less during expiration. In inspiration the elastic pressure $Kdiv(\boldsymbol{u})$ is thus reduced. The behavior of p_{eff} is a balance between the elastic and the coupling pressure. At a time in the breathing cycle when flow is high, pressure drops along the tree are increased and the increase of the coupling pressure compensates the decrease of the elastic pressure. Regions fed by a higher resistive path expand less. This is what is observed in Figure 31: the effective pressure and the volume expansion maps are anti-correlated. Moreover, Pedley resistances are higher than Poiseuille's. Thus, the effective pressure map is more heterogeneous. When the tree resistances are set to zero, the effective pressure reduces to the elastic pressure. The latter is homogeneous since a homogeneous pleural pressure is applied around the parenchyma. Note that at times of the breathing cycle when the flow is lower, pressure drops are reduced and the effective pressure maps would then be more homogeneous.

Next we simulate a bronchoconstriction of the branch feeding lobe LL by reducing its diameter by a factor of 5. We compare the resulting lobar volume evolutions obtained using the Poiseuille and Pedley models as shown in Figure 32.

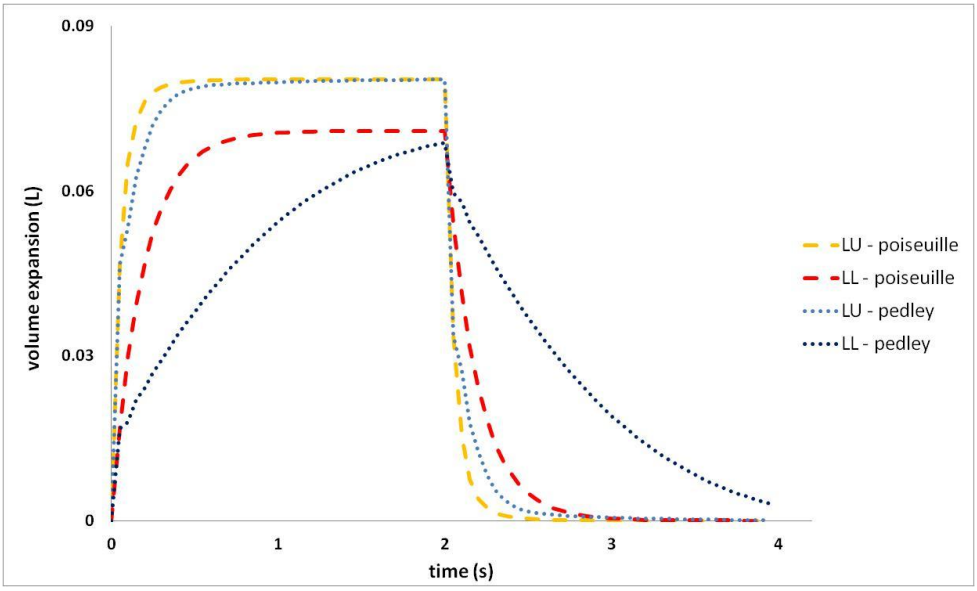

Figure 32: left lung lobar volume evolution with a bronchoconstriction simulated on the branch feeding lobe LL. Comparison of Poiseuille and Pedley resistance models.

A diameter reduction induces a resistance increase. Lobar volume dynamics obtained with Poiseuille and Pedley models exhibit notable differences showing that resistance non-linearities have to be taken into account when modeling ventilation distribution in pathological situations. Again, we observe an increasing phase shift with higher resistances. This is consistent with other studies [**98**]. Compared to the healthy configuration, ventilation of lobe LL is logically reduced: the driving effort is constant while the energy necessary to induce flow through the bronchoconstricted branch increases. Again, volume expansion and effective pressure are anti-correlated (see Figure 33).

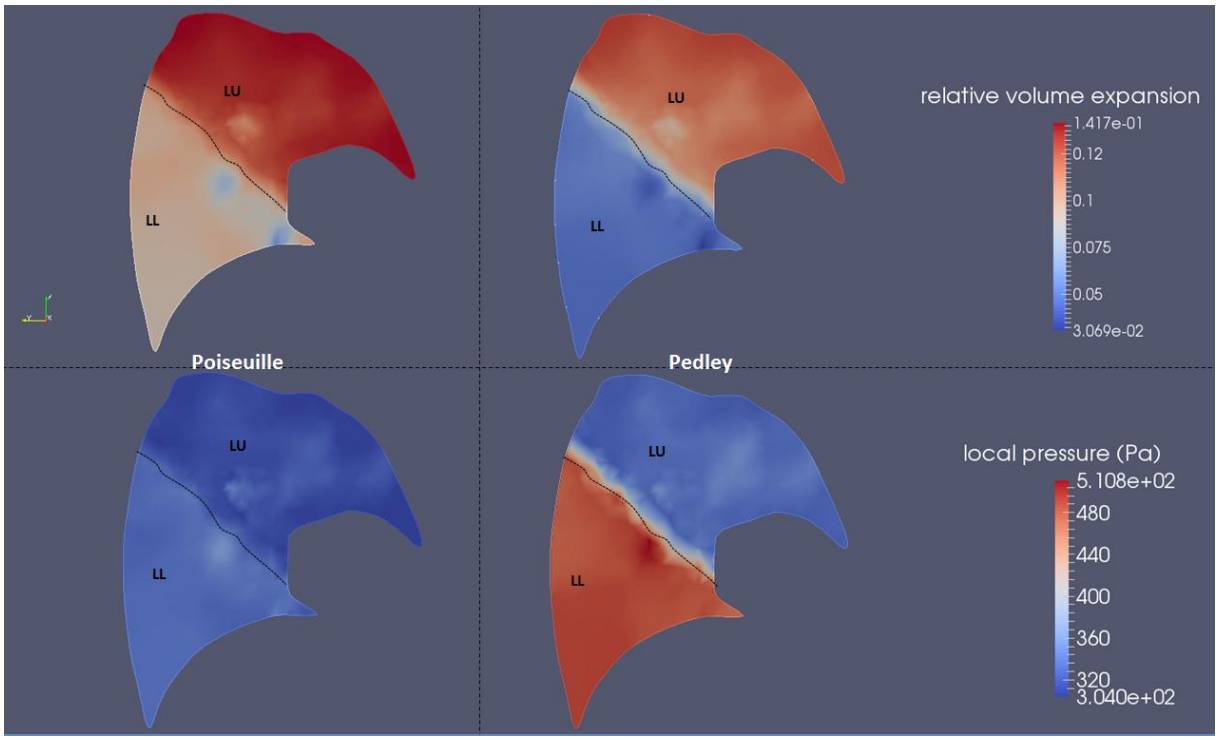

Figure 33: relative volume expansion from the reference state and effective pressure (38) magnitude maps on a left lung slice. The homogeneous constant piecewise pressure shown in Figure 30 is applied around the parenchyma. A uniform diameter reduction of factor 5 is applied to the branch feeding lobe LL. Comparison at time 0.25 s for Poiseuille and Pedley resistance models. The dashed line represents the lobar frontier.

11.2. Mechanical independence in the exit compartment model

In the exit compartment framework, terminal compartments are mechanically independent. This may not properly describe the continuous nature of the parenchyma. Here we simulate pulmonary fibrosis and compare results from both models. To mimic tissue stiffening associated with this pathology, the Young's modulus of lobe LL is multiplied by ten. Equivalently, compliances of exit compartments belonging to lobe LL are divided by ten. Resistances are computed with Pedley's model (4). A homogeneous smoothed piecewise constant in time pressure is applied to both models. Lobar volume evolution of the left lung is plotted in Figure 34.

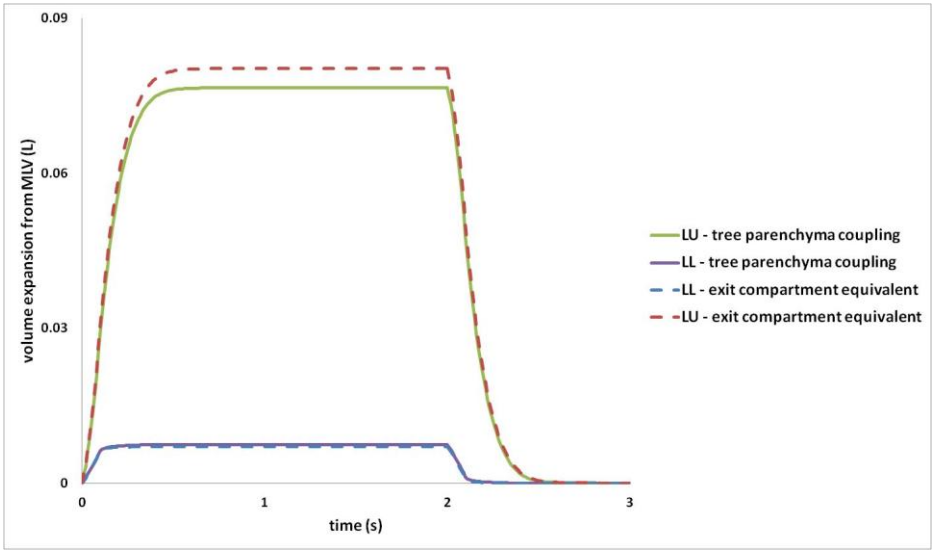

Figure 34: left lung lobar volume evolution from the reference state, fibrosis simulated on lobe LL. Comparison of the tree-parenchyma coupling and the exit-compartment models.

Lobe LL is indeed less ventilated in both models. In the exit-compartment framework no mechanical connection exists between both lobes. LU is not affected by fibrosis while in the tree-parenchyma coupling case LU ventilation is slightly reduced, but lobar ventilation shows little difference. Effects are mainly local as demonstrated in Figure 35 and Figure 36.

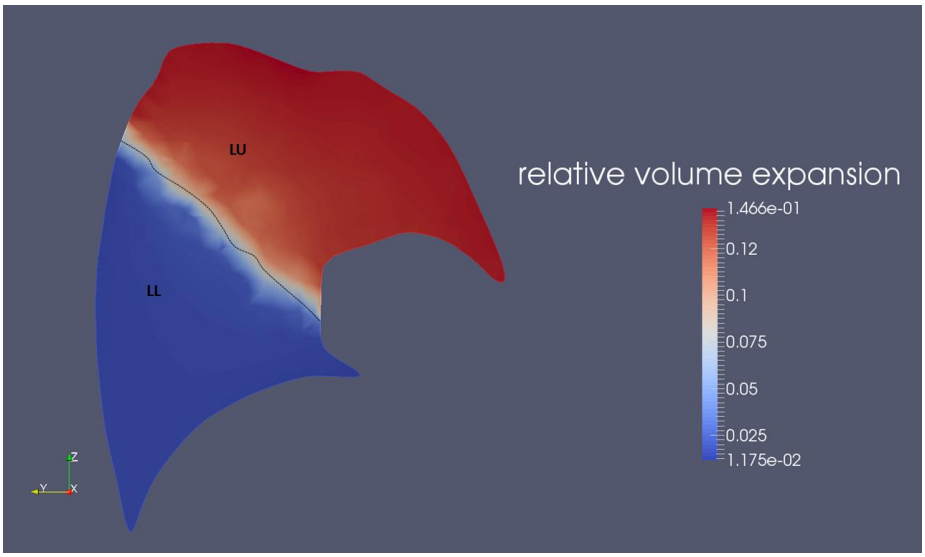

Figure 35: relative volume expansion on a left lung slice, from basis to apex. The homogeneous piecewise constant pressure shown in Figure 30 is applied around the parenchyma. The map is shown at time 0.5 s.

Figure 35 represents the relative volume expansion field within a left lung slice in the frame of the

tree-parenchyma coupled model. As expected the expansion of the diseased lobe is reduced compared to the healthy one, stiffening makes volume change harder. We note that, due to the mechanical interaction between both lobes, LU regions next to LL are affected by fibrosis although their mechanical properties are unchanged.
For the 477 terminal regions ex_i of the left lung, we plot the expansion ratios defined as

$$r_i = \frac{\left(V_{ex_i}(t) - V_{ex_i}(0)\right)_{fibrosis}}{\left(V_{ex_i}(t) - V_{ex_i}(0)\right)_{healthy}}$$

for both exit-compartment and tree-parenchyma coupled models at t=0.5s.

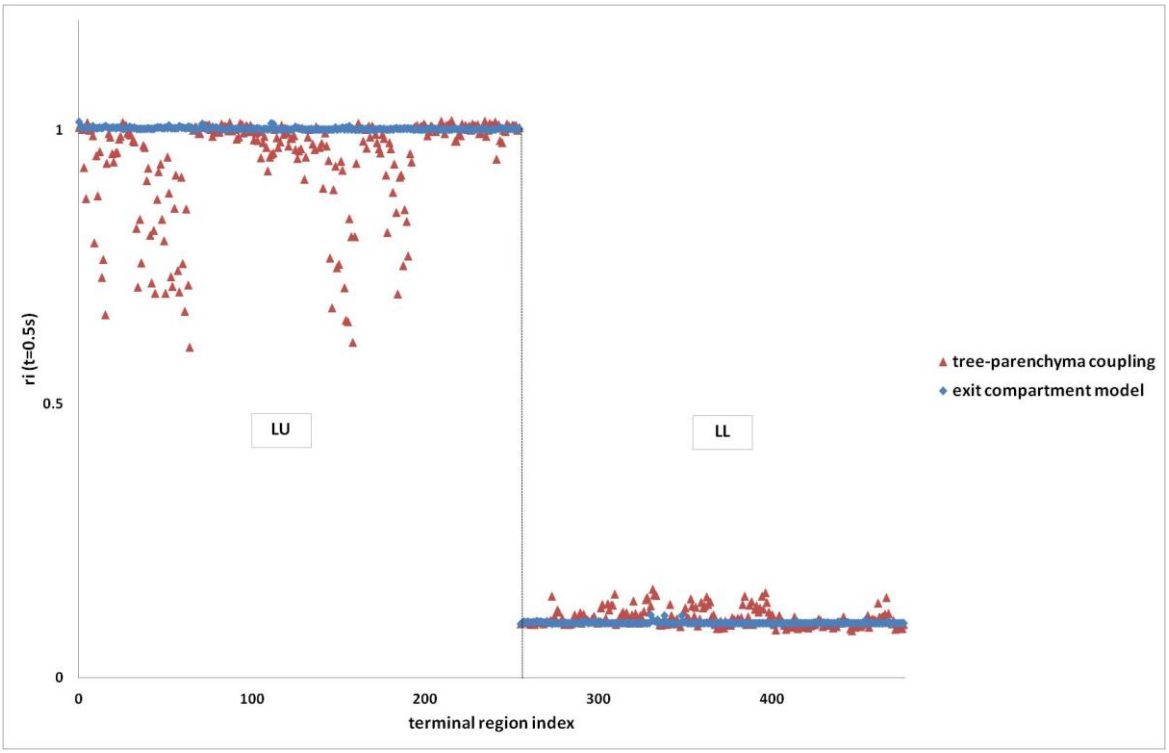

Figure 36: Expansion ratios of the left lung 477 terminal regions at a given lung expansion for the exit-compartment and the tree-parenchyma coupled models. Simulations are performed with homogeneous pressure boundary conditions. To simulate fibrosis, lobe LL compliance (resp. Young's modulus) was divided by ten.

In the exit compartment framework, expansion ratios are uniform in each lobe. The healthy lobe behavior is independent of the diseased region and $\forall ex_i \in LU,\ r_i = 1$. Since compliance is divided by ten in the fibrosed lobe LL, expansion ratios are uniformly divided by ten: $\forall ex_i \in LL,\ r_i = 0.1$. This demonstrates the mechanical independence of terminal regions in the exit compartment framework. As observed in Figure 35, regions do mechanically interact in the tree-parenchyma coupling framework. Some regions of lobe LU expand less when LL is fibrosed because they are affected by the stiffening of neighboring areas. Some regions of LL expand more than in the exit compartment model because they are pulled by neighboring healthy areas. From this result and other pathological simulations (results not shown here: healthy configuration, bronchoconstriction on one branch, regional bronchoconstriction) we conclude that taking into account the mechanical interaction between regions does impact the ventilation distribution.

11.3. From the tree-parenchyma coupled model to boundary conditions for the exit-compartment model

We showed in subsection 11.2 a possible limitation associated with exit-compartment models. In subsection 8.4 a method to compute applied forces for the exit-compartment model based on the tree-parenchyma coupled model simulations has been described. We apply this approach to the case presented in subsection 11.2. Simulating pulmonary fibrosis as in subsection 11.2 we get results presented in Figure 37.

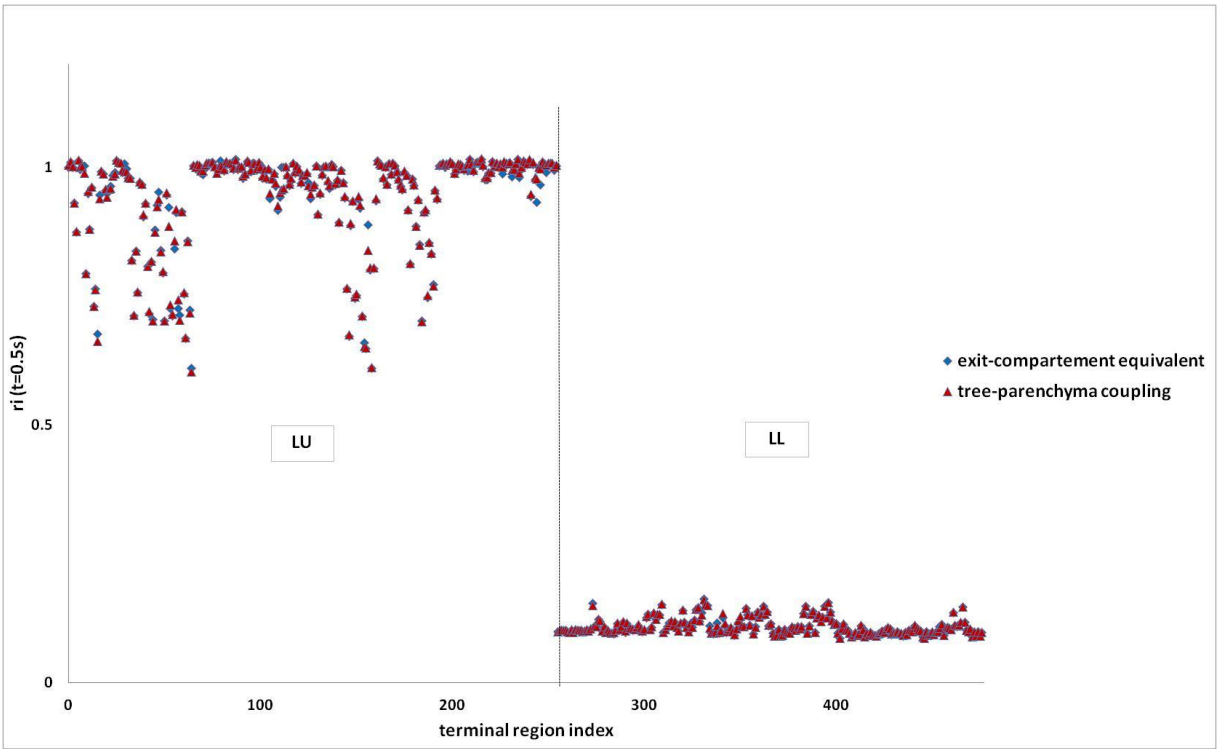

Figure 37: Expansion ratios of the left lung 477 terminal regions at a given lung expansion for the tree-parenchyma coupled model with homogeneous pressure boundary conditions and the exit compartment model with equivalent boundary conditions. To simulate fibrosis, lobe LL compliance (resp. Young's modulus) is divided by ten.

We recover the same ventilation distribution in both cases. Here, the pressure applied around the parenchyma in the tree-parenchyma coupled model is homogeneous. In order to recover the same ventilation results in the exit-compartment model this pressure has to be heterogeneously distributed such that it accounts for the mechanical interaction between terminal regions. Yet, as shown in the next section, the pressure around the parenchyma itself is heterogeneous when applying Dirichlet boundary conditions coming from image registration.

11.4. Dirichlet boundary conditions registered from medical images

In this section we reconstruct the lung parenchyma surface evolution based on HRCT data provided by [**91**]. It can be applied as a boundary condition to our finite element model.

11.4.1. Impact of boundary conditions on lung regional expansion

In addition to MLV data, [**91**] provides TLC HRCT scans of the lung envelope along with lobar segmentation. Following subsection 10.3 we perform non-linear surface registration from the MLV to the TLC state. Physiological landmarks and surface lobe fissures (see subsection 13.6) can be included in the segmentation process (see Figure 38).

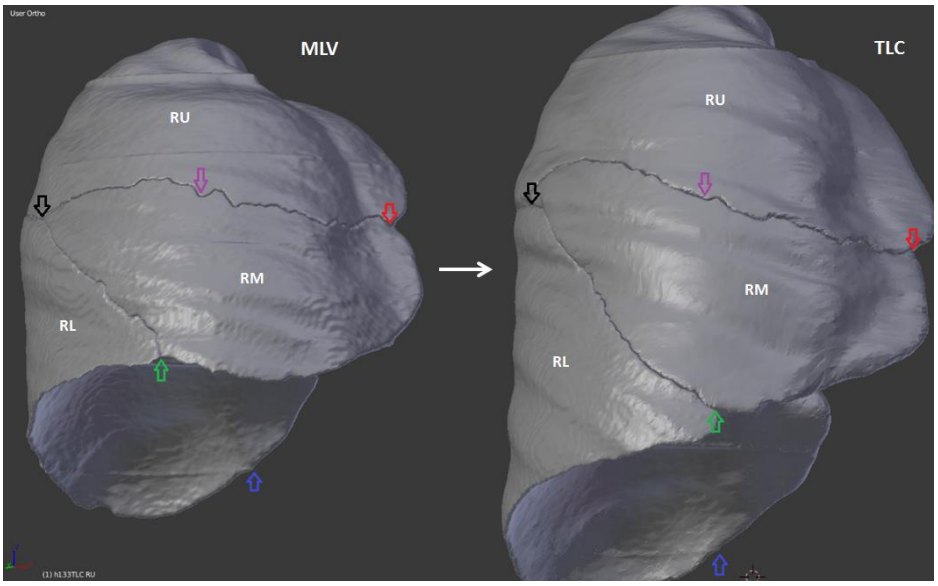

Figure 38: from MLV to TLC with landmarks and lobe fissures – illustration on an imaged right lung

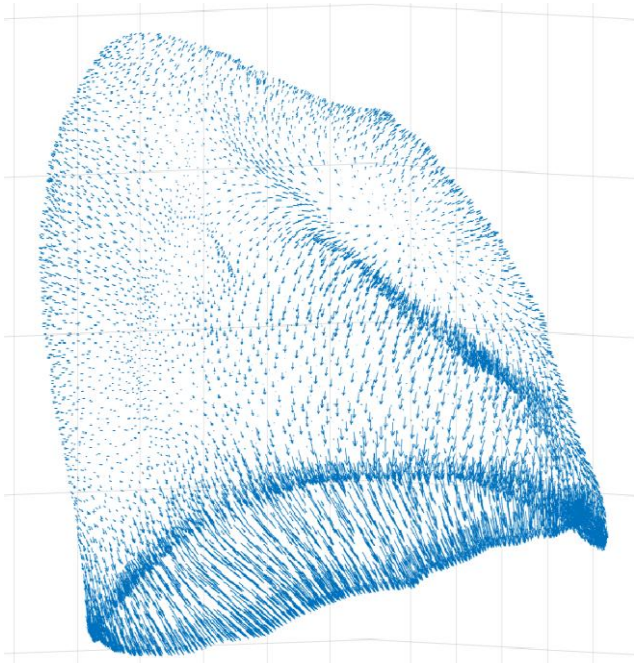

Figure 39: surface displacement field registered from MLV to TLC states.

In what follows we assume MLV to be the reference state. Here imaging measurements are static. Thus we do not consider any dynamics in the transition from MLV to TLC, and airway resistances are set to zero. The registered displacement field is used as Dirichlet boundary conditions.

In Figure 40 we compare experimental lobar ventilation ratios (issued from image segmentation) with results obtained from the model in three cases: surface displacement field registered without landmarks or lobe fissures, with landmarks only (10 on the left lung surface, 16 on the right one), and with both landmarks and lobar fissures.

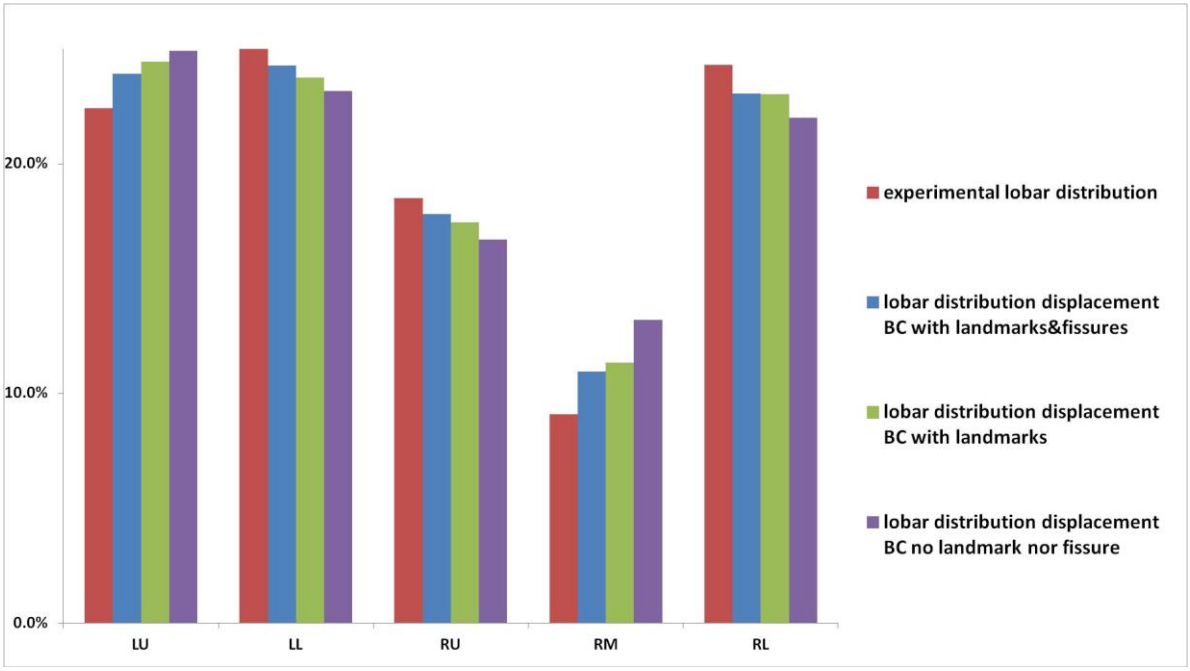

Figure 40: lobar ventilation distribution, simulation vs. experimental data. Experimental data are deduced from lobar segmentations on CT images at the two inflation states. Simulations are carried out with Dirichlet boundary conditions issued from image registration. Three registered surface displacement fields are used: crude registration performed without landmarks or lobar fissures, registration performed with landmarks, and registration performed with both landmarks and lobar fissures.

As we add physiological information to the registration process, results get more accurate. Whether landmarks or fissures contribute more to the improvement depends on the number of landmarks used and on their relevance. Here adding landmarks to the process improves the result by 7% on average. Adding fissures brings a further 2% improvement. The residual error can have several sources: here we neglect the lobe sliding, though it may affect the parenchyma displacement field [**100**]. The volume increase from MLV to TLC is about 70%: intermediary states images between the two configurations would ensure a better registration and hence more accuracy in ventilation prediction. Linear elasticity is a rough approximation for large displacements. With this constitutive relation, recoil effort is increasingly underestimated as the parenchyma expands. Displacement may be well predicted but a proper effort computation requires an appropriate mechanical law for the parenchyma. Despite these strong assumptions, results are encouraging. This shows that surface parenchyma displacement field is an appropriate boundary condition when it comes to lung ventilation modeling. This points out also how crucial it is for the registration to be precise. If 4D-CT [**80**] or 4D-MRI [**81**] data along with segmented upper airways were available in a pathological case where tree resistance is increased, it would be of great interest to run the model with dynamic Dirichlet boundary conditions and to compare the resulting simulation to the corresponding dynamic ventilation acquisition; depending on the tree resistance distribution the tree-parenchyma coupling could then be emphasized.

Moreover, it has been widely assumed that esophageal pressure can be used as a surrogate for pleural pressure [**89**]. However, esophageal pressure is a scalar that cannot account for spatial heterogeneity. Some studies have applied a homogeneous pressure as the boundary condition [**58**], [**101**]. In [**57**] a pressure gradient is applied to account for gravity effects. In this section, we investigate how heterogeneities in boundary conditions impact ventilation distribution. As a post-process of the ventilation distribution simulation (Figure 40) we can compute the equivalent average normal time varying effort $P_{\Omega}^{eff} = -\int_{\partial\Omega} \sigma \boldsymbol{n} \cdot \boldsymbol{n} dS$ (notations defined in subsection 8.4) and apply it as a forcing term for comparison.

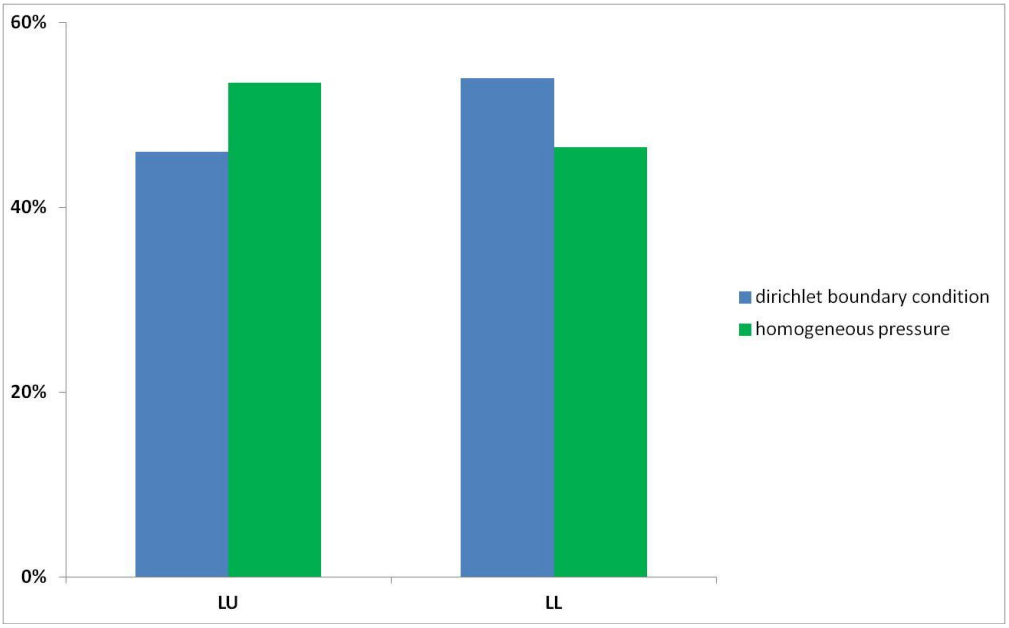

Figure 41: left lung lobar distribution at TLC state obtained with Dirichlet boundary conditions issued from image registration vs. homogeneous pressure boundary conditions.

In the framework of linear elasticity, when a homogeneous pressure is applied and tree resistances are set to zero, the ventilation of a region is proportional to its volume. Thus lobe LU expands more than LL because it is bigger. With Dirichlet boundary conditions obtained from imaging, LL is more ventilated because the diaphragm has a larger contribution to parenchyma expansion than the ribs.
In Figure 42 we plot the displacement field magnitude on a lung slice obtained with the two previous boundary conditions at a given volume expansion.

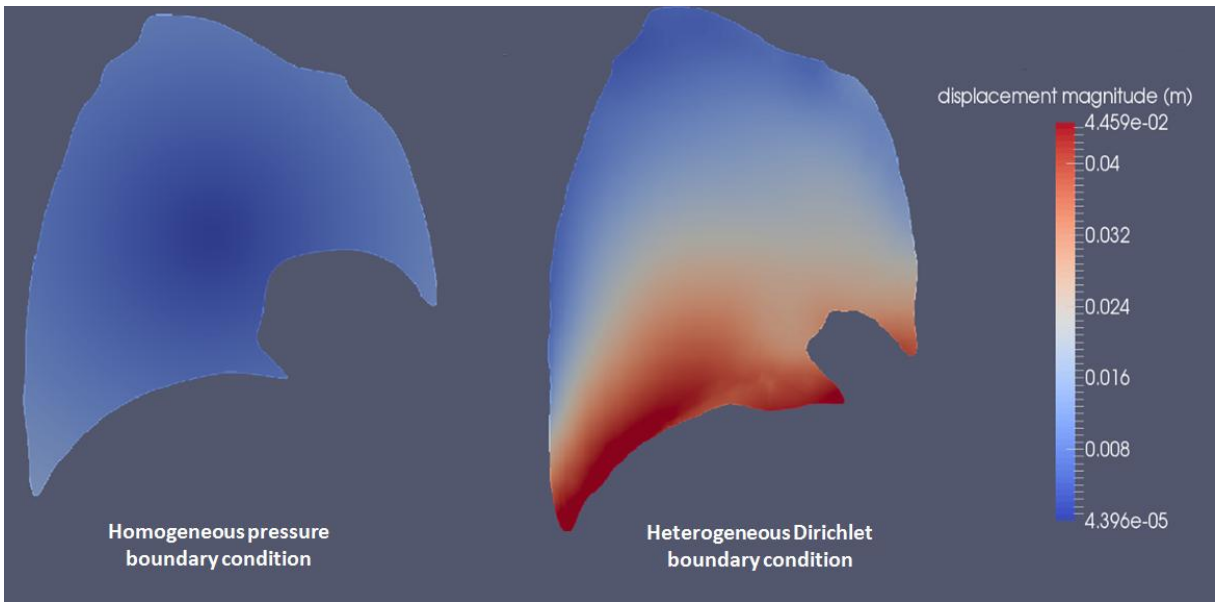

Figure 42: magnitude displacement field on a left lung slice. On the left, homogeneous pressure boundary conditions are applied; on the right Dirichlet boundary conditions issued from imaging are applied.

The displacement magnitude is much more heterogeneous with the Dirichlet boundary conditions registered from images than with homogeneous pressure boundary conditions. The parenchyma is more stretched at the base, where the diaphragm pulls, than at the apex.

Boundary conditions have a crucial impact on ventilation. This points out the need to take into account their heterogeneities when modeling ventilation. Here tree resistances have been set to

zero. Imposing a displacement field while increasing some branch resistances in the tree because of pathological patterns could lead to more heterogeneities.

11.4.2. Tree-parenchyma coupled model with Dirichlet boundary conditions

The displacement field built in previous section maps the MLV to the TLC configuration. To generate a tidal look alike breathing pattern, we bound it and impose a sinusoidal dynamics as described in Appendix 13.7. A four seconds time period is chosen (see Figure 43). The overall relative volume amplitude from the reference state is 22%.

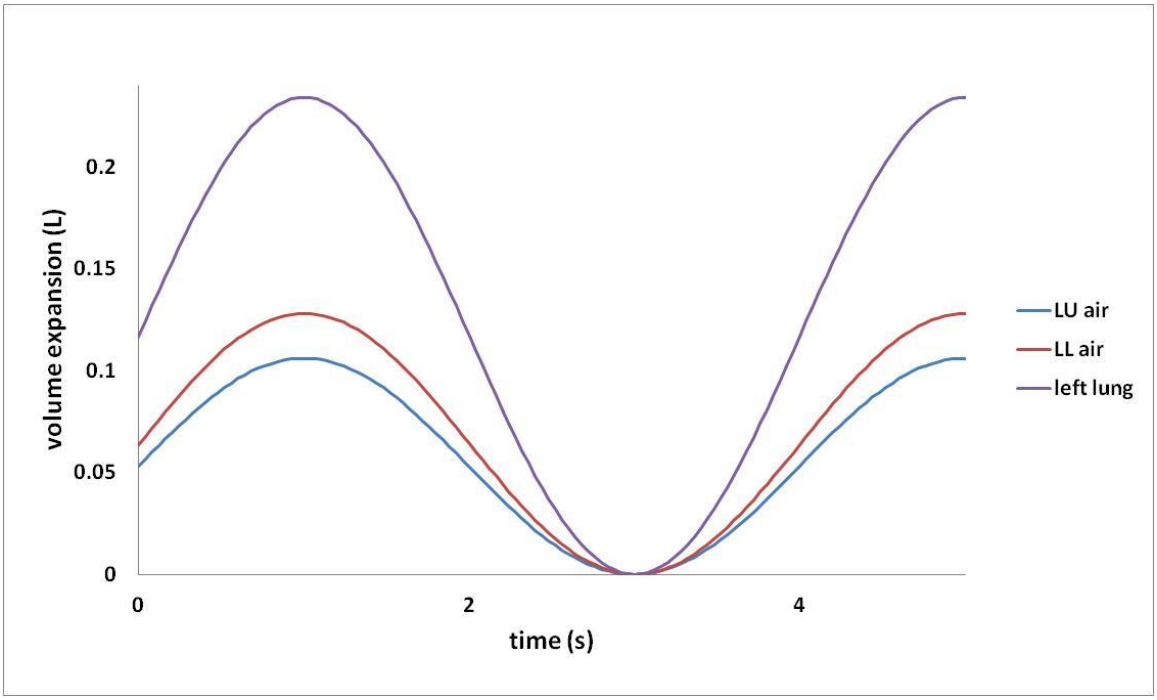

Figure 43: left lung and lobar volume evolutions from the reference state in a healthy configuration. Dirichlet boundary conditions with sinusoidal time evolution are applied. Resistances are computed with the Pedley resistance model. Results shown after a few iterations, when the stationary regime has been reached.

We compare the ventilation (Figure 44) and pressure (Figure 45) distributions obtained in a healthy case and when a bronchoconstriction with ratio 7 is applied on the branch feeding lobe LU.

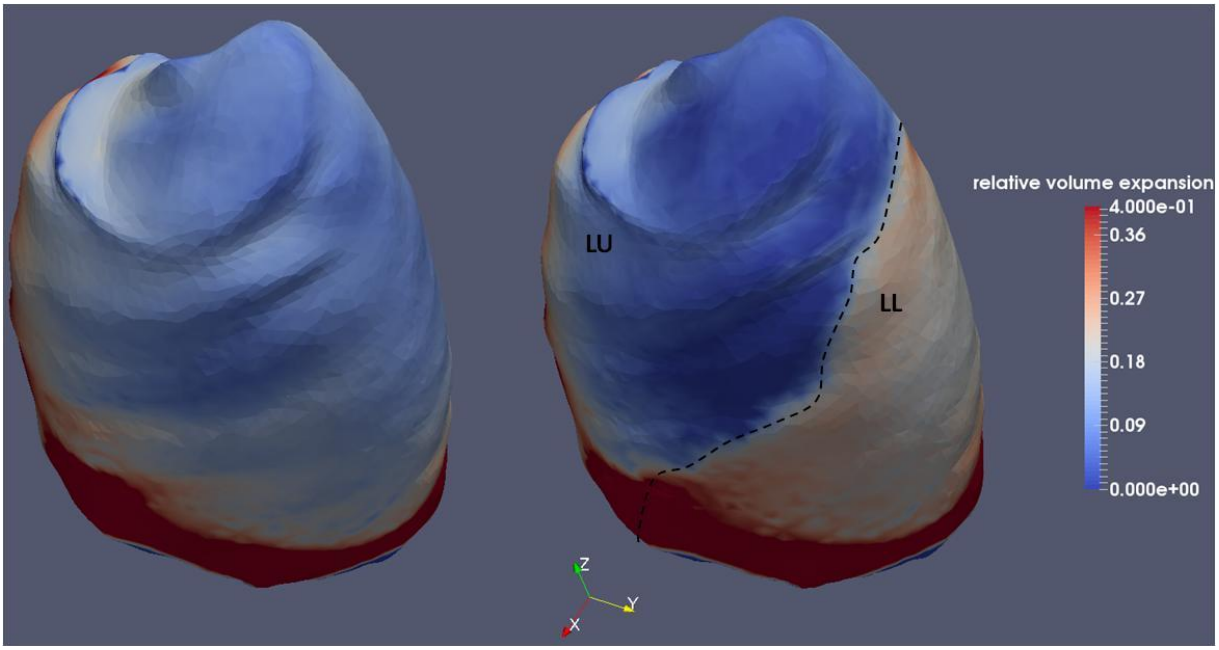

Figure 44: Relative volume expansion $3D$ map on a left lung geometry. Dirichlet boundary conditions with sinusoidal time evolution are applied. Resistances are computed with the Pedley resistance model. On the left side a healthy configuration is simulated, on the right side a bronchonconstriction with ratio 7 on the branch feeding lobe LU is applied. Plot at time t=3s.

As noted in subsection 11.4.1, volume distribution is heterogeneous. In the pathological case, lobe LU expands less than in the healthy situation. Here applied boundary conditions prescribe the lung total volume evolution, so lobe LU reduced ventilation is associated with an increased expansion of lobe LL.

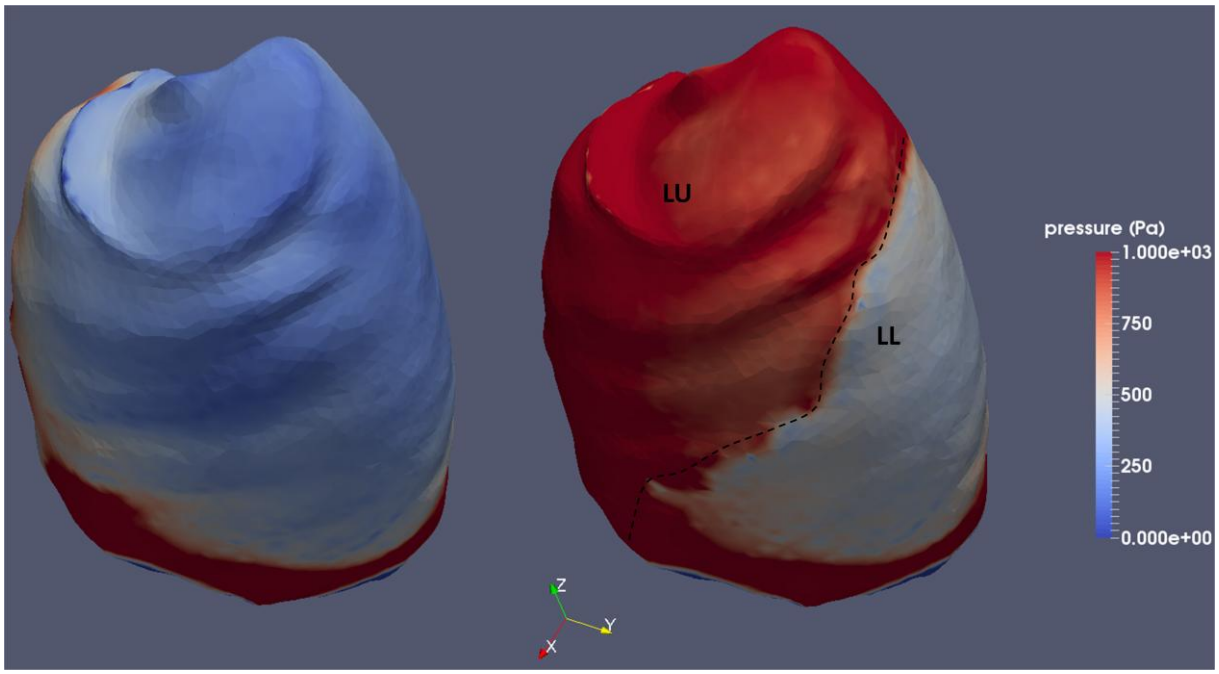

Figure 45 : effective pressure (38) magnitude map on a left lung geometry. Dirichlet boundary conditions with sinusoidal time evolution are applied. Resistances are computed with the Pedley resistance model. On the left side a healthy configuration is simulated, on the right side a bronchonconstriction with ratio 7 on the branch feeding lobe LU is applied. Plot at time t=3s.

The effective pressure magnitude is higher next to the diaphragm than near the apex. As lobe LU is harder to expand, the pressure applied to generate a prescribed volume expansion is greatly increased in that region.

11.5. Pressure controlled mechanical ventilation

In this section, a pressure controlled mechanical ventilation scenario is simulated on the left lung. The system is governed by (37) . As depicted in subsection 8.2, chest and diaphragm resistance to lung expansion are modeled through non-linear Robin boundary conditions that prevent lobes from expanding over their TLC volume. Segmented lobe volumes at TLC are taken from [**91**]. In this scenario, the ventilator pressure increases till both lobes are maximally expanded and then suddenly drops to zero (see Figure 46). This is not a clinically realistic pattern. The simulation rather aims at validating the Robin boundary conditions. To isolate the effect of the imposed boundary conditions, tree resistances are set to zero. Chosen parameters for the simulation (defined in subsection 9.1) are: $\Delta t = 0.02s$, *tol*=0.02, *stepMin*=0.001, *stepMax*=0.5, *nbItS*=30, ∀i c_i=1 (23).

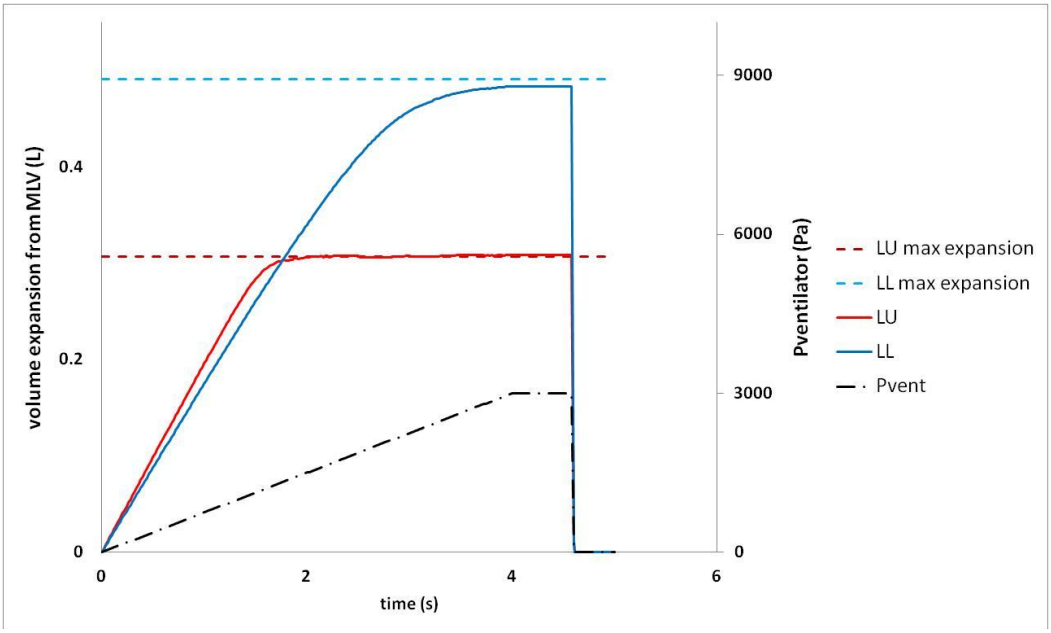

Figure 46: Pressure controlled mechanical ventilation – lobar volume expansion from the reference sate. Maximum expansion is the TLC.

Lobar volumes achieve and remain at their maximum values. It takes more pressure to saturate LL than LU. The reason is that the relative difference between MLV and TLC volume states is higher for LL. When zero pressure is applied, the system instantaneously goes back to the equilibrium position. This is coherent with the facts that inertia is negligible and tree resistances are set to zero.

Remark 5: As in subsection 11.4.1 the linear elasticity assumption does not hold true for large displacements. Taking lobe sliding into account may change the required effort to reach TLC. Here the Robin function k is homogeneous at the lobar level; it should be heterogeneous in order to account for real efforts which are probably heterogeneous since the ribs and diaphragm have specific actions on the parenchyma [**102**].

11.6. Computation time

Both the exit compartment and tree-parenchyma coupled models are implemented in an efficient way. In the exit compartment case, matrix-vector product and matrix inversion are performed

without operator storage. This is made possible by the dyadic property of the tree [**73**]. In the tree-parenchyma coupling case we also take advantage of the tree structure to compute matrix-vector product without storing the full coupling matrix (see subsection 9.1). Simulations are run on a single processor of ZBook15, Intel®Core™ i7-4810MQ CPU@2.80GHz*8. The simulation shown in Figure 30 takes 279 s (CPU time) for eighty time steps on a 51495 tetrahedrons mesh, the equivalent simulation with the exit-compartment model takes 15 s (CPU time) for a 1229 exits tree.

12. Limitations and conclusion

We have assumed linear elastic behavior of the lung parenchyma, this is valid for low tidal breathing frequency and since one of our goals is to propose an accurate numerical treatment of the action of the bronchial tree on the lung tissue based on the observation that it induces viscous effects on the global behavior law. Nevertheless it is clear that such a simple model may not reproduce accurately the whole lung tissue physiology in all the respiratory regimes (see subsection 1.2) and for all pathological cases. In particular to take into account perfusion or other viscoelastic effects one could consider some poroelastic laws as in [**41**] (see also [**103**] for fully non linear poroelastic models) or more realistic viscoelastic non linear laws [**75**]. Note that our numerical strategy may as well be extended to such situations in particular if one considers a non linear behavior law then the theoretical framework has to be changed as follows. The term F is still given by (9) but with Q given by (7). Finally, $\frac{\partial F}{\partial \dot{\mathbf{u}}}.\boldsymbol{w}$, the term of the variationnal formulation relative to the tree, writes $\frac{\partial F}{\partial \dot{\mathbf{u}}}.\boldsymbol{w} = {}^{t}\left(\int_{\partial\Omega_i} \dot{\boldsymbol{u}} \cdot \mathrm{cof}\,(I+\nabla \boldsymbol{u})\boldsymbol{n}\right) A \left(\int_{\partial\Omega_i} \boldsymbol{w} \cdot \mathrm{cof}\,(I+\nabla \boldsymbol{u})\boldsymbol{n}\right)$.

Note that even if one considers more complex laws, there is no consensus on the actual parenchyma constitutive relation and parameter values [**104**], thus the more sophisticated law to be used remains an open question.

Another limitation of our work is, as stated in subsection 8.1, the use of the Pedley resistance model at expiration. In addition we do not consider the variation of airways dimensions along the breathing cycle, though a quasi-static evolution would be compatible with our framework.

Moreover, as emphasized and illustrated previously the surrounding pressure applied to the lung parenchyma (induced by muscle contraction as well as chest wall elasticity) is heterogeneous. Here we impose Dirichlet boundary conditions based on lung surface evolution analysis (see subsection 11.4) to overcome the lack of knowledge of this applied pressure. Nevertheless the accuracy of the numerical results is influenced by the quality of the reconstruction of the boundary displacement field. An alternative is to link the action of the ribs and the surface evolution as done in [**76**] or, as we propose in subsection 11.5 to consider a Robin boundary condition to account for chest wall heterogeneity.

Finally, gravity was neglected in this work although it may significantly influence the ventilation distribution [**57**], [**105**]. However there is no consensus on the magnitude of its impact [**106**]. The potential mechanical influence of neighboring organs, such as the heart, on lung dynamics is also neglected.

In conclusion, we have built a computationally efficient mechanical model of the lung in which the tracheo-bronchial tree and parenchyma are coupled. It gives relevant and promising results. Simulations performed on a 477 exits tree took a few seconds per time step. The results pointed out the importance of nonlinearities in the airway tree for pathological conditions. Furthermore, we addressed the crucial question of boundary conditions. Applying Dirichlet boundary conditions based on parenchyma surface registration proves to generate good results in comparison with experiments. We also investigated limitations inherent to the exit compartment models. Both the lack of information on the pleural pressure spatio-temporal heterogeneity and the mechanical independence of the compartments can lead to inaccurate ventilation predictions. To overcome

these drawbacks, we proposed a method to compute pressure boundary conditions that includes mechanical interaction between compartments and surface displacement patterns and which, applied to the exit-compartment model, provided good ventilation results. Our framework is able to deal with pressure, surface displacement and also nonlinear Robin boundary conditions. We can thus model mechanical ventilation with constraints on the boundary that ensure lung volumes cannot expand over TLC.
Future work would include a more realistic non-linear constitutive relation for the parenchyma along with a study of the effect of gravity on ventilation. An experimental validation of the tree-parenchyma coupling could be performed based on dynamic parenchyma CT acquisition.

13. Appendix

In this section are presented appendix developments that were not put in the main body of the text for the sake of clarity.

13.1. On the evolution of pressure drops along the tree

It is mentioned in subsection 8.1 that the pressure drops are smaller in distal generations than in proximal tree regions. In this section pressure drops at each generation along a tree path are computed with Poiseuille and Pedley resistance models on a simplified symmetric geometry with dimensions taken from [**5**]. Tracheal flow is set to 0.33 $L.s^{-1}$. As observed in Figure 47, starting from around generation 5, the pressure drops decreases with the generation level. Most distal generations have a negligible impact.

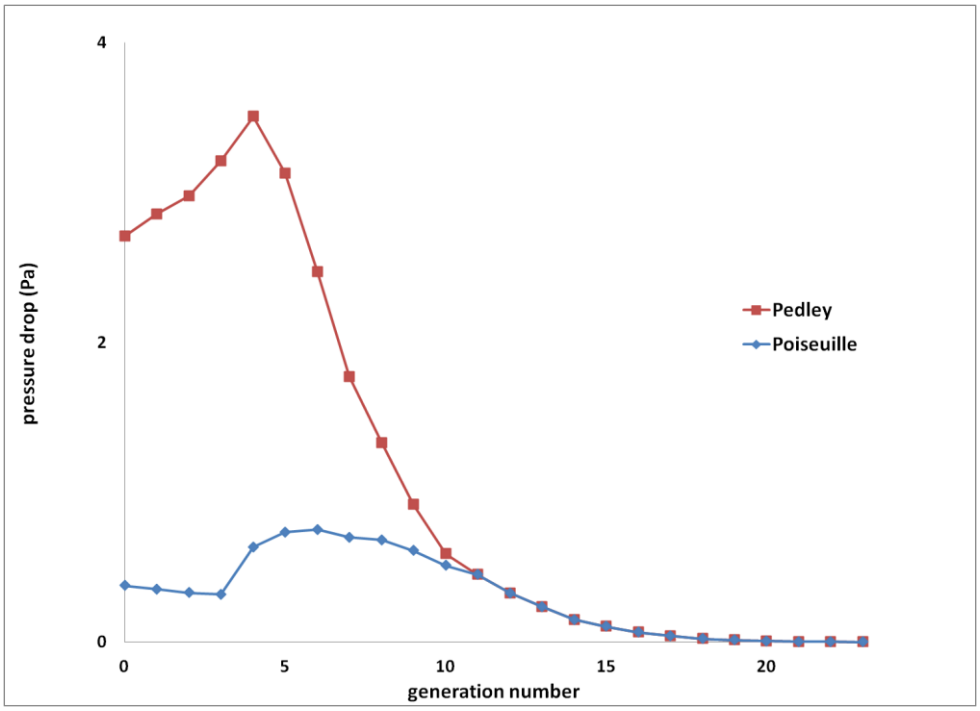

Figure 47: pressure drop at each generation of a Weibel [5] symmetric tree, computed with Pedley and Poiseuille resistance models, with flow at the trachea of 0.33 $L.s^{-1}$.

13.2. On the link between exit tree pressures and flows

In this section, we illustrate result (5) on the five-exit tree showed in Figure 48.

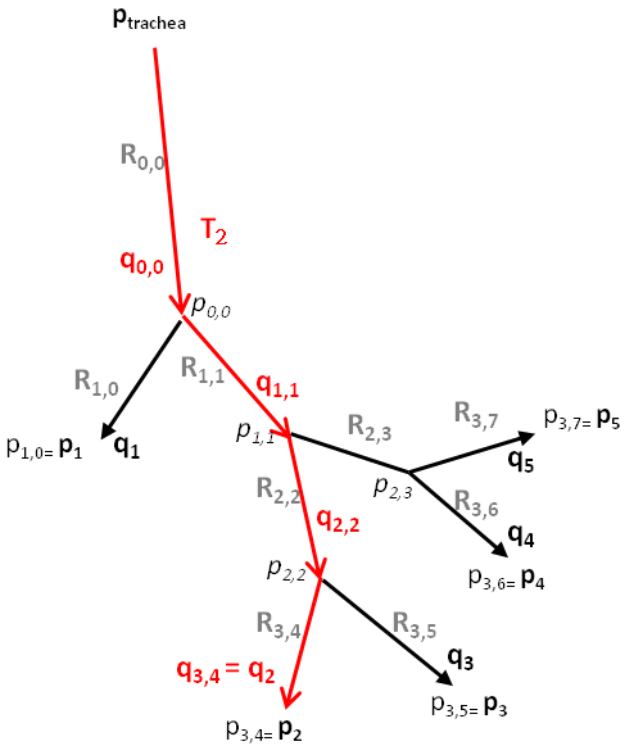

Figure 48: schematic of a five-exit tree. The flow $q_{n,k}$ and pressure drop along airway (n,k) are linked through its resistance $R_{n,k}$.

Let us compute the pressure drop along the path T_2. Assuming flow conservation we have:

$$\begin{cases} p_{trachea} - p_{0,0} = R_{0,0}q_{0,0} = R_{0,0}(q_1 + q_2 + q_3 + q_4 + q_5) \\ p_{0,0} - p_{1,1} = R_{1,1}q_{1,1} = R_{1,1}(q_2 + q_3 + q_4 + q_5) \\ p_{1,1} - p_{2,2} = R_{2,2}q_{2,2} = R_{2,2}(q_2 + q_3) \\ p_{2,2} - p_2 = R_{3,4}q_{3,4} = R_{3,4}(q_2) \end{cases}.$$

By summing those equations we get the pressure drop along T_2:

$$p_{trachea} - p_2 = q_1 R_{0,0} + q_2\left(R_{0,0} + R_{1,1} + R_{2,2} + R_{3,4}\right) + q_3\left(R_{0,0} + R_{1,1} + R_{2,2}\right) + q_4\left(R_{0,0} + R_{1,1}\right) + q_5\left(R_{0,0} + R_{1,1}\right).$$

which writes

$$p_{trachea} - p_2 = q_1 \sum_{(n,k)\in T_{12}} R_{n,k} + q_2 \sum_{(n,k)\in T_2} R_{n,k} + q_3 \sum_{(n,k)\in T_{32}} R_{n,k} + q_4 \sum_{(n,k)\in T_{42}} R_{n,k} + q_5 \sum_{(n,k)\in T_{52}} R_{n,k}.$$

Repeating the process on other paths we get $AQ = P$ where $\left[A_{ij}\right]_{ij} = \sum_{(n,k)\in T_{i,j}} R_{n,k}$, $Q = \begin{pmatrix} q1 \\ q2 \\ q3 \\ q4 \\ q5 \end{pmatrix}$, and $P = \begin{pmatrix} p_{trachea} - p_1 \\ p_{trachea} - p_2 \\ p_{trachea} - p_3 \\ p_{trachea} - p_4 \\ p_{trachea} - p_5 \end{pmatrix}$.

13.3. On assuming flow into the mother branch equals the sum of the flows entering the daughters

Some studies [**58**], [**60**] include compliant airways in the tree model following the description given in Figure 49. Airway compliance is given by $C_{aw} = \frac{2Lr_{aw}^3}{E_{aw}t_{aw}}$ with $E_{aw} \sim 3.3\ kPa$ and $t_{aw} = k_1 r_{aw}^2 + k_2 r_{aw} + k_3$ where k_1=-0.0057 mm^{-1}, k_2=0.2096, k_3=0.0904mm.

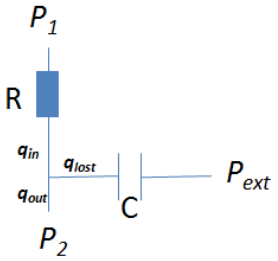

Figure 49: resistive compliant airway model.

In Figure 49, q_{in} is the flow entering the airway, q_{lost} is the instantaneous volume variation per unit time of the airway, q_{out} is the flow leaving the airway and P_{ext} is the pressure in the parenchyma region surrounding the branch. Assuming, as in [**58**], that P_{ext} is constant, we can write $q_{in} = \frac{P_1 - P_2}{R}$ and $q_{lost} = C\frac{dP_2}{dt}$. We have $q_{in} = q_{lost} + q_{out}$. Formulas (5) and (6) are valid only if the flow going through an airway equals the flow going through its daughters; this requires $q_{lost} \ll q_{in}$, which means airways are close to rigid. In the following we investigate the validity of this assumption on the model given by Figure 50.

Let us compute the order of magnitude of the flow at each generation using a rigid-tree model. To get general insights of the flows in the tracheo-bronchial tree, we work on simple models such as a purely symmetrical Weibel tree representation [**5**] with homogeneous exit pressure. In this model flows equally distribute at every bifurcation. Given an alveolar pressure $P_{alv}(t)$ and assuming Poiseuille law, pressures P_i and flows q_i at each generation i can be computed analytically. Assuming airways rigidity, flows are over-estimated. Based on the flows we can then compute an over-estimation of q_{lost_i} at each generation i and finally compare the total inlet flow q_{in} and the total lost flow $q_{lost} = \sum_i q_{lost_i}$ (see Figure 50).

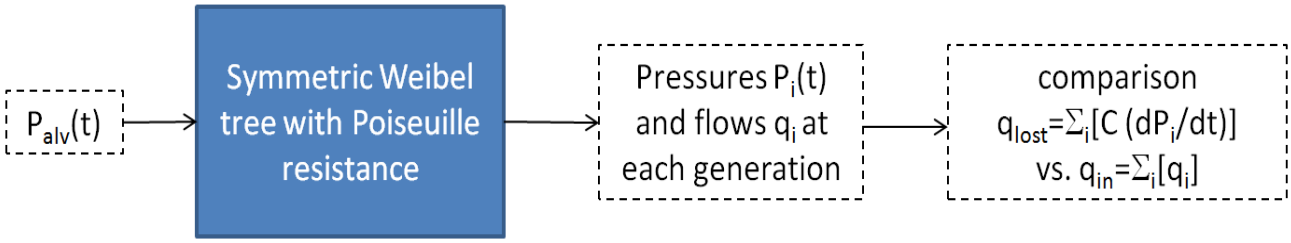

Figure 50: process to assess the significance of airway branch compliance. Assuming an alveolar pressure evolution at tree exits, we can compute the flow and pressure distribution in a symmetrical tree. The flows q_{lost} and q_{in} can be deduced and compared.

With lung tree resistance R=2.10^5 Pa.m^{-3}s^{-1} [**1**] and a maximum tidal flow at the trachea of Q=0.5 L.s^{-1}, the pressure drop within the tree is close to $\Delta P = RQ = 100Pa$. We assume a zero tracheal pressure and a sinusoidal alveolar pressure profile: $P_{alv}(t) = 100\sin(0.5t)$. Results are shown in Figure 51.

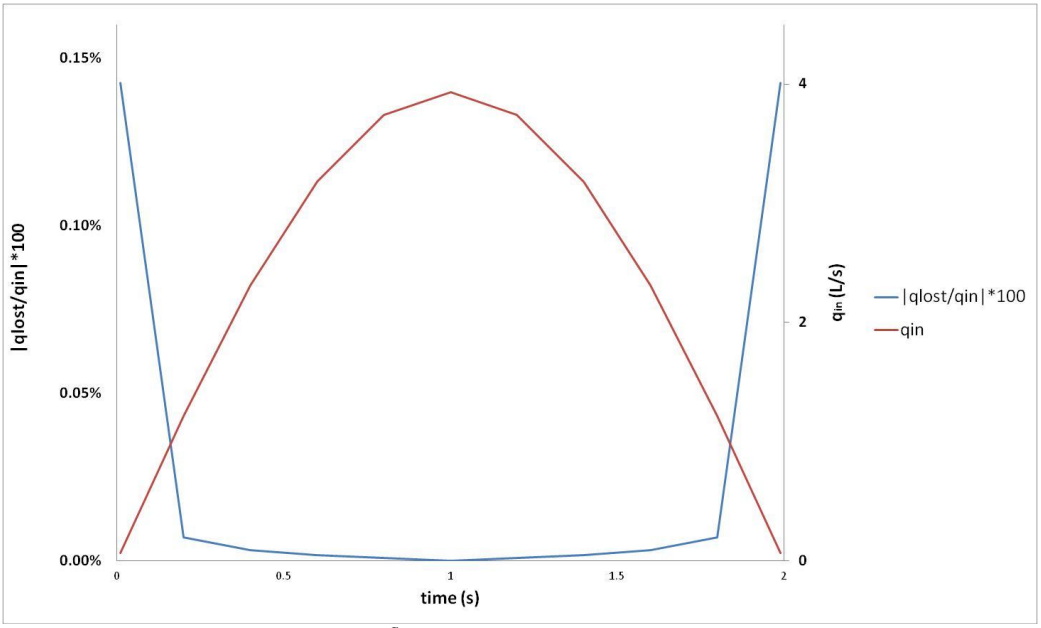

Figure 51: evaluation of the ratio of $\frac{q_{lost}}{qin}$ along an inspiratory breathing cycle for a given inlet flow.

The flux q_{lost} is much lower than q_{in} all along the inspiration cycle. Thus, airways can be considered rigid when considering the flow distribution along the tree. A test was conducted with a uniform branch resistance increase of a factor 100 (results not shown here), the lost flux remains negligible; the conclusion is unchanged when using Pedley's model instead of Poiseuille's or considering pathological resistances.

Remark 6: Equation (5) is compatible with compliant branches provided that Kirchoff's law at the bifurcation is satisfied at each time step. For example, we could allow airway dimensions to depend on transmural pressure and update resistances in consequence.

13.4. Robustness of the resolution scheme

To assess the robustness of the preconditioned conjugate gradient resolution scheme (see subsection 9.1), we simulate a highly heterogeneous pathological case. We work on the system defined in the introduction of section 11. Sinusoidal Dirichlet boundary conditions similar as the one used in subsection 11.4.2 are applied and Pedley resistance model is used.
Each branch of the tree is constricted, its diameter being divided by a random number uniformly sampled in the interval [1;10]. The Young's modulus of each terminal region is multiplied by a random number uniformly sampled in the interval [0.1;5] (see Figure 52) so that some areas are much more elastic than in the healthy case and some are less.

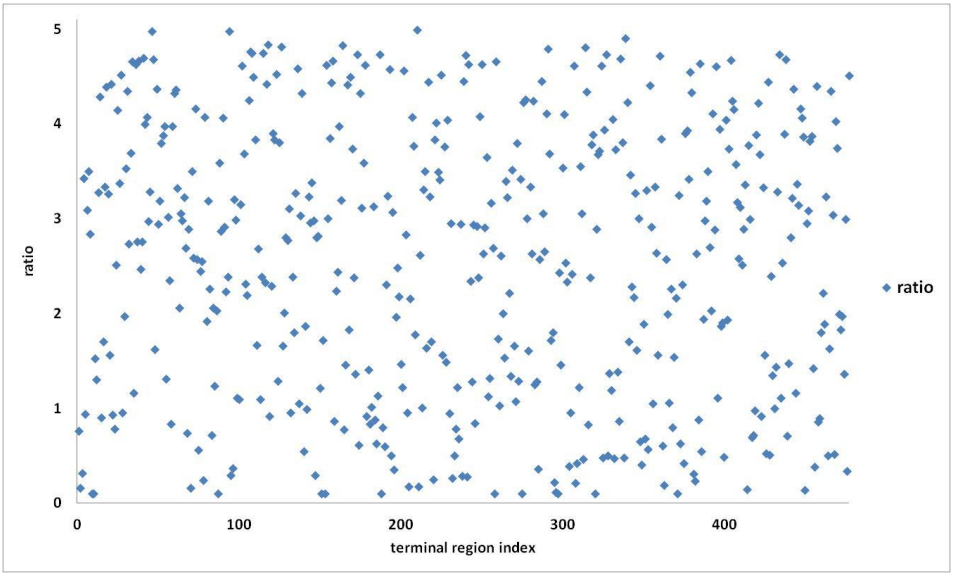

Figure 52: the Young's modulus of each terminal region is mulitplied by a ratio uniformly sampled in the interval [0.1 ;5]

In Figure 53 we plot the evolution of the normalized residual error for resolution at time 2s. For each time step the system converged in a few dozens of iterations.

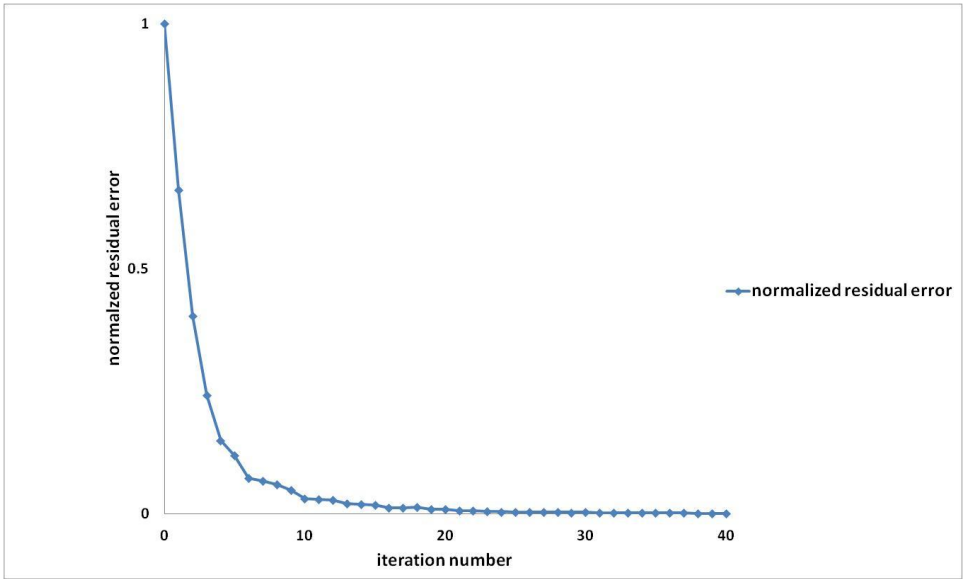

Figure 53: evolution of the normalized residual error in the preconditioned conjugate gradient scheme. Resolution at time 2s.

The obtained ventilation is highly heterogeneous as shown in Figure 54.

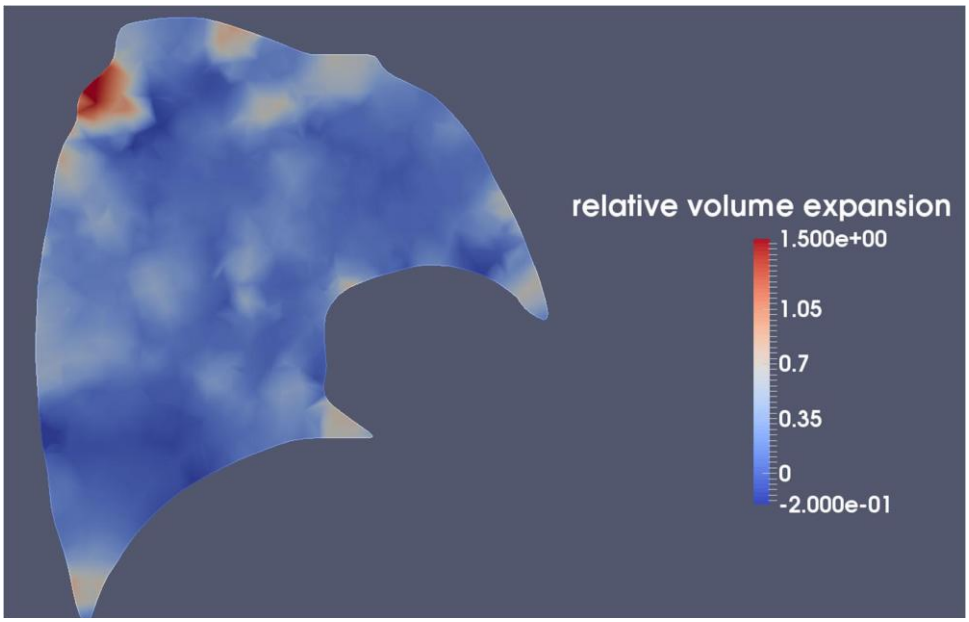

Figure 54: relative volume expansion on a left lung slice, from basis to apex. Airways were constricted with a diameter reduction ratio uniformly sampled in [1;10] and the Young's modulus of each terminal region was multiplied by a ratio uniformly sampled in [0.1;5]. The map is shown at time 2 s.

13.5. Mesh and time convergence analysis

To choose the time step and lung mesh resolution (see introduction of section 11), a convergence study is led. We simulate a case in which a stenosis with constriction ratio 10 is applied to the branch feeding lobe LL. High constrictions in localized regions lower the conditioning of the FE system, induce ventilation heterogeneities and time delay. This is why such a test case is chosen for the convergence analysis. Pedley resistance model is used. We compare the local ventilation and pressure results obtained on a 24688, a 51495 and a 70476 tetrahedron mesh (see Figure 55 and Figure 56). Pressure and volume differences simulated with the 51495 tetrahedron mesh compared to the finer one are less than 1%. Based on those results, in this chapter, a 51495 tetrahedron mesh is used.

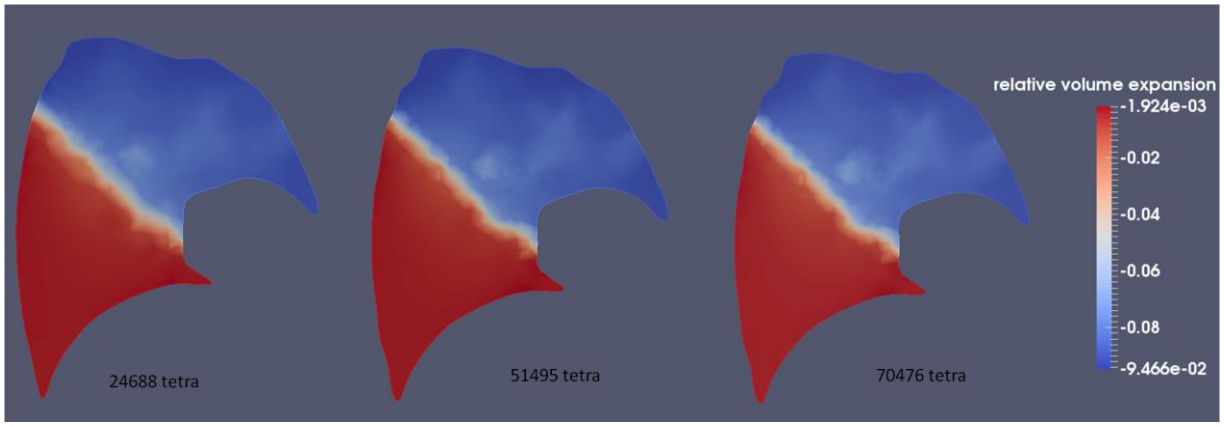

Figure 55: mesh convergence study, comparison of the local relative expansion on a left lung cut. A stenosis with constriction ratio 10 was applied to the branch feeding lobe LL (in blue on the figure).

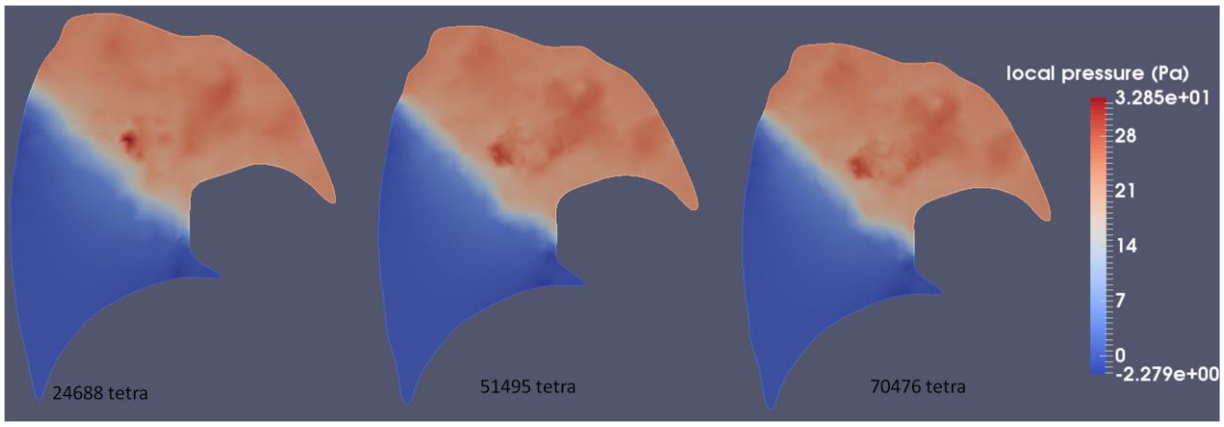

Figure 56: mesh convergence study, comparison of the local pressure defined by (38) on a left lung cut. A stenosis with constriction ratio 10 was applied to the branch feeding lobe LL (in orange on the figure).

In Figure 57 lobar flow rates are plotted for time steps 0.04 and 0.01 s. Volume differences are less than 1%. Time 0.04s has been chosen for the simulations in this chapter.

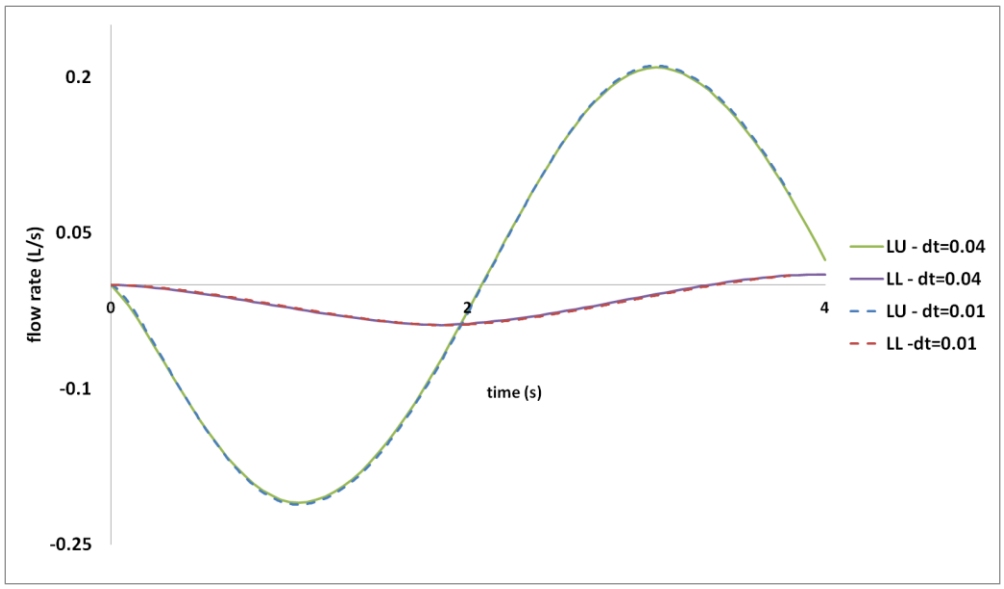

Figure 57: time convergence study, comparison of lobar flow rates for time steps 0.01s and 0.04s. A stenosis with constriction ratio 10 was applied to the branch feeding lobe LL.

13.6. Lobar surface fissure detection

Adding lobar surface fissures to the registration process improves its quality. We perform an automatic detection based on available lobar segmentations, i.e. a 3 by 3 voxel matrix in which each voxel gets a label depending on the lobe it belongs to. The process is divided into three steps. First, based on a neighboring analysis, each voxel belonging to the lung surface and getting at least one neighbor belonging to a different lobe is selected. At this stage, we get a set of non-ordered points defining lobar fissures (see Figure 58). In a second step, for each fissure, we order those points. To this end they are projected on the plane that best fits the fissure (see Figure 59), clustered and ordered based on an angular discretization (see Figure 60). Finally we apply this ordering back into the $3D$ space (see Figure 61) and perform a smoothing [**107**], [**108**] of the resulting one-dimensional manifold. Figure 62 illustrates the result on a right lung.

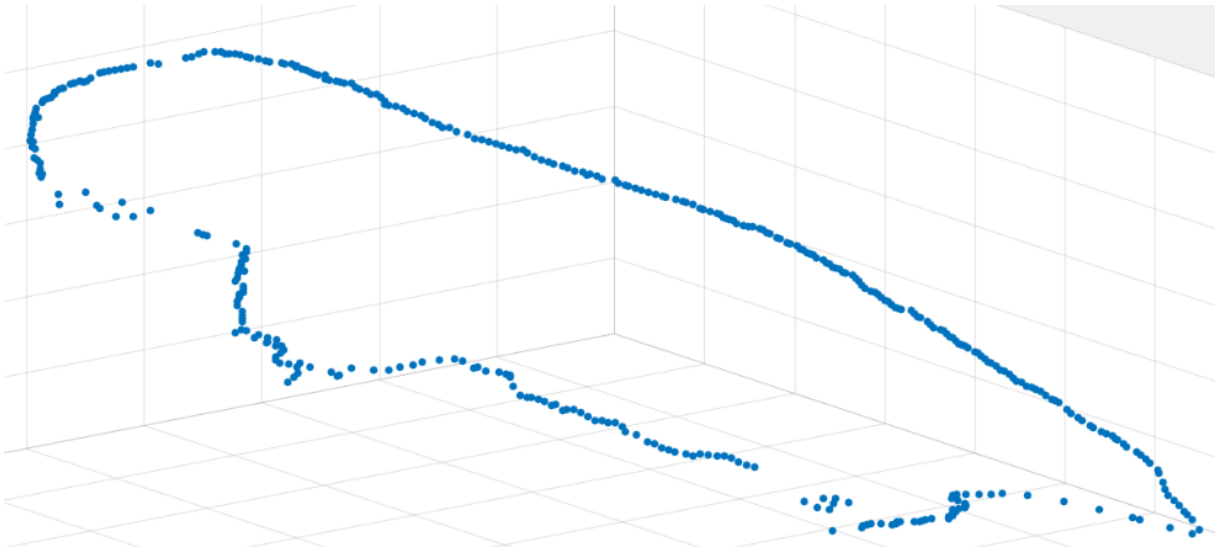

Figure 58: set of non-ordered points belonging to the lobe fissure separating lobes LU and LL.

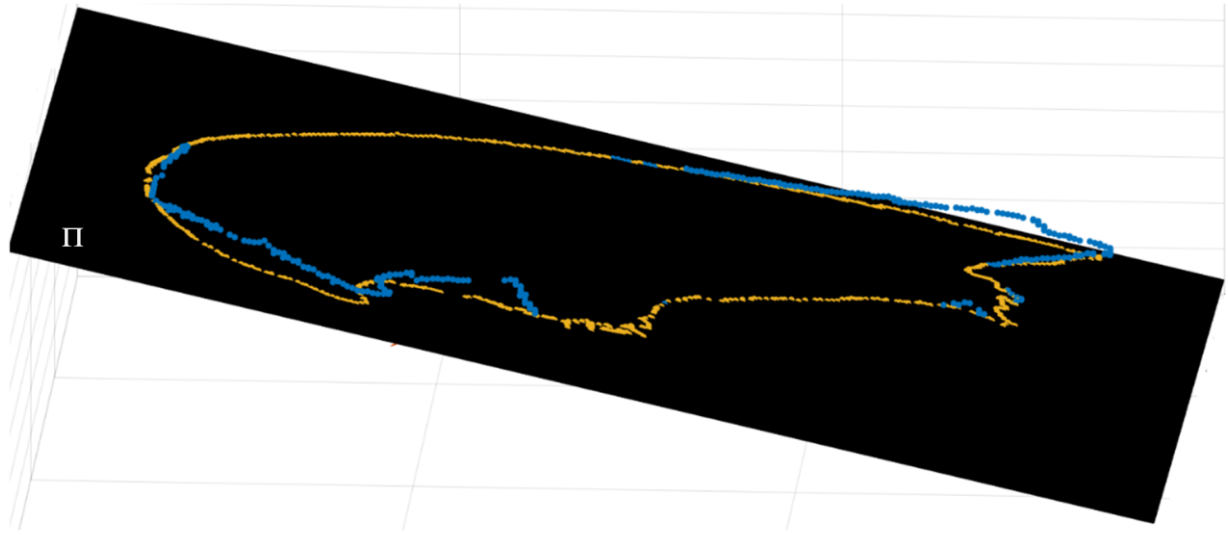

Figure 59: projection of the set of non ordered points on the plane Π that best fits the fissure. In blue the non ordered points in the $3D$ space, in yellow their projection. Plane Π is defined by the two principal directions of the point set and contains its barycenter.

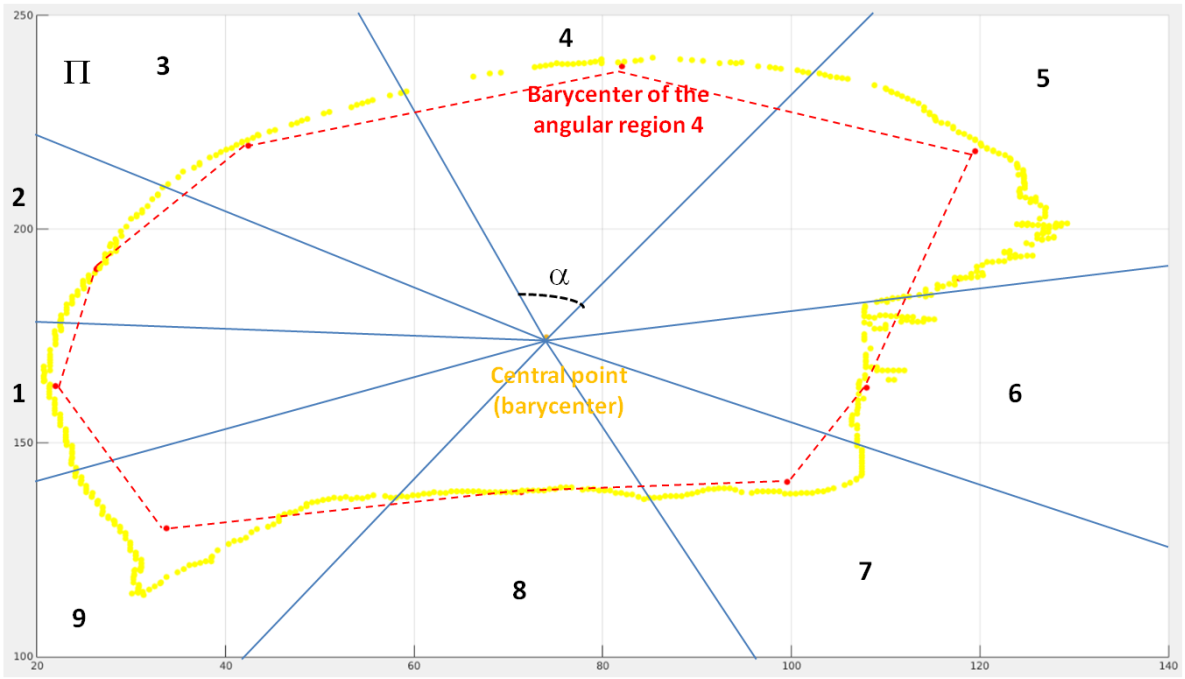

Figure 60: angular discretization of the point set on plane Π. The plane is divided in angular regions separated by lines going through the central point (barycenter of the point set) successively rotating of an angle α. Points are clustered based on their angular position. The barycenter on each cluster is computed. The final curve interpolates those local barycenters. Here, for the sake of clarity, illustration on a rough angular discretization with α=40°.

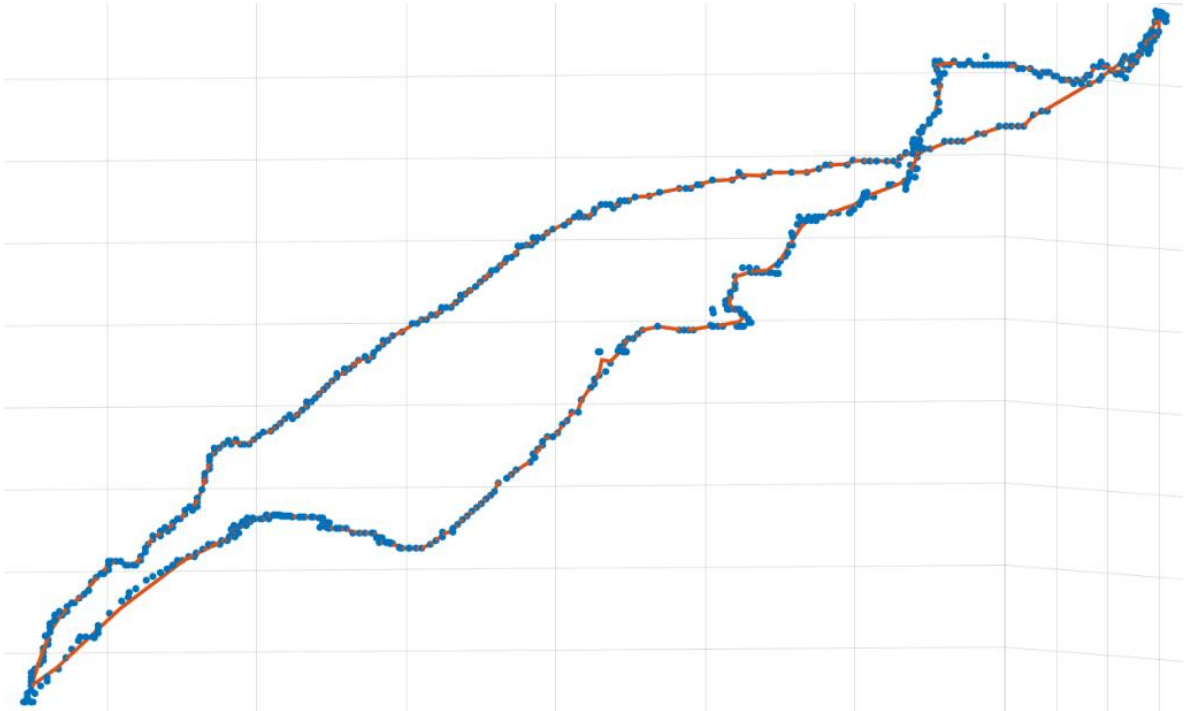

Figure 61: Lobar fissure approximation. Applying the angular ordering back to the $3D$ space and smoothing the curve joining the points we get an approximation of the lobar fissure.

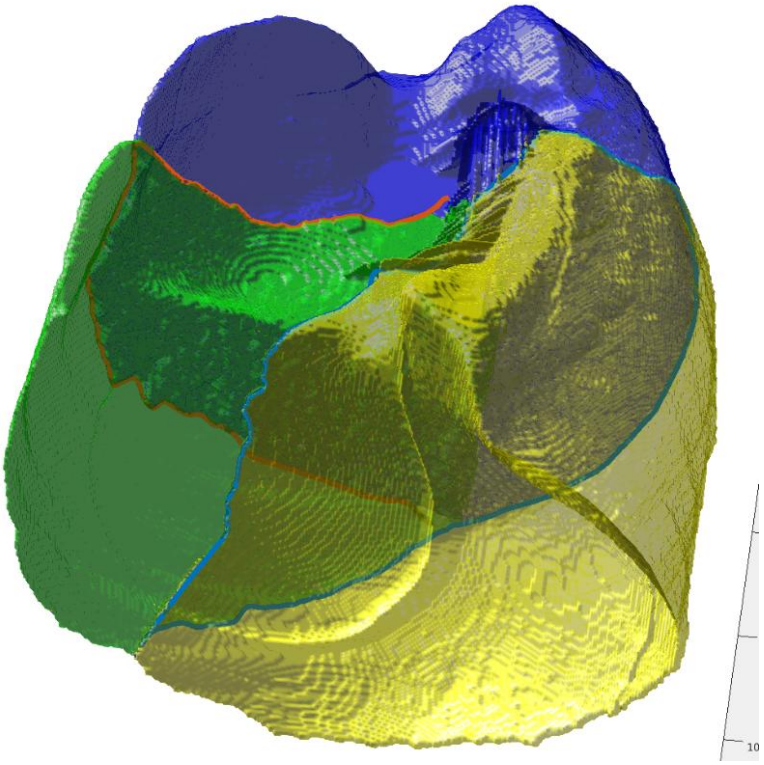

Figure 62: detected surface lobe fissures on a right lung, built based on lobar segmentation.

13.7. Dynamical surface displacement built based on two static images

As mentioned in subsections 10.3 and 11.4, Dirichlet boundary conditions are constructed based on two lung geometries of the same patient at MLV and TLC states. Let $\boldsymbol{u_{MLV \to TLC}}$ be the registered displacement from MLV to TLC. To impose tidal look-alike boundary conditions, with sinusoidal dynamics, we consider the surface displacement field $\boldsymbol{u_{tidal}}(t)$ defined by:

$$\boldsymbol{u_{tidal}}(t) = \alpha \boldsymbol{u_{MLV \to TLC}}(1 - \cos(\omega t))$$

Where α is a positive scalar smaller than 1, used to bound the volume evolution, and ω is the pulsation of the imposed dynamics.
Note that when expanding from MLV to TLC, intercostal muscles are solicited whereas they play little role in tidal breathing. Thus when homogeneously bounding $\boldsymbol{u_{MLV \to TLC}}$ to construct a tidal displacement, one may over-estimate the costal displacement.

CHAPTER III- Calculated ventilation and effort distribution as a measure of respiratory disease and Heliox effectiveness

In spite of numerous clinical studies, there is no consensus on the benefit Heliox mixtures can bring to asthmatic patients in terms of work of breathing and ventilation distribution. In this chapter we use the $3D$ finite element mathematical model of the lung presented in CHAPTER II to study the impact of asthma on effort and ventilation distribution along with the effect of Heliox compared to air. Lung surface displacement fields extracted from computed tomography medical images are used to prescribe realistic boundary conditions to the model. Asthma is simulated by imposing bronchoconstrictions to some airways of the tracheo-bronchial tree based on statistical laws deduced from the literature. This study highlights potential mechanisms for patient responsiveness to Heliox when affected by obstructive pulmonary diseases. Responsiveness appears to be function of the pathology severity, as well as its distal position in the tracheo-bronchial tree and geometrical position within the lung.
The content of this chapter has been accepted for publication [**43**].

14. Introduction

The lung is a complex multiscale system. Furthermore, many in-vivo measurements, especially as a function of position within the lung parenchyma, are difficult or impossible to perform. Thus, mathematical models can provide a unique understanding of physical phenomena associated with fundamental physiology and respiratory disease. In [**41**] and [**74**] $3D$ lung models were developed and used to study the impact of airway bronchoconstrictions on ventilation and pressure distributions within the parenchyma. In this chapter we perform in silico asthma experiments and focus on the variety of response to a helium-oxygen mixture (Heliox or HeO_2).

Helium is a low density inert gas. Heliox has been studied as a means to ease breathing and improve ventilation in obstructive lung diseases since the 1930s [**109**]. However, consistent benefit demonstrated in randomized clinical trials has yet to follow thus preventing widespread use. For example, a Cochrane review [**49**] concluded that current evidence is insufficient to support the use of HeO_2 mixtures in the treatment of acute exacerbations of COPD and future controlled trials are advocated. Recently, a large trial (16 intensive care units, 6 countries) found that HeO_2 improves respiratory acidosis, encephalopathy and respiratory rate more quickly than Air/O_2 for COPD patients but does not prevent NIV failure [**110**]. In [**111**] healthy controls, moderate to severe asthmatic and COPD patients inhaled HeO_2 during exercise. The impact on lung function and metabolic cost showed no statistical difference compared to air even though in each group there were some responders and non-responders. The authors emphasized the need to better understand the influence of disease and disease severity on responsiveness to Heliox.

There are few modeling attempts to study the effect of breathing HeO_2 compared to Air. In [**15**] a resistance model accounting for gas density effect on pressure drops in a bifurcation is proposed and applied to Heliox mixtures. In [**82**] the impact of breathing HeO_2 on particle deposition is studied, CFD, in-vivo imaging and bench study suggest deeper deposition compared to air. In this chapter, we use a numerical modeling approach to give insights on why, for a given pathology, some patients respond to HeO_2 and some others do not. In the following, responsiveness to Heliox is judged based on how the gas helps to decrease work of breathing and reduce ventilation defects compared to air. We use the model presented in subsection 8.2. To simulate obstructive diseases, some airways can be constricted. Depending on which and how many airways are narrowed, we evaluate responsiveness to HeO_2.

15. Model and methods

15.1. Tree-parenchyma coupling and measure of the effort

In this chapter, the tree-parenchyma coupling model presented in subsection 8.2 is used. As we want to emphasize the effect of gas density, we use the Pedley non linear resistance model (4). As described before (see subsection 8.2), momentum equation of the system is:

$$div\left(\sigma_{mat}(\boldsymbol{u}) + \sigma_{coupling}(\dot{\boldsymbol{u}})\right) = \rho_{par}\frac{\partial^2 \boldsymbol{u}}{\partial t^2}, \quad in\ \Omega,$$

where ρ_{par} is the parenchyma density and $\sigma_{coupling}$ is the tree-parenchyma coupling term given by

$$\sigma_{coupling} = -p_{tree}I,$$

p_{tree} being defined by (17). To complete the problem, a periodic lung surface motion, typical of tidal breathing, is prescribed as the boundary condition to Equation (19) (see subection 11.4.2). The same

global ventilation scenario is thus imposed, whatever the disease state and inhaled gas.
Then to evaluate the benefit of Heliox compared to air we propose local $3D$ quantities as well as global average markers to account for respiratory effort. We use the pressure distribution within the parenchyma called local effective pressure p_{eff} and defined by (38). It consists in an elastic component $p_{elastic}$ (27) associated with the elastic recoil and a component $\delta_{tree}(\dot{\boldsymbol{u}})$ (15) associated with the tree. It is given at time t by:

$$p_{eff}(\boldsymbol{x},t) = Kdiv\big(\boldsymbol{u}(\boldsymbol{x},t)\big) + \delta_{tree}(\dot{\boldsymbol{u}}(\boldsymbol{x},t)) \;\; in\, \Omega$$

where K is the parenchyma bulk modulus defined by (28). In this definition shear stress and inertia are neglected. We also define the global average quantities

$$P_{elastic} = \int_{\Omega} |p_{elastic}| \tag{39}$$

and

$$P_{tree} = \int_{\Omega} |\delta_{tree}| \tag{40}$$

which can respectively be seen as a measure of the instantaneous effort needed to deform an elastic material along the displacement field $\boldsymbol{u}$, and the effort needed to induce the corresponding flow distribution through the tree.
The work W of p_{eff} over a time period *T*, i.e. a complete breathing cycle, is defined as:

$$W = \int_0^T \int_{\Omega} \Big[\Big(Kdiv\big(\boldsymbol{u}(\boldsymbol{x},t)\big) + \delta_{tree}(\boldsymbol{x},t)\Big)\, div\big(\boldsymbol{v}(\boldsymbol{x},t)\big)\Big] \tag{41}$$

where $\boldsymbol{v}$ is the parenchyma velocity field defined by $\boldsymbol{v} = \frac{\partial \boldsymbol{u}}{\partial \boldsymbol{t}}$. Integrating over inspiration only, we get the inspiratory work.

15.2. Modeling disease of the tracheo-bronchial tree

Asthma and COPD affect the tracheo-bronchial lung tree structure. Inflammation can induce airway constrictions [**112**], [**113**] up to closure [**22**], [**26**]. While some studies argue these pathologies mostly occur in small airways [**114**], [**115**], autopsies on patients who died from status asthmaticus [**25**], [**26**] and CT scans of diseased subjects have shown upper airways can also be affected [**22**]. Little quantitative data is provided in the literature about which particular airways are affected in asthma and to what extent. Some studies show slight but frequent airway narrowing. In [**26**] measured lumen area exhibited radius decreases of about 10% on average compared to controls. In [**112**] CT measurements showed reductions of 10 to 25%. In addition to those small constrictions, [**115**] demonstrates the presence of airway closures in asthmatic patients. In [**22**] segmented images of asthmatic patients indicate that severe stenoses can completely occlude airways. Non-published data from this study give the number of closures per segmented tree.
To simulate a bronchoconstriction with diameter reduction ratio c_r (simply referred as "ratio" in the following) we divide the diameter of the affected branch by c_r ranging from 1 (healthy) to 10 (airway closure). This constriction ratio is thus defined as

$$c_r = \frac{d_{healthy}}{d_{constriction}} \tag{42}$$

where $d_{healthy}$ and $d_{constriction}$ are respectively the diameter the airway would have in a healthy configuration and its diameter in the constricted case.
Furthermore, based on CT scan measurements data provided in [**112**] and [**116**] (see Figure 63) we simulate an asthma attack with constriction ratios generated according to a log-normal law $\mathcal{L}$ with average $log(1.2)$, standard deviation 0.3 and within bounds $[1; 3]$ (see Figure 63). We also impose $n_{closure}$ severe constrictions (plugs), $n_{closure}$ being an integer randomly selected with uniform law in the interval $[\![1; 40]\!]$. Plugs are applied at random positions and with constriction ratios randomly selected with the uniform law in the interval $[4; 10]$. In order to compare the effect of severe and moderate obstructions, we can impose $n_{closure}$ severe plugs only, or, alternatively, only divide all the airways diameters by ratios computed following $\mathcal{L}$. Resulting trees will be qualified respectively as "plug only" and "plug free".

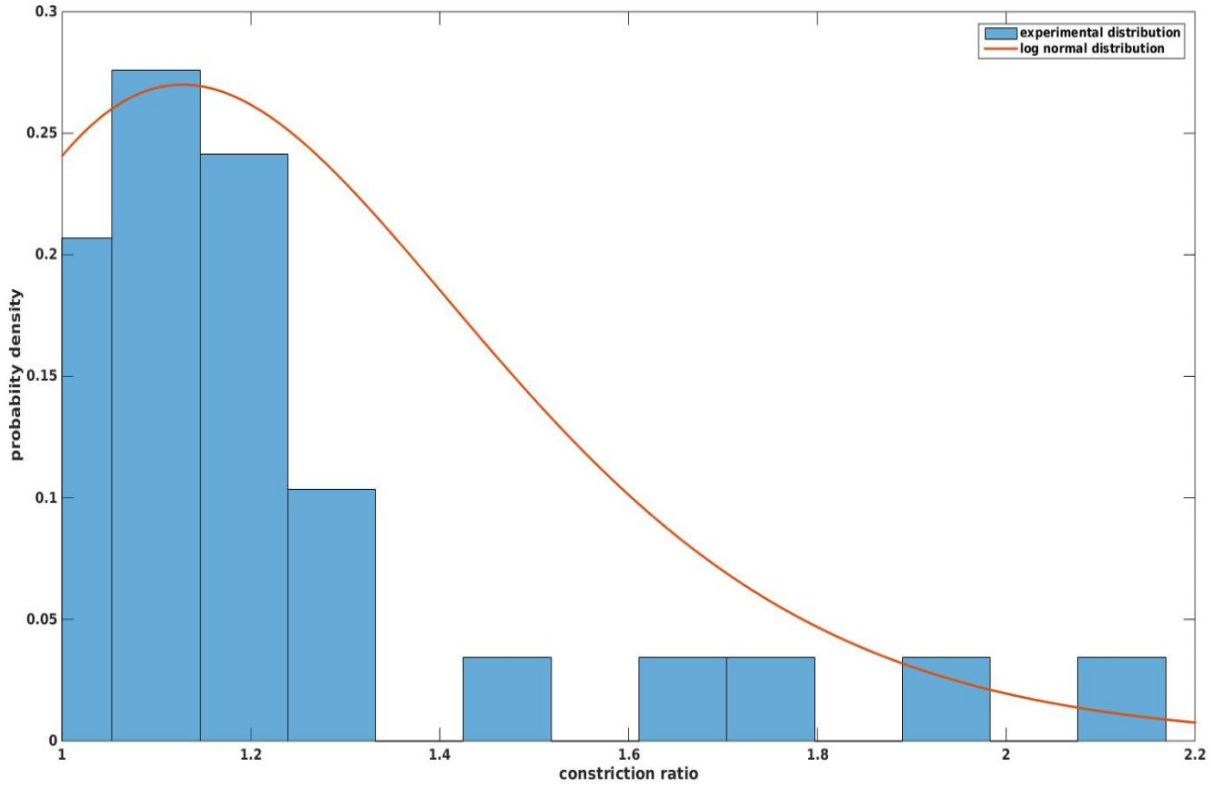

Figure 63: in blue, histogram representing the experimental constriction ratios probability density distribution in asthmatic patients: aggregated data from studies [112**] and [**116**]. In red, probability density function of the log normal law used to simulate moderate constrictions in asthma.**

16. Results and discussion

In this section lung ventilation simulation results and breathing effort are provided. Local and global differences between healthy and pathological cases are explored. We first simulate a single bronchoconstriction on an upper airway and study the effect of breathing HeO_2 compared to air on both ventilation and $\dot{W}$. We then analyze how responsiveness to HeO_2 evolves depending on which region of the lung is affected and when smaller airways are constricted. After having described the physical principles on simplified bronchoconstrictions, asthma attacks are introduced following subsection 15.2.
Simulations are performed on a left lung geometry. The mesh is the same as those used in subsection 11.4.2. Mechanical properties are defined in the introduction of section 11. The tree contains ten generations leading to 477 exits. Each exit airway resistance includes an additive term to account for

the remaining sub-tree resistance. The lobe nomenclature is defined in section 11. Branches feeding lobes LU and LL are called the "LU branch" and "LL branch", respectively. Each region "Reg" contains two sub-regions "RegR" and "RegL" served by a "RegR branch" and a "RegL branch" respectively. If not specified, the breathing period is 4s, the reference state lung volume is 1.04L and maximum volume expansion is 0.23L. Air density and viscosity at 37°C are respectively 1.125 $kg.m^{-3}$ and 18.95 10^{-6} Pa.s, the HeO_2 mixture contains 78%He/22% O_2, density is 0.434 $kg.m^{-3}$ and viscosity is 22.56 10^{-6} Pa.s. As in subsection 11.4.2, a sinusoidal displacement boundary condition built along the lines described in subsection 13.7 is applied. The overall lung volume evolution is thus imposed and, if not specified, identical for all the simulations.

16.1. Impact of a bronchoconstriction

In this section a bronchoconstriction with varying ratios is imposed on the LU branch. Lobar volume expansions are plotted for both air and HeO_2. First a healthy case is simulated (Figure 64), volumes evolve in phase and lobar ventilation is not affected by the inhaled gas, inertial effects are negligible. In Figure 65 are the results for a bronchoconstriction with ratio 7 applied to the LU branch. Lobe LU expands less and does not expel all the gas it contains, gas trapping is typical of asthma and COPD [**117**]. Ventilation of the diseased region is improved when breathing HeO_2 compared to air. Indeed, velocity in the constricted airway, and hence inertial effects, are increased because of the diameter reduction. This effect is all the more important when the gas density is high (see equation (4)) so resistance to Air is higher than resistance to HeO_2. Finally, in order to breathe a given amount of gas, HeO_2 flow results in lower pressure drops than air making it easier to breathe. For a given lung surface displacement, gas distributes preferentially in regions where it goes more easily so lobe LL is more ventilated.

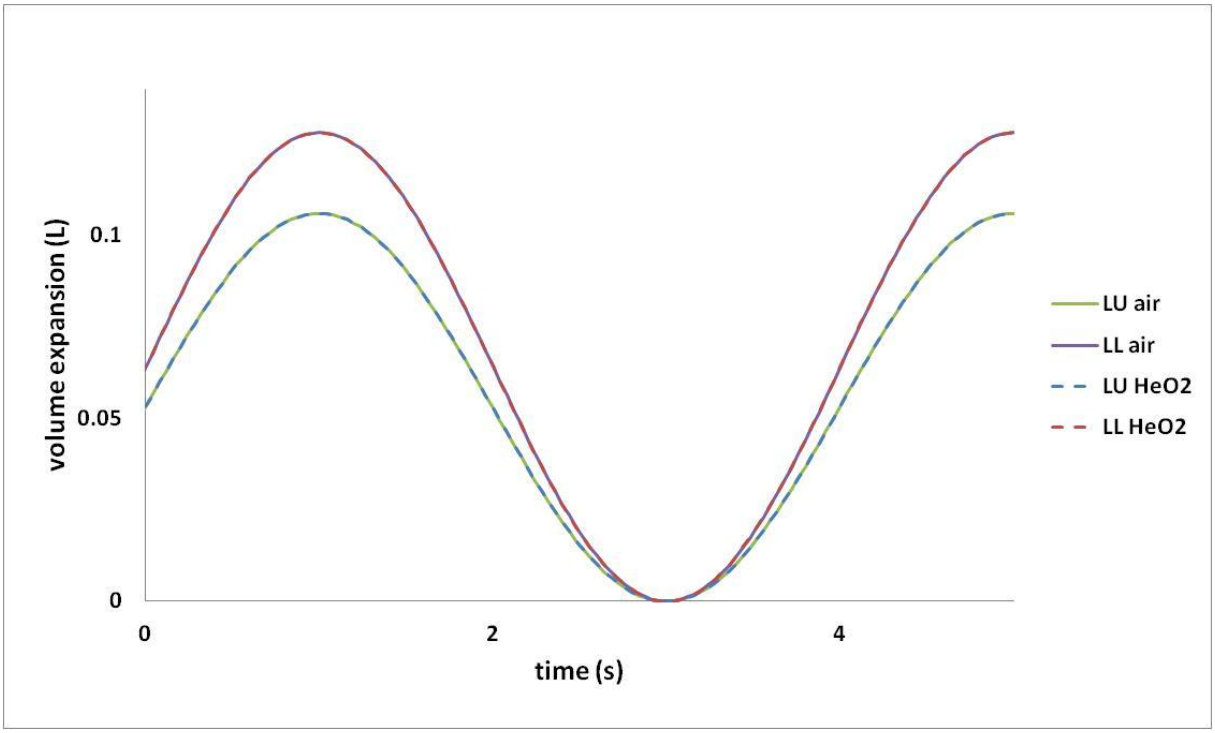

Figure 64: Lobar ventilation through a sinusoidal respiration cycle for both air and HeO_2 in a healthy situation.

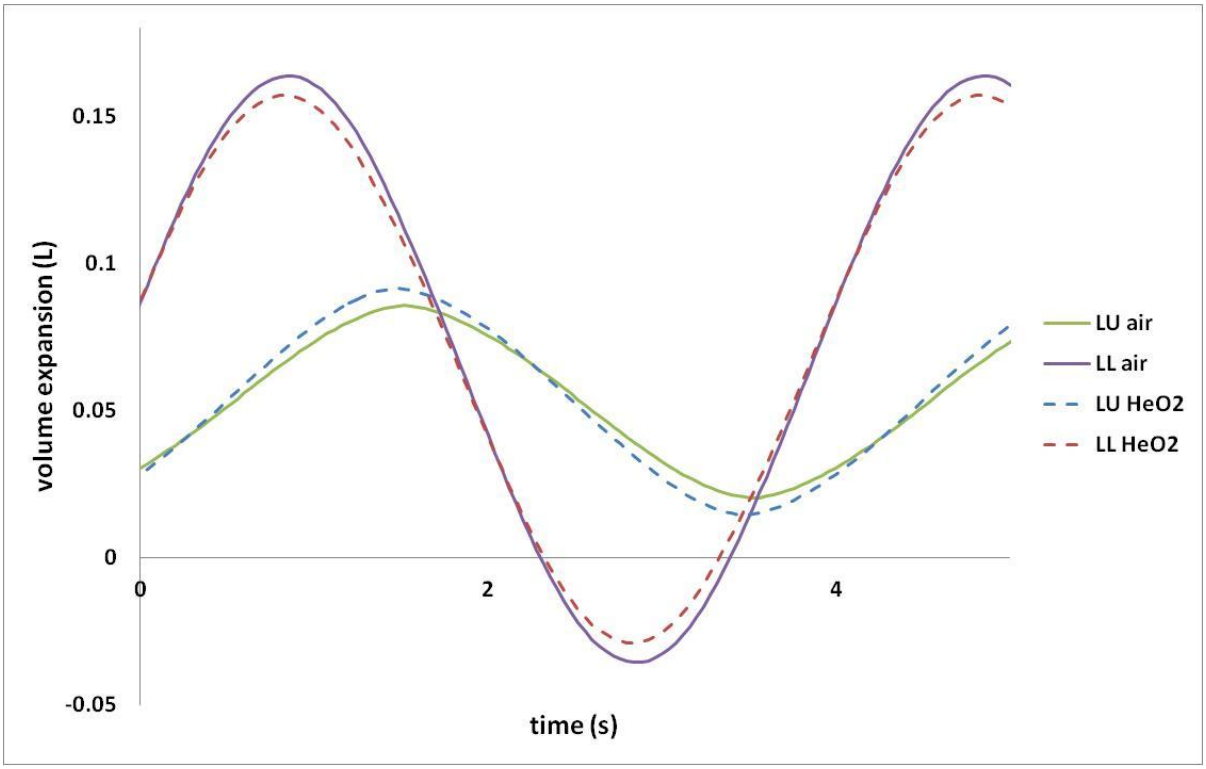

Figure 65: Lobar ventilation through a sinusoidal respiration cycle for both air and HeO_2 in case a bronchoconstriction with ratio 7 is applied to LU branch. See the text for ratio choices.

In Figure 66 and Figure 67, $P_{elastic}$ (39) and P_{tree} (40) are plotted. In the healthy case (Figure 66), $P_{elastic}$ is much greater than P_{tree}. Regarding ventilation effort, it is negligibly changed when inhaling HeO_2. In Figure 67 a bronchoconstriction with ratio 5 is applied to the LU branch. This ratio was chosen for representation because it emphasizes most pressure differences between healthy and constricted configurations while a factor 7 exhibited a higher gap for ventilation. Component P_{tree} is no longer negligible compared to $P_{elastic}$. Breathing HeO_2 is clearly easier.

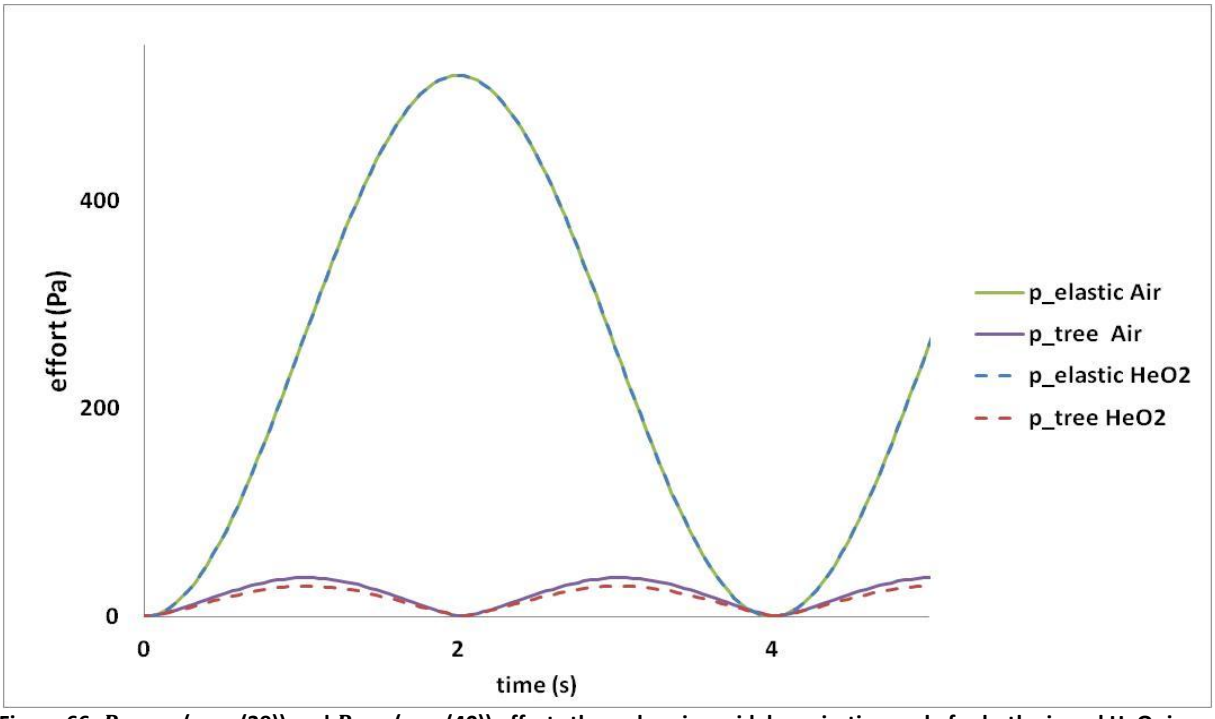

Figure 66: $P_{elastic}$ (eqn. (39)) and P_{tree} (eqn.(40)) efforts through a sinusoidal respiration cycle for both air and HeO_2 in a healthy situation.

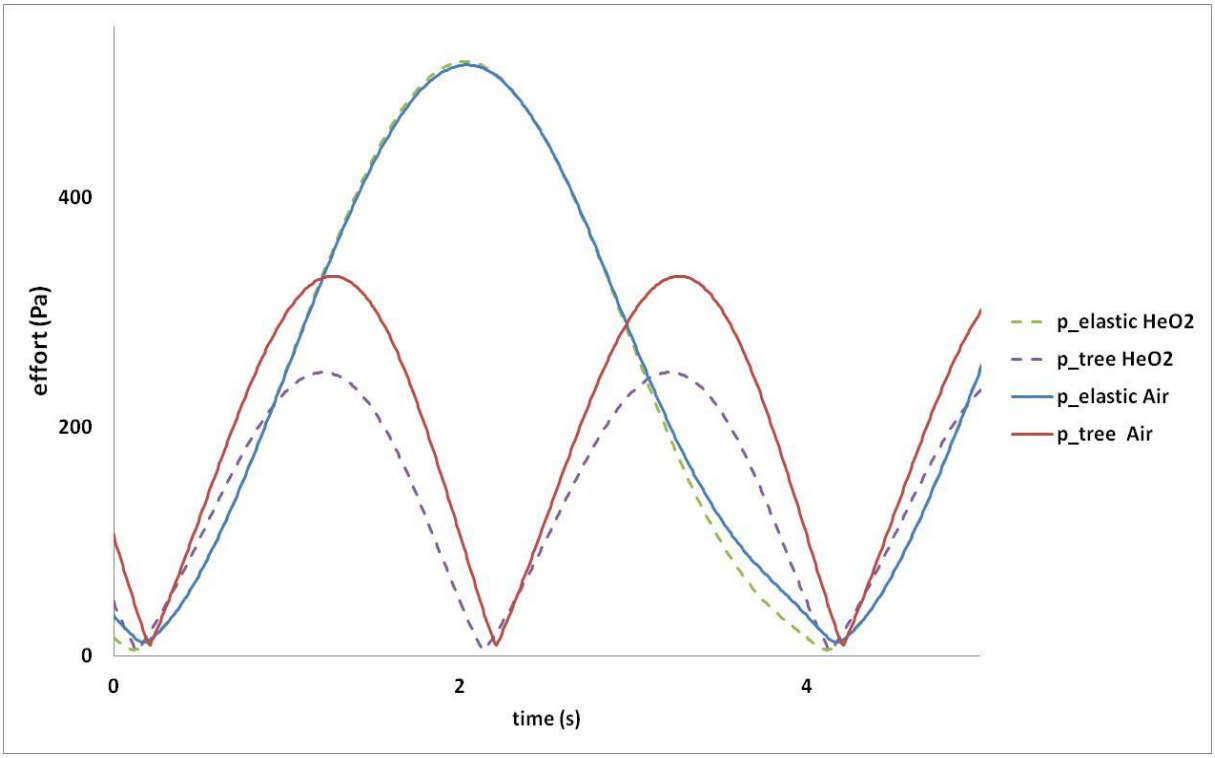

Figure 67: $P_{elastic}$ (eqn. (39)) and P_{tree} (eqn.(40)) efforts through a sinusoidal respiration cycle for both air and HeO_2 case a bronchoconstriction with ratio 5 is applied to LU branch. See the text for ratio choices.

Figure 68 shows contour plots of the relative volume expansion $div(\boldsymbol{u})$ on lung cut at time 1.68s for both gases in a healthy case and for bronchoconstrictions with ratio 5 and 7 applied on the LU branch. We first note that volume expansion is heterogeneous and greater at the base than the apex. Indeed the diaphragm is more active than the ribs during tidal breathing. As already observed in Figure 64, the ventilation distribution is not affected by the gas in the healthy model. In the pathological situation, the LU lobe is less expanded, and breathing HeO_2 mitigates the ventilation heterogeneity. The more severe the constriction, the higher the heterogeneity. In Figure 69 are plots of p_{eff}, as defined by (38), at time 1.68s. The local effort in the diseased region is reduced with HeO_2, consistent with Figure 67.

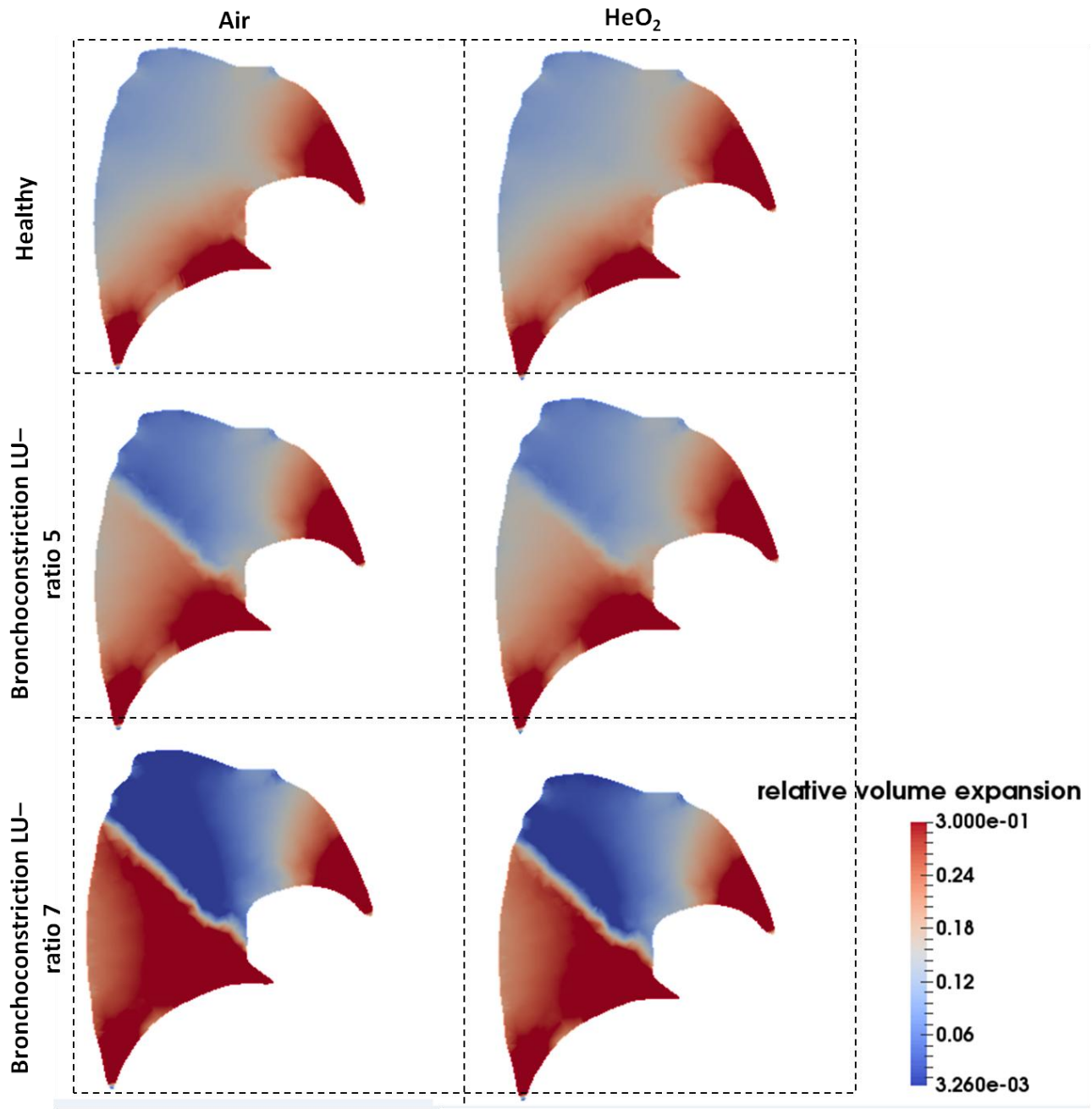

Figure 68: Left lung slice from basis to apex representing the relative volume expansion $div(u)$ in a healthy case and when bronchoconstrictions with ratio 5 and 7 are applied to LU branch, for both Air and HeO_2 at time 1.68s.

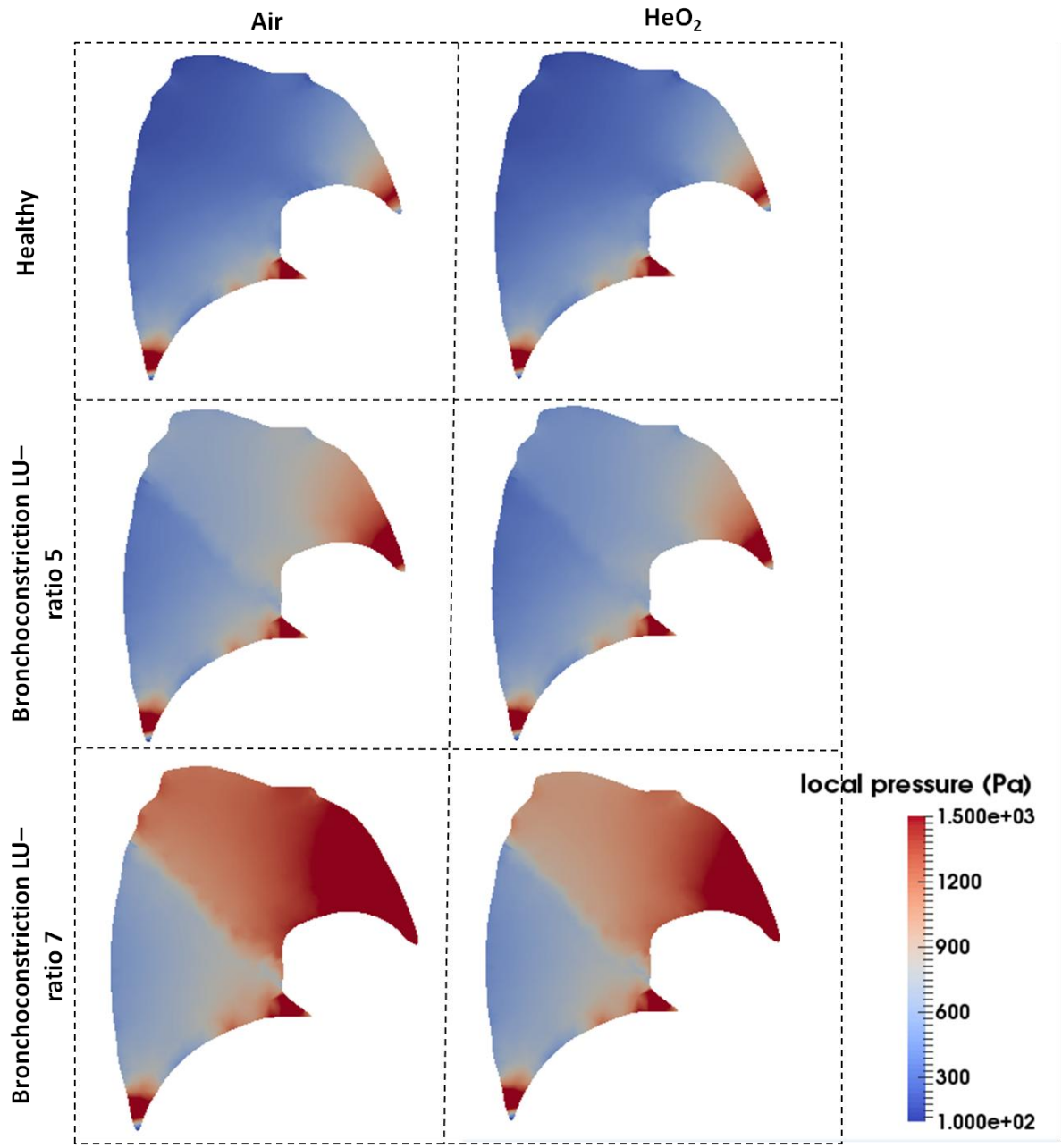

Figure 69: Left lung slice from basis to apex representing the local pressure p_{eff} defined by (38) in a healthy case and when bronchoconstrictions with ratio 5 and 7 are applied to LU branch, for both Air and HeO_2 at time 1.68s.

Depending on the pathology severity, response to HeO_2 varies. Figure 70.A shows the evolution of the LU lobe volume amplitude as a function of the bronchoconstriction applied to the LU branch; for both gases. For every ratio the LU lobe is more ventilated with HeO_2 than with air. The more the diameter reduction, the more the inertial effects and the higher the ventilation difference between both gases, up to 27% for tested cases. In Figure 70.B, W over one respiration cycle is studied. Up to a ratio 7, it appears easier to breathe HeO_2 than air. For higher ratios the difference between the two gases is inversed. As a function of the pressure drop along the tree, W is a balance of resistances and flows. As the constriction gets more severe, inertial effects are increased so the resistance to air flow increases more than the resistance to HeO_2. Concurrently to the resistance ratio decrease, the HeO_2 to air flow rate ratio increases. Thus, after an interval of constrictions where W is lower for HeO_2, it becomes comparable for the two gases and eventually W is higher for HeO_2. Note that the total volume variation is imposed, whatever the effort it takes to reach; so for strong ratios the system may exhibit non-physiological efforts.

In conclusion, responsiveness to HeO_2 depends on the pathology severity. A low density gas helps reducing W if the pathology is not too severe and improves ventilation of diseased regions in all studied cases. However, this model does not include a resistance through the extra-thoracic region where inertial losses may be sufficient to make HeO_2 consistently easier to breath than air [**118**].

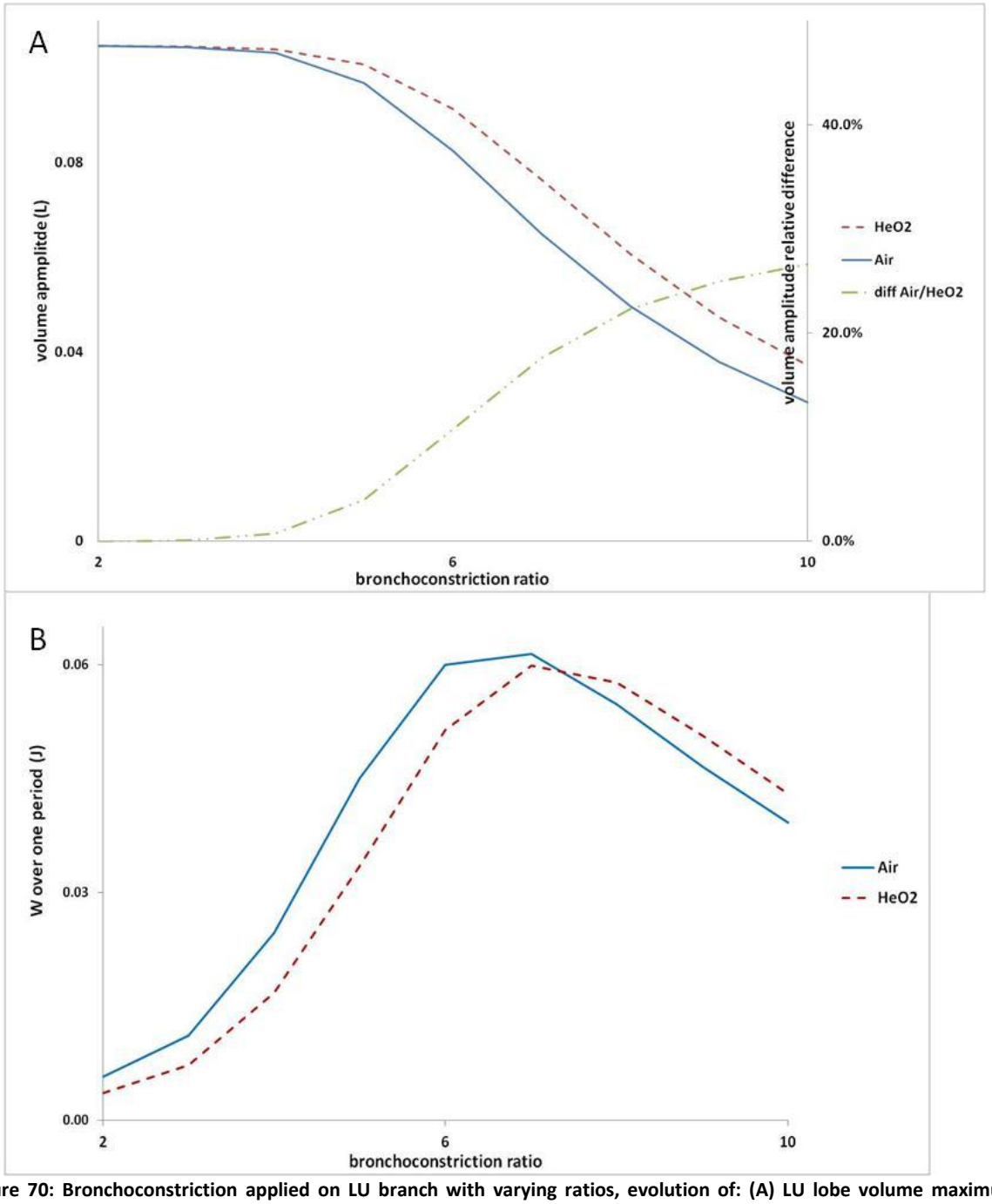

Figure 70: Bronchoconstriction applied on LU branch with varying ratios, evolution of: (A) LU lobe volume maximum amplitude over a breathing period for both Air and HeO_2, and the relative difference between both gases, (B) W (defined by eqn. (41)) over a breathing period for both Air and HeO_2.

16.2. Impact of the regional position

In this section we study how the regional position of the pathology within the lung influences the responsiveness to HeO_2. To do so we compare the ventilation in three lung regions LURL, LULR, LULL

for varying reduction ratios. Those regions have the same reference state volume but different expansions over the breathing cycle (Figure 71). We also compare the work it takes to inspire when the parenchyma mechanical properties of those regions are changed, namely simulating stiffening generated by a fibrosis. Note that in equation (41), the elastic contribution to the work of breathing is negative. The energy spent to expand the lung is returned to the system at expiration. By considering the inspiratory part only, we account for the extra-difficulty it takes to breath when mechanical properties are changed. To model fibrosis, we proceed as in subsection 11.2: the Young modulus of the region is multiplied by a coefficient greater than one, a so-called fibrosis ratio.

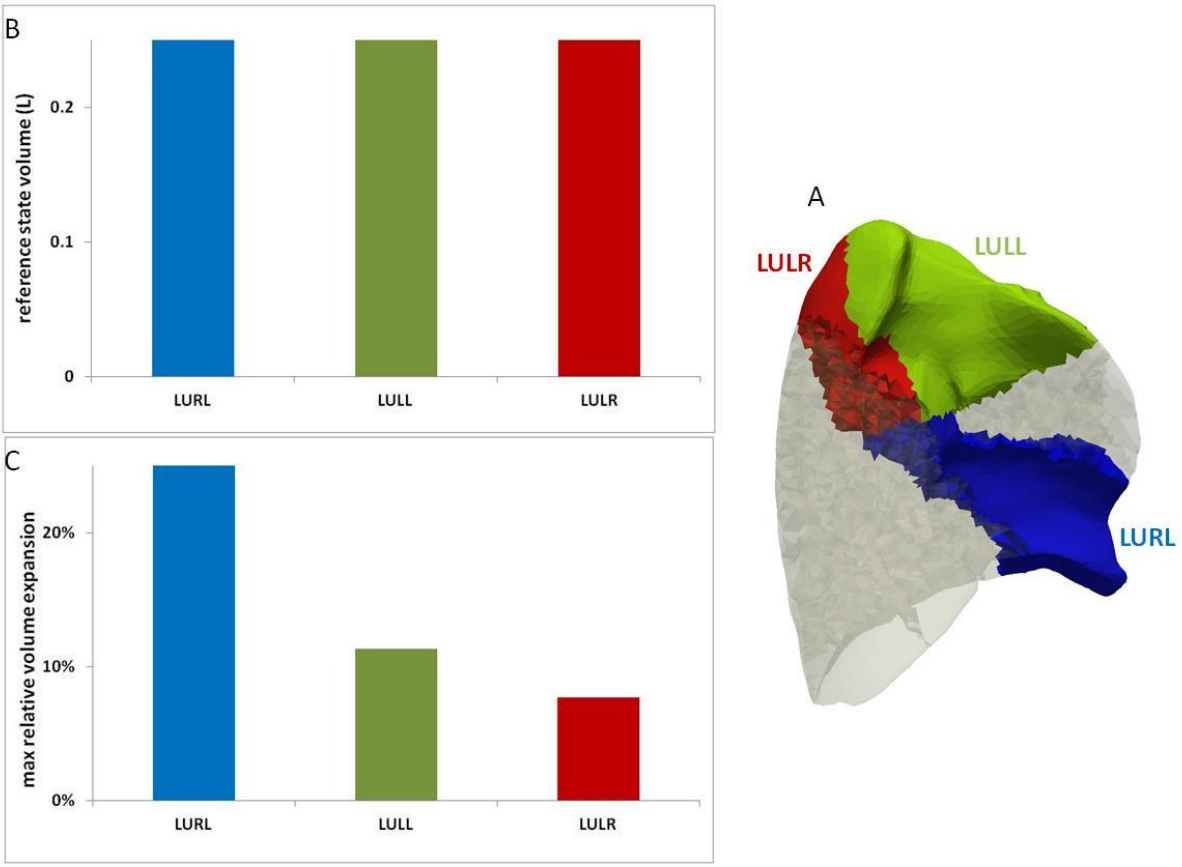

Figure 71: Three comparable regions belonging to the left lung are chosen (A). They have the same reference state volume (B) but different volume expansions over the breathing cycle (C).

In Figure 72 we see that for high reduction ratios the resulting flow rates are too low to induce inertial effects so HeO_2/air differences become insignificant. Note that in the absence of inertial effects pressure drops are purely viscous; since air viscosity is lower, the relative difference becomes negative though absolute values are close. For intermediate ratios, the difference between both gases increases with regional expansion because inertial effects are larger.

As a conclusion responsiveness to HeO_2 is highest for intermediate pathology severity and depends on the position within the lung.

In Figure 73 the inspiratory work of breathing (see subsection 15.1) as a function of the fibrosis ratio affecting each of the three regions is plotted. It takes more energy to inspire as the region is stiffer. The work increase depends on the regional position of the pathology, and is higher for regions that expand more. Those results are shown when breathing air. As the tree is not affected there is no difference when breathing Heliox (see Figure 74).

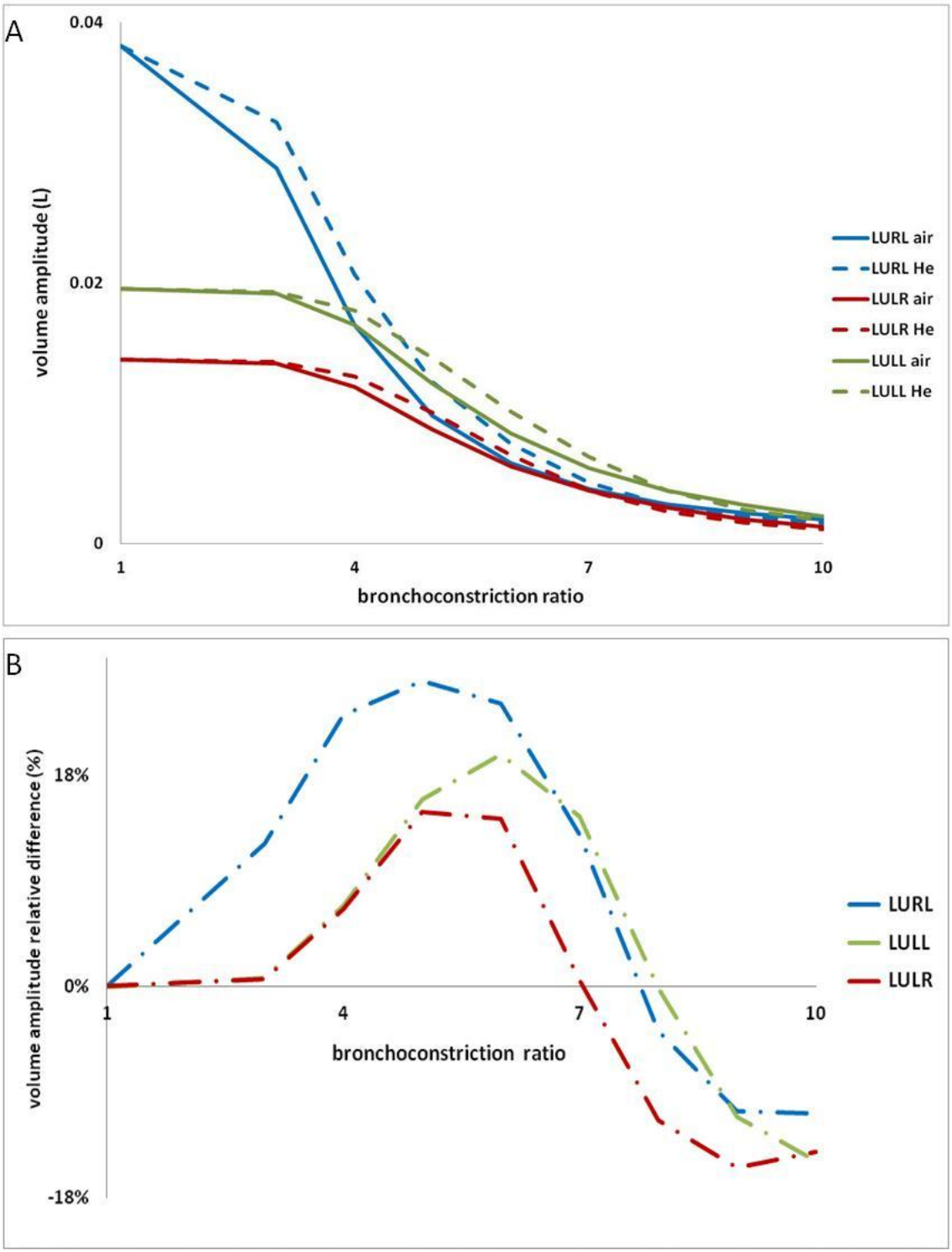

Figure 72: Ventilation in three lung regions. Volume amplitude with Air and HeO_2 for varying ratios (A) and relative difference between both gases for each region (B).

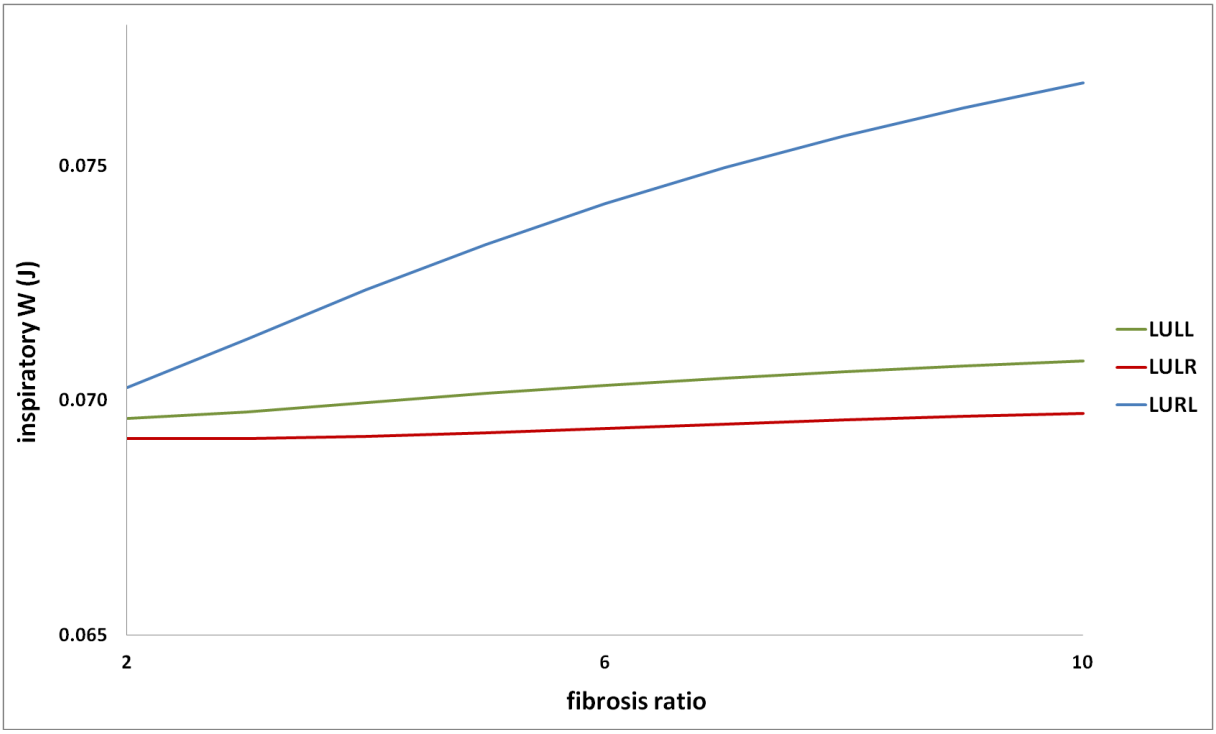

Figure 73: Inspiratory work of breathing when a parenchyma region is stiffened by a fibrosis. To model fibrosis, the Young modulus of the pathological region is multiplied by the so-called fibrosis ratio. Here are plotted the works for varying fibrosis ratios, for the three regions described in Figure 71 A.

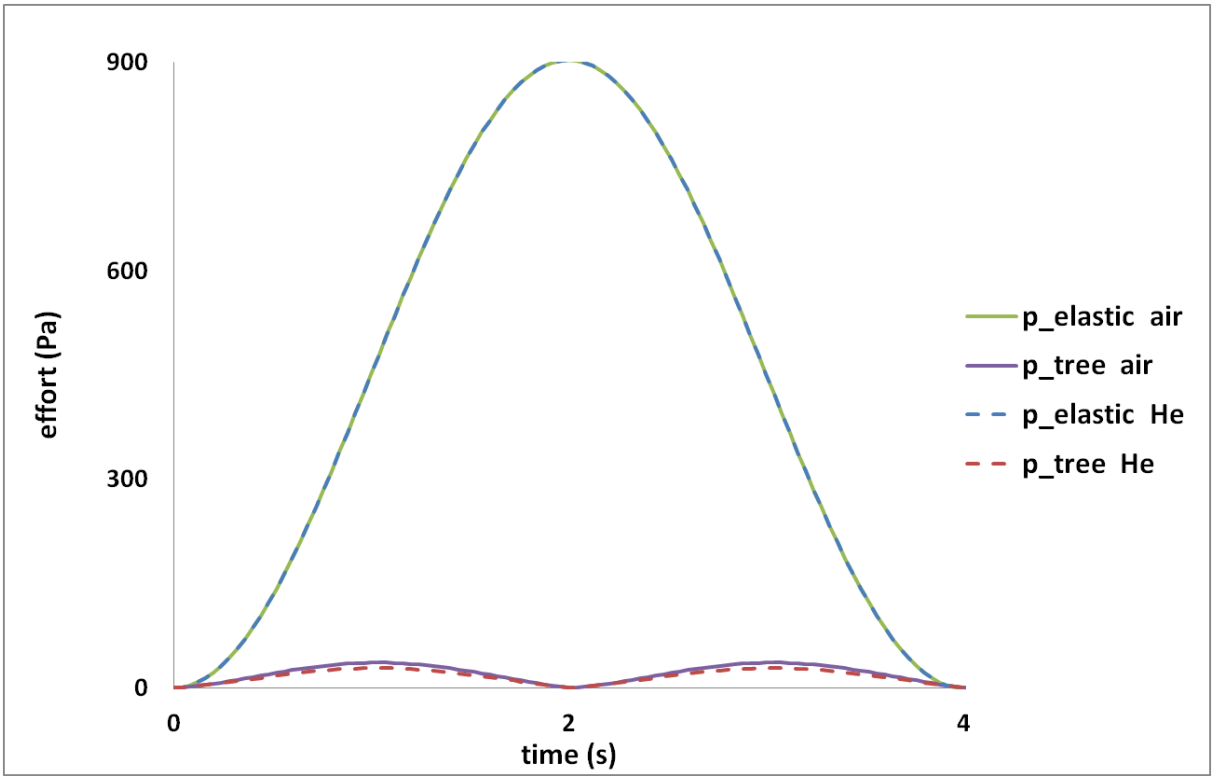

Figure 74: $P_{elastic}$ (eqn. (39)) and P_{tree} (eqn.(40)) efforts through a sinusoidal respiration cycle for both air and HeO_2 in case a fibrosis with ratio 10 is applied to region LURL.

16.3. Impact of the generational position

As noted before, responsiveness to HeO_2 is higher for higher flows. From proximal to tidal regions, flows decrease as they distribute within the tree. Depending on which generations are affected by the pathology, responsiveness to HeO_2 may be different. In this section we apply a bronchoconstriction on all the airways of the LU lobe belonging to generation n, for $n \in [\![2; 8]\!]$. For each "diseased generation", ventilations obtained with both gases are compared for varying ratios.
Figure 75 shows two different regimes. When proximal generations (2 and 3) are affected, responsiveness to HeO_2 increases with the bronchoconstriction ratio. For more distal generations responsiveness increases with constriction severity, but then decreases as flows become too slow to induce inertial effects. Starting at generation 8, HeO_2 brings no benefit compared to air. As a conclusion, in the case of bronchoconstriction, HeO_2 seems to be beneficial when upper airways are affected, but this is not the case as the pathology reaches more distal areas, here after generation 8.

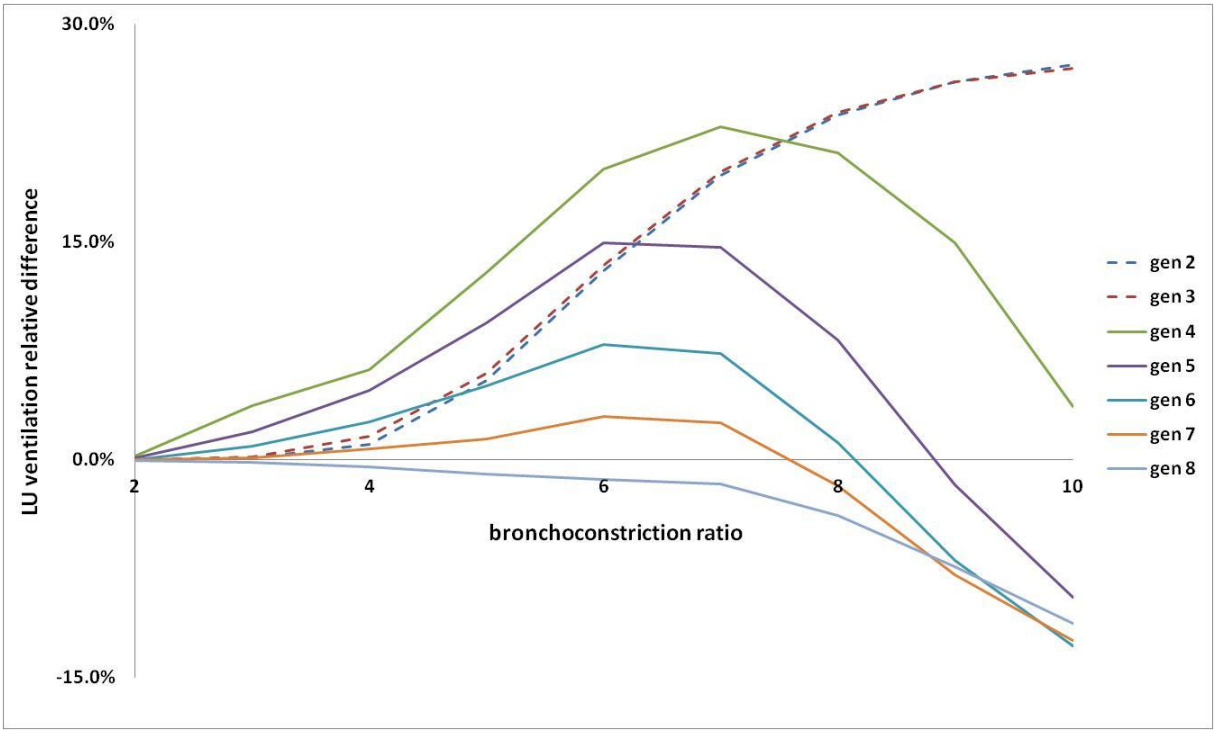

Figure 75: Bronchoconstrictions are applied to all the airways of a given generation belonging to LU lobe. Each curve corresponds to a different "diseased generation" and shows the maximum inhaled volume relative difference between both gases ($\frac{Vmax_{HeO_2} - Vmax_{Air}}{Vmax_{Air}}$) for varying ratios.

16.4. Asthma attack simulation

In previous sections one or more localized bronchoconstrictions with diameter reduction ratios varying from 2 to 10 were simulated. Here we simulate an asthma crisis with a combination of severe obstructions and lower radius changes, as described in subsection 15.2. Following this process fifty "asthma attack trees" are built. To compare the effect of severe and moderate obstructions, "plug free" and "plug only" related trees are simulated (see subsection 15.2).
During a crisis patients may panic, experience breathing difficulties and tend to breathe faster with lower volumes, even though slow breathing is advised [**119**]. To study the effect of breathing HeO_2 and the impact of respiration frequency we perform the simulations listed in Table 2. Results are presented in Figure 76 and Figure 78. In Figure 77 we study the specific impact of plugs characteristics on the work of breathing.

Inhaled gas / ΔV_{frc}(L) & T(s) – tree model	Air	HeO_2
0.23 L & 4 s - healthy	1 simulation	1 simulation
0.16L & 2 s - asthma	50 simulations	50 simulations
0.23 L & 4 s - asthma	50 simulations	50 simulations
0.23 L & 8 s - asthma	50 simulations	⊠
0.23 L & 4 s – plug only	50 simulations	50 simulations
0.23 L & 4 s – plug free	50 simulations	50 simulations

Table 2: simulations performed on the asthma model. We generate fifty "asthma attack trees", for each we run breathing simulations with sinusoidal displacement boundary conditions, time period is T and volume expansion along the cycle is ΔV_{frc}. To simulate a crisis, we consider reduced ΔV_{frc} and T. To evaluate the benefit of slow breathing we take a longer period, this is done for air only since Heliox has little impact for low flows. An "asthmatic" tree contains both severe and moderate bronchoconstrictions as described in subsection 15.2. Trees qualified as "plug only" and "plug free" respectively contain only severe bronchoconstrictions and only diffuse moderate bronchoconstrictions (see subsection 15.2). "Healthy" means no bronchonconstrictions. Blue and red refer respectively to Figure 76 and Figure 78.

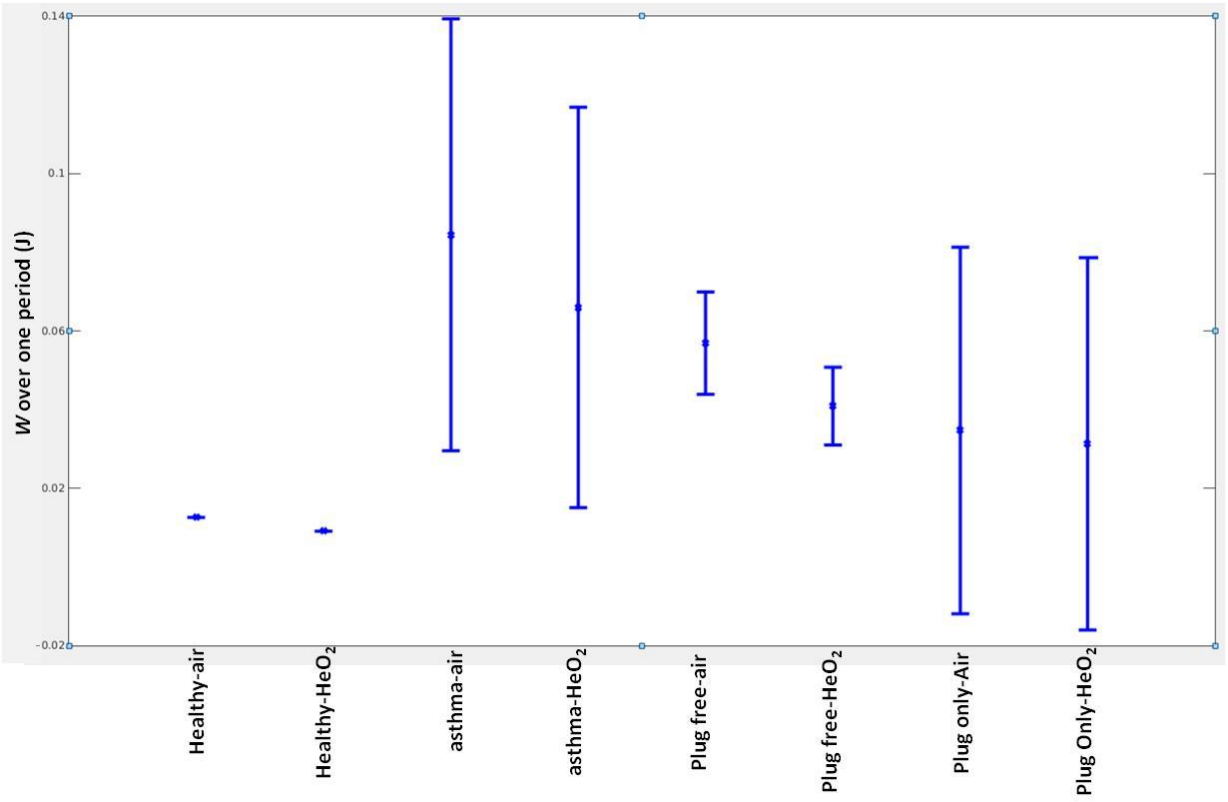

Figure 76: average and standard deviations of W over a respiration cycle in different configurations: one healthy patient breathing air and HeO_2, fifty asthmatic configurations with bronchoconstrictions simulated according to subsection 15.2, fifty patients with only diffuse moderate bronchoconstrictions (plug free) and fifty patients with only severe bronchoconstrictions (plug only).

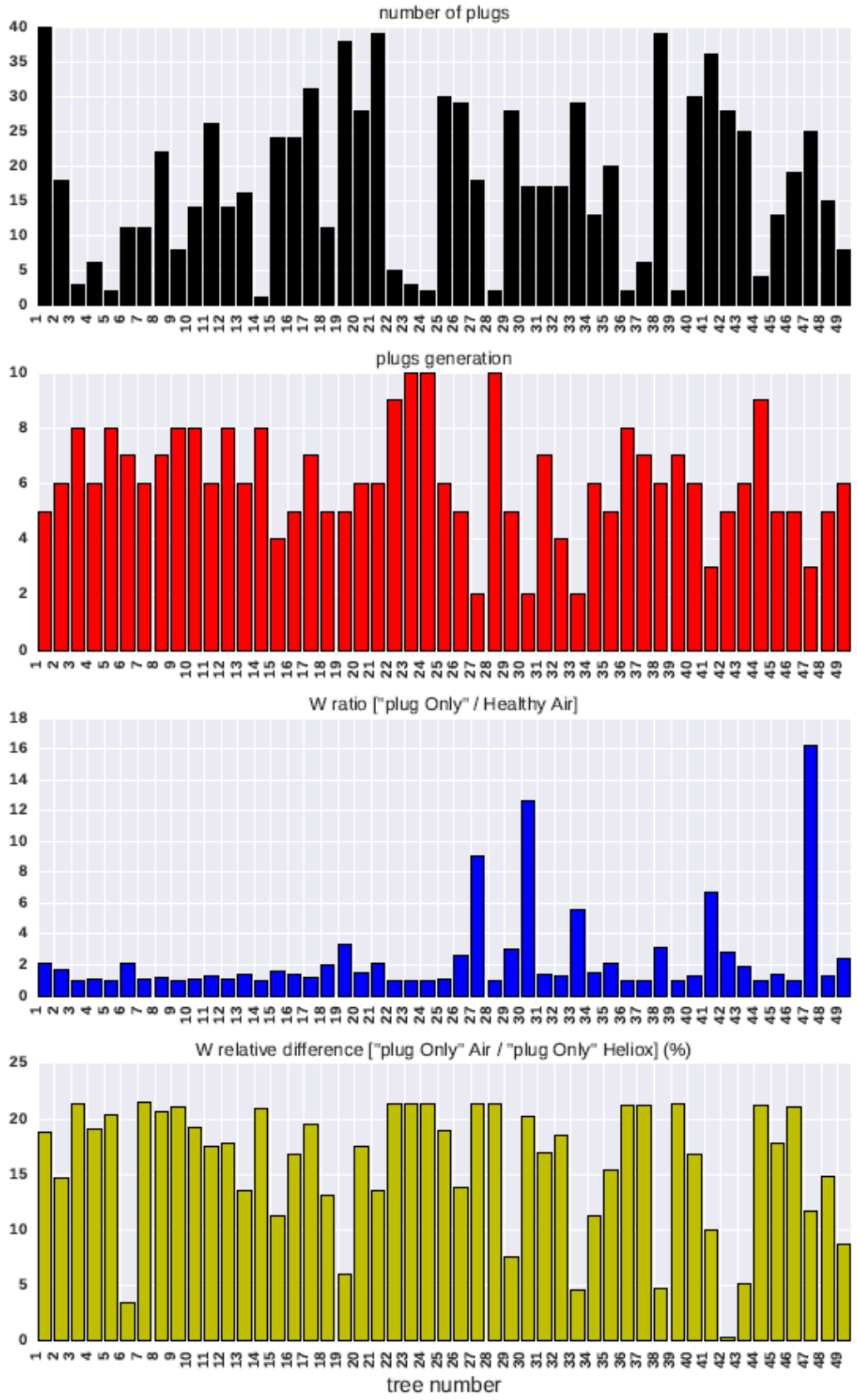

Figure 77: in the top first figure are the number of plugs per tree for each tree; in the second one the number of the generation containing, for each tree, the most proximal plug; in the third one the ratio, for each tree, between W in the "plug Only" and the healthy cases; in the last one the relative difference, for each tree, between W in the "plug Only" case when breathing Air compared to Heliox.

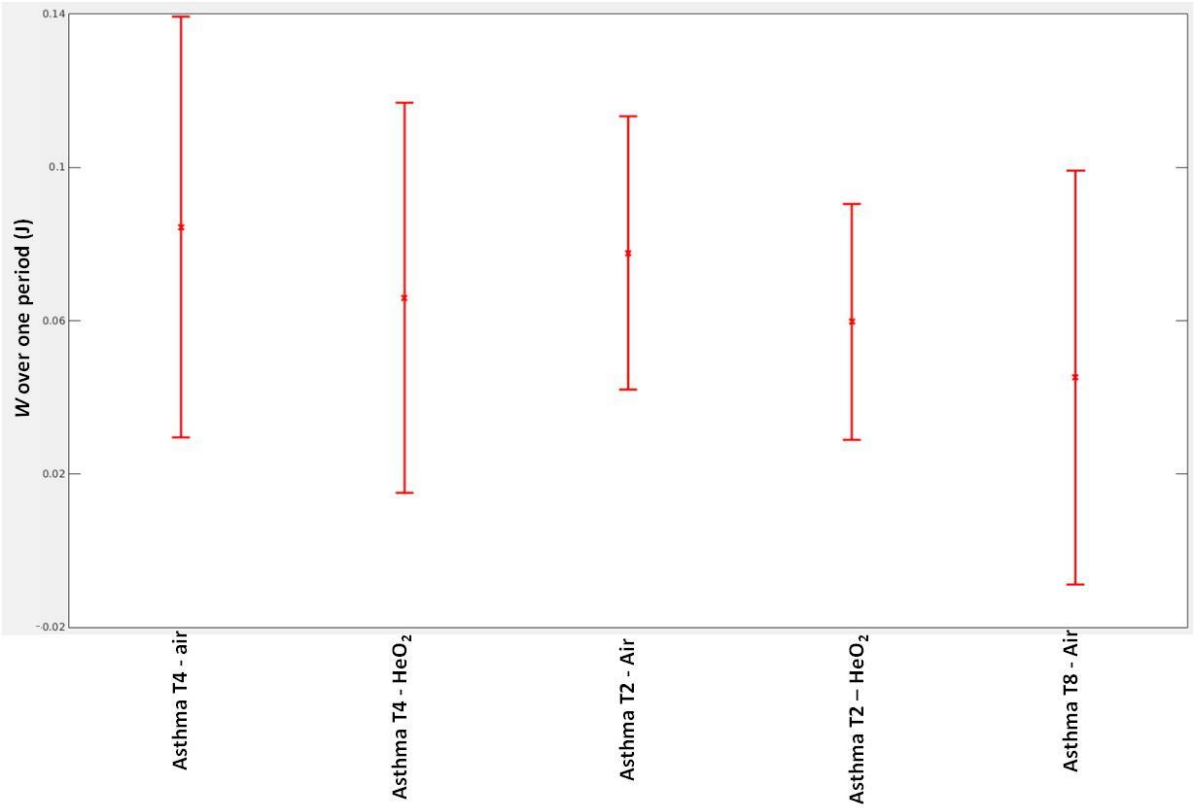

Figure 78: average and standard deviation of W over a respiration cycle in different configurations: one healthy patient breathing air and HeO_2, fifty asthmatic patients with bronchoconstrictions simulated according to subsection 15.2 breathing air and HeO_2 with time period 4s and volume expansions 0.23L (T4), the same fifty asthmatic patients breathing air and HeO_2 with time period 2s and volume expansions 0.16L (T2), the same fifty asthmatic patients breathing air with time period 8s and volume expansions 0.23L (T8).

In the healthy case, HeO_2 does not ease breathing. For asthmatic attack models, there is high breathing effort variability. Heliox brings a 24% improvement on average and up to 30%. Note that W is increased on average by a factor 6.7 from healthy cases to asthma when breathing air but by a factor 5.2 when breathing Heliox. Variability is reduced when only moderate bronchoconstrictions are simulated but Heliox does perform better than air in both "plug free" and "plug only" configurations. Note that on average breathing is harder with numerous moderate plugs than with a few severe ones; but variability is much higher in the latter case. This is consistent with the results in previous sections. Results plotted in Figure 77 show that the work of breathing is not correlated with the number of plugs. However, plugs generational positions have a major impact: the tree configurations in which the most proximal plugs are in upper generations (27, 30 and 47 for example) are those for which W is most increased from the healthy to the "plug only" configuration. In addition, comparing the third and last plots of Figure 77 we see that the correlation between plugs proximality and responsiveness to Heliox is not good. Plugs generational positions are not the only determinant of the work difference between both gases. Moderate constrictions play a leading role although, as noted before, severe constrictions are the ones responsible for the inter-patients variability.

In the two second breathing period case (so-called "T2"), breathing is faster and shortened. In this configuration, flow rates are increased, inertial effects are more important and Heliox reduces W over one period by 23%. A similar reduction is observed in the four second breathing period "T4" case, but in terms of energy spent per unit of time, Heliox is two times more beneficial in the fast breathing case. It also appears that breathing air two times more slowly brings more profit regarding effort reduction than breathing HeO_2 at the same pace.

A Kolmogorov-Smirnov test was performed and showed no statistical differences between the gases. That is, on average there is no statistical benefit but there are responders to HeO_2 that do benefit.

17. Conclusion

This study provides insights on respiratory diseases in the form of bronchoconstrictions and their effect on ventilation distribution and effort together with Heliox responsiveness. We focus on why some patients might respond to HeO_2 and others do not. Low density mixtures can be beneficial compared to air when flows within the tree exhibit marked inertial effects. This is especially true when constricted airways are in proximal generations. Simulating localized constrictions provides a physical understanding of the effects leveraging responsiveness to HeO_2. There is a range of constriction ratios, where HeO_2 is most beneficial, and this range depends on the regional and generational positions. Asthma was then simulated based on the geometrical variability reported in the literature. The work of breathing is multiplied in average by a factor 6.7 from health to asthma when breathing air, and by a factor 5.2 when breathing Heliox. During an asthma crisis, breathing can be volume restricted and frequency increased. Heliox mixtures prove to be more helpful in that case. Slow breathing can be a more efficient way than HeO_2 to decrease efforts and improve ventilation distribution. These findings may help diagnose potential responders based on their tracheo-bronchial morphometry.

CHAPTER IV-
From 4D lung dynamical maps to plugs distribution in asthma – a diagnosis tool

In asthma and COPD, some airways of the tracheo-bronchial tree can be constricted, from moderate narrowing up to closure (see subsection 15.2). Those pathological patterns affect the lung ventilation distribution. While some imaging techniques enable visualization and quantification of constrictions in proximal generations, no non-invasive technique provides precise insights on what happens in more distal areas. In this work, we propose a process that exploits ventilation measures provided by $4D$ dynamical lung images such as 4D-CT and 4D-MRI to access positions of airways closures in the tree. This identification approach combines the lung ventilation model developed in CHAPTER II along with a machine learning approach. Based on synthetic data generated with typical temporal and spatial resolutions as well as reconstruction errors, we obtain very encouraging results with a detection rate higher than 90%.

18. Introduction

As mentioned in subsection 15.2, some pathologies such as asthma or COPD can induce airway constriction [**113**], [**112**] and generate ventilation defects [**39**], [**40**]. In CHAPTER III, we showed how Heliox treatment may depend on airway closure severity and position within the lung (generational and regional position). Thus knowing their locations could give predictive insights on the treatment efficiency. Another use would be to predict aerosol deposition, which can be greatly affected by bronchoconstrictions [**79**].
Some dynamic imaging techniques such as $4D$ computed tomography (4D-CT) [**31**], [**120**] and $4D$ magnetic resonance imaging (4D-MRI) [**32**], [**33**] can give insights on lung ventilation distribution along the breathing cycle. To the best of our knowledge, no study has used those dynamical data in asthma or COPD in order to assess the pathological tree patterns. High resolution computed tomography (HRCT) shows the presence of constrictions in asthmatic patients [**23**], [**22**] but only proximal airways are easily accessible with current resolutions. However, histological analysis demonstrates that more distal branches can be constricted [**121**], [**115**].
In this work, we propose an approach that exploits $4D$ dynamical ventilation maps to identify which regions of the tracheo-bronchial tree are severely bronchoconstricted. The process combines the lung ventilation model presented in CHAPTER II, along with a plug identification step that includes a supervised machine learning technique. Approaches combining machine learning and modeling have been proposed to speed up calculations [**122**] or to improve diagnosis quality [**123**].
In a first part are presented some reminders of the ventilation model described in CHAPTER II. Then the theoretical background of the plug identification approach is presented. Results on synthetic data are finally shown.

19. Direct ventilation model and identification problem approaches

19.1. Global methodology

As observed experimentally through dynamic $4D$ images [**31**], [**32**], [**33**], stenoses affect the lung ventilation distribution. It takes more energy for the gas to flow through a constricted path and downstream parenchyma regions are less irrigated (see CHAPTER II and CHAPTER III).
Simulation results presented in subsection 21.1 indicate that ventilation defects caused by constrictions are mainly due to plugs rather than moderate narrowings, although the former are less frequent. Thus, ventilation information provided by $4D$ scans may give insights on plugs distribution. While the ventilation model described in subsection 8.2 enables to compute the flow distribution knowing the stenoses repartition within the tree, we aim at using the ventilation data provided by medical images in order to determine which airways are plugged. This is an identification problem for which unknowns are the tree branches radii (see subsection 19.3). There is inter-variability in airway dimensions [**124**] and typical normal radii values are in a range. Based on physiological knowledge, we assume that for each airway, a representative radius it would have in a normal case is known. Note that doing so, variability among healthy configurations is neglected (see *Remark 9*). The ratio between the pathological radius and the one in healthy configuration then reveals the constriction.
Radii are accessed through the determination of airway resistances. Flows at the tree exits and pressure drops from the tree entrance to the exits are linked through airway resistances by:

$$AQ = P$$

where $Q = (q_i)_i$ with q_i the flow at the i^{th} exit. Under the assumption of small displacement around the reference state q_i is defined by (8). The i^{th} element of P is the pressure drop from the tree entrance to the i^{th} exit. Matrix A is defined by (46) and includes information on the tree resistance

distribution. Knowing Q and P, one could get insights on airway resistances and hence on the constrictions. From $4D$ scans, registration techniques can provide the parenchyma displacement field and finally Q through equation (8). In this study, we propose to determine P through a minimization problem (see subsection 19.3) based on the ventilation model described in CHAPTER II. In subsection 19.3, it is shown that for the identification problem to be well-posed the maximum number of unknowns is, at least, two times smaller than the number of airways within the tree. Thus only a subset of the branches can have an unknown radius. To select them, an *a priori* prediction process is proposed. Based on ventilation features extracted from $4D$ scans (see subsection 19.4.1), a machine learning (ML) technique determines which airways are more likely to be constricted (see subsection 19.4.2). If the prediction process is good, non-selected airways are little constricted at most. Since their radius cannot be set among unknowns, they are assumed to have known dimensions which are set in the normal physiological range. The *a priori* prediction step leads to a system that contains as many unknown resistances as equations. Though, this system may not be invertible. An extra step, so called *resistance removal step*, is proposed so as to get an invertible extraction. The identification problem can then be solved, outputting a constriction prediction for the unknown set (see subsection 19.3). This is the *inversion step*. From there, plugged airways i.e. those with severe constrictions, are identified.
Note that in this study, $4D$ ventilation maps are simulated with the tree-parenchyma coupled model presented in subsection 8.2: those are synthetic data. Some noise is added to the synthetic data so as to reproduce realistic measurements.
See Figure 79 for a synthetic scheme describing the whole process.

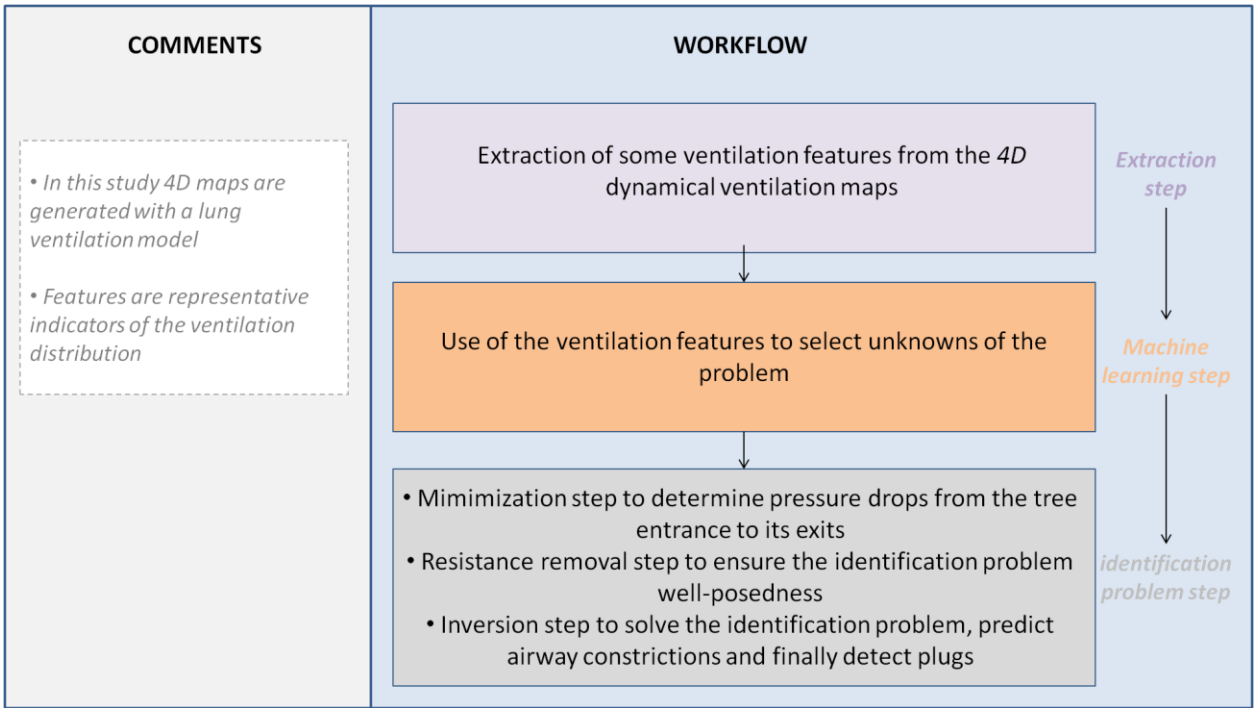

Figure 79: global process to determine the plug distribution in the tree based on dynamic ventilation maps.

In the next section, the ventilation model is described.

19.2. Direct ventilation problem

Models for both the parenchyma and tree used in this study as well as the coupling between them are described in subsection 8.2. Recall that when neglecting gravity, the strong formulation associated with the tree-parenchyma coupled model is:

$$div(\sigma_{mat}) - \boldsymbol{\nabla} p_{tree} = \rho_{par} \frac{\partial^2 \boldsymbol{u}}{\partial t^2}, \quad in\ \Omega. \tag{43}$$

Here ρ_{par} is the parenchyma density and p_{tree} is the piecewise constant function defined by (17). In the following, without loss of generality, we assume the pressure at the trachea is equal to zero. Dirichlet boundary conditions are prescribed to the parenchyma, the surface displacement being given by $\boldsymbol{u} = \boldsymbol{u_D}$ on $\partial\Omega$. As in CHAPTER II, the variationnal formulation associated with (19) is for any $\boldsymbol{w}$ sufficiently smooth such that $\boldsymbol{w} = 0$ on $\partial\Omega$,

$$\rho_{par} \int_\Omega \ddot{\boldsymbol{u}} \cdot \boldsymbol{w} + \int_\Omega \sigma_{mat}(\boldsymbol{u}) : \varepsilon(\boldsymbol{w}) - \int_\Omega p_{tree}\, I : \varepsilon(\boldsymbol{w}) = 0, \tag{44}$$

where

$$\begin{pmatrix} p_{tree_{/\,\Omega_1}} \\ \vdots \\ p_{tree_{/\,\Omega_N}} \end{pmatrix} = -P = -AQ. \tag{45}$$

As described in subsection 8.2, matrix A includes information on airways resistances and thus on their dimensions. It is defined by

$$A_{ij} = \sum_{(n,k)\in T_{ij}} R_{n,k}, \tag{46}$$

with $R_{n,k}$ the resistance of branch (n,k) (see Figure 19). In this study, we use the Pedley model (4) and those resistances are time dependant.
By considering the time and finite element discretizations introduced in CHAPTER II, we obtain the following linear system:

$$E\, X^{m+1} + B^T P^{m+1} = F^{m+1} \tag{47}$$

with P^{m+1} given by

$$P^{m+1} = A^m B X^{m+1}.$$

Vector X is the discrete FE representation of the velocity field $\dot{\boldsymbol{u}}$, E stands for the FE mass and elastic matrices and contains information on the parenchyma mechanical properties. The right hand side F is defined by (36) and contains terms relative to surface displacement and velocity thus depending on $\boldsymbol{u_D}$ and $\dot{\boldsymbol{u}}_{\boldsymbol{D}}$. Matrix B is defined by $B = \left[\int_{\Omega_i} div(\boldsymbol{e_j})\right]_{ij}$ where $\boldsymbol{e_l}$ is the l^{th} element of the finite element basis; it links the discrete velocity field and the flow distribution Q through

$$BX^{m+1} = Q^{m+1}. \tag{48}$$

As mentioned in subsection 15.2, some airways can be constricted in asthmatic lungs, from numerous moderate closures to a few severe constrictions. As a consequence, some lung regions irrigated by constricted paths may be poorly ventilated, as seen with 4D-CT [**31**] and 4D-MRI [**39**] images. Knowing the tree structure with constrictions severity and position, information included in matrix A, the parenchyma mechanical properties ρ_{par}, λ, μ (see subsection 8.2) and the parenchyma surface displacement field over time $\boldsymbol{u_D}$, one can compute the displacement field $\boldsymbol{u}$ within the lung and deduce the flow distribution within the tree. Though, the positions and severity of closures in the tree as well as mechanical properties are not *a priori* known. Some high-resolution imaging techniques enable to see constrictions in proximal airways typically only until generation 5 or 6 [**23**]. In the frame of this study, we assume that the lung parenchyma mechanical properties are known.

This is not the case in practice but some techniques such as magnetic resonance elastography [**125**] may give relevant estimations. As described in subsection 19.1, we propose to use dynamic ventilation maps to get insights on the constriction distribution and identify plugged airways. This approach will be referred to as *identification problem*.

19.3. Identification problem

Function p_{tree} is linked to the flow distribution Q through the resistance matrix A (see equation (45)). If both p_{tree} and Q were known, one could get insights on matrix A, so on airway resistances (see (46)) and finally on their radius through equation (4). This identification is done following a three-step approach. Image analysis on $4D$ dynamic maps gives access to the parenchyma displacement field $\boldsymbol{u}$ (see subsection 19.4.1) from which Q can be computed given a parenchyma partition (8). Knowing the displacement field $\boldsymbol{u}$ along the breathing cycle, and assuming that both the parenchyma mechanical properties and the tree topology are known, one can use the ventilation model described in previous subsection to define a function p^*_{tree} satisfying a minimization problem. This is the minimization step. Pressure drops from the tree entrance down to the tree exits are linked to the flows within the tree through airway resistances, the related system contains as many resistances as there are airways within the tree. However, from the knowledge of Q and p_{tree}, there is not enough information to recover every airway resistances. Based on the process described in this subsection, the number of unknowns is reduced so as to get an invertible system. This is the resistance removal step. In a last step this system is inverted and airway radii are determined. This is the inversion step. Plugged airways are thus identified

Minimization step:
From the knowledge of the displacement field $\boldsymbol{u}$ and assuming that the mechanical properties of the parenchyma are known, we are going to define a tree pressure p^*_{tree} that is piecewise constant on each terminal region Ω_i (notations defined in subsection 8.2). The idea, based on the direct problem (43), is to minimize the distance between $\boldsymbol{\nabla} p^*_{tree}$ and $D = div(\sigma_{mat}) - \rho_{par}\frac{\partial^2 \boldsymbol{u}}{\partial t^2}$ which is known by assumption. After time discretization, this minimization problem reads formally, at each time step:

$$\begin{cases} min\ \big|\big|\boldsymbol{\nabla} p^*_{tree} - D_d\ \big|\big|, \\ p^*_{tree} = \sum_i p_{tree_{/\,\Omega_i}} \mathbb{1}_{\Omega_i}, \\ p^*_{tree_{/\,\Omega_h}} = p_h \end{cases}$$

where h and p_h are given, D_d is a time discretization of D . Note that we have prescribed the value of p^*_{tree} on Ω_h to ensure the uniqueness of p^*_{tree} which is unless defined up to an additive constant. Note also that D depends on the measurement of $\boldsymbol{u}$ as well as on the mechanical model chosen to describe the parenchyma behavior. The measures and the chosen model inaccuracies are two possible sources of errors. After discretization, we get the discretized related minimization problem $(\mathcal{P}_d)$ defined at each time step m by:

$$(\mathcal{P}_d): \begin{cases} \min\limits_{P^{*m}} \big|\big|B^T P^{*m} - S^m\ \big|\big|^2 \\ P^{*m}_h = p_h \end{cases} \tag{49}$$

where P^{*m}_h is the h^{th} component of P^{*m} and S^m is defined following (47) by

$$S^m = F^{m+1} - E\ X^{m+1}\ .$$

Note that B^T is the FE operator corresponding to the gradient operator acting on piecewise constant functions on the partition $(\Omega_i)_i$. Since $dim(ker(B^T)) = 1$ (see Appendix 23.1), P^{*m} is defined up to a constant vector. This is the reason why a constraint on P_h^{*m} is added. For the sake of clarity, temporal indices are removed in following equations. The pressure constraint is enforced as described in subsection 20.2 by penalizing equation $BB^T P^* = BS$.

To solve $(\mathcal{P}_d)$, the pressure drop p_h along one path T_h has to be known. Which path to use is determined based on the *a priori* prediction process described in subsection 19.4. Along this path we suppose airway dimensions are known (see *Remark 7*). To get the pressure drops through each airway, flows shall also be known (see equation (4)). Since the gas is incompressible and because airways are assumed to be rigid, the flow in branch (n,k) equals the sum of the flows in its daughters:

$$q_{n,k} = q_{n+1,2k} + q_{n+1,2k+1}. \tag{50}$$

So the determination of exit flows (see subsection 19.4.1) enables by recursion to assess flows in every airway. Knowing airway dimensions and flows along T_h, we can finally compute p_h as $p_h = -\sum_{(n,k)\in T_h} R_{n,k}\, q_{n,k}$.
Note that $(\mathcal{P}_d)$ is solved at each time step. Knowing flows and pressures, we now want to get insights on the resistance distribution.

Resistance removal step:
In the following, we look for a resistance distribution such that vectors $A\,Q$ and P are close (see equation (45)) where both P and Q are known. This leads to a linear system for which resistances $R_{n,k}$ are the unknowns. Once they are determined, since flows and airway lengths are supposed to be known, equation (4) gives the radii $r_{n,k}$ from which we can deduce the radii reduction ratios defined by

$$red_{n,k} = \frac{r_{n,k}}{r_{healthy}{}_{n,k}}. \tag{51}$$

and finally identify plugged airways. The smaller the reduction ratio, the more closed the airway.
The pressure drop along any path T_i is given by:

$$\sum_{(n,k)\in T_i} R_{n,k} q_{n,k} = -p_i \tag{52}$$

The tree is dyadic: if it has N exits there are $2N-1$ airways. Thus the system (52) has size N and contains $2N-1$ unknowns. It is not invertible, the number of unknowns has to be reduced. The *a priori* prediction process described in subsection 19.4. provides for each airway a prediction of the radius reduction ratio (51) seen as a "constriction likeliness", based on which airways can be sorted. The lower the likeliness, the closer the airway to its healthy configuration. From this ranking, the N unknown resistances associated to the airways that are most likely to be plugged are kept, the $N-1$ airways associated to the remaining unknowns are assumed to have healthy radius. At this stage, system (45) contains as many unknowns as equations. However, there is no guarantee that these equations are independent. In practice, the system is invertible if the pressure at the nodes of unknown resistances are known, i.e $R_{n,k}$ can be determined if $p_{n,k}$ and $p_{n-1,\left\lfloor \frac{k}{2} \right\rfloor}$ are known. Notation $\lfloor k \rfloor$ refers to the floor value of k.
Let U_N be the set of indices of airways which resistances are unknown. For each path T_i from the tree mother branch to its i^{th} exit, let us denote $T_{i_N}^u = T_i \cap U_N$. Then, $\forall i \in [\![1; N]\!]$, (52) writes:

$$\sum_{(n,k)\in T_{i_N}^u} R_{n,k}q_{n,k} = -p_i - \sum_{(n,k)\in T_i\setminus T_{i_N}^u} R_{n,k}q_{n,k}\,.$$

Let us set a new indexation for airways with unknown radius. We denote ζ_N a bijective function that maps elements of U_N to the integer interval $[\![1;N]\!]$ based on the ranking provided by the *a priori* prediction process described in subsection 19.4: index 1 is associated to the airway that is predicted with highest radius reduction ratio i.e. the least likely to be constricted, and so on till index N associated to the airway predicted with lowest radius reduction ratio i.e. the most likely to be constricted. By extension, $\forall (n,k) \in U_N$ we note $R_{n,k} = R_i$ with $i = \zeta_N(n,k)$ and $q_{n,k} = q_i$ (see Figure 81).
Let Z_N be the matrix of $\mathcal{M}_N(\mathbb{R})$ defined by:

$$Z_{N\,ij} = \begin{cases} 1 & if\ \ {\zeta_N}^{-1}(j) \in T_{i_N}^u, \\ 0 & else. \end{cases}$$

A given line i of Z_N contains 1 at position j if the two following conditions are satisfied: R_j belongs to the set of unknown resistances, and the airway associated to R_j belongs to path T_i; otherwise the line contains 0 at position j.
We also define the vectors $G_N = (R_i q_i)_{i=1\dots N}$ and $H_N = \left(-p_i - \sum_{(n,k)\in T_i\setminus T_{i_N}^u} R_{n,k}q_{n,k}\right)_{i=1\dots N}$.
With those notations system (52) is equivalent to:

$$Z_N G_N = H_N. \tag{53}$$

Information on airway resistances and hence on their radius is contained in G_N. One has to solve system (53) to recover the resistances knowing the right hand side H_N. However, matrix Z_N may not be invertible. The strategy is thus to extract from Z_N an invertible matrix, which will be of maximal rank. To decide which resistance shall be removed from the unknowns, we define an iterative process taking advantage of the *a priori* prediction made on the likeliness constriction of a branch. The higher the predicted reduction ratio for an airway, the less likely this airway is constricted. At iteration 1 the resistance R_1 of the airway with highest radius reduction ratio is removed with highest priority and the radius of the associated airway is set as "healthy". This corresponds to removing the first column of Z_N. The resulting matrix is not squared and contains at least two collinear rows, otherwise Z_N would have been invertible (see demonstration in Appendix 23.2); to keep a square system, one of these collinear rows is removed, defining matrix Z_{N-1}. Vectors G_N and H_N are modified accordingly, defining G_{N-1} and H_{N-1}. If $rank(Z_{N-1}) = N-1$, Z_{N-1} is invertible and unknown resistances can be determined. If $rank(Z_{N-1}) = rank(Z_N) < N-1$, Z_{N-1} is not invertible and we proceed to iteration 2. Otherwise, in case $rank(Z_{N-1}) < rank(Z_N)$, R_1 is set back among the unknowns and the second airway resistance that is less likely to be plugged, R_2, is removed; the process goes on till $rank(Z_{N-1}) = rank(Z_N)$. Then the algorithm moves to iteration 2 and so on. Doing so, airways predicted as severely constricted by the *a priori* prediction process are less likely to be removed from the unknowns. Note that for reasons explained in *Remark 7*, we enforce the resistance of airway $(0,0)$ among the unknown set and prevent it from being removed. The algorithm is described in Figure 80.
In the following, for a vector V of $\mathbb{R}^p$ and an integer $c \leq p$ we denote by $V\{c\}$ the vector of $\mathbb{R}^{p-1}$ obtained by removing the c^{th} element of V. For a matrix M of $\mathcal{M}_p(\mathbb{R})$, we denote by $M\{c_1, c_2\}$ the matrix of $\mathcal{M}_{p-1}(\mathbb{R})$ obtained by removing the c_1^{th} line and c_2^{th} column of M. For a matrix M we denote $M(c,:)$ the c^{th} row of M. Vector and matrix indexations start at one.

Initialization :

- Index exits in $\{1, \dots, N\}$
- $l = N$
- $Z_l = Z_N$
- $k = 0$

While $rank(Z_l) \neq l$

- **step 1** $k \leftarrow k + 1$
  If $\zeta_l{}^{-1}(k) = (0,0)$
  - $k \leftarrow k + 1$

  $R_{0,0}$ is kept as unknown
- **step 2** $i = 0, j = 0, s = 0$
  While $s = 0$
  - $i = i + 1$
  - ***For*** $j' = i + 1$ *to* l
    - ***If*** $Z_l(j', :)$ collinear to $Z_l(i, :)$
      - $s = 1$
      - $j = j'$
      - $Z_{l-1}^{j} = Z_l\{j, k\}$
      - ***Exit for***

  Sub-system extraction

  End while

  If $rank\left(Z_{l-1}^{j}\right) = rank(Z_l)$
  - ***If*** $rank\left(Z_{l-1}^{j}\right) = l - 1$
    - Set R_k as healthy
    - $Z_{l-1} = Z_{l-1}^{j}$
    - $G_{l-1} = G_l\{k\}$
    - $H_{l-1} = H_l\{j\}$
    - $l \leftarrow l - 1$

    The sub-system is invertible. End
  - ***Else***
    - $Z_{l-1} = Z_{l-1}^{j}$
    - $U_{l-1} = U_l\{\zeta_l{}^{-1}(k)\}$
    - Set ζ_{l-1} a function from U_{l-1} to $[\![1; l-1]\!]$ based on the *a priori* prediction process*
    - Reindex exits $\{1, \dots, j-1\} \cup \{j+1, \dots, l\}$ in the interval $\{1, \dots, l-1\}$
    - $l \leftarrow l - 1$

    The sub-system is not invertible. Continue extraction: ***step*** **1**

  Else if $rank\left(Z_{l-1}^{j}\right) < rank(Z_l)$
  - Proceed to step 1

  Wrong extraction go back to ***step*** **1**

* **ζ_{l-1} is chosen such that unknown R_1 is the resistance associated with the airway that has highest predicted reduction ratio by the a priori prediction process, R_2 with the airway with second highest predicted reduction ratio,… and R_{l-1} with the airway with lowest predicted reduction ratio.**

Figure 80: Resistance removal algorithm for unknown selection. Resistances are removed one by one according to the predicted radius reduction ratio in order to make the system (53) invertible.

This algorithm converges: indeed if $l = 1$ then $Z = Z_1 = [1]$ which is invertible.

Inversion step:
If Z_l is invertible we have, from (53), $G_l = Z_l^{-1} H_l$ and since the flows in all airways are known we can then determine the unknown resistances. We have $\forall i \in [\![1; l]\!], G_{l_i} = R_i q_i$. Then the radii can be determined from the Pedley formula (4).

$$r_i = \begin{cases} \left[\frac{q_i}{G_{b_i}} \frac{8\mu_f L}{\pi}\right]^{\frac{1}{4}}, & if \quad \gamma \left(\frac{4\rho|q_i|}{\mu_f \pi L}\right)^{\frac{1}{2}} < 1, \\ \left[\frac{q_i}{G_{b_i}} \gamma 16 \left(\frac{\rho \mu_f |q_i| L_i}{\pi^3}\right)^{\frac{1}{2}}\right]^{\frac{1}{4}}, & else. \end{cases}$$

Recall that for each airway with resistance in the unknown set, a radius is computed at each time step, and the final prediction is taken as the time average of these values. Note that the resistance removal step is performed one time only, the resulting invertible matrix Z_l does not depend on the time step.
The identification problem step will be all the more accurate that resistances removed from the process are associated to airways with healthy dimensions. In practice, most of them are moderately constricted. Assuming they are healthy will induce some errors in the right hand side H_l and thus some prediction errors on unknowns, since they will have to account for a higher pressure drop on their paths.

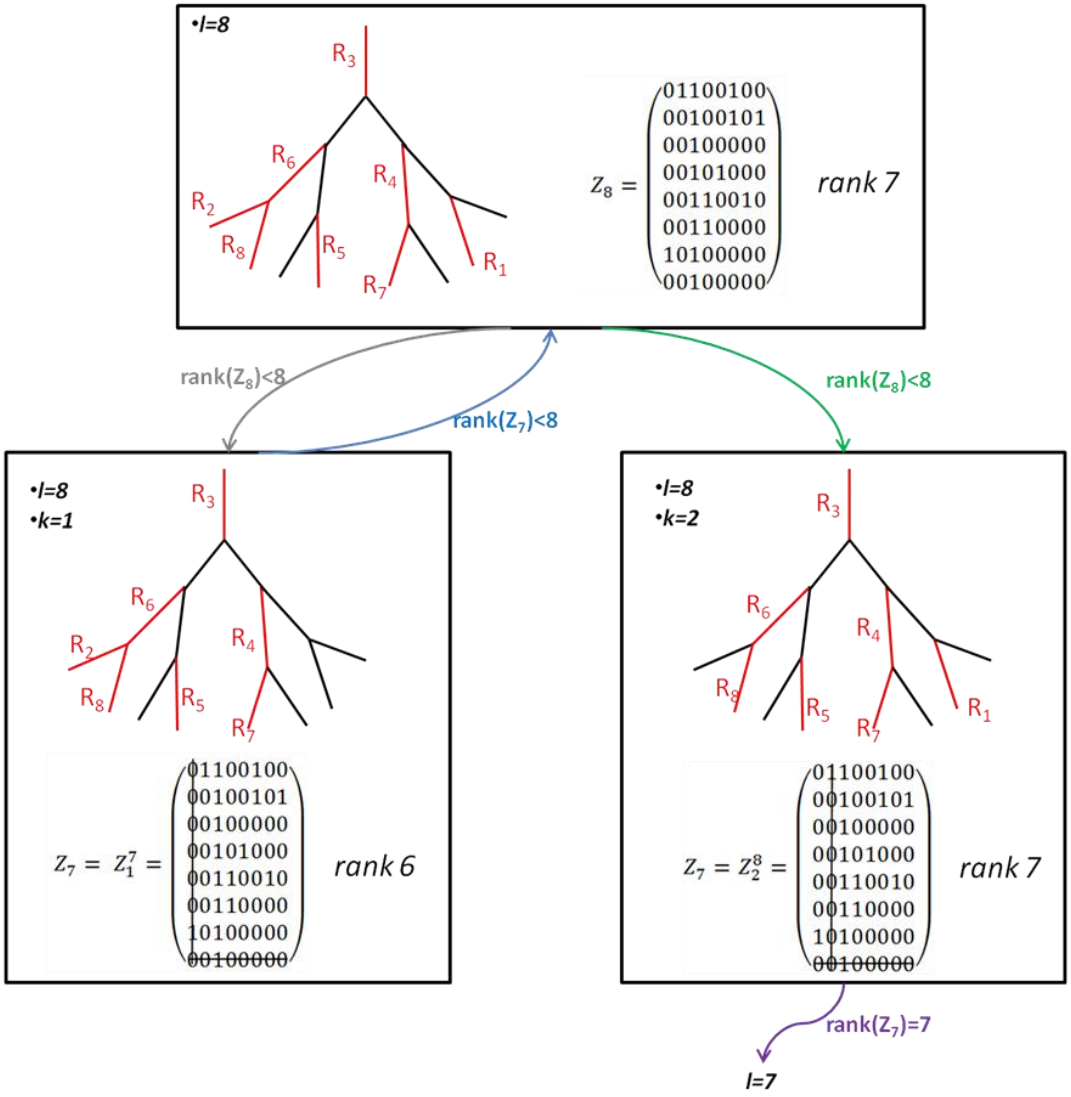

Figure 81: illustration of the resistance removal algorithm on an eight-exit tree. Branches in red are those with unknown resistance. Matrix Z_8 of the initial system is not invertible (top square). Following the process described in Figure 80, R_1 is first removed from the set of unknowns, a line and a column are removed from Z_8 leading to Z_7 (bottom left square); rank(Z_7)< rank(Z_8) so R_1 is set back among unknowns (top square) and R_2 is removed instead (bottom right square). Resulting reduced matrix Z_7 has now the same rank as Z_8 so the removal is confirmed. At the end of the process the tree contains several paths with $R_{0,0}$ ($= R_3$) as only unknown, so a pressure along a path can be computed so as to solve the minimization problem (49), see *Remark 7*.

Remark 7: To solve (49), the pressure drop along a path has to be imposed. To compute the pressure drop p_h along a path T_h, radii of airways belonging to T_h need to be known (recall that lengths and flows are supposed to be known). The *a priori* prediction process described in subsection 19.4 is used to generate the set of airways which radii are unknown. At this stage it may happen that every path from the trachea down to tree exits contains at least an airway with unknown radius; in that case no pressure drop p_h can be computed. To make sure that at least one path contains airways with known dimensions only, the resistance of airway $(0,0)$ is enforced among the unknowns of system (52) and prevented to be removed during the process described in Figure 80. Doing so, one path T_h of the tree will contain no other unknown than airway $(0,0)$. Indeed, if $R_{0,0}$ is enforced among unknowns, one has to access $p_{1,0}$ to ensure invertibility. To that end, there needs to be a path with no unknown from node $(1,0)$ to an exit. In practice, airway $(0,0)$ would be the trachea. Its dimensions can be measured with bronchoscopy for example and enforcing $R_{0,0}$ among unknowns is an artifice designed to enable

p_h computation. So dimensions of airways along T_h are all known and the pressure drop p_h along this path can be computed.

Remark 8: Note that by solving an extracted system from (53) we do not ensure (52) is satisfied. To verify (52) some compatibility conditions on the right hand side would be needed. The last invertible extracted system $Z_l G_l = H_l$ could be enriched by adding unknown resistances while keeping the system invertible. But our first aim here is not to get a resistance distribution that enables to recover the displacement field measured on the 4D dynamical maps. The goal of this study is rather to identify plugged airways.
Note that if the resistance of an airway that is actually plugged is removed from the set of unknowns, it will not be identified as a plug.

As a summary, the identification problem aims at determining which airways are severely constricted. It is made of three steps. First, the minimization problem $(\mathcal{P}_d)$ is solved to determine the pressure drops from the tree entrance to its exits. This is done at each time step. Pressure drops are linked to the flows within the tree through airway resistances by system (52). This system contains more unknown resistances than independent equations. The unknown set has to be reduced: this is the resistance removal step which is performed one time and valid for every time steps. This leads to an extracted system than can be inverted at each time step.

As mentioned before, an unknown selection process is needed to determine which resistance to remove from the unknown set. This process shall keep, among others, the airways that are actually plugged and remove some healthy or moderately constricted airways, i.e. some that have negligible effect on ventilation distribution. Indeed, as mentioned in subsection 15.2, asthma affects the lung structure from frequent moderate radius constrictions to a few airway closures. Using the ventilation distribution information provided by dynamic images, we propose a way to make an *a priori* prediction on airways constriction likeliness (see subsection 19.4).

Remark 9: We aim to keep in the unknown set resistances associated to the most constricted airways. If the *a priori* prediction process provides an appropriate ranking, airways which resistances do not belong to that set are moderately constricted at most. Their radius is supposed to have a typical "healthy" value known from morphometric studies (see subsection 20.1.3) although normal airway dimensions are submitted to an inter- and intra- variability [**124**]. However, possible radius variations within this "healthy" or "normal" range are much lower than those induced by severe bronchoconstrictions. The errors caused by considering an arbitrary "healthy" radius are thus expected to have little impact on the pressure drop distribution compared to plugs.

19.4. *A priori* prediction process

Following the process described in subsection 19.3, to get insights on plugs distribution, only a sub-set of airway resistances can be considered as unknowns. The tracheo-bronchial tree has a dyadic structure: if it contains N exits it has $2N - 1$ airways. At most N have their resistance initially set as unknown (see subsection 19.3). One could try all the combinations of N airways such that system (53) is invertible, inverse the system for each combination, and keep as final result the one that minimizes the distance between vectors AQ and P. However, it can be shown that there are more than 2^{N-1} of those combinations: this makes this approach costly when the tree contains a few hundred exits as done in this study. Thus, before the identification problem step, an *a priori* prediction process is required to determine which branches are likely to be constricted and which ones rather have close to healthy dimensions. Those latter are removed with highest priority.

The prediction process described in this section is based on $4D$ ventilation maps analysis. It uses a machine learning technique to map the observed ventilation distribution with constrictions positions and strengths within the tree.

19.4.1. Ventilation information extraction

Ventilation distribution, i.e. flows within the tree, is related to the tree structure. In the following, some features characterizing the ventilation are set as inputs of a machine learning algorithm so as to determine which airways are likely to be plugged. The ventilation distribution can be determined from the parenchyma velocity field. Indeed, from (8) one can compute tree exit flows. Under the incompressibility assumption, the flow distribution within the tree is then obtained (50).

19.4.2. Machine learning process

The machine learning approach proceeds in two steps. First a correspondence is established between ventilation features extracted from $4D$ maps, and known airways radius reduction ratios (51) associated to these features. This mapping is built on a large synthetic database, so-called *learning base*, so as to capture the diversity of ventilation distribution patterns. In a second step, for a 4D map associated to an unknown constrictions distribution, ventilation features are extracted, and airway reduction ratios are determined.

Ventilation features:
Which ventilation features to consider is the object of this subsection. Bronchoconstrictions influence the ventilation distribution. To quantify a disease severity and get insights on its geometrical distribution, ventilation pathological patterns can be compared to the ones that would be obtained if there were no constrictions.
In this study we assume that for a given asthmatic patient, lung mechanical properties are known. We also consider we know the tree topology, i.e. nodes positions, and typical dimensions airways would have if they were not constricted. So a “healthy” tree configuration is available. We finally assume we can access the lung geometry and the parenchyma surface displacement along breathing. Those are the necessary input data to use the tree-parenchyma coupled model described in subsection 8.2. A reference “healthy” ventilation distribution can be simulated.

In the following, variables with subscript “asthma” refer to the ventilation in an asthmatic case while “healthy” refers to the one simulated when the tree has no bronchoconstriction.
The machine learning step aims at determining, given a ventilation distribution, which airways are likely to be constricted and with which severity. To do so, we need to define at the airway level some features that correlate with the ventilation distribution.
As noted above (see subsection 21.3), we know the flow rate evolution and hence the volume of gas transiting in every airways over a breathing cycle. For the airway (n,k) we note respectively $V_{n,k}^{max}$ and $V_{n,k}^{min}$ the maximum and minimum of $V_{n,k}(t) = \int_0^t q_{n,k}$.
We define the following feature:

$$c_{n,k} = \frac{\left(V_{n,k}^{max} - V_{n,k}^{min}\right)_{asthma} - \left(V_{n,k}^{max} - V_{n,k}^{min}\right)_{healthy}}{\left(V_{n,k}^{max} - V_{n,k}^{min}\right)_{healthy}}.$$

If $c_{n,k} < 0$, less flow goes through airway (n,k) than in the healthy reference case. This may indicate there are constrictions in the paths going through (n,k). They could be upstream, downstream or

both. The value of $c_{n,k}$ correlates with the constriction severity. To get more insight on where constrictions could occur, we define:

$$\alpha_{n,k} = \begin{cases} 1, & if\ c_{n-1,\left\lfloor \frac{k}{2} \right\rfloor} > 0, \\ 0, & else. \end{cases}$$

Note that airway $\left(n-1, \left\lfloor \frac{k}{2} \right\rfloor\right)$ is the mother of (n,k).
A value of 1 indicates that there is more flow going through the mother than in the healthy case. Thus this branch is less likely to be affected and constriction may rather be downstream. On the contrary, when the value is 0, the mother or ascending airways may rather be affected. In the same spirit we define:

$$\begin{cases} \beta_{n,2k} = \begin{cases} 1, & if\ c_{n,2k+1} > 0, \\ 0, & else, \end{cases} \\ \beta_{n,2k+1} = \begin{cases} 1, & if\ c_{n,2k} > 0, \\ 0, & else. \end{cases} \end{cases}$$

If $c_{n,k} < 0$ and $\beta_{n,k} = 0$, both airway (n,k) and its sister have reduced flows compared to the healthy case, so some constrictions may exist upstream. To add information on the downstream environment we define:

$$\gamma_{n,k} = \begin{cases} 2, & if\ c_{n+1,2k} > 0\ and\ c_{n+1,2k+1} > 0, \\ 0, & if\ c_{n+1,2k} < 0\ and\ c_{n+1,2k+1} < 0, \\ 1, & else. \end{cases}$$

Note that airways $(n+1, 2k)$ and $(n+1, 2k+1)$ are the daughters of airway (n,k).
For a value of 0, both daughters have reduced flows compared to the healthy case so airway (n,k) or ascending branches may be constricted. If the value is 1 some constrictions would rather occur downstream.
We also define the distribution ratio:

$$\begin{cases} \delta_{n,2k} = \dfrac{\left(V_{n,2k}^{max} - V_{n,2k}^{min}\right)_{asthma}}{\left(V_{n,2k}^{max} - V_{n,2k}^{min}\right)_{asthma} + \left(V_{n,2k+1}^{max} - V_{n,2k+1}^{min}\right)_{asthma}}, \\ \qquad\qquad \dfrac{\left(V_{n,2k}^{max} - V_{n,2k}^{min}\right)_{healthy}}{\left(V_{n,2k}^{max} - V_{n,2k}^{min}\right)_{healthy} + \left(V_{n,2k+1}^{max} - V_{n,2k+1}^{min}\right)_{healthy}} \\ \delta_{n,2k+1} = \dfrac{\left(V_{n,2k+1}^{max} - V_{n,2k+1}^{min}\right)_{asthma}}{\left(V_{n,2k+1}^{max} - V_{n,2k+1}^{min}\right)_{asthma} + \left(V_{n,2k}^{max} - V_{n,2k}^{min}\right)_{asthma}}. \\ \qquad\qquad \dfrac{\left(V_{n,2k+1}^{max} - V_{n,2k+1}^{min}\right)_{healthy}}{\left(V_{n,2k+1}^{max} - V_{n,2k+1}^{min}\right)_{healthy} + \left(V_{n,2k}^{max} - V_{n,2k}^{min}\right)_{healthy}} \end{cases}$$

It compares the volume distribution between an airway and its sister. If $\delta_{n,k}$ is significantly smaller than 1, airway (n,k) or some downstream branches may be constricted.

Those features may behave differently depending on the airway generation as the effect of constrictions depends on the flow which itself decreases with the generation level [**43**]. So we add the generation level n as a feature.
We use a random forest regressor algorithm to map for each airway (n,k) its feature vector $[c_{n,k}, \alpha_{n,k}, \beta_{n,k}, \gamma_{n,k}, \delta_{n,k}, n]$ and its radius reduction ratio $\frac{r_{n,k}}{r_{healthy_{n,k}}}$. Quality of the prediction results is shown in subsection 21.2. The random forest method was chosen because it is fast and insensitive to noise.

Remark 10: Note that ventilation distribution is influenced by factors that do not appear among the selected features. In particular, it is a function of the position within the lung: for instance, in tidal regime, displacements are more important around the diaphragm than near the lung apex. To make the prediction more accurate, one could add as features the lobar position of the airway, or even its exact position within the lung. Though doing so would dramatically increase the problem dimensionality. Rather than providing a precise prediction of the constriction ratio, we aim at predicting a good ranking of plugged airways (see results subsection 21.2). For that reason, the output of the machine learning algorithm may be referred to as "*constriction likeliness*" rather than radius reduction ratio. Airways could have been sorted based on another criterion. For instance, one could have enforced proximal airways in the unknown set (see subsection 19.3) by modulating the prediction with the airway generation.

Data base construction:
To build a learning base the following approach is adopted: first the parenchyma displacement field is extracted from the $4D$ map, so-called *target map*, associated to a tree which plug distribution has to be determined. Knowing the tree structure, the lung mechanical properties, and assuming that the parenchyma behavior can be accurately described by a Hooke law, a healthy ventilation simulation is performed based on the tree-parenchyma coupled model described in subsection 8.2. The extracted surface displacement is used as Dirichlet boundary conditions. Imposing stochastic constrictions distributions as described in subsection 15.2, synthetic pathological ventilations are simulated with the same given Dirichlet boundary conditions. So all synthetic patients breathe with the same surface displacement. From those synthetic data, airway ventilation features described in subsection 19.4.2 are computed. Note that the associated radius reduction ratios are known since the trees have been generated. The learning phase is performed on this synthetic database by mapping the features and the related known airway constrictions. If the tree contains $2N-1$ airways and if m_p pathological cases are simulated, there are $(2N-1)*m_p$ couples [airway features; radius reduction ratio] in the learning base.
Then, the machine learning algorithm is used to predict airway radius reduction ratios associated to the target $4D$ ventilation map. As mentioned in subsection 19.1, in this study the target map is synthetically generated with the tree-parenchyma coupled model.

19.5. Global approach summary

In this section we summarize the overall process that enables to go from a $4D$ dynamical map and tree topology to the tree plugs distribution, see Figure 82.
For the identification problem (*step 4,* see subsection 19.3) to be well-posed, not every airway resistances can be considered as unknowns. An *a priori* prediction process (*step 3*) is used to select a subset of airways that are more likely constricted and shall hence be put in the unknown set. Based on a machine learning technique (see subsection 19.4.2) ventilation features extracted from the $4D$ map (*step 1,* see subsection 19.4.1) are used to predict constriction likeliness for each airway. To generate synthetic data for the learning phase, the tree-parenchyma ventilation model presented in subsection 8.2 is used. Extracted parenchyma surface is used as Dirichlet boundary conditions.

Ventilation simulations are performed with a healthy tree model and various asthmatic configurations (*step 2,* see subsection 19.4.2). The healthy tree model is built following subsection 20.1.3, segmented branches are used along with the parenchyma envelope to generate a complete tree geometry. Asthmatic configurations are obtained by imposing stochastic constrictions as described in subsection 15.2.

Using the *a priori* constriction likeliness ranking, one can finally proceed to the identification problem step (*step 4*) which is done in three stages. First a minimization problem is solved to determine exit tree pressures. The system linking flows and pressures through airway resistances is *a priori* not invertible. An invertible extraction is obtained thanks to the resistance removal step. The resulting system is inverted and plugs are finally identified.

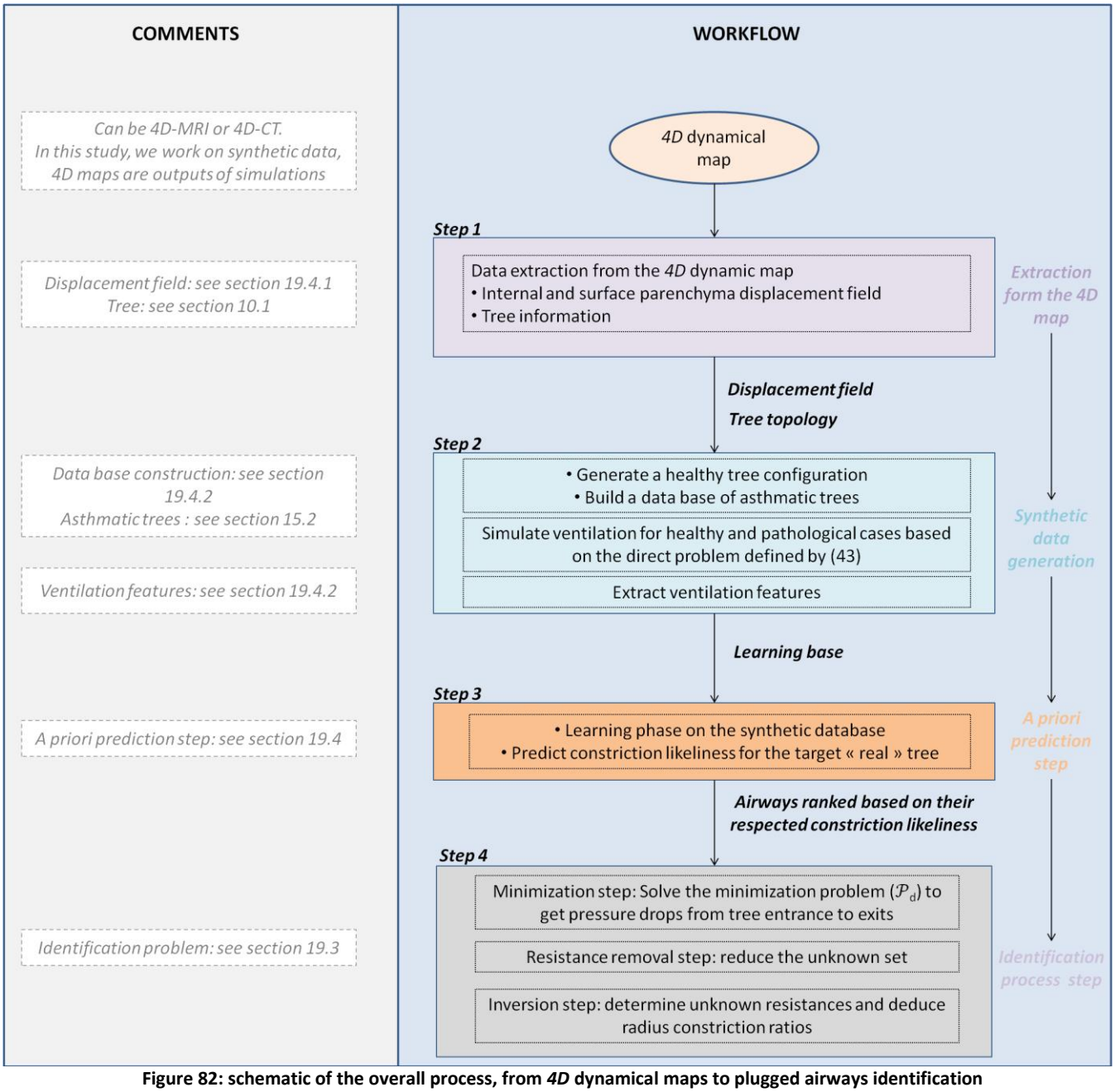

Figure 82: schematic of the overall process, from *4D* dynamical maps to plugged airways identification

20. Numerical methods and patient-specific data exploitation

In this section we give insights on patient-specific data construction, numerical strategies and systems resolution.

20.1. Input data construction

For the process described in Figure 82, the lung geometry, its displacement over the breathing cycle and the tree structure are needed.

20.1.1. Lung geometry

From $4D$ scans the lung envelope can be segmented. We work on a human left lung geometry. Segmented HRCT data acquired in [**126**] are used to build a patient-specific tree and a parenchyma geometry.
A surface mesh of the parenchyma is generated with Meshlab [**93**]. From there a tetrahedral volume mesh is built with GMSH [**95**]. It is subdivided based on the tree structure in as many regions as there are terminal branches (see Figure 28) according to an algorithm described in Figure 24. The mesh contains 250594 tetrahedrons, which corresponds to achievable 4D-CT spatial resolution (see subsection 20.1.2). There are 140091 degrees of freedom.

20.1.2. Temporal and spatial resolutions

Synthetic $4D$ maps generated from the tree-parenchyma coupled model described in subsection 8.2 are used in this study. Spatial and temporal resolutions are chosen coherently with what available devices can provide. Simulations performed to generate those maps are done with a small time step to ensure precision but only a few time points are then kept to cope with experimental temporal resolutions.
The parenchyma surface Dirichlet boundary conditions are built along the lines described in Appendix 13.7 based on HRCT geometries segmented from [**126**]. In this study we work in tidal breathing conditions, i.e. for respiration at rest and with normal volume expansion. As in CHAPTER III sinusoidal dynamics with time period 4s are prescribed so as to impose plausible tidal volume evolution. Time step for simulations is 0.04 s.
As mentioned in subsection 19.3, $3D$ registration enables to deduce a velocity field from $4D$ maps. Here we work on synthetic data: the field $\boldsymbol{u}(t)$ is the output of a simulation based on the mechanical model described in subsection 8.2. Depending on the device and reconstruction techniques, 4D-CT lead to various spatial and temporal resolutions [**34**], [**35**], [**36**]. We assume a spatial resolution of 4 mm^3 isotropic and we use a mesh refined accordingly (see subsection 20.1.1). Temporal resolution is 0.4 s (i.e. ten images per breathing cycle with the considered dynamic). Synthetic ventilation data are generated with a much smaller time step of 0.04 s and only one point every 0.4 s is finally kept to perform the machine learning step (see results in subsection 21.2). Information from the ten resulting time points is aggregated to proceed with the identification problem step (see results in subsection 21.3).
Whatever the technique, registration is not exempt from errors. In the following we conduct the identification process both on noise-free and noisy data. Based on [**34**], [**35**], [**36**], noisy data are generated by multiplying at each time step m each component i of X^m, FE approximation of the velocity field at time $m\Delta t$**,** by a factor $(1+\theta_i^m)$ where θ_i^m is generated according to a uniform law in the interval $[-0.3; 0.3]$.

20.1.3. Tree structure

From $4D$ scans, upper airways can be segmented and used along with the parenchyma surface to propagate a conductive tree model with a patient-specific space filling approach, as described in subsection 10.1, see Figure 23.
The resulting structure contains a faithful representation for segmented upper branches, and a tree representation model for the remaining airways. This model is built based on both general physiological knowledge and patient data; it generates nodes positions, airway lengths and radii. While stenoses may be seen on segmented upper airways [**23**], the propagated part of the tree does not account for pathological cases. Indeed there is no *a priori* knowledge on the distribution of constricted branches, which is specific to each patient. Nodes positions and airways lengths of the propagated part are known. Airways radii $r_{healthy_{n,k}}$ are in a healthy configuration range (see *Remark 9*). Note that since upper airways geometry is known from segmentation, their resistance would not need to be included among the unknowns of the identification problem described in subsection 19.3. Though, in this study, we work on synthetic pathological trees with stochastic constrictions generated along the process described in subsection 15.2 and we consider all branches radii including proximal ones are *a priori* unknowns.
In the following, we work on ten-generation space filling trees. Downstream sub-trees are treated as symmetric units and characterized by equivalent resistances. Those units are irrigated by airways referred to as *tree exits*. Constrictions in such subtree would be accounted for by a resistance increase of the related exit. The resulting tree on the studied left lung contains 954 airways among which 477 are terminal branches. When simulating asthma, we generate $n_{closure}$ plugs with $n_{closure}$ randomly chosen in the interval $[\![1; 40]\!]$ (see subsection 15.2), this interval being set based on non published data from [**92**]. As in subsection 15.2, the position and severity of moderate constrictions are set following a log-normal law.

20.2. Numerical methods

Direct problem:
System (47) is solved through a conjugate gradient descent with Jacobi preconditioning, as mentioned in subsection 9.1.

Machine learning:
The machine learning step is performed with a random forest regressor. The number of elements in the forest is chosen to be 50 and other parameters (as proposed by scikit-learn library [**127**]) are set to their default value. In order to predict the airway radius reduction ratios of a patient, synthetic data are generated as described in subsection 19.4.2 and used for the learning phase.
In this study we work on one healthy tree and 49 asthmatic ones, the mechanical parameters and constitutive relation being the same in every cases. Iteratively, one of those pathological trees is taken as target, the aim being to predict the radius reduction ratios of its airways. The 48 other ones are used to build the learning base, which thus contains more than 45000 airways. Prediction results are shown in subsection 21.2.
Airways are ranked based on their predicted ratios, and this ranking is used for the unknown selection (see subsection 19.3). As mentioned in subsection 20.1.2, the identification problem is performed on both noise-free and noisy synthetic maps. Note however that in this study, the machine learning step is done on features extracted from noise-free target maps only. The obtained ranking is then used for identification in both the noise-free and noisy cases.

Identification problem:

To solve the minimization problem $(\mathcal{P}_d)$ (see (49)) with constraint $P_h = p_h$, the system is penalized as follows:

$$BB^T_{penalized} = BB^T + \frac{1}{\varepsilon} I_h$$

where

$$[I_h]_{ij} = \begin{cases} 1, & if\ i = j = h, \\ 0, & else \end{cases}$$

with $\varepsilon > 0$ and small. The penalized matrix $BB^T_{penalized}$ is invertible. And

$$BS_{penalized} = BS + \frac{1}{\varepsilon} V_h,$$

$$[V_h]_i = \begin{cases} \frac{1}{\varepsilon} p_h, & if\ i = h, \\ 0, & else. \end{cases}$$

We then solve $BB^T_{penalized} P = BS_{penalized}$ with the conjugate gradient method.

Then, as described in subsection 19.3, an extracted system of (53) is solved ten times along the breathing cycle (see temporal resolution in subsection 20.1.2). At each resolution, radius reduction ratios of airways belonging to the unknown set are computed. If the average radius reduction ratio defined by (51) over the ten time points is below 0.3, the airway is classified as a plug. This bound is set based on the radius reduction ratio distributions (see subsection 15.2). Some airways that are actually severely constricted are indeed predicted as plugged (they are true positive), some are missed (thus are true negative), and some that are only moderately constricted are classified as plugged (thus are false positive).

21. Results

In this section we present some results relative to the direct problem (see subsection 8.2), the machine learning step (see subsection 21.2) and the identification problem (see subsection 21.3).
The direct problem simulations are performed on a left lung geometry model. Time step is 0.04 s.
Same homogeneous mechanical properties as set in section 11 are considered.

21.1. Results for the direct problem

Since dynamic maps generated by 4D-CT or 4D-MRI techniques enable to assess ventilation distribution, they should help to detect defects induced by pathologies such as asthma. As explained in subsection 15.2, an asthmatic tree contains both few severe constrictions and numerous moderate constrictions. Those closures modify the ventilation distribution. Here we want to compare the influence of moderate and severe bronchoconstrictions on ventilation distribution. To do so we first build 49 stochastic asthmatic trees following the process described in subsection 15.2. Then we generate so-called “plug only” trees built from the asthmatic trees by removing moderate constrictions, and “plug free” trees built from asthmatic trees by removing the plugs (see subsection 15.2). We compare first the ventilation distribution obtained in the asthma and the “plug free” cases,

and then the ventilation distribution obtained in the asthma and the “plugs only” cases. In Figure 83, we plot for each of the 49 trees the ratio

$$diff_{plugsOnly} = \frac{100}{N}\sum_{i=0}^{N}\left|\frac{\left|V_i^{max} - V_i^{min}\right|_{onlyPlugs} - \left|V_i^{max} - V_i^{min}\right|_{asthma}}{\left|V_i^{max} - V_i^{min}\right|_{asthma}}\right|$$

where index i refers to tree exit i. The sum is over the N tree exit airways, here 477, and notations V_{max} and V_{min} have been defined in subsection 19.4.2. Similarly we define $diff_{plugsFree}$.

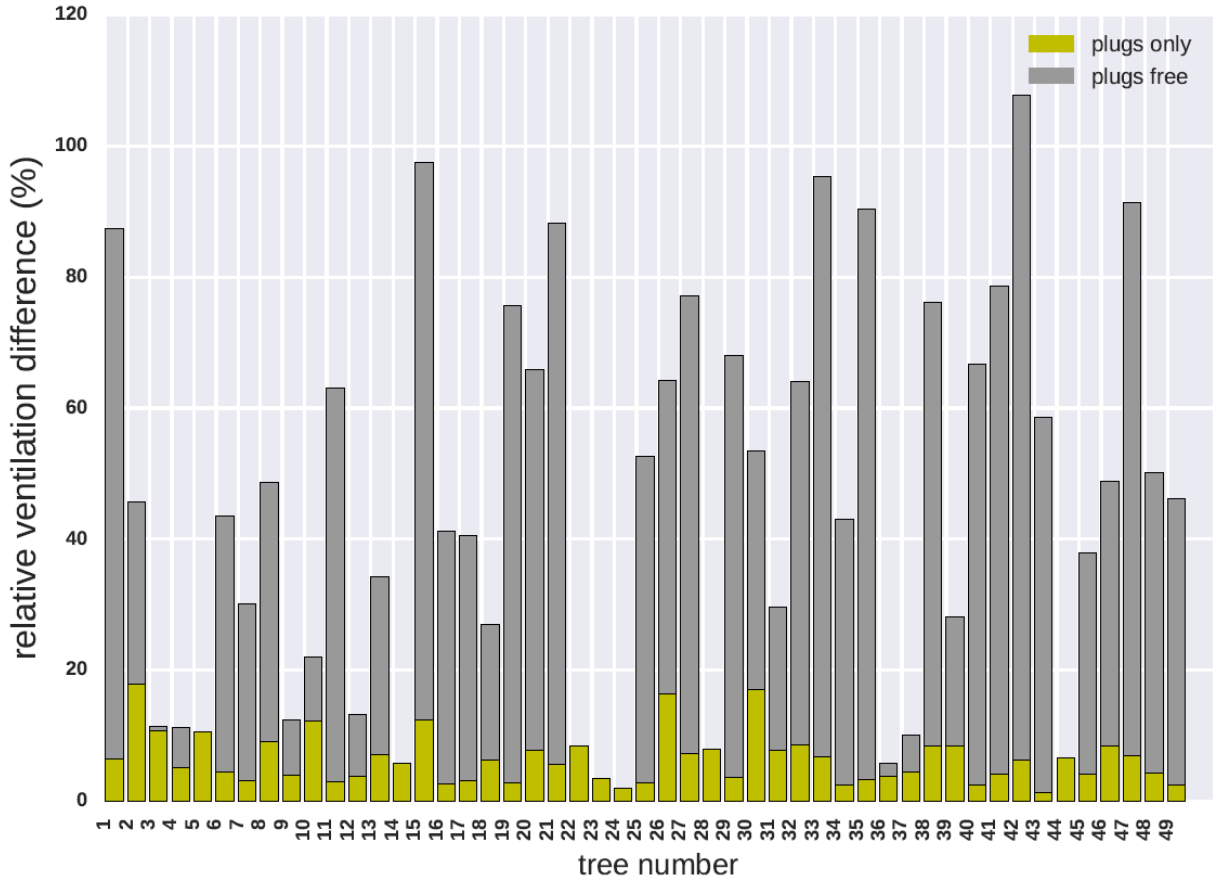

Figure 83: Plot of $diff_{plugsOnly}$ (yellow) and $diff_{plugsFree}$ (grey) for each of the 49 asthma trees.

We observe that in all cases the ventilation distribution obtained with plugs only is close to the one obtained with both plugs and moderate constrictions (6% difference on average). In most cases there is a high discrepancy between the asthma and the “no plugs” ventilation (45% difference on average). As a conclusion, plugs are much more influential than moderate constrictions on ventilation distribution in asthma. This gives ground to get insights on their position and severity based on $4D$ imaging ventilation maps. In some cases (trees 14 or 22 for example), plugs have little influence on the ventilation distribution. Those are configurations in which the number of plugs in fact is low (see Figure 84).

21.2. Results for the machine learning step

In this section, we assess the quality of the machine learning step described in subsection 19.4.2. As explained in subsection 19.3, not all the tree resistances can be considered as unknowns of the process. First, among the 954 airways, N=477 have to be selected. A radius reduction ratio (51) (which is in range $[0; 1]$) is predicted for each airway and branches are sorted in increasing order. The

smaller the ratio, the more likely the airway is constricted. In Figure 84, we plot, for each of the 49 synthetic asthma trees, the total number of plugs and among them the number for which the predicted radius reduction ratio is sorted among the first 477.
Note that in this study, the machine learning step is performed on features extracted from noise-free maps only (see subsection 20.2). The output constriction likeliness ranking is then used to perform the identification step both in the noise-free and noisy cases.

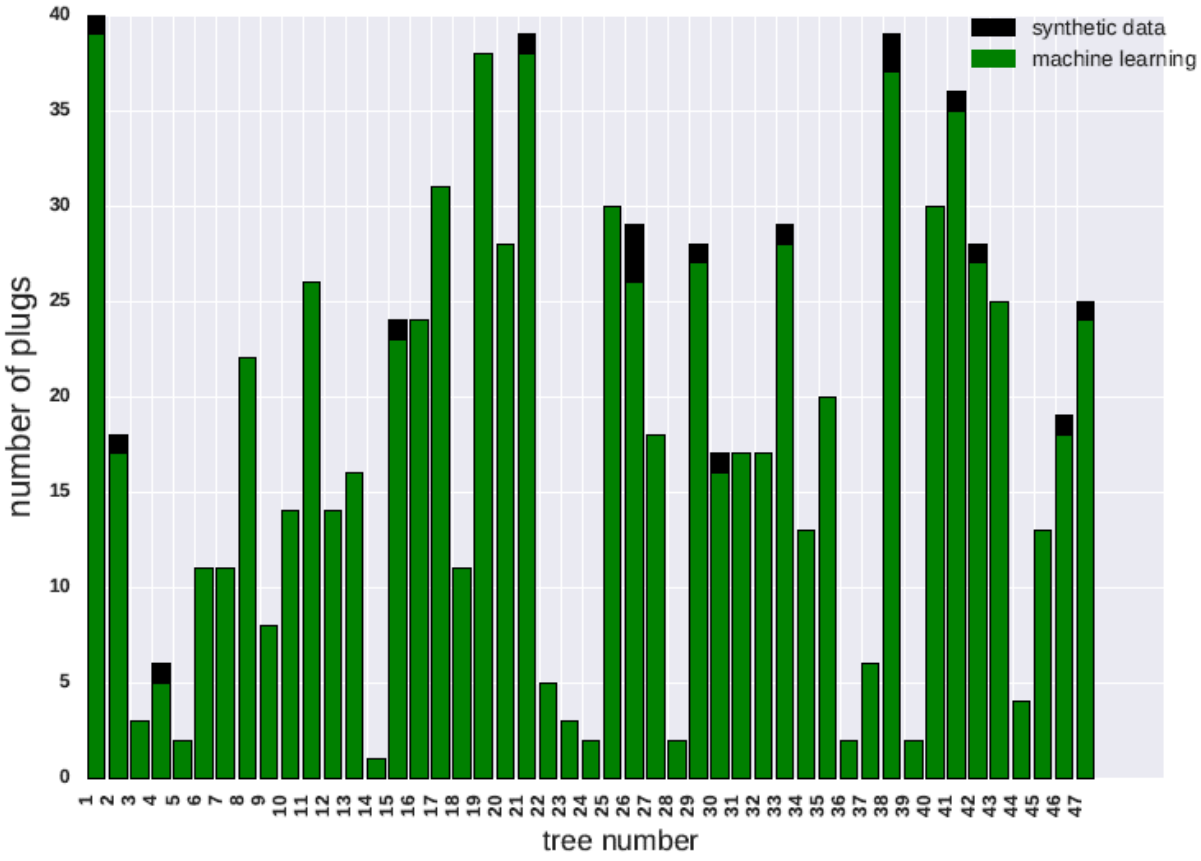

Figure 84: Machine learning classification success. The machine learning step predicts for each airway a radius reduction ratio. A low ratio corresponds to a severe constriction. Airways are sorted in increasing order with respect to their predicted ratio. Thus, each airway has a rank; the smaller the rank the smaller the predicted radius reduction ratio. For each asthmatic tree are plotted the total number of plugs (synthetic data), and among them the number of plugs that are classified with radius constriction ratio in the first half by the machine learning step. Trees contain 954 airways.

At this stage, for all trees, a large majority of the plugged airways if not all have their resistances kept in the unknown set, 98.5% in average (see Table 3). Among those N unknowns, some will be removed to get an invertible extraction of system (53) (see subsection 19.3) based on the constriction likeliness ranking provided by the machine learning step. For airway with rank k, we call $\frac{k}{N}$ its normalized rank. The smaller the normalized rank, the less likely the airway is removed from the unknown set. The *a priori* prediction process is judged to be good when plugged airways have a low normalized rank and are thus likely to be kept in the final unknown set. Note that in average on the 49 trees, after the resistance removal process (see Figure 80), there are 250 kept unknowns over the 954 initial tree airways.
In Figure 85 we plot, for each tree, the average normalized rank of plugged airways.

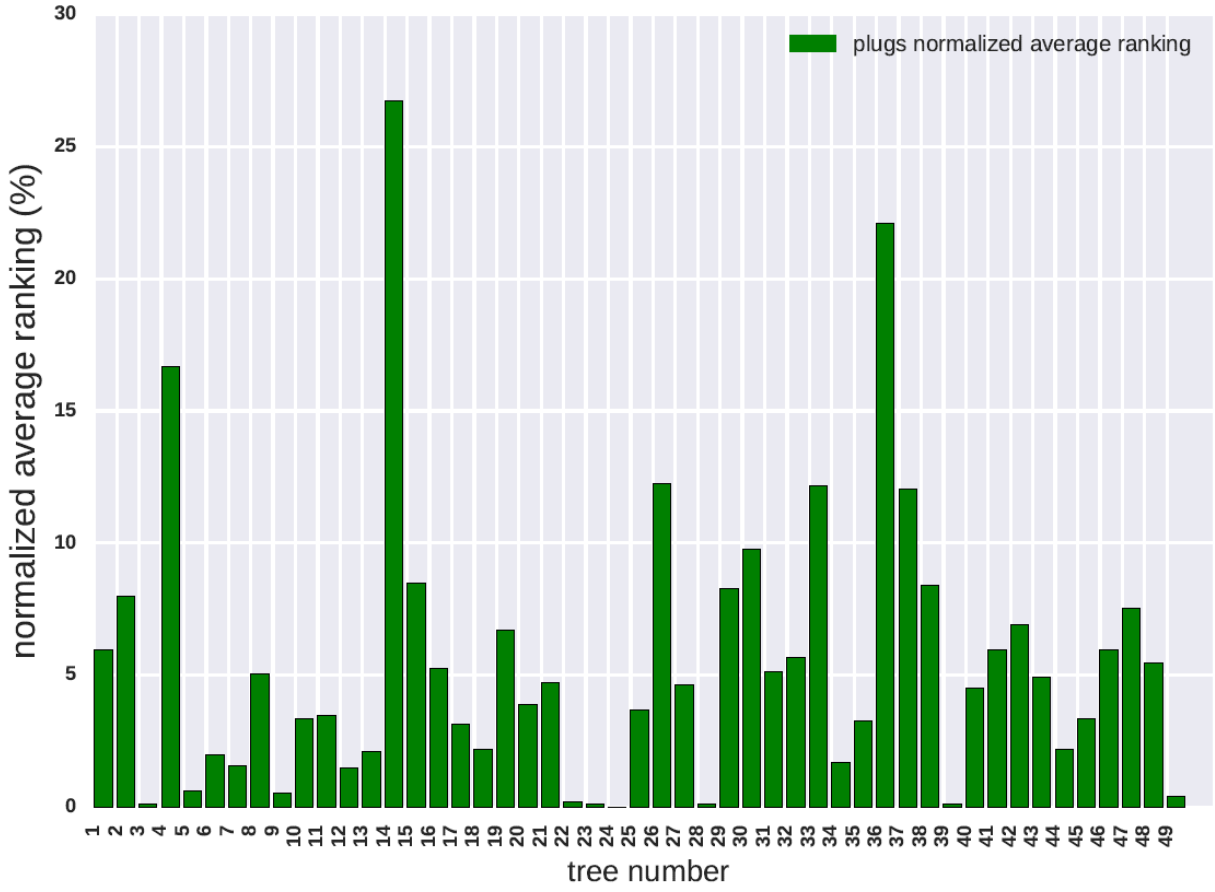

Figure 85: Normalized average ranking of plugged airways by the machine learning step. The machine learning step predicts for each airway a radius reduction ratio. A low ratio corresponds to a severe constriction. Airways are sorted in increasing order according to their predicted ratio. Thus, each airway has a rank; the smaller the rank the smaller the predicted constriction ratio. For each asthmatic tree is plotted the average predicted rank of plugged airways divided by 954, the total number of airways. The lower this normalized average rank, the more likely resistances of plugged airways will be kept in the unknown set during the removal process (see subsection *19.3*)

Note that the average normalized rank depends on the number of plugs within the tree which goes from 1 to 40 (see subsection 20.1.3). If a tree contains one plug only, as for tree number 24, the best achievable average rank is obtained when the plug ranks first and its value is 1/954≈0.1%. If a tree contains 40 plugs, as for tree number 1, the best achievable average rank is obtained when the plugs rank among the 40 first and its value is 20/954≈2%.
In about 90% of the cases plugged airways are classified in the first decile. The average rank is good, thus airways that are actually plugged are not likely to be removed during the selection process described in Figure 81.
We can now proceed to the identification problem.

21.3. Results for the identification problem step

In this section are presented the results of the identification problem step (see subsection 21.3) without and with noise added to the velocity field. As mentioned in section 19 the inputs come from synthetic data generated by the tree-parenchyma coupled model (see subsection 8.2). Simulations are performed over one breathing cycle. The identification problem classification process is described in subsection 19.3.
In Figure 86, we plot for each asthmatic tree the number of plugged airways that are properly identified as plugged by the identification problem step, and the number of false positive.

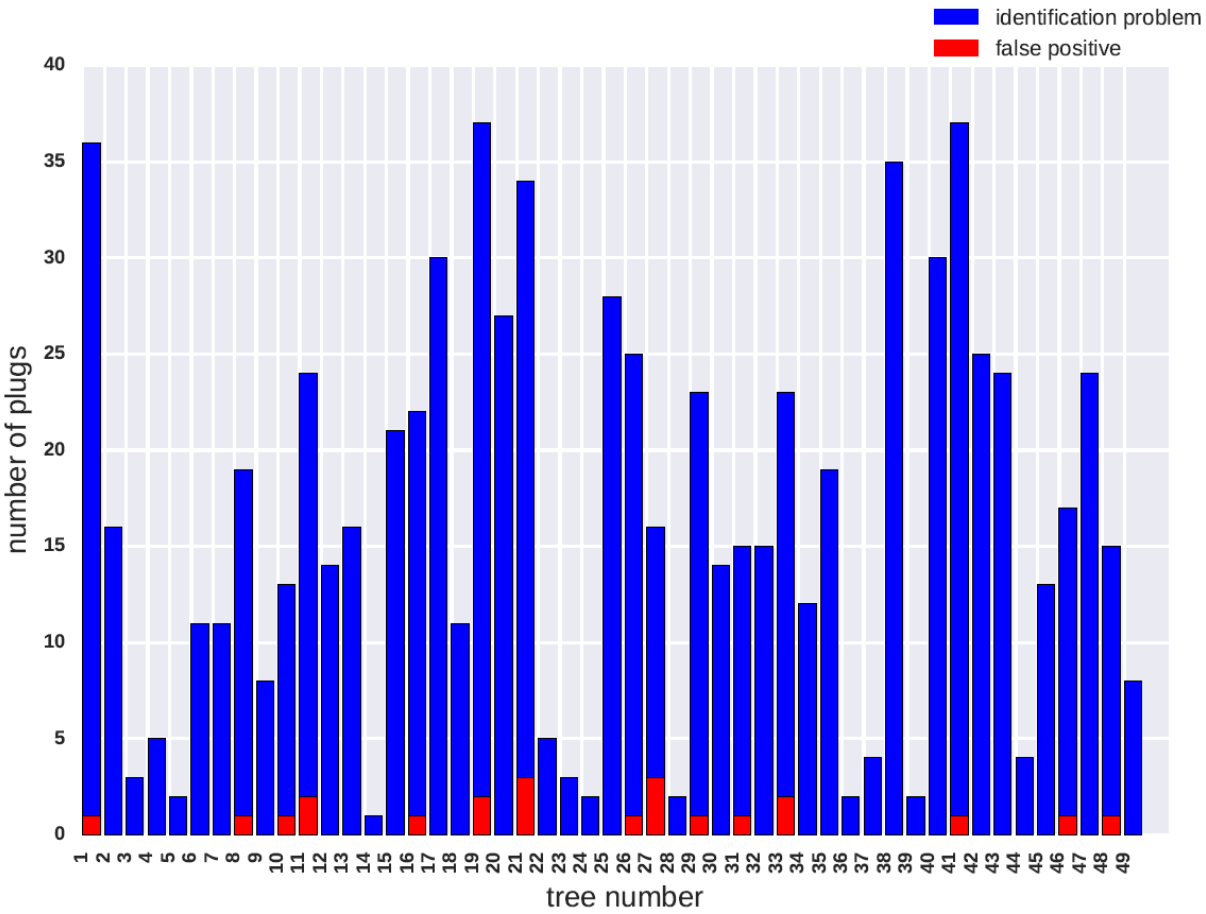

Figure 86: plugs detection for the noise-free case. For each asthmatic tree are plotted: in blue the number of plugged airways that are indeed predicted as plugged by the identification problem step, in red the number of airways predicted as plugged by the identification problem step whereas in practice they are moderately constricted at most, those are false positive.

Most of the plugs are detected. In some cases, airways radius reduction ratios are too much overestimated by the identification problem step and they are not classified as plugged although they should be. For a few airways, the ratio is too much under-estimated and they are classified as plugged although they should not be. Thus, they appear as false positive. To visualize the plug detection loss at each step of the process, we plot relative detection rates (see Figure 87). The identification problem detection rate quantifies the proportion of plugged airways that are properly classified by the identification problem step. The false positive detection rate quantifies the proportion of airways classified as plugs while they are actually moderately constricted at most.

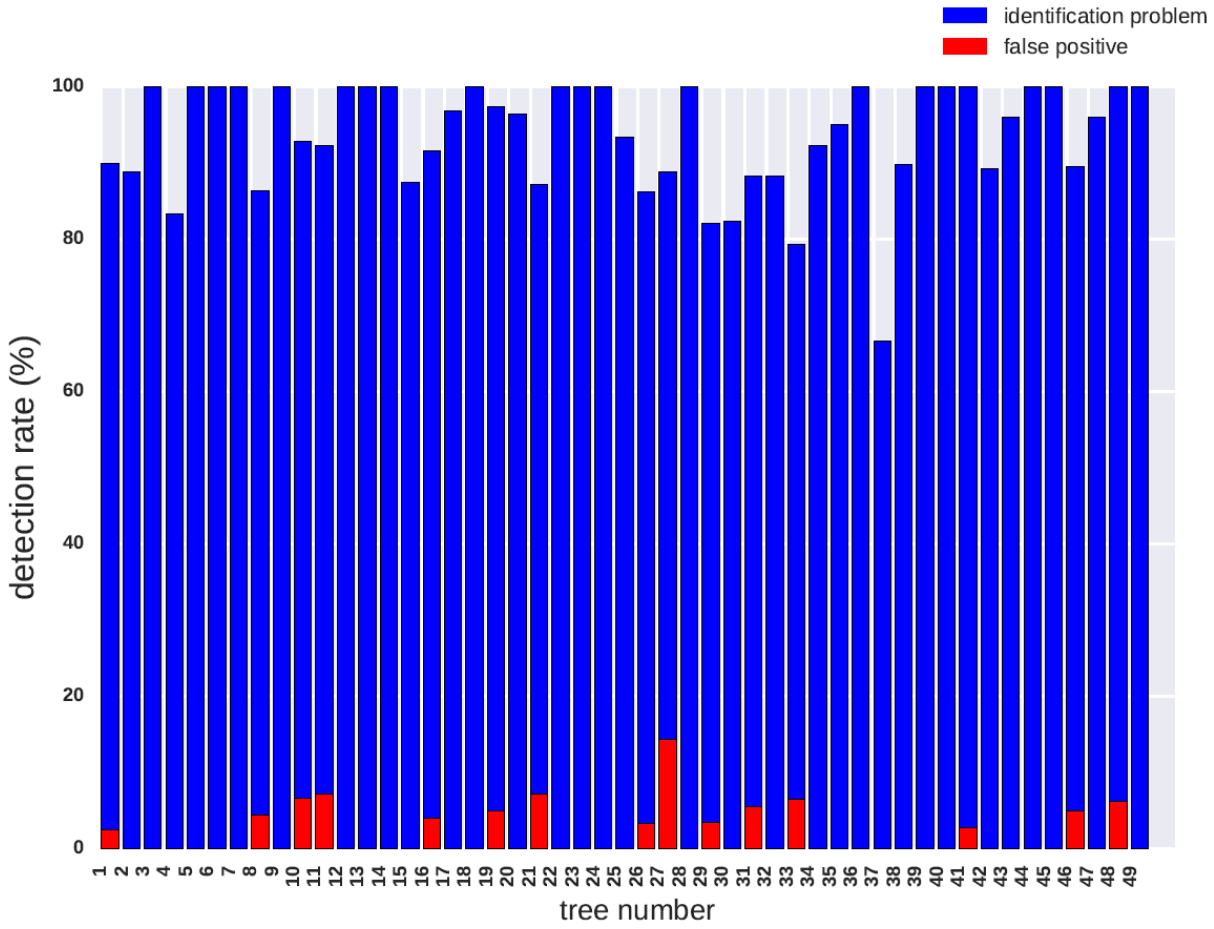

Figure 87: plugs detection for the noise-free case. For each of the asthmatic tree are plotted: in blue the proportion of plugged airways that are indeed predicted as plugged by the identification problem step, in red the proportion that are predicted as plugged by the identification problem step whereas in practice they are moderately constricted at most, those are false positive.

Average detection rates are summed up in Table 3. A more detailed analysis shows that some plugs have little influence on ventilation distribution: they will logically not be detected by the process. This can be because they are in regions where some other plugs have more impact or because they affect downstream generations where low flows result in low pressure drops even in case resistances are increased (see Figure 91). When analyzing the detection rate, one shall consider that if the tree contains a few plugs only, one missed airway notably depreciates the classification rate. In tree 37 for example, 4 plugs over 6 are actually properly classified.

Note that the space-filling tree is a model. Specifying which precise airway is plugged would require a perfect knowledge of the tree architecture even in downstream generations, which is not achievable. More reasonably, we can deduce from the analysis insights on which lung regions and tree generations are affected by plugs. This is useful information when predicting particle deposition [**79**] or response to Heliox treatments (see CHAPTER III and [**43**]). In Figure 88, we plot the true positive detection rate as a function of the false positive detection rate in two cases: assuming a false positive is actually properly classified if its mother or daughters airways are plugged, and the strict case from Figure 87. As summarized in Table 3 and Figure 90 the detection rate is slightly improved by 0.5% while the false positive rate is reduced by 29%.

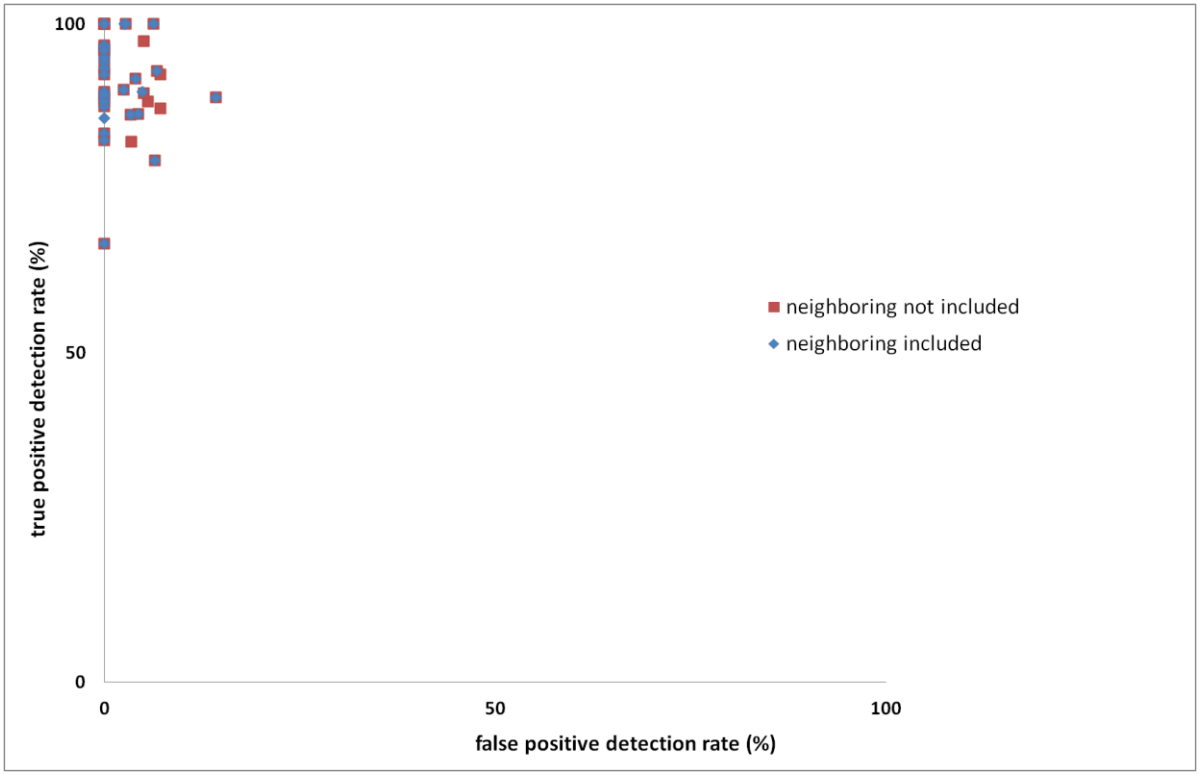

Figure 88: true positive detection rate as a function of false positive detection rate plotted for each of the asthmatic tree. In blue, results obtained when including airway neighboring on the analysis: it is considered that if a non severely constricted airway is predicted as plugged by the identification problem step and has a mother or daughter that is actually plugged, this airway is a true positive rather than a false positive. In blue results obtained when the neighboring is not included in the analysis. In both cases, the identification problem is performed on noise-free data.

In the following, we perform a similar analysis in case the velocity field used as input of the indentification problem step is noisy (see subsection 20.1.2), see Figure 89. As expected, detection rates are reduced compared to the case without noise; though a large majority (86.5%) of the plugs are detected and the amount of false positive remains low (see Table 3).

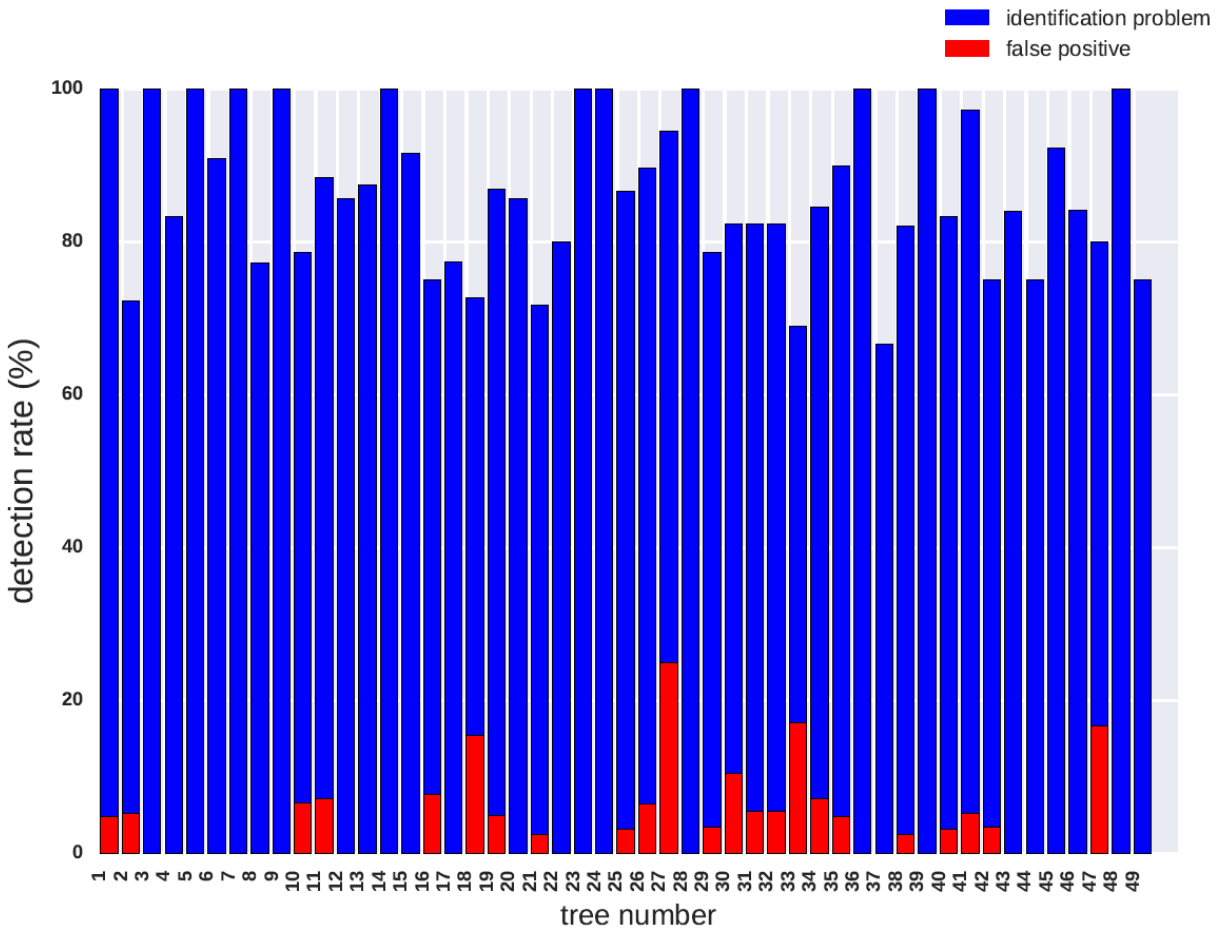

Figure 89: plugs detection ratio for noisy displacement data. For each of the asthmatic tree are plotted in blue the proportion of plugged airways that are indeed predicted as plugged after the identification problem step, in red the proportion that are predicted as plugged by the identification problem step whereas in practice they are moderately constricted at most; those are false positive. If a moderately constricted airway is predicted as plugged and it has a mother or daughter that is actually plugged, classification is judged to be good and this airway is not considered as false positive.

In Figure 90, detection rates obtained in the noise-free and noisy cases are compared.

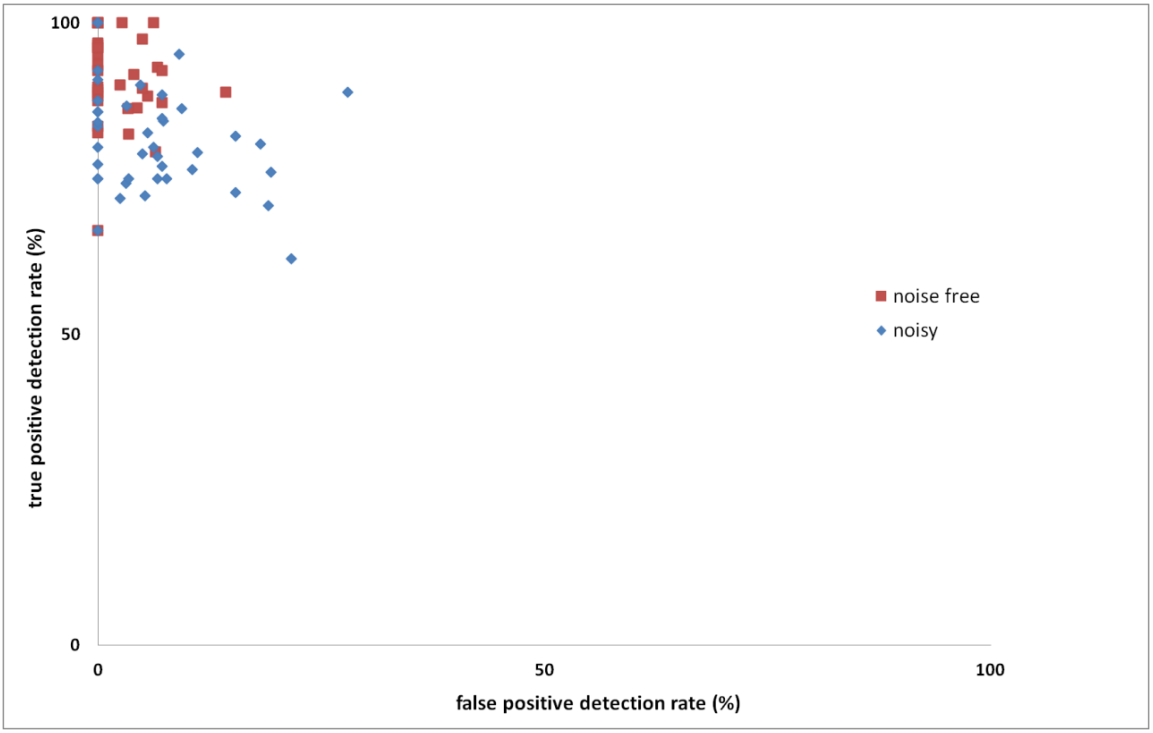

Figure 90: true positive detection rate as a function of false positive detection rate plotted for each of the asthmatic tree. In red, results obtained when the inverse problem step is performed on noise-free data, in blue results obtained when it is performed on noisy data.

	Noise-free			***With noise***		
	ML	IP	FP	ML	IP	FP
No neighbors	98.5	93.8	1.7	98.5	84.2	5.4
Neighbors	98.5	94.3	1.2	98.5	86.5	3.6

Table 3: Summary of plug classification and detection results, in %, by the machine learning step (ML), by the identification problem step (IP), and proportion of false positive (FP). A plug is considered to be properly classified by the ML step if its predicted radius reduction ratio ranks in the first half (see subsection 20.2). A plug is considered to be properly classified by the IP step if its average computed radius reduction ratio over the ten time points is under 0.3 (see subsection 20.2). Results given for both noise-free and noisy displacement data.

As mentioned in *Remark 8*, this study does not aim at predicting precise radius reduction ratios for plugged airways. The ventilation model (see subsection 8.2) upon which the identification problem step is built has various limitations (see section 12) and since not every tree branch resistance can be considered as unknown of the process (see subsection 19.3), there is intrinsic error in the radius prediction.

In the following, we analyze the detection rate by generation. Plugs in upper airways have a high influence on ventilation distribution (see CHAPTER III and [**43**]). This is not the case when constrictions occur in distal generations. It is thus expected that dynamic maps such as 4D-CT enable to access constriction information in proximal tree regions, which are critical, rather than in downstream areas which are less impacting. In Figure 91 are plotted the identification problem detection rates per generation. Note that we work on a half lung, fed by an airway belonging to generation one. In simulated cases, there is no constriction on this airway since there need to be an unknown-free path for the system to be invertible (see subsection 19.3). In practice, bronchoscopy enables to trace plugs in the most proximal airways [**128**] which can thus be removed from the unknown set.

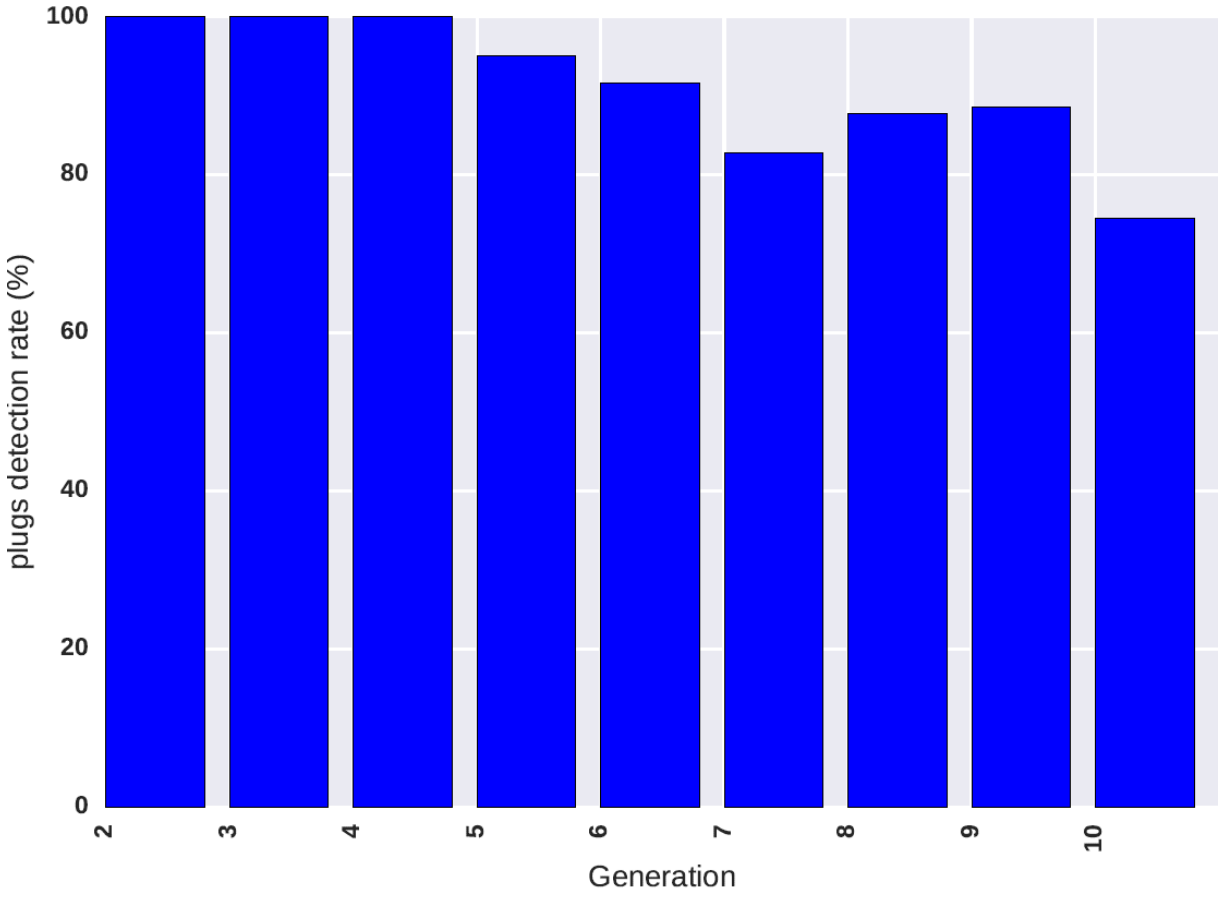

Figure 91: plugs detection rate per generation, for noisy displacement data. For each generation starting at two are plotted the identification problem plug detection rates in average on the 49 asthmatic trees.

Plugs in proximal generations are all detected. The detection rate drops under 80% at generation 10. The tree has a dyadic structure, there are about two times more airways at generation $n+1$ that at generation n. So a bad detection rate at a distal generation has a large influence on the overall detection rate result although plugs in those airways have less impact on ventilation distribution. In Table 3 detection rates are summarized. When not considering small airways (commonly defined as those with internal diameter inferior to 2mm [**121**], starting around generation 8 [**124**]) more than 90% of the plugs are detected by the process.

22. Limits and conclusions

Limitations of the ventilation model used in this study are pointed out in section 12. We assume a linear elastic behavior of the lung parenchyma which is likely to be valid for low tidal breathing frequency and displacement regimes. Although there is no consensus on which constitutive relation shall be considered [**41**], [**129**], [**104**], the actual parenchyma law is much more complex. The identification problem approach proposed in this chapter gives insights on the tree structure assuming mechanical properties are known, which is not the case in practice, representative values from the literature were assumed.

As mentioned in subsection 20.1.3, we assume the generated space-filling tree is a proper approximation of the real one in terms of topology. Although it has good statistical properties [**130**], this remains a model. Validation of this topology and of the predicted constriction ratios on imaging data of high resolution is warranted.

Another limitation of our work is, as stated in section 12, the use of the Pedley resistance model at expiration. In addition airways are assumed to be rigid which is not the case in practice. Their dimensions may evolve along the breathing cycle, though this has little impact in tidal regime (see subsection 13.3) and a quasi-static evolution would be compatible with our framework.
Note also that, as mentioned in subsection 20.2, only noise-free target maps are considered in the machine learning process. Obtained rankings are then used in the identification step for both noise-free and noisy related maps.

In conclusion we proposed a plug detection approach that couples machine learning and ventilation modeling. Considering common 4D-CT/4D-MRI temporal and spatial resolution techniques we obtain very encouraging results. More than 85% of the plugs are detected and when not considering severe constrictions in small airways, which have a lower impact on ventilation distribution, the detection rate reaches more than 90%.
Some in-vivo techniques aim at determining the parenchyma mechanical properties based on image analysis [**131**], though in cases where the ventilation is strongly affected by pathological patterns within the tree, the tree-parenchyma coupling (see subsection 8.2) shall be taken into account. Indeed, some regions with normal mechanical behavior may not inflate because they are irrigated by constricted paths. To that end identification problems for parenchyma mechanical properties and plugs distribution may be coupled. Finally, in this study, we tested the process with synthetic data, future works shall include application to real imaging and validation based on experimental data.

23. Appendix

23.1. On the dimension of $\boldsymbol{ker(B^T)}$

Let us compute the kernel of B^T. For a vector $P = \begin{pmatrix} p_1 \\ \vdots \\ p_N \end{pmatrix}$ we have

$$(B^T P)_j = \left(\sum_i p_i \int_{\Omega_i} div(\boldsymbol{e_j}) \right)_j$$

where $(\boldsymbol{e_j})_j$ are the finite element basis functions. With the imposed Dirichlet boundary conditions, they are such that $\int_\Omega div(\boldsymbol{e_j}) = 0$. Let P be a non null vector such that $B^T P = 0$. Let us consider the k^{th} element of $B^T P$:

$$(B^T P)_k = \sum_i p_i \int_{\Omega_i} div(\boldsymbol{e_k}).$$

For e_k with support included in Ω_l, we have for $i \neq l$ that $\int_{\Omega_i} div(\boldsymbol{e_k}) = \int_\Omega div(\boldsymbol{e_k}) = \int_{\partial\Omega} \boldsymbol{e_k}.\boldsymbol{n} = 0$ since $\boldsymbol{e_k} = 0$ on $\partial\Omega$. And $\int_{\Omega_l} div(\boldsymbol{e_k}) = \int_\Omega div(\boldsymbol{e_k}) = 0$. If $\boldsymbol{e_k}$ has a support intersecting the border between regions Ω_l and Ω_j then $\int_{\Omega_j \cup \Omega_l} div(\boldsymbol{e_k}) = 0$ and

$$(B^T P)_k = p_l \int_{\Omega_l} div(\boldsymbol{e_k}) + p_j \int_{\Omega_j} div(\boldsymbol{e_k}) = (p_l - p_j) \int_{\Omega_l} div(\boldsymbol{e_k})$$

So $(B^T P)_k = 0 \Rightarrow p_l = p_j$. As this is true for any frontier between neighboring regions, we conclude

$$B^T P = 0 \Rightarrow \exists\, p_0 \in \mathbb{R} \,/\, P = p_0 \begin{pmatrix} 1 \\ \vdots \\ 1 \end{pmatrix}.$$

So $\ker(B^T) = span\left\{\begin{pmatrix} 1 \\ \vdots \\ 1 \end{pmatrix}\right\}$ and $\dim\,(ker(B^T)) = 1.$

23.2. On the reason why if Z_b is not invertible, it has some collinear lines.

Let Z_b be the extracted matrix at a given iteration of the resistance removal step (see subsection 19.3). A given line i of Z_b contains 1 at position j if the two following conditions are satisfied: resistance R_j belongs to the set of unknown resistances, and the airway associated to R_j belongs to path T_i; otherwise the line contains 0 at position j.
Lemma: assume $rank(Z_b) < b$, then any line of Z_b cannot be linear combination of several of the others and thus, necessarily, Z_b has some collinear lines.

Proof of the lemma: we denote $\mathcal{U}$ the set of airways $(a_i)_{i=1\ldots b-1}$ excluding the mother branch and which resistances are unknowns. A path T_l goes from the mother branch down to exit l. Along this path, only a subset $\mathcal{A}_l$ of airways belongs to $\mathcal{U}$. Let us denote g_l the l^{th} line of Z_b.
Let us note, $m_l = \sum_k [Z_b]_{lk} = \sum_k g_{l_k} = cardinal(\mathcal{A}_l)$ and $\mathcal{G} = \{g_l \,/\, \forall j \neq l, m_l \geq m_j\}$ the set of lines containing most ones. We randomly select a line g_s in $\mathcal{G}$. We will show that g_s cannot be a linear combination of several vectors $g_{t\neq s}$. Let a_d be the most distal airway of $\mathcal{A}_s$. Path T_s is the only one that contains a_d. If another path Γ_q contained a_d, because a_d is the most distal branch of T_s, the tree structure would impose $\mathcal{A}_s \subset \mathcal{A}_q$. If $\mathcal{A}_s \neq \mathcal{A}_q$ then $m_q > m_s$ which is in contradiction with the fact $g_s \in \mathcal{G}$. Thus $\mathcal{A}_s = \mathcal{A}_q$. Finally we have that $g_{s_d} = 1$ and $\forall j \neq s, g_{j_d} = 0,$ so g_s cannot be a linear combination of several $g_{t,\forall t\neq s}$. Repeating the same process $b-1$ times with vectors $g_{t\neq s}$ we conclude that any line of Z_b cannot be linear combination of several the others.

CHAPTER V- Perspectives

In this section are presented some prospective works developed during the thesis.
While imaging techniques are costly, the most common pulmonary test to assess lung diseases is spirometry (see section 2). It consists of a full inspiration and a forced expiration. Related displacements are large and associated flow rates are much higher than during tidal breathing so specific modeling techniques have to be developed. In the first section of this chapter, extensions of the lung ventilation models presented in CHAPTER II are developed. They are steps towards spirometry modeling.
In a second section a model to link the lung surface with the tracheo-bronchial structure is proposed. It is part of a broader perspective that would map macroscopic measurements on a patient such as thoracic cage height or perimeter and input data required to run the tree-parenchyma coupled model (see subsection 8.2). Doing so, a gap would be bridged from routine practice to patient-specific simulations.
Finally a quick development on model validation by comparison to experimental data is proposed.

24. On spirometry modeling

24.1. Introduction

Imaging techniques such as CT or MRI are not used in daily medical routine. They are costly and prescribed in specific cases such as lung cancer [**132**] or acute respiratory distress syndrome [**133**]. The most common of the pulmonary function tests is spirometry. It measures the volume and flow of air that can be inhaled and exhaled during forced respiration. Parenchyma tissue properties and airway constrictions impact the flow distribution within the lung (see CHAPTER III); flow-volume curves obtained from spirometry are used as a tool to assess diseases such as COPD [**134**], asthma [**135**] or cystic pulmonary fibrosis [**136**] and their severity.
It has been shown experimentally [**137**] that the peak expiratory flow, i.e. the maximum exhaled flow under forced expiration, is limited and reaches a maximum value independent of the expiratory effort. This is called flow-limitation. Several attempts have been made to model this phenomenon. In these works, typical flow-volume curves associated with spirometry maneuvers are recovered. In [**50**] the tracheo-bronchial tree is modeled as a single equivalent non rigid airway with radius deduced from a pressure-area law. It does not account for the tree asymmetry but is able to recover look-alike spirometry curves. In [**51**] asymmetry is taken into account through an empirical pressure drop law, the parenchyma being modeled as a set of independent compartments. A few generations of the tree can be considered. Compared to experimental data provided in [**137**], the pressure peak is underestimated. In [**52**] a full dissymmetric tree is modeled, each airway of a given generation being characterized by a pressure-area law with proper parameters. Again the parenchyma is modeled as a set of independent compartments, and flow limitation is recovered. Those studies are led on simplified tree structures and with simplistic parenchyma multi-compartment models. In [**138**], instead of a physics-based modeling approach, the authors propose to classify flow-volume curves associated with breathing disorders using data mining techniques.
In this prospective section, we do no not try to account for flow limitation, but we propose to extend the exit-compartment (see subsection 8.3) and tree-parenchyma coupled models (see subsection 8.2) with the final aim of simulating spirometry tests.

24.2. Exit-compartment model

In a spirometry test, the patient expands his or her lung until TLC and then expires as fast as possible until lung volume is reduced to the residual volume (RV). From FRC to TLC and then to RV, the parenchyma volume dramatically changes. Ratio RV/TLC varies from about 20% to 40% depending on age and morphology [**139**]. The framework of linear elasticity (see subsection 8.2 and 8.3) may no longer be valid. In this section we extend the exit-compartment model with a non-linear compliance law. We also demonstrate the need for more sophisticated resistance models.

24.2.1. Model and methods for compartments mechanical behavior

In [**56**], the authors propose the following non linear lung compliance law based on static measurements:

$$p_{alv} - p_{ext} = \alpha \left(\frac{1}{V_{TLC} - V_{FRC} - V} - \frac{1}{V + V_{FRC} - V_{RV}} - \beta \right), \tag{54}$$

with $\alpha = E \left(\frac{1}{(V_{TLC} - V_{FRC})^2} + \frac{1}{(V_{FRC} - V_{RV})^2} \right)^{-1}$ and $\beta = \frac{1}{V_{TLC} - V_{FRC}} - \frac{1}{V_{FRC} - V_{RV}}$, where V_{TLC}, V_{FRC}, V_{RV} are respectively the lung volumes at TLC, FRC, RV, V is the volume expansion/contraction from FRC, and E is the parenchyma elastance which is defined as the inverse of the compliance. With law (54),

it is harder to contract the lung when its volume gets closer to RV, and harder to expand it when it gets closer to TLC. To expand this model to a multi-compartment description, we define a pressure law per compartment i following:

$$P_{alv_i} - P_{ext_i} = \varphi_i(V_i) = \alpha_i.\left(\frac{1}{V_{TLC_i} - V_{FRC_i} - V_i} - \frac{1}{V_i + V_{FRC_i} - V_{RV_i}} - \beta_i\right)$$

where subscript i refers to compartment i. For instance, V_{TLC_i}, V_{FRC_i} V_{RV_i} are the volume of compartment i at TLC, FRC and RV respectively, $\alpha_i = E\left(\frac{1}{\left(V_{TLC_i} - V_{FRC_i}\right)^2} + \frac{1}{\left(V_{FRC_i} - V_{RV_i}\right)^2}\right)^{-1}$ and $\beta_i = \frac{1}{V_{TLC_i} - V_{FRC_i}} - \frac{1}{V_{FRC_i} - V_{RV_i}}$. Extending equations from subsection 9.2, the system describing the volume dynamic of each compartment i is governed by

$$A\dot{V} + \varphi(V) = P_{trach} - P_{ext} \tag{55}$$

where $\varphi(V) = \begin{pmatrix} \varphi_1(V_1) \\ \vdots \\ \varphi_N(V_N) \end{pmatrix}$, $V = \begin{pmatrix} V_1 \\ \vdots \\ V_N \end{pmatrix}$.

When neglecting gravity we may choose: $V_{TLC_i} = \frac{V_{0_i}}{V_0} V_{TLC}$ and $V_{RV_i} = \frac{V_{0_i}}{V_0} V_{RV}$ as done for the compliance distribution in subsection 8.3. To take into account the gravity effect depending on the position within the lung, we refer to Appendix 24.4.1.

Discretizing (55) with a time implicit Euler scheme, we get

$$A_n \frac{(V^{n+1} - V^n)}{\Delta t} + \varphi(V^{n+1}) = (P_{trach} - P_{ext})_{n+1}$$

and finally

$$(A_n + \Delta t.\varphi'(V^n)).V^{n+1} = A_n V^n \ + \Delta t.(P_{trach} - P_{ext})_{n+1} + \Delta t.(V_n.\varphi'(V^n) - \varphi(V^n))$$

where φ' is the derivative of φ. Matrix $(A_n + \Delta t.\varphi'(V^n))$ is not stored and it is efficiently inversed following [**73**].

24.2.2. Results

We work on a ten-generation tree, containing 954 exit-compartments. Lung elastance is set to C=5.10^5 Pa/m^3 [**27**]. The Pedley resistance model (4) is used. To simulate spirometry, a homogeneous pressure profile of $p_{trachea} - p_{ext}$ (see Figure 92) is applied as boundary condition to each exit ($p_{trachea}$ being the pressure at the trachea entrance and p_{ext} the one around each exit compartment). The pressure is first negative so as to account for full inspiration; it then quickly increases during forced expiration. The FRC is taken as reference state, and the maximum expired volume after full inspiration, $V_{TLC} - V_{RV}$, is taken to be 2.6 L which is in typical range for a human adult lung.

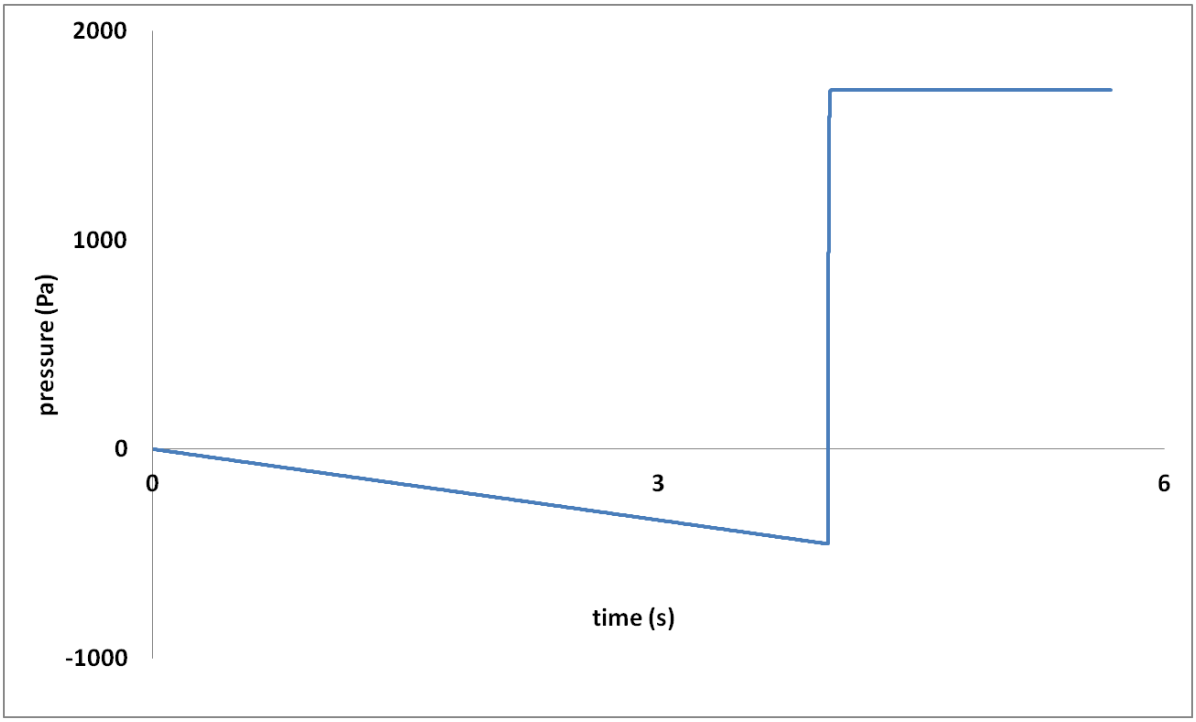

Figure 92: pressure boundary condition $p_{trach} - p_{ext}$, homogeneously applied to each exit-compartment i to simulate spirometry.

Two cases are simulated, a healthy one and a configuration in which airways of lobe LL are constricted with a ratio two. Plotting the flow as a function of the expired volume we get curves shown in Figure 93.

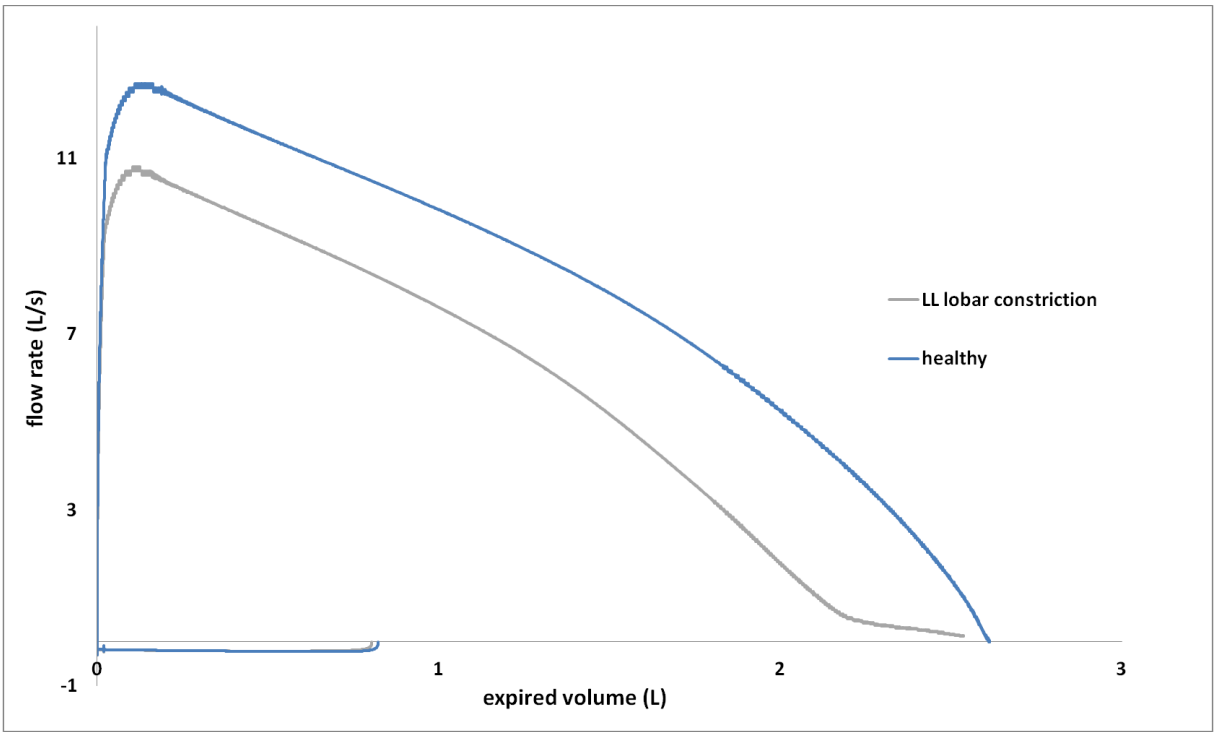

Figure 93: flow volume forced expiration curves. Homogeneous pressure boundary conditions are applied to two configurations, a healthy case and one in which constrictions with ratio two are applied to airways of lobe LL.

In the pathological case, the peak expiratory flow is reduced compared to the healthy situation and the flow-volume curve concavity is changed at late expiration, as it can be observed in practice [**140**].

Other configurations tested did not lead to an earlier concavity change although this is more common for patients with bronchoconstrictions [**140**], [**141**].
Curves shapes are strongly dependent upon the applied pressure boundary about which we have a limited knowledge. There is no insight on its spatial dependence, and available esophageal measurements may not be faithful indicators of the pleural pressure [**89**]. Note that the chosen applied pressure peak (see Figure 92) is underestimated by a factor five compared to esophageal measurements provided in [**137**]. It was chosen to obtain a realistic peak expiratory flow in the healthy configuration. This may indicate that pressure drops in the tree and hence airway resistances are under estimated. Several reasons can account for that, see details in next subsection. Note finally that here, the extra-thoracic part is not considered, and major pressure drops are expected at the glottis constriction.

24.2.3. Towards a more sophisticated resistance model

As mentioned in the previous section, at high expiratory flows, resistances are underestimated with Pedley model (4). Several reasons can account for it. First this model has been designed for inspiration only and for a particular bifurcation angle (see section 12). It was also developed for lower flows than those reached here, and in the framework of rigid airways, which is no longer the case in forced expiration [**1**]. As perspectives for resistance modeling, one could for instance account for airway elasticity and fluid structure interaction as in attempts proposed by [**50**], [**52**].
Another source of discrepancy may be that airways are considered as straight tubes. They are actually curved with varying radius along their centerline and as noted in Appendix 24.4.2 little geometrical perturbations can generate important supplementary pressure drops. A better description of the tree geometry accounting for deviation from tubular patterns shall thus be considered when modeling spirometry.

24.3. Tree-parenchyma coupled model

In this thesis, no non linear constitutive relation was considered for the continuous parenchyma model. However some developments allow us to compute a boundary force field that would account for volume variations observed in spirometry, in the frame of a simple linear elastic law.

24.3.1. Model and methods

In the tree-parenchyma model framework (see subsection 8.1), both Dirichlet and Neumann boundary conditions can be imposed. The spatio-temporal distribution of the force field around the lung cannot be measured in vivo while imaging techniques enable to access lung surface evolution (see subsection 10.3). In this section, we show how the knowledge on the surface displacement along with mechanical and tree properties can be used to calculate the force field surrounding the parenchyma.
Let $\boldsymbol{u}_{dir}$ be the displacement field computed with Dirichlet boundary conditions. To get the surface force field that would induce the same solution in case the tree configuration and mechanical properties were the same, we use equation (18). When neglecting gravity this leads to:

$$\int_{\partial\Omega} \boldsymbol{f}\cdot\boldsymbol{w} = \rho_{par}\int_{\Omega}\ddot{\boldsymbol{u}}_{dir}\cdot\boldsymbol{w} + \int_{\Omega}\sigma_{mat}(\boldsymbol{u_{dir}}):\varepsilon(\boldsymbol{w}) - \int_{\Omega} p_{tree}(\dot{\boldsymbol{u}}_{dir})I:\varepsilon(\boldsymbol{w}) \tag{56}$$

where $\boldsymbol{f}$ is the surface force field. Notations are defined in subsection 8.2.
When imposing the surface displacement, the global volume evolution is enforced and does not depend on the tree structure (though local volume variations are impacted by the tree structure). In the case of bronchoconstriction, the work of breathing is increased to whatever it takes to get the

prescribed surface displacement (see CHAPTER III). This is not the case in practise. To avoid spending too much energy the patient may inflate less. Imposing a given force field instead of Dirichlet boundary conditions, the lung would expand less when airways are bronchoconstricted.
In the following section, Dirichlet boundary conditions are imposed so as to simulate a spirometry test. It is generated by scaling and imposing a proper dynamics to the displacement field registered in subsection 10.3. The equivalent force field is computed in a healthy configuration. Assuming a patient with constricted airways generates the same force during the spirometry test, we compute flow-volume loops obtained in pathological cases.

24.3.2. Results

Simulations were performed on a left lung, with the mesh used in section 16. The volume differences between the reference and TLC and RV states are 0.83L and 0.51L respectivelly. As seen on the overall lung volume evolution plotted in Figure 94 an inspiration from the reference to the TLC state is first simulated, then the patient shortly holds his/her breath before quickly expiring to the RV state. As advised by practicians, the breath hold shall be short: no more than 1 or 2 seconds [**142**]. The corresponding flow evolution is plotted in Figure 95. In Figure 96 are shown the flow-volume loops obtained with Dirichlet boundary conditions and when applying the equivalent force field defined by (56); as expected they superimpose. Note that this force may not be physiological, especially because the parenchyma is described as a linear elastic material. This boundary force is computed in a healthy configuration. Assuming the patient would generate the same effort if his/her tree was affected by bronchoconstrictions, we simulate pathological cases with this force as Neumann boundary condition. Results are plotted in Figure 97. When an airway is constricted, the peak flow is decreased, the more the constriction the more the decrease. Little curvature change is observed.

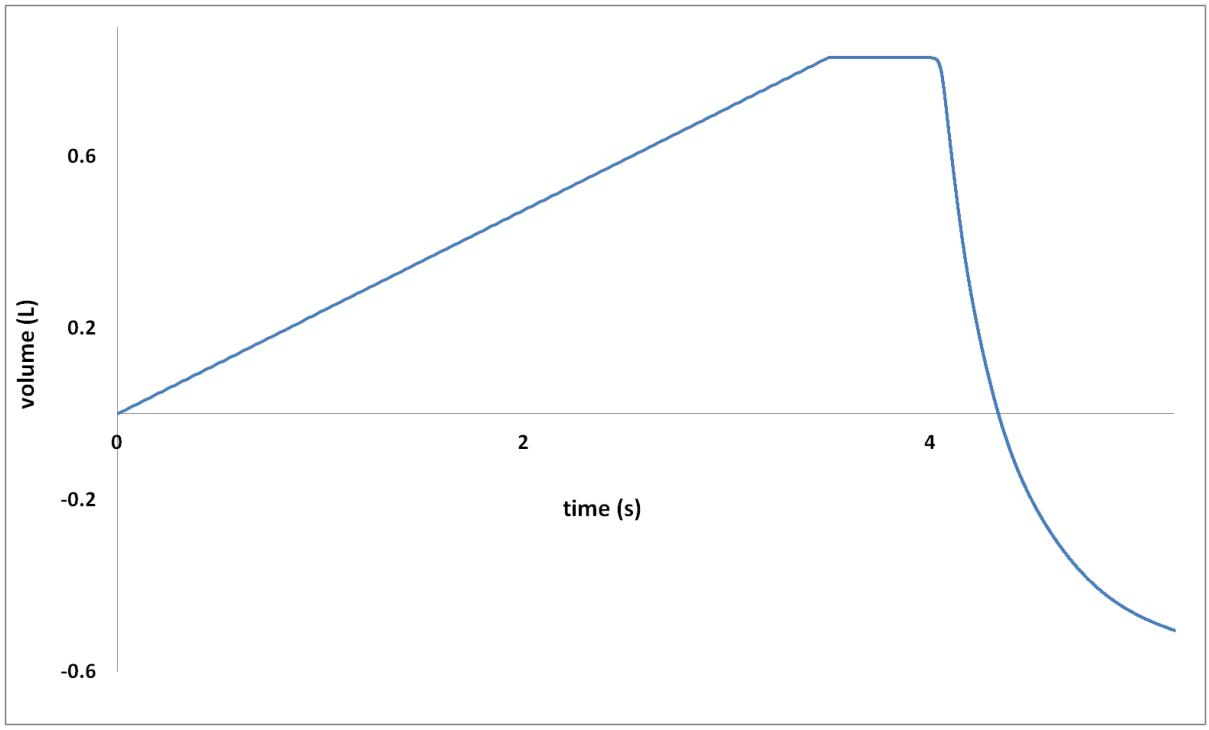

Figure 94 : left lung volume evolution from the reference state, imposed by Dirichlet boundary conditions. During a spirometry test, the patient first inspires to TLC, then holds his/her breath, before quickly expiring to RV.

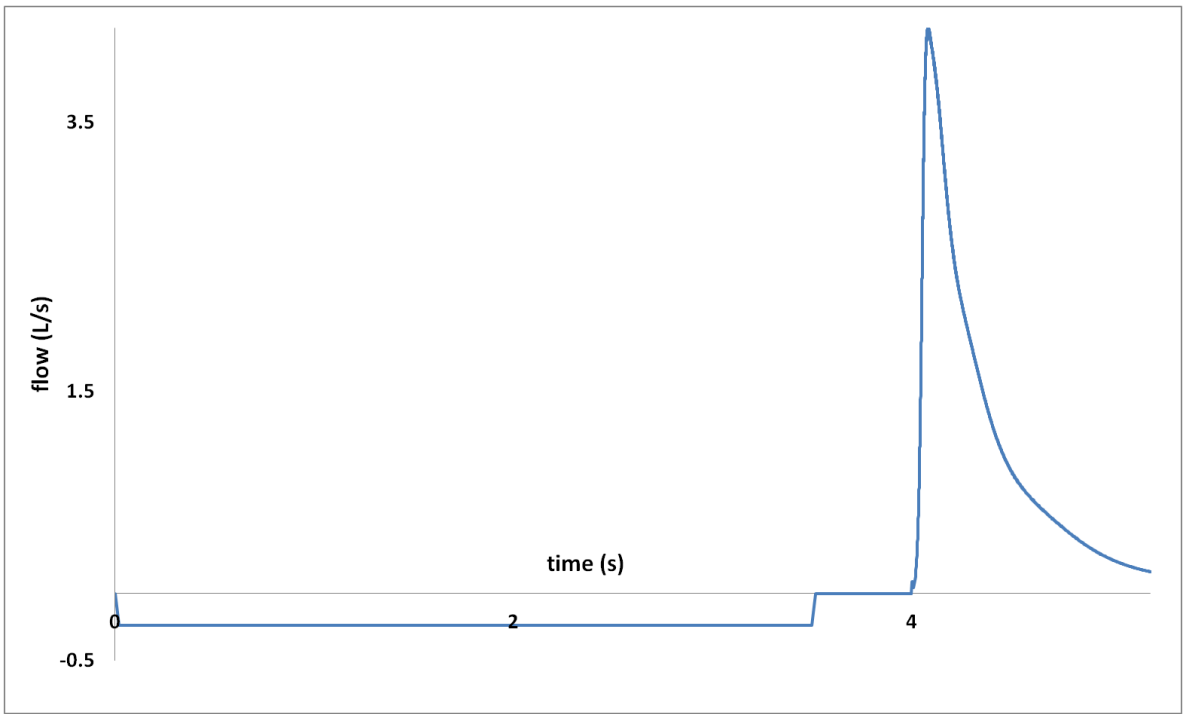

Figure 95: left lung expired flow evolution. During a spirometry test, the patient first inspires to TLC, then holds his/her breath, before quickly expiring to RV.

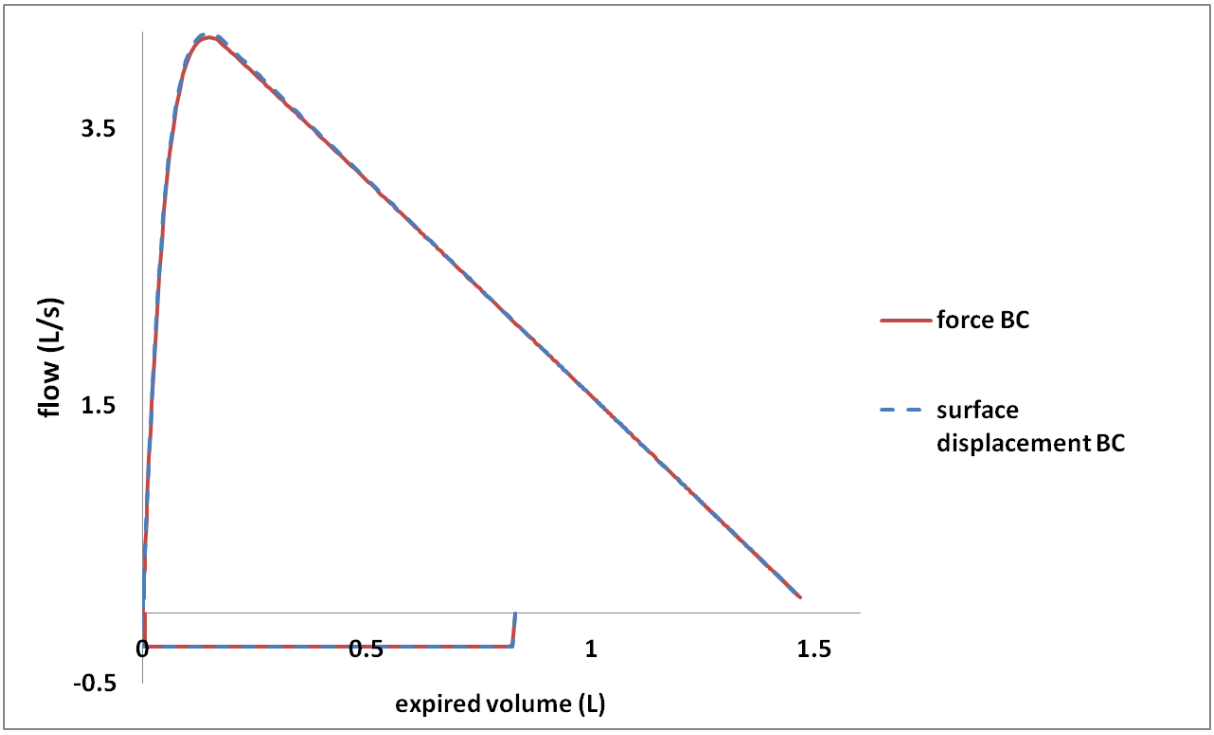

Figure 96: simulated spirometric flow-volume curve. A simulation is done with a surface displacement boundary condition (BC), the equivalent force field defined by (56) is computed based on the method described in subsection 24.3.1 and applied as new (Neumann) boundary condition.

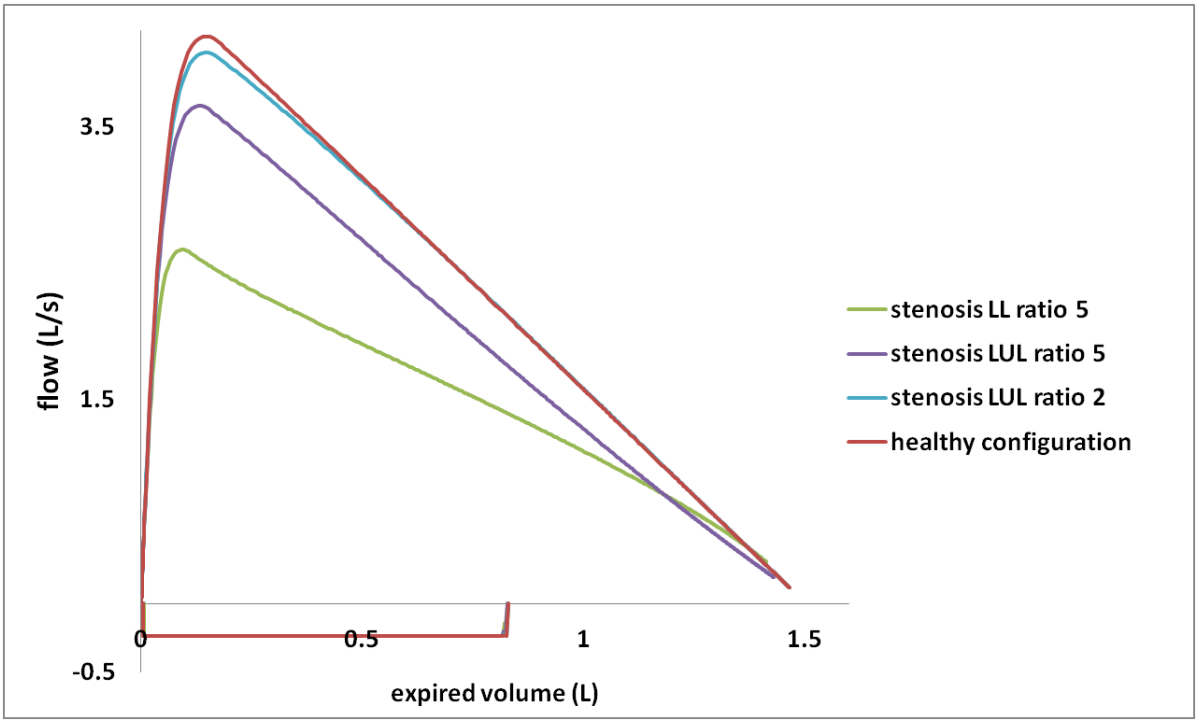

Figure 97: simulated spirometric flow-volume curves. A Neumann boundary condition defined by (56) is computed in a healthy configuration and applied in cases of bronchoconstriction. Plots in a healthy case, and in case a stenosis is applied on airway LUL with constriction ratio 2, on airway LUL with constriction ratio 5 and on airway LL with constriction ratio 5.

To conclude, some developments for the two lung ventilation models described in section 8 were proposed in order to describe spirometry maneuvers. Because of high flow rates, the underlying physics is complex and those descriptions do not enable to observe classic spirometric trends such as clear concavity inversion in case of obstructive lung disease, high pressure drops within the tracheo-bronchial tree or flow limitation. Though classic flow-volume loops shapes and peak flow decrease due to constrictions are obtained.
Some effort shall be made to account for fluid-structure interaction. Tree geometry variability impact on pressure drops could be studied and specific resistance models to describe the pressure drops at high flows in bifurcating structures may be developed.

24.4. Appendix

24.4.1. Gravity consideration in the exit-compartment model

Using the model described in subsection 24.2.1 gravity can be included assuming the volume distribution at FRC depends on the altitude within the lung. The pressure gradient within the parenchyma may have different origins: the weight of the lung itself which induces higher load at the top, but also the weight of the diaphragm or other components inducing a load homogeneously distributed over the whole lung. We define a theoretical zero-gravity volume V_{0g} as the volume the lung would have under zero-gravity and when no force is exerted on it. We also define $\Delta V_{homogeneous}$ and $\Delta V_{lungWeight}$ the lung volume variations induced respectively by homogeneous loads on the lung (as the one induced by the diaphragm in a first approximation) and by the weight of the lung itself. Assuming the lung is “held” by “the top”, i.e. by its point with highest position, the volume distribution at FRC is modeled as:

$$V_{FRC_i} = \frac{V_{0_i}}{V_0} \cdot [\,(V_{FRC_{0g}} + \Delta V_{homogeneous}) + \Delta V_{lungWeight} \cdot \frac{z_i - z_m}{\sum_k \frac{V_{0_i}}{V_0}(z_k - z_m)}\,]$$

where z_i is the altitude of compartment i and z_m the altitude of the lowest compartment. Distribution at RV and TLC are supposed to be gravity and load force independent. This would be valid if the forces required to expand to TLC or to contract to RV were big compared to gravity and load. To obtain knowledge of $\Delta V_{homogeneous}$, $\Delta V_{lungWeight}$ we would need to model the effects of gravity and loads on the lung volume. More insights could be deduced from experiments in micro-gravity conditions [**143**].

We denote $\omega = \frac{V_{FRC_{0g}} + \Delta V_{homogeneous}}{V_{FRC}}$. In a case with neither load, nor gravity, $\Delta V_{homogeneous} = 0$, $V_{FRC} = V_{FRC_{0g}}$ so $\omega = 1$. The smaller ω, the more the effect of load and gravity. Applying a homogeneous sinusoidal pressure boundary condition and computing the lobar ventilation ratio as an average over a breathing cycle for erect, supine and prone positions, we get the following results.

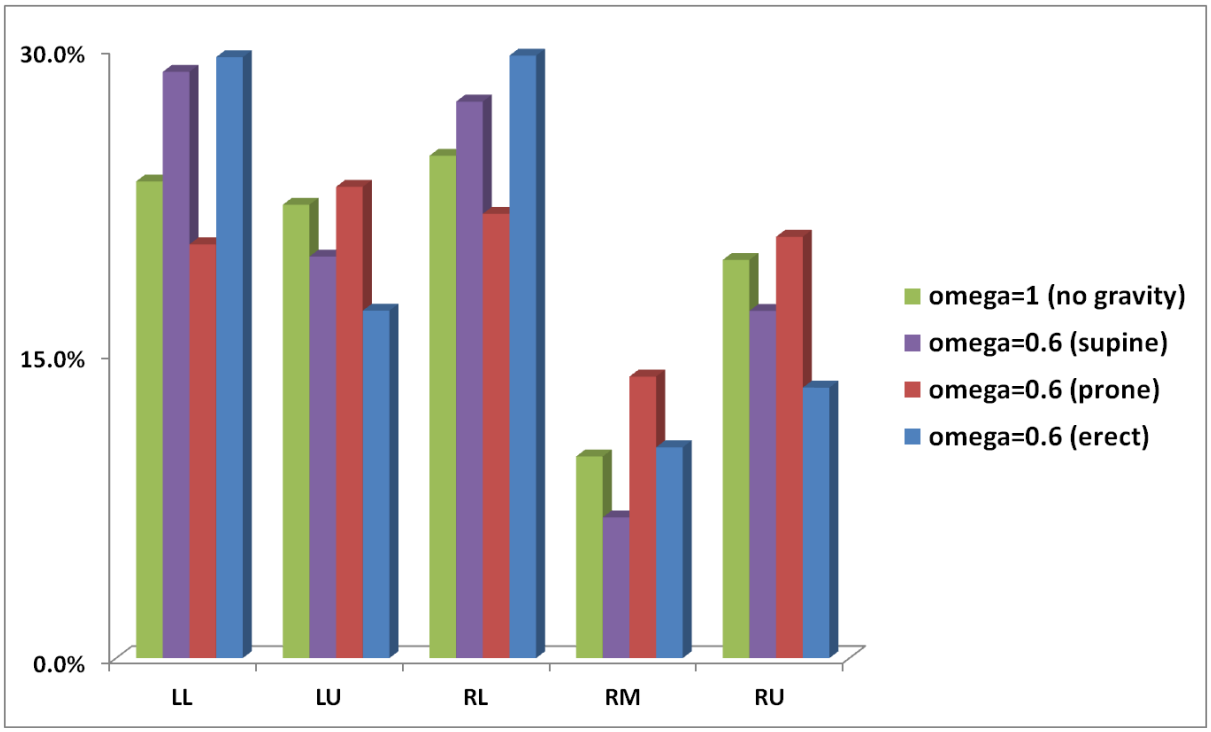

Figure 98: lobar ventilation distribution for different positions. A homogeneous pressure boundary condition is applied Ratios are obtained by averaging the ventilation over a breathing cycle. Pedley resistance model (4) is used.

In the supine position, ventilation is shifted towards posterior lobes. In the prone position ventilation is shifted towards anterior lobes. In the erect position, ventilation is shifted towards lower lobes compared to no gravity because pre-extended lobes are harder to expand so they grow less for a given applied external pressure.

24.4.2. Effect of geometrical perturbations on the pressure drops at forced expiratory flows

Results shown here were taken from simulations performed by Ludovic Boilevin-Kayl in the frame of his internship at Air Liquide Santé International, under my supervision.

We investigated how small geometrical perturbations impact the pressure drops in the trachea at flows that can be reached under forced expiration. The trachea is modeled as a straight tube with dimensions from [**124**]: length 10.5 cm and diameter 1.57 cm. Small stenoses with varying

constriction ratios, seen as geometrical perturbations, are applied at the center of the tube (see Figure 99). A Poiseuille parabolic flow profile is imposed at the inlet, a zero pressure at the exit and no-slip on the walls. A convergence study led to a 600 000 cells tetrahedral mesh refined around the constriction. A k-ω SST turbulence model was used, with low-Reynolds correction and production limiter as recommended in [**144**]. Simulations were done with Fluent software (ANSYS, USA).

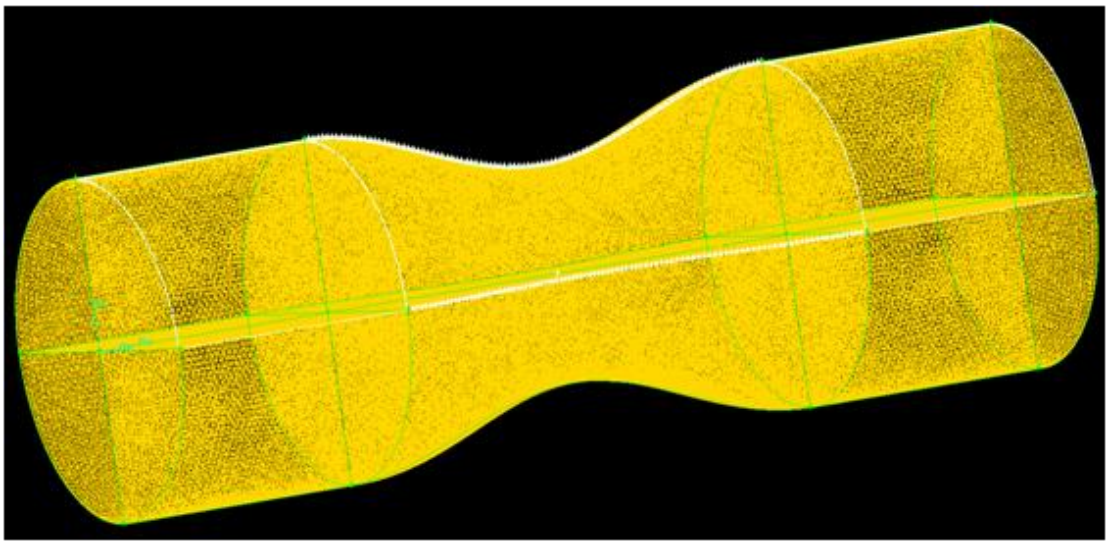

Figure 99: Tetrahedral 600 000 cells mesh of a stenosed trachea.

In Figure 100 we compare numerical pressure drops for flows of 5 L/s and 10 L/s in a stenosed trachea with varying small geometrical perturbations (defined as the inverse of the constriction ratio (51)) and the pressure drops computed with Colebrook-White model [**145**], which has been designed for turbulent flows in a pipe, in case where the radius was homogeneously reduced with the same ratio. For sufficiently small Reynolds numbers, the Colebrook-White pressure drop along a pipe of length L, radius R in which a fluid of density ρ flows with Reynolds Re and mean velocity U, is given by:

$$\Delta p_{Colebrook-White} = 0.079 Re^{-0.25} \rho U^2 \frac{L}{R}.$$

Pressure drops are computed along the constriction pattern, which spreads on 10% of the trachea length. Results are plotted in Figure 100 and summed up in Table 4.
For a non-constricted pipe, there is good agreement between the CFD results and the analytical formula. Small geometrical perturbations induce important shifts. The larger the perturbation or the the flow, the greater the gap. Thus, even with a proper resistance model, a precise geometrical description seems to be needed when flows reach values encountered in forced expiration.

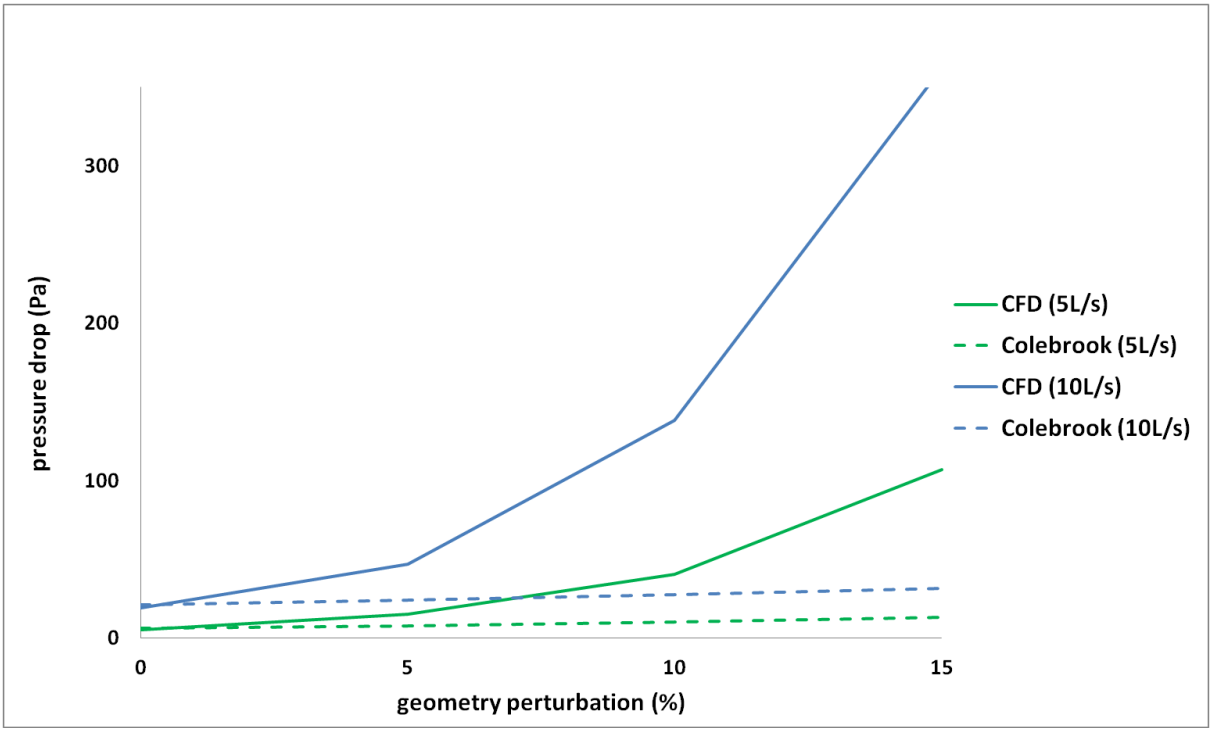

Figure 100: pressure drops in the trachea when the geometry is perturbed by a constriction. The inverse of the constriction ratio (51) is here referred to as *geometry perturbation*. Pressure drops are computed along the constriction, on 10% of the trachea length, numerically with a CFD code and analytically with Colebrook-white model. For the analytical calculation, the trachea radius is homogeneously multiplied by the geometry perturbation. Comparison for flows of 5L/s and 10L/s.

Geometry perturbation (%)	Pressure drops (Pa) for 5 L/s		Pressure drops (Pa) 10 L/s	
	CFD	Colebrook	CFD	Colebrook
0	5.5	6.3	19	21.2
5	15.1	7.9	47	24.1
10	40.6	10.1	138.5	27.5
15	107	13.1	362.3	31.8

Table 4: pressure drops in the trachea when the geometry is perturbed by a constriction. The inverse of the constriction ratio (51) is here referred to as *geometry perturbation*. Pressure drops are computed along the constriction, on 10% of the trachea length, numerically with a CFD code and analytically with Colebrook-white model. In the analytical calculation, the trachea radius is homogeneously multiplied by the geometry perturbation. Comparison for flows of 5L/s and 10L/s.

25. Towards a statistical lung model

25.1. Introduction

Lung ventilation models in general [**41**], [**75**], [**74**] require complex patient-specific input data such as lung geometry, tree structure or lung surface evolution over the breathing cycle. They are accessible through imaging techniques such as HRCT [**23**], 4D-CT [**31**] or 4D-MRI [**32**], but those technologies are costly and not routinely available. If we could correlate body characteristics such as the thoracic cage perimeter, height, or lung volume, easily measured or calculated, with input data of the model (see Figure 101), a gap would be bridged from routine practice to patient-specific simulations. Note that local lung mechanical properties as well as airway constrictions distributions (see CHAPTER III) are also required as input data; but they are not treated in this section.

There exist some correlations between outer body characteristics and lung characteristics. For instance, the dead space is correlated to the lung volume and body size [**146**], the pulmonary tissue volume is related to the body surface area [**147**]. Some models have also been developed to track parenchyma internal displacement by linking it to respiratory surrogates. Surrogates can be a spirometry signal [**148**], [**149**] as well as patient chest or abdomen motion measured via optically tracked infra-red markers [**150**] or with a respiratory belt. There are applications in the context of radiation treatments for lung cancer, as there is no direct monitoring of the tumor motion along the breathing cycle.

To apply the ventilation model presented in subsection 8.2 to a specific patient, it would be suitable to deduce its lung surface, tree structure and parenchyma surface evolution from outer body surface measurements later referred to as "*macroscopic measurements*". From the thoracic cage height, perimeter at different locations and other relevant parameters, one could try to build an approximation of the lung shape. In this study we focus on the correlation between the lung shape and the tracheo-bronchial tree, more specifically the tree nodes positions of proximal airways (see Figure 102).

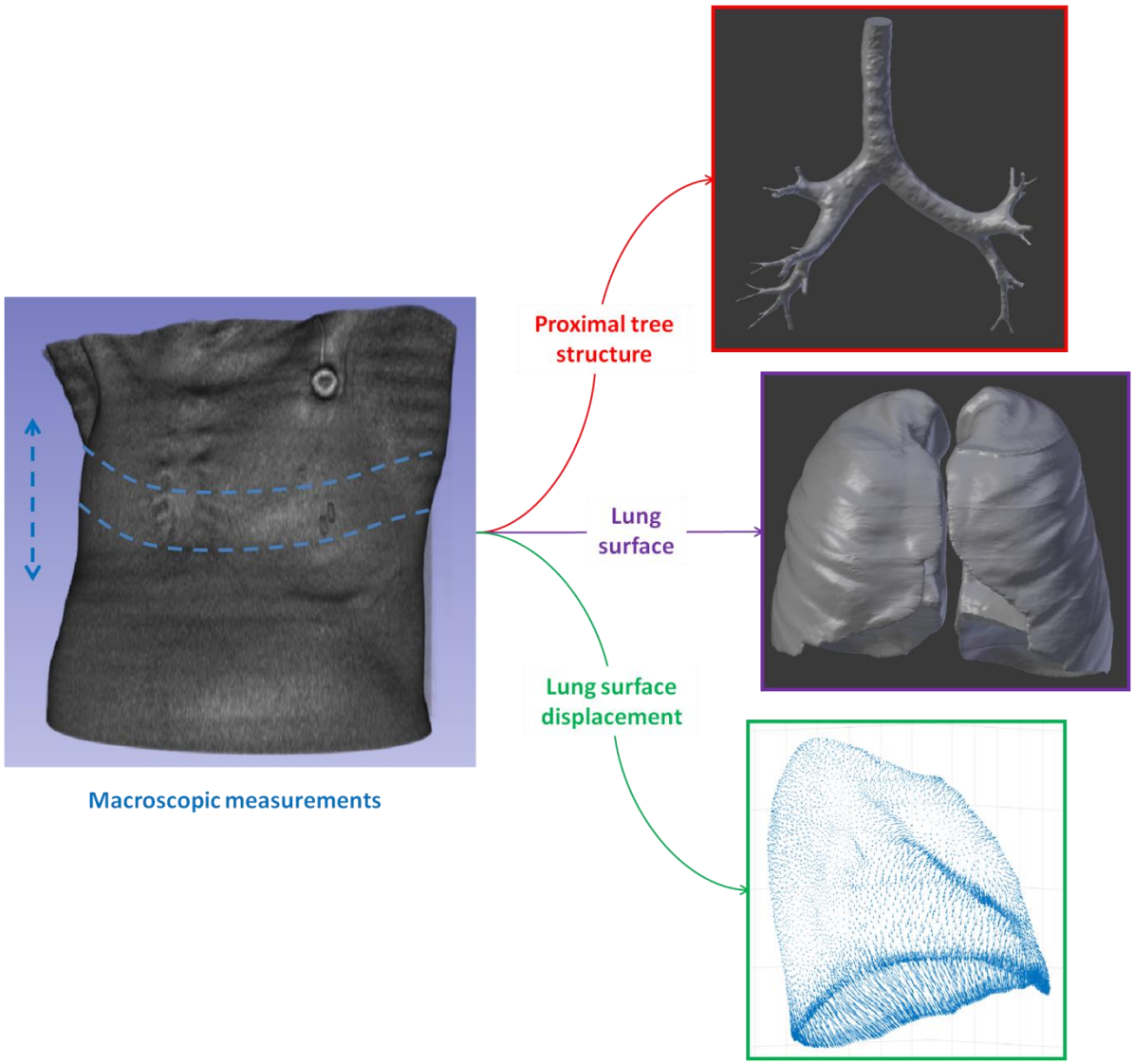

Figure 101: From outer body characteristics such as thoracic cage height and perimeters at different locations, we aim at determining the tree proximal structure as well as the lung surface. From respiratory surrogates, some other studies have worked on parenchyma displacement [148], [149], [150].

25.2. Methods and results

In this study we assume the lung shape of the patient is known, and we aim to predict the positions of proximal airways bifurcations. To do so we need to correlate representative features of the lung shape with nodes positions (see Figure 102), from which branches lengths can be deduced. To get usable input data for the ventilation model, we would need to predict airway radius which is not done here. From the upper airways structure along with lung envelope, the space-filling tree (see subsection 10.1) can then be built.

We use a machine learning technique to predict the bifurcation positions from the lung shape. First, working on a database of lung shapes and related tree nodes positions, a mapping model is built. This is the learning phase. It is then validated on couples [lung shape features; nodes position] that were not incorporated in the learning phase. We use a database of 23 segmented shapes and related proximal tree structures from which nodes positions are extracted. Those data are segmented from HRCT scans at MLV [**91**]. In the following, we work on left lungs only. The database contains adult lungs of both men and women of various ages, size and weight.

A shape can be defined as a set of points belonging to its surface (see Figure 103). The higher the point set resolution, the better the surface description. Each shape i is described by N points $P_1^i, P_2^i, \dots, P_N^i$. Let S_i be the vector defined by

$$S_i = \begin{pmatrix} P_{1_x}^i \\ P_{1_y}^i \\ P_{1_z}^i \\ \vdots \\ P_{N_z}^i \end{pmatrix}.$$

Where $(P_{k_x}^i, P_{k_y}^i, P_{k_z}^i)$ are the $3D$ coordinates of point P_k^i. Vector S_i has size $3N$, which increases linearly with the number of points. Vector S_i will be referred to as *shape* or *shape vector*. To reduce the shape description dimensionality, we perform a Principal Component Analysis (PCA). For PCA to be applicable, elements of shape vectors have to correspond to one another i.e. $\forall i, \forall j \in [\![1; n_{db}]\!]$ and $\forall k \in [\![1; N]\!]$, P_k^i and P_k^j need to have comparable physiological positions on lungs i and j (see Figure 104), n_{db} being the number of shapes in the database. To do so, each shape is first discretized with the same number of points N. At this stage, there is no point correspondence between each vector. A shape S_r of the database is chosen as reference, and for each $S_{i,i\neq r}$, a transformation map T_{ir} is computed through a non-linear registration so as to minimize $\left|\left|T_{ir}(S_i) - S_r\right|\right|$ according to a metric defined in [**96**]. The number of points N has to be sufficiently high to properly describe local shapes variations, and small enough for the registration process to be manageable.
In practice, segmented images from HRCT scans are treated with Matlab (Natick, USA) in order to extract surface points. From there, Meshlab [**93**] is used to generate a fine surface mesh which is decimated to contain $N = 1502$ points, and smoothed (see Figure 105). Then all the shapes $S_{i,i\neq r}$ are rigidly registered to S_r with the iterative closest point algorithm [**151**]. Finally non-linear registration is performed with Deformetrica [**96**] (see Figure 104).

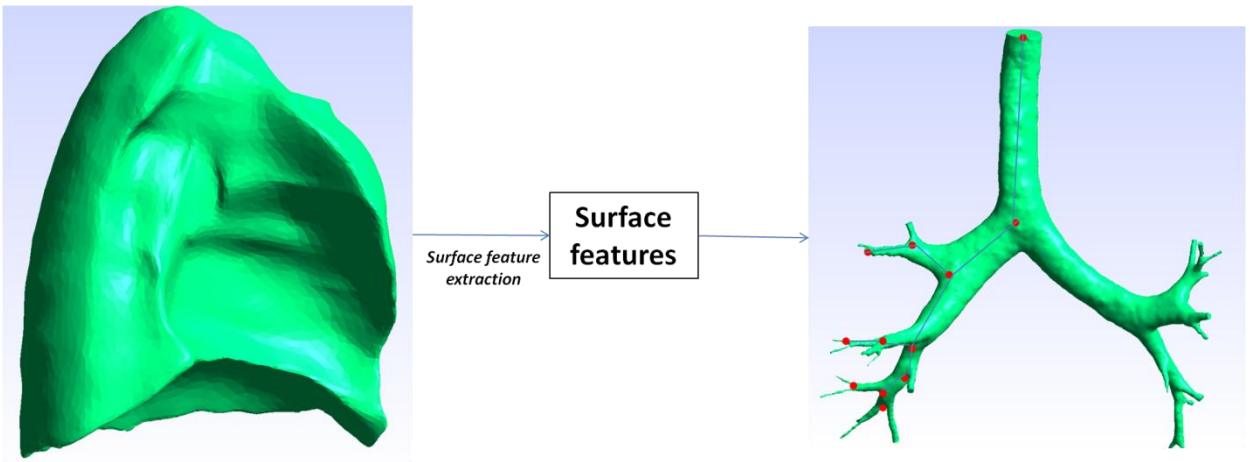

Figure 102 : from the lung shape (here left lung), surface features are extracted and used to predict the proximal nodes (red dots) of the tracheobronchial tree (here part of the tree irrigating the left lung).

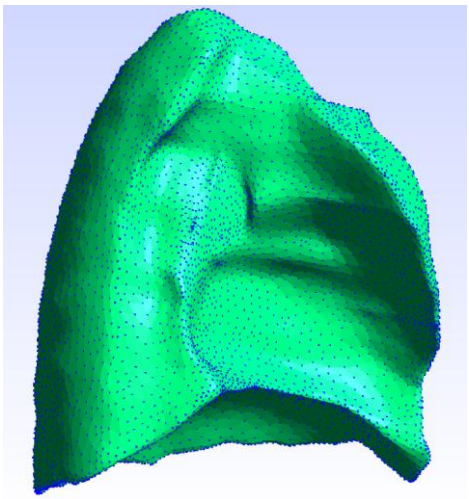

Figure 103: A shape can be described as a set of points belonging to its surface (blue dots).

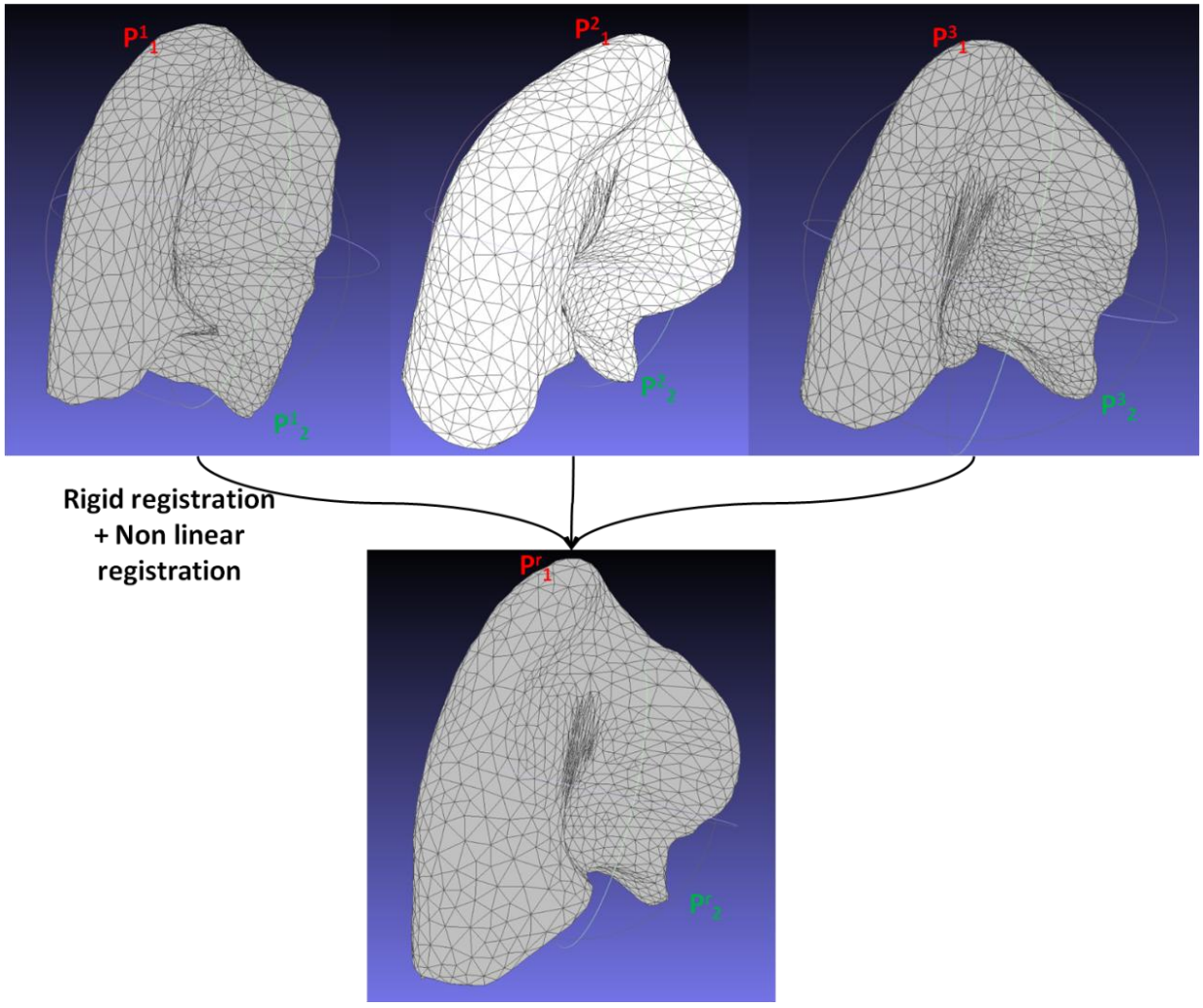

Figure 104: mapping of various lung shapes to a reference geometry through rigid and non linear registrations. Each point of a shape is associated to its physiologic correspondant on the reference geometry.

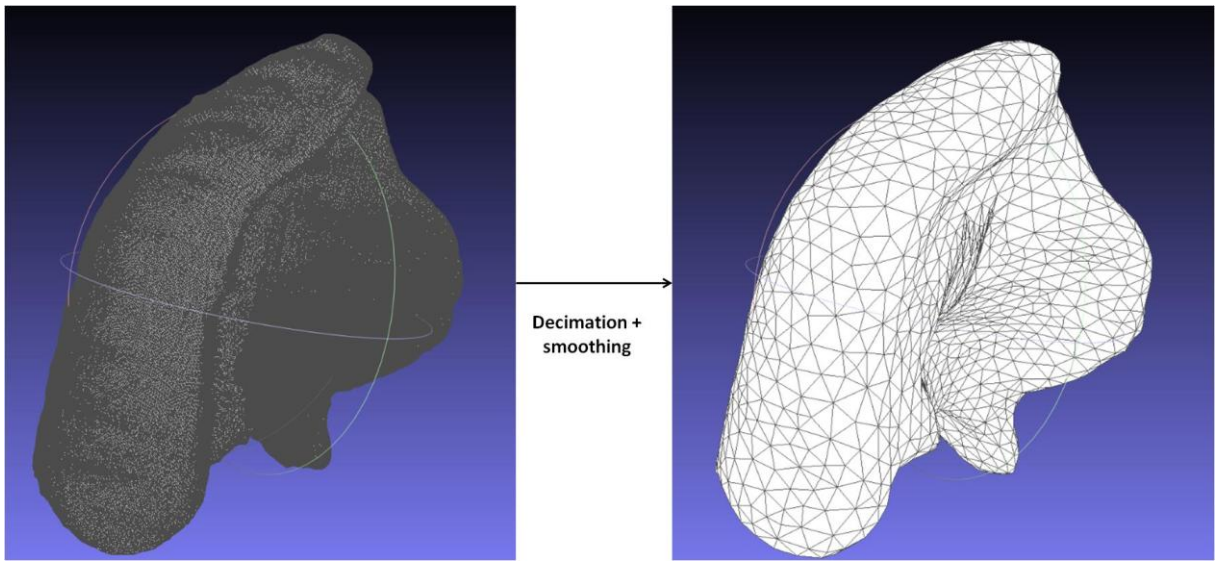

Figure 105: from a fine description of the shape, decimation and smoothing process are performed.

Let us denote $S = [S_1, S_2, \dots, S_{n_{db}}]$ the matrix of size $3N * n_{db}$ and $\forall j \in [\![1; n_{db}]\!]$ where for all shapes, points have been ordered to match the reference configuration. Let S^j be the matrix obtained from S by removing its j^{th}column. We denote $\tilde{S}^j = [S_1 - \widetilde{S_j}, S_2 - \widetilde{S_j}, \dots, S_{j-1} - \widetilde{S_j}, S_{j+1} - \widetilde{S_j}, \dots, S_{n_{db}} - \widetilde{S_j}]$ where $\widetilde{S_j} = \frac{1}{n_{db}-1}\sum_{k\neq j}^{n_{db}} S_k$. The orthonormal eigen vectors $\{V_1^j, \dots, V_{n_{db}-1}^j\}$ of $\tilde{S}^j \, \tilde{S}^{j^T}$ are called principal components, they are sorted in descending order based on their associated eigen values. We denote $\mathcal{P}_h^j$ the vector space generated by $\{V_1^j, \dots, V_h^j\}$, the h first principal components, i.e. those associated to the h highest eigen values, with $h < n_{db} - 1$. We denote $p_h(S_j)$ the projection of S_j on $\mathcal{P}_h^j$.

In Figure 106 we plot, for a given j, $p_h(S_j)$ for various h. The projection on the first component already gives a visually satisfying result. The more the components, the smaller $\left|\left|p_h(S_j) - S_j\right|\right|$. In Figure 107, v_h defined by (57) is plotted: the percentage of the variance in shape explained as a function of the number h of components taken into account. It is given by:

$$v_h = \frac{\sum_{k=1}^{h} \lambda_k}{\sum_{k=1}^{n_{nb}} \lambda_k}. \tag{57}$$

The first component accounts for 60% of the variance, the first ten more than 90%. In Figure 108 are plotted the projection of various shapes k on $\mathcal{P}_{n_{nb}-1}^k$. Any shape of the database can be determined by the information contained in the other ones. Thus, instead of describing a shape k as a set of points belonging to its surface, we characterize it by the coordinates of $p_{n_{nb}-1}(S_k)$ in $\mathcal{P}_{n_{nb}-1}^k$. From $3N = 4506$, the dimensionality of the shape description drops to a dozen.

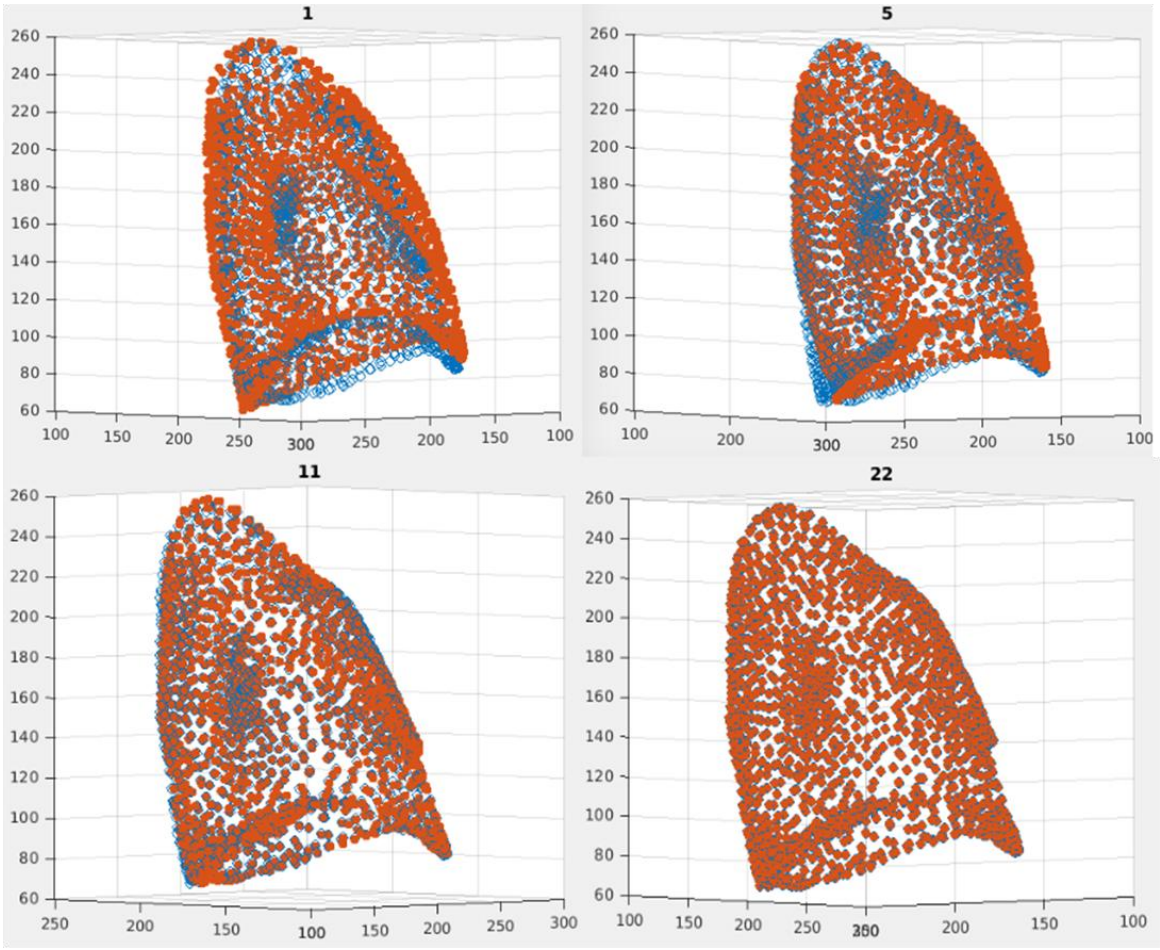

Figure 106: projection of a lung vector shape *j*, blue dots, on the first PCA principal components, orange dots. The PCA basis is built by considering every shape except *j*. The title number indicates the number of principal components considered for the projection. Scale in mm.

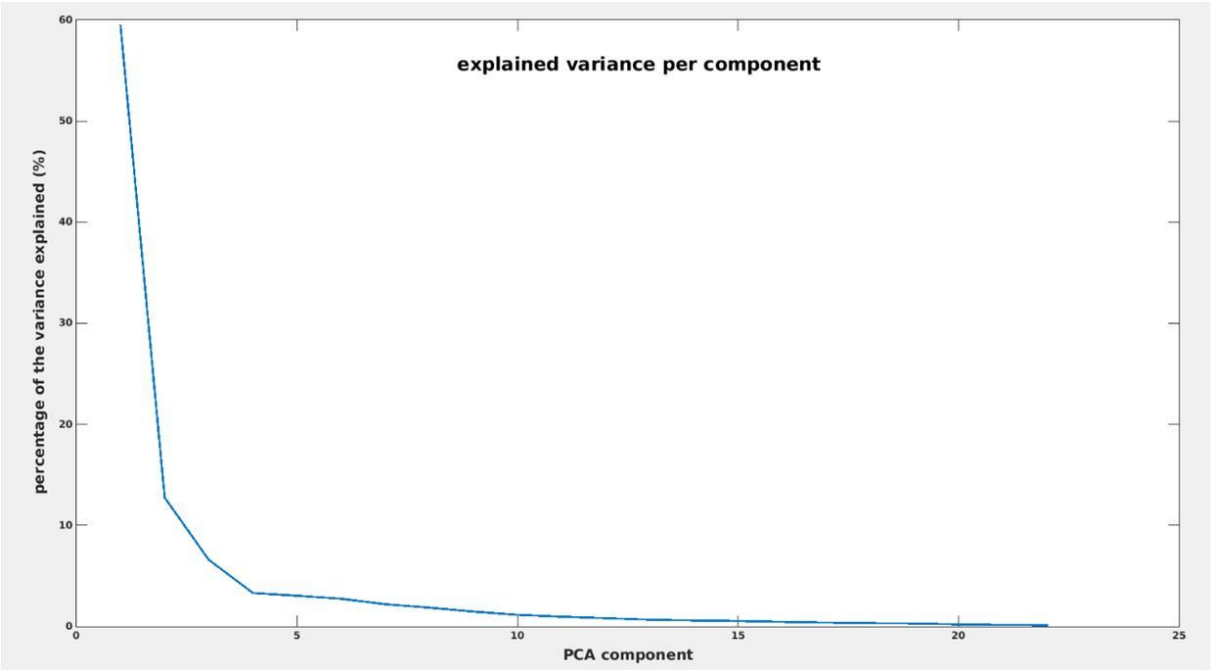

Figure 107: percentage of the variance accounted for as a function of the number of principal components considered (57). The PCA basis is built on a 22 lung shapes database. The first component carries a large amount of the information and the first ten ones account for more than 90% of the variance.

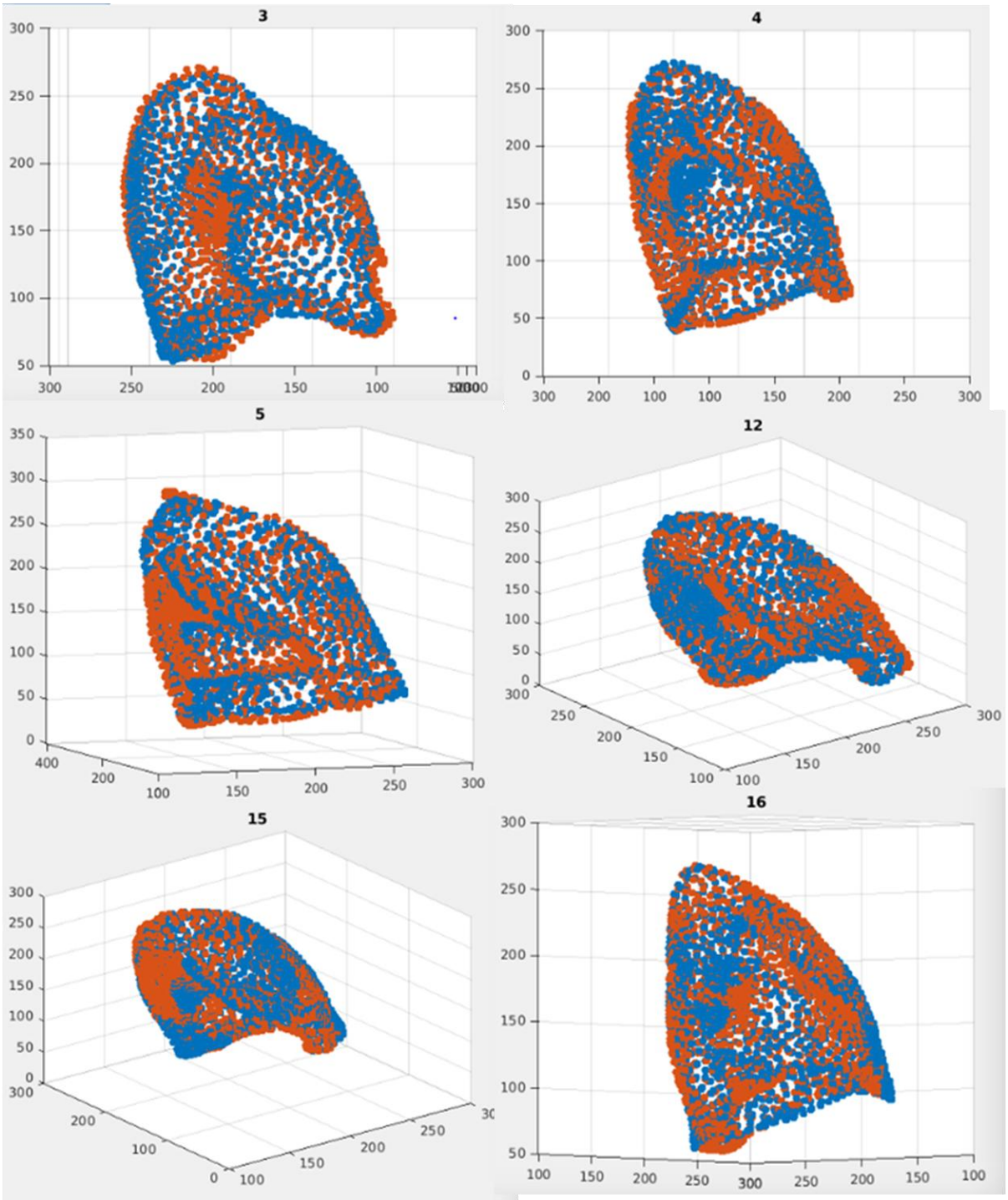

Figure 108: Comparison of the actual lung *j* shape (blue dots) and its projection (orange dots) on the principal components of the PCA basis built on every shapes except *j*. The number title refers to which lung of the data base is considered. Scale in mm.

Now that shape dimension is reduced, we proceed to the machine learning step. Our aim is to map the coordinates in the shape PCA basis with the tree nodes coordinates. To do so, a consistent database description of the nodes coordinates is required. Available segmented trees from HRCT scans have various depths, only common nodes can be used so to get enough of them, trees with too few nodes are removed from the database. The final database contains 21 lungs with proximal trees of 17 nodes (i.e. 51 unknowns to get their positions). To map the PCA coordinates with nodes positions, we use and compare two machine learning techniques: Neural networks (NN) and Support Vector Regression (SVR). For NN we use Keras library [**152**] running on top of Theano [**153**]. The

network has a single layer. A parametric study was performed to determine the optimal number of hidden units which is set to 150. Activation functions are chosen to be sigmoids. For SVR we use scikit-learn [**127**] (NuSVR function), and default parameters are used. In both cases a leave-one-out cross validation is applied, i.e. the learning phase is performed on 20 lungs. Computations are cheap, a few seconds per lung for neural networks and much less for SVR.

Both methods lead to comparable encouraging results, though errors are not negligible compared to the lung size. In average there is a 1.32 cm shift for neural network and 1 cm shift for SVR but with some variability (see Figure 110 and Figure 109). Figure 111 shows a simulated set of tree nodes compared to one obtained from segmentation. These are promising results: they show that there exists a correlation between the lung shape and the proximal tree structure. Though, errors can be significant compared to the lung dimensions.

	Lung1	Lung2	Lung3	Lung4	Lung5	Lung6	Lung7	Lung8	Lung9	Lung10	Lung11	Lung12	Lung13	Lung14	Lung15	Lung16
Nodes1	0.91	1.27	1.25	1.22	1.75	0.93	1.37	0.81	1.30	0.69	0.76	1.02	1.60	1.06	0.95	0.39
Nodes2	0.72	0.78	1.30	1.63	1.46	1.36	1.15	0.65	1.20	1.24	1.34	2.56	0.94	1.49	1.41	1.58
Nodes3	1.26	1.70	1.11	1.08	1.59	0.79	1.23	0.56	1.02	0.46	0.96	1.85	2.35	0.82	1.36	0.94
Nodes4	0.44	2.02	1.75	0.81	1.08	1.04	0.74	1.28	0.82	0.94	0.28	1.22	0.99	1.40	0.45	1.27
Nodes5	1.72	0.98	1.10	0.99	0.75	0.79	0.48	0.90	0.85	0.96	1.04	1.29	1.60	1.90	1.45	1.59
Nodes6	1.58	0.75	1.22	2.88	1.47	1.66	0.48	0.34	1.15	0.62	1.45	1.23	0.25	2.14	1.61	0.93
Nodes7	1.37	0.33	1.60	1.20	0.91	2.59	1.04	0.94	0.68	1.21	1.19	0.74	0.59	0.38	0.42	0.97
Nodes8	0.50	0.79	2.91	0.39	0.80	3.01	1.06	0.75	0.74	0.78	1.31	0.99	2.62	0.05	1.70	2.50
Nodes9	0.26	1.76	1.15	2.15	0.52	3.05	1.50	1.63	1.33	1.55	1.98	1.50	0.44	1.42	1.28	1.30
Nodes10	1.19	1.79	1.21	1.87	1.24	3.21	1.64	1.71	1.06	0.49	2.03	0.33	0.56	1.12	1.36	0.87
Nodes11	0.98	0.69	0.86	2.27	1.28	3.11	0.60	0.60	0.56	0.72	1.22	1.40	0.41	1.30	1.99	0.40
Nodes12	1.25	0.55	1.57	2.20	0.98	2.52	0.95	0.25	1.90	1.08	0.53	1.82	3.73	0.88	1.88	0.97
Nodes13	1.11	1.03	2.53	0.69	2.00	1.30	1.32	1.53	2.39	0.72	0.71	1.18	3.18	0.76	2.86	0.48
Nodes14	0.80	0.83	1.43	0.47	1.42	1.40	1.17	0.60	2.42	0.88	0.58	0.99	3.35	1.09	2.34	0.31
Nodes15	1.42	1.49	1.18	0.93	0.80	1.10	1.49	1.09	1.09	1.06	1.15	1.45	1.48	1.72	2.06	0.36
Nodes16	1.20	1.13	1.68	1.15	0.93	0.68	2.34	0.67	1.99	0.45	1.10	1.72	2.56	1.64	0.60	0.45
Nodes17	0.98	1.90	0.91	1.41	1.24	1.27	2.01	1.36	0.48	0.67	0.76	0.72	2.69	1.81	1.58	0.53

Figure 109: distances in cm between the real nodes positions and the predicted ones with NN. Each column represents the nodes of a given lung. Results shown for 16 lungs of the data base. Colors are correlated to the prediction error, in green lowest errors, on red highest errors.

	Lung1	Lung2	Lung3	Lung4	Lung5	Lung6	Lung7	Lung8	Lung9	Lung10	Lung11	Lung12	Lung13	Lung14	Lung15	Lung16
Nodes1	1.16	0.61	0.52	0.83	0.20	0.29	1.22	0.43	1.01	0.25	0.49	0.54	0.65	1.45	0.31	0.44
Nodes2	0.89	0.38	1.11	0.40	0.35	0.43	1.63	0.57	0.82	0.54	0.31	1.16	0.65	0.67	0.57	1.44
Nodes3	0.87	0.90	0.86	0.46	0.22	0.24	1.10	0.31	0.54	0.40	0.36	0.51	0.69	0.90	0.35	0.28
Nodes4	0.38	1.01	1.01	0.61	0.46	0.46	0.88	0.86	0.41	0.45	0.51	0.91	0.46	0.67	0.38	0.49
Nodes5	0.22	0.34	1.06	0.44	0.87	0.26	0.51	0.59	0.84	0.14	0.19	0.54	0.22	0.93	0.40	0.22
Nodes6	0.91	0.76	1.15	0.85	1.62	0.84	2.38	0.42	1.02	0.44	0.83	0.61	0.14	0.70	0.14	0.24
Nodes7	0.69	0.95	1.19	1.62	2.24	1.14	2.93	0.15	0.67	0.17	0.64	0.57	1.09	0.84	0.44	0.26
Nodes8	0.27	1.66	1.69	1.20	2.03	1.62	2.73	0.36	0.90	0.36	0.64	1.00	2.16	0.77	0.87	1.00
Nodes9	0.32	1.90	0.95	1.53	2.27	1.54	3.51	0.21	0.36	1.24	1.14	0.91	0.55	1.30	0.91	0.42
Nodes10	0.69	1.94	1.19	1.85	2.31	1.50	3.41	0.38	0.85	0.81	0.88	0.55	0.40	0.99	0.49	0.61
Nodes11	1.19	1.37	1.26	1.96	2.92	1.65	3.00	0.09	0.43	0.34	0.31	1.00	0.76	0.54	0.65	1.36
Nodes12	2.43	1.04	0.67	2.04	2.33	1.40	1.48	0.53	1.27	0.54	0.52	1.36	1.09	0.74	1.52	0.98
Nodes13	2.43	1.07	0.37	0.63	1.86	0.69	1.02	0.49	1.73	0.80	0.57	0.89	0.58	0.39	2.44	0.99
Nodes14	2.30	1.10	0.60	0.50	1.75	0.49	0.39	0.52	1.54	0.87	0.66	0.89	0.72	0.18	2.54	1.06
Nodes15	1.38	0.90	0.27	0.56	0.88	0.36	0.93	0.71	0.42	0.48	1.15	0.77	0.54	0.55	2.45	0.53
Nodes16	1.41	0.71	0.23	0.75	0.77	0.44	1.99	0.84	0.43	0.73	0.97	0.45	0.49	0.13	2.24	0.16
Nodes17	1.29	1.29	0.39	1.94	0.49	0.35	0.96	0.36	0.62	0.56	0.72	0.57	0.19	0.23	1.77	0.51

Figure 110: distances in cm between the real nodes positions and the predicted ones with SVR. Each column represents the nodes of a given lung. Results shown for 16 lungs of the data base. Colors are correlated to the prediction error, in green lowest errors, on red highest errors.

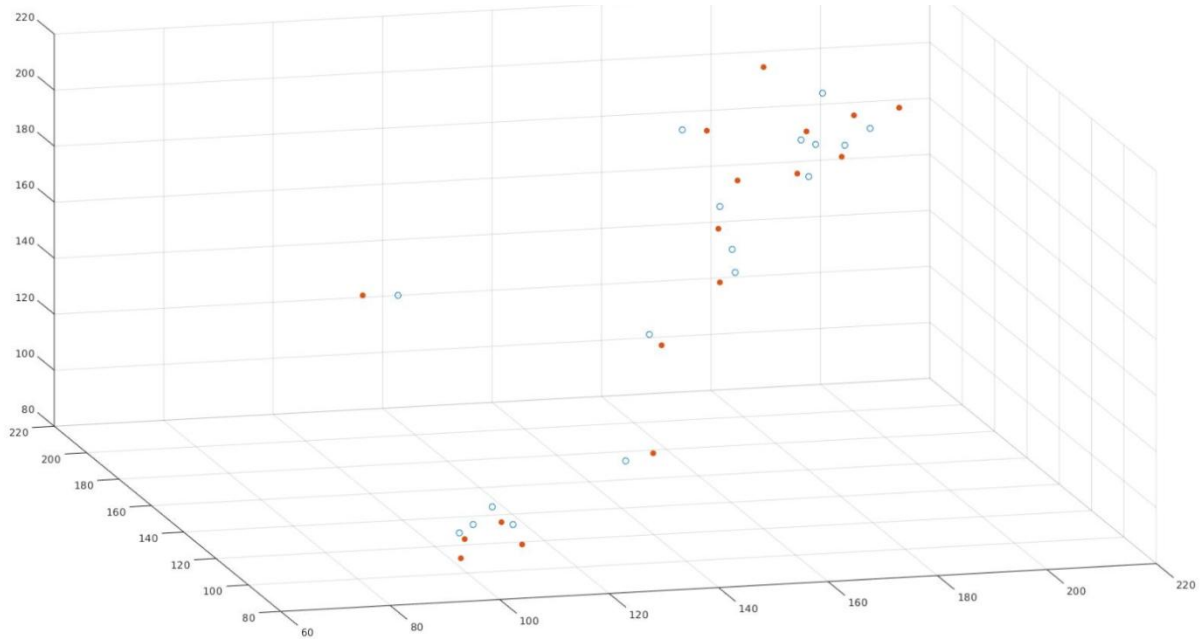

Figure 111: for a lung of the data base, tree nodes positions predicted with SVR (empty blue dots) and actual positions (filled orange dots). Scale in mm.

In this study, shape dimensionality reduction was successfully achieved through a PCA analysis. Here any shape can be explained based on the information provided by other shapes of the data base which contains lungs from both men and women with various ages, sizes and weights. A specific database may have to be used for children. Taking PCA coordinates as input shape features, machine learning techniques enable to predict tree nodes positions with encouraging precision although there can be significant errors. To improve these results, one could enrich the process by adding some physiological information such as a statistical distribution for airway lengths and bifurcation angles. Also, predicting the tree centerline instead of a few nodes positions could generate more accurate results since it is more representative of the tree structure and because nodes positions are not easily determined from segmented airways.
Next steps would include a model to correlate outer body characteristics and lung shape described by PCA features

26. Experimental validation of the tree-parenchyma coupled model

Future work should include an experimental validation of the tree-parenchyma coupled model (see subsection 8.2). Model validation requires a description of upper airways tree structures and the dynamic displacement field of the parenchyma along the breathing cycle. They could respectively be acquired by HRCT scan [**23**], and 4D-CT [**31**] or 4D-MRI [**32**]. These measurements on rats are currently being led at IR4M group in the frame of ANR OxHealease. To have a better fit with experimental data, a non-linear elastic law may have to be used, as done in [**41**] or [**75**]. Mechanical properties might be inferred from non invasive in-vivo measurements with magnetic resonance elastography [**125**]. In elastography, shear waves are generated in the parenchyma and induced local displacements are acquired from MRI images. Based on an *a priori* mechanical model, an inverse problem [**154**] is solved to determine local mechanical properties. Those parameters are determined for a given excitation frequency, typically between 20 Hz and 20 kHz [**155**]. An open question related to the use of elastography in this context is that in case the tissue is dispersive, which happens at high frequencies, the material response depends on the signal pulsation. Whether mechanical

coefficients inferred from the inverse problem can be used to model breathing, which is a much lower frequency phenomenon, is not guaranteed.

The plug identification process presented in CHAPTER IV could also be tested on real data. For instance, knowing the proximal tree topology from a HRCT scan, the mechanical properties from elastography and dynamic ventilation maps from 4D-CT or 4D-MRI, one could check whether constrictions in upper segmented branches are properly identified.

To have a better control on the experimental setting, the measurement could be led on a phantom, as done in [**155**]. Artificial stenoses with controlled geometries could be imposed.

Conclusion

This thesis dealt with lung ventilation modeling. In chapter II, a model in which the tree and parenchyma are strongly coupled was presented. The coupling was performed based on gas incompressibility and obtained from the least-action principle. The action of the tree on the parenchyma constitutive relation is similar to a viscous term. The greater the pressure drops within the tree, the harder it is to induce parenchyma volume variations. In the finite element framework, this term led to a full matrix. A physical interpretation is that the tree couples all the degrees of freedom of the system. Taking advantage of the tree structure, an efficient numerical strategy was developed to avoid storing high memory demanding objects and the system was solved iteratively. We worked on a patient-specific geometry segmented from HRCT scans. A surface displacement registered from images was applied as a boundary condition and ventilation results were compared with those obtained when applying a classic homogeneous pressure as often used in the literature; significant differences were obtained. Moreover, some diseases such as asthma can affect the tree structure. A typical pathological pattern is airway constriction. The effect of bronchoconstrictions on ventilation distribution was studied. Results from this model were also compared to those obtained with an exit-compartment description. It showed that mechanical interactions between parenchyma regions need to be taken into account when ventilation is heterogeneous, as it is the case in some pathological situations.

In chapter III, the tree-parenchyma coupled model was used to study the effect of asthma on ventilation distribution and breathing effort. Based on a literature review on tracheo-bronchial tree imaging and histological studies, stochastic laws for the distribution of bronchoconstrictions were developed and used to generate “asthmatic” trees. The effect of breathing a low density gas mixture of helium and oxygen instead of air was investigated. Clinical studies on Heliox do not provide consensual results. In this study, we proposed lines of thoughts on why some asthmatic patients respond to Heliox mixtures while others do not. Both the pathology severity, its spatial distribution within the lung and the distality of affected airways influence responsiveness.

As demonstrated in chapter III, constrictions alter the ventilation distribution. Some dynamical imaging techniques such as 4D-CT or 4D-MRI provide maps of the ventilation and its evolution along the breathing cycle. In chapter IV, we investigated how information on ventilation can be used to assess the plug distribution within the tree. Tree exit pressures were obtained as the result of a minimization problem using the tree-parenchyma coupled model. From the knowledge on flow distribution, deduced from images, and computed pressures, a linear system with airway resistances as unknowns is obtained. For this plug identification problem to be well-posed the number of unknowns had to be reduced. To that end a machine learning technique was applied, then plugs classification was achieved thanks to a specific algorithm. Encouraging results were obtained.

As perspectives, two more studies were presented in chapter V. First, to model spirometry tests, some extensions to both the exit-compartment and tree-parenchyma coupled descriptions were proposed. For the former, a non-linear compliance model adapted from the literature was developed so as to bound the volume evolution in physiological ranges. For the tree-parenchyma coupled model, Neumann boundary conditions generated to fit the evolution induced by surface-displacement boundary conditions were obtained and used to simulate spirometry in pathological situations. However, the underlying physics of forced expiration is complex and models used in this thesis do not account for it. Finally, in a last section, we presented a model to determine the tracheo-bronchial tree nodes positions based on a known lung surface. This development is part of a lung statistical description that would provide information on the lung structure based on easy

measurements on the outer body. To do so, dimensionality reduction along with a machine learning technique were used leading to encouraging results.
Many more developments could be performed. The tree-parenchyma model suffers from various limitations: in particular linear elasticity may be a rough approximation of the lung constitutive relation, as the airway rigid wall assumption made in this thesis. Model validation through comparison to experiments would be a necessary step.

List of Figures:

References

[1] JHT Bates, "Lung Mechanics," 2009.

[2] C Vannier, "Modélisation mathématique du poumon humain," PhD thesis Hal Id: tel-00739462, 2012.

[3] B Maury, *The Respiratory System in Equations*.: Springer, 2013, vol. 7.

[4] PF Villard, "Simulation du Mouvement Pulmonaire pour un Traitement Oncologique," Thèse de doctorat tel-00858260, 2006.

[5] AR Weibel, *Morphometry of the human lung*.: Springer, 1963.

[6] ER Weibel, *The pathway for oxygen: structure and function in the mammalian respiratory system*, Harvard universty press, Ed. Cambridge, 1984.

[7] C Kleinstreuer and Z Zhang, "Airflow and particle transport in the human respiratory system," *Annual review of fluid mechanics*, no. 301-334, 2010.

[8] RG Crystal, JB West, ER Weibel, and PJ Barnes, *The lung: scientific foundations*.: Lippinott-Raven press, 1997.

[9] JL Black and PR Johnson, "Airway smooth muscle in asthma," *Respirology*, no. 1(3):153-8, 1996.

[10] CM Evans, K Kim, MJ Tuvim, and BF Dickey, "Mucus hypersecretion in asthma: causes and effects," *Curr Opin Pulm Med*, no. 15(1):4-11, 2010.

[11] C Bergeron, MK Tulic, and Q Hamid, "Airway remodelling in asthma: from benchside to clinical practise," *Can respir J*, no. 17(4):e85-e93, 2010.

[12] T Vos and et al, "Global, regional, and national incidence, prevalence, and years lived with disability for 310 diseases and injuries, 1990-2015: a systematic analysis for the Global Burden of Disease Study 2015," *Lancet*, no. 388(10053):1545-1602, 2016.

[13] WM Thrlbeck and NL Müller, "Emphysema: definition, imaging and quantification," *AJR Am J Roentgenol*, no. 163(5):1017-25, 1994.

[14] H et al. Wang, "Global, regionaln and national life expectancy, all-cause mortality, and cause-specific mortality for 249 causes of death, 1980-2015: a systematic analysis for the Global Burden of Disease Study 2015," *Lancet*, no. 388(10053):1459-1544, 2016.

[15] IM Katz et al., "The ventilation distribution of helium-oxygen mixtures and the role of inertial losses in the presence of heterogeneous airway obstructions," *J Biomech*, no. 44(6):1137-43, 2011.

[16] T Jalusic-Gluncic, "What happens with airway resistance (RAW) in asthma and COPD exacerbation," *Med arh*, no. 65(5):270-3, 2011.

[17] TJ Pedley, RC Schroter, and MF Sudlow, "Energy losses and pressure drops in models of human airways," *Respir Physiol*, no. 9(3):371-86, 1970.

[18] JB West, *Respiratory physiology*, ninth ed., Lippincott Williams & Wilkins, Ed. Baltimore, 2012.

[19] D Papandrinopoulou, V Tzouda, and G Tsoukalas, "Lung compliance and chronic obstructive pulmonary disease," *Pulm med*, no. 2012:542769, 2012.

[20] A Cavazza et al., "The role of histology in idiopathic pulmonary fibrosis: an update," *Respir med*, no. 2010 Jul;104 Suppl 1:S11-22, 2010.

[21] H Shikata, G McLennan, EA Hoffman, and M Sonka, "Segmentation of pulmonary vascular trees from thoracic 3D CT images," *Int J biomed imaging*, no. 2009:636240, 2009.

[22] S Montesantos et al., "Airway morphology from high resolution computed tomography in healthy subjects and patients with moderate persistent asthma," *The anatomical record*, no. 296:852-866, 2013.

[23] P Grenier, C Fetita, and PY Brillet, "Quantitative computed tomography imaging of airway remodelling in severe asthma," *Quant Imaging Med Surg*, no. 6(1):76-83, 2016.

[24] R Kakinuma, "Ultra-high-resolution computed tomography of the lung: image quality of a prototype scanner," *PLoS One*, no. 10(9):e0137165, 2015.

[25] MS Dunnill, "The pathology of asthma, with special reference to changes in the bronchial mucosa," *J Clin Pathol*, no. 13(1): 27-33, 1960.

[26] T Aikawa, S Shimura, H Sasaki, M Ebina, and T Takishima, "Marked goblet cell hyperplasia with mucus accumulation in the airways of patients who died of severe acute asthma attack," *Chest*, no. 101(4):916-21, 1992.

[27] MA.Farrell Epstein and JR.Ligas, *Respiratory biomechanics*.: Springer-Verlag, 1990.

[28] Y Yin, J Choi, EA Hoffman, MH Tawhai, and CL Lin, "A multiscale MDCT image-based breathing lung model with time-varying regional ventilation," *J Comput Phys*, no. 244:168-192, 2013.

[29] N Jahani, Y Yin, EA Hoffman, and CL Lin, "Assessment of regional non-linear tissue deformation and air volume change of human lungs via image registration," *J Biomech*, no. 47(7):1626-33, 2014.

[30] JE Roos, HP McAdams, SS Kaushik, and B Driehuys, "Hyperpolarized gas MRI: technique and applications," *Mag reson imaging clin N am*, no. 23(2):217-229, 2016.

[31] N Jahani et al., "Comparison of regional ventilation and lug deformation for asthmatic vs. healthy human lungs using 4d-CT image data," *J Appl Physiol*, no. 15;119(10):1064-74, 2016.

[32] C Kolb et al., "Regional lung ventilation analysis using temporally resolved magnetic resonance imaging," *J Comput Assist Tomogr*, no. 40(6):899-906, 2016.

[33] J Biederer et al., "MRI of the lung (2/3). Why. when. how?," *Insights Imaging*, no. 3(4):355-71, 2012.

[34] V Boldea, GC Sharp, SB Jiang, and D Sarrut, "4D-CT lung motion estimation with deformable registration: quantification of motion nonlinearity and hysterisis," *Med Phys*, no. 35(3):1008-18, 2008.

[35] A Hilsmann et al., "Deformable 4DCT lung registration with vessel bifurcations," *International journal of computer assisted radiology and surgery*, no. 39015418, 2007.

[36] J Vandemeulebroucke et al., "Automated segmentation of a motion mask to preserve sliding motion in deformable registration of thoracic CT," *Med Phys*, no. 39(2):1006-15, 2012.

[37] J Vandemeulebroucke, S Rit, J Kybic, P Clarysse, and D Sarrut, "Spatiotemporal motion estimation for respiratory-correlated imaging of the lungs," *Med Phys*, no. 38(1):166-178, 2011.

[38] (2013, July) GP-training.net. [Online]. http://www.gp-training.net/protocol/respiratory/copd/spirometry.htm

[39] D Leary et al., "Hyperpolarized He3 magnetic resonance imaging ventilation defects in asthma: relationship to airway mechanics," no. 2016 Apr;4(7), 2016.

[40] J, Parameswaran, H Lui, M Albert, and K Lutchen, "Linking ventilation heterogeneity quatified via hyperpolarized He3 MRI to dynamic lung mechanics and airway hyperresponsiveness," *PLos One*, no. 16;10(11):e0142738, 2015.

[41] L Berger et al., "A poroelastic model coupled to a fluid network with applications in lung modelling," *Int J Numer Method Biomed Eng*, vol. 32(1):e02731, 2015.

[42] B Sul, A Wallqvist, MJ Morris, J Reifman, and V Rakesh, "A computational study of the respiratory airflow characteristics in normal and obstructed airways," *Comput Biol Med*, no. 52:130-43, 2014.

[43] N Pozin et al., "Calculated ventilation and effort distriubtion as a measure of respiratory disease and Heliox effectiveness (accepted)," *JBiomech*, 2017.

[44] AA Rostami, "Computational modeling of aerosol deposition in respiratory tract: a review," *Inhal Toxicol*, no. 21(4):262-90, 2009.

[45] J Oakes, A Marsden, C Grandmont, C Darquenne, and I Vignon-Clementel, "Distribution of aerosolized particles in healthy and emphysematous rat lungs: Comparison between

experimental and numerical studies," *Journal of biomechanics*, vol. 48(6):1147–1157, 2015.

[46] OS Usmani, MF Biddiscombe, and PJ Barnes, "Regional lung deposition and bronchodilator response as a function of beta2-agonist particle size," *Am J respir crit care med*, no. 15;172(12):1497-504, 2005.

[47] L Augusto, G Lopes, and J Gonçalves, "A CFD study of deposition of pharmaceucal aerosols under different respiratory conditions," vol. 33, no. 3, 2016.

[48] K Zhu, KJ Wang, and RBH Tan, "CFD study on aerosol depostion in human upper respiratory tract," in *AIChE Anual meeting*, 2004.

[49] G Rodrigo, C Pollack, C Rodrigo, and B Rowe, "Heliox for treatment of exacerbations of chronic obstructive pulmonary disease," *Cochrane Database Syst Rev*, no. 2002;(2):CD003571, 2002.

[50] RE Hyatt, JR Rodarte, TA Wilson, and RK Lambert, "Mechanisms of expiratory flow limitation," *Ann biomed eng*, no. 9(5-6):489-99, 1981.

[51] RK Lambert, "Epiratory flow from a non-homogeneous human lung model," in *Proceedings of the annual international conference of the IEEE*, 1988.

[52] AG Polak and KR Lutchen, "Computational model for forced expiration from asymmetric normal lungs," *Ann biomed eng*, no. 31(8):891-907, 2003.

[53] TB Bezzant and JD Mortensen, "Risks and hazards of mechanical ventilation: a collective reiew of published litterature," *Dis mon*, no. 40(11):581-638, 1994.

[54] M Klaas, E Koch, and W Schröder, *Fundamental medical and engineering investigations on protective artificial respiration*, Springer, Ed. Berlin, 2011.

[55] EJ Van Drunen et al., "Expiratory model-based method to monitor ARDS disease state," *Biomed eng online*, no. 2013;12-57, 2013.

[56] S Martin and B Maury, "Modeling of the oxygen transfer in the respiratory process," *ESAIM*, no. (2013):935-960, 2013.

[57] AJ Swan, AR Clark, and MH Tawhai, "A computational model of the topographic distribution of ventilation in healthy human lungs," *J Theor Biol*, vol. 300:222-31, 2012.

[58] M Ismail, A Comerford, and WA Wall, "Coupled and reduced dimensional modeling of respiratoy mechanics during spontaneous breathing," *Int. J. Numer. Meth. Biomed. Engng*, no. 29(2013):1285-1305, 2013.

[59] MH Tawhai, AJ Pullan, and PJ Hunter, "Generation of an anatomically based 3D model of the conducting airways.," *Ann Biomed Eng*, vol. 28(7):793-802, 2000.

[60] CJ Roth, M Ismail, L Yoshihara, and WA Wall, "A comprehensive computational human lung model incorporating inter-acinar dependencies: Application to spontaneous breathing and mechanical ventilation," *International Journal for Numerical Methods in Biomedical Engineering*, 2015.

[61] C VanErtbruggen, C Hirsh, and M Paiva, "Anatomically based three-dimensional model of airways to simulate flow and particle transport using computational fluid dynamics," *Journal of Applied Physiology*, vol. 98(3):970-980, 2005.

[62] AP Kuprat, S Kabilan, JP Carson, RA Corley, and DR Einstein, "A bidirectional coupling procedure applied to multiscale respiratory modeling," *J comput phys*, no. 10.1016/j.jcp.2012.10.021, 2014.

[63] JM Oakes, AL Marsden, C Grandmont, SC, Darquenne, C Shadden, and IE Vignon-Clementel, "Airflow and particle deposition simulations in healthy and emphysema: from in vivo to in silico animal experiments," *Ann Biomed Eng*, no. 42(4):899-914, 2014.

[64] B Mauroy, "3D hydrodynamics in the upper human bronchial tre: interplay between the geometry and flow distribution," , vol. IV, Birkhauser Basel, 2005, pp. 43-53.

[65] I Katz et al., "The influence of lung volume during imaging on CFD within realistic airway models," *Aerosol science and technology*, no. 51:2,214-223, 2016.

[66] EE Greenblatt et al., "What causes uneven aerosol deposition in the bronchoconstricted lung? A quantitative imaging study," *J. aerosol Med. pulmonary drug del*, no. 29(3):260-272, 2015.

[67] CL Lin, MH Tawhai, G McLennan, and EA Hoffman, "Characteristics of the turbulent laryngeal jet and its effect on airflow in the human intra-thoracic airways," *Respir Physiol Neurobiol*, no. 1;157(2-3):295-309, 2007.

[68] Y Yin, EA Hoffman, and Lin CL, "Mass preserving nonrigid registration of CT lung images using cubic B-spline," *Med phys*, no. 36(9):4213-22, 2009.

[69] Y Yin, J Choi, EA Hoffman, MA Tawhai, and CL Lin, "Simulation of pulmonary air flow with subject-specific boundary condition," *J Biomech*, vol. 43(11):2159-2163, 2010.

[70] RE Jacob, JP Carson, M Thomas, and DR Einstein, "Dynamic multiscale boundary conditions for 4D CT of healthy and emphysematous rats," *PLoS ONE*, no. 8(6):e65874.

[71] M Malvè et al., "CFD analysis of the human airways under impendance-based boundary conditions: application to healthy, diseased and stented trachea," *Comput Methods Biomech Biomed Engin*, no. 16(2):198-216, 2013.

[72] C Grandmont, B Maury, and N Meunier, "A viscoelastic model with non-local damping application to the human lungs," *ESAIM*, no. hal-00265567, 2006.

[73] P Cazeaux and C Grandmont, "Homogenization of a multiscale viscoelastic model with nonlocal damping, application to the human lungs," *Mathematical Models and Methods in Applied Sciences*, vol. 25(06):1125–1177, 2012.

[74] N Pozin et al., "A tree-parenchyma coupled model for lung ventilation simulation," no. 10.1002/cnm.2873, 2017.

[75] L Yoshihara, CJ Roth, and WA Wall, "Fluid-structure interaction including volumetric coupling with homogenised subdomains for modeling respiratory mechanics," *Int J Numer Method Biomed Eng*, no. 10.1002/cnm.2812, 2016.

[76] AL Didier et al., "A chest wall model based on rib kinematics," *Proceedings of the 2009 Second International Conference in Visualisation*, no. 10.1109/VIZ.2009.45, pp. 159-164, 2009.

[77] J Saadé et al., "A preliminary study for a biomechanical model of the respiratory system," in *ECSMIO*, Angers, 2010, pp. 509-515.

[78] AL Dider, PF Villard, JY Bayle, M Beuve, and B Shariat, "Breathing thorax simulation based on pleura behaviour and ribs kinematics," in *Information visualization - MediVis*, Zurich, 2007, pp. 35-40.

[79] S Taheriann, H Rahai, BZ Gomez, T Waddington, and JR Bonifacio, "Tracheal stenosis: a CFD approach for evaluation of drug delivery.," in *ASME International Mechanical Engineering Congress and Exposition*, 2015.

[80] J Ehrhardt and C Lorenz, *4D modeling and estimation of respiratory motion for radiation therapy*.: Springer, 2013.

[81] J Cai, Z Chang, Z Wang, Paul, W Segars, and FF Yin, "Four-dimensional magnetic resonance imaging (4D-MRI) using image-based respiratory surrogate: a feasibility study.," *Med Phys*, no. 38(12):6384-94, 2011.

[82] I Katz et al., "Using helium-oxygen to improve regional deposition of inhaled particles: mechanical principles," *J Aerosol Med Pulm Drug Deliv*, no. 27(2):71-80, 2014.

[83] WG Teagu, NJ Tustison, and TA Altes, "Ventilation heterogeneity in asthma," *J Asthma*, no. 51(7):677-84, 2014.

[84] B Fuerst et al., "A personalized biomechanical model for respiratory motion prediction," *Med Image Comput Comput Assist Interv*, no. 15(03):566-573, 2012.

[85] MY Kang, J Hwang, and JW Lee, "Effect of geometric variations on pressure loss for a model bifurcation of the human lung airway," *J.Biomech*, no. 44(6):1196-9, 2011.

[86] B Maury, D Salort, and C Vannier, "Trace theorems for trees and applications to the human lungs," *NHM*, no. 10.3934/nhm.2009.4.xx, 2009.

[87] B Mauroy and N Meunier, "Optimal poiseuille flow in a finite elastic dyadic tree," *ESAIM*, no. (2008):507-533, 2008.

[88] G Allaire, "Homogenization and two-scale convergence.," *SIAM J. Math. Anal.*, no. 23(6):1482-1518, 1992.

[89] SL Lai-Fook, "Pleural mechanics and fluid exchange," *Physiol Rev*, no. 84(2):385-410, 2004.

[90] FELIScE: Finite Elements for LIfe SCiences and Engineering, https://gforge.inria.fr/projects/felisce/.

[91] EE Greenblatt et al., "Analysis of three-dimensional aerosol deposition in pharmacologically relevant terms: beyound black or white ROIs," *J Aerosol Med Pulm Drig Deliv*, no. 28(2):116-29, 2014.

[92] S Montesantos, I Katz, M Pichelin, and G Caillibote, "The creation and statistical evaluation of a deterministic model of the human bronchial tree from HRCT images," *PLOS one*, 2016.

[93] Meshlab - developped with the support of 3D-CoForm project - meshlab.sourceforge.net.

[94] G Taubin, "Curve and surface smoothing without shrinkage," , 1995, pp. 852-857.

[95] C Geuzaine and JF Remacle, "Gmsh: a three-dimensional finite element mesh generator with built-in pre- and post-processing," *Int. J. Numer. Meth. Engng*, vol. 79(11):1309-1331, 2009.

[96] S Durrleman et al., "Morphometry of anatomical shape complexes with dense deformations and sparse parameters," *NeuroImage*, vol. 101:35-49, 2014.

[97] M Vaillant and J Glaunès, "Surface Matching via Currents," *Lecture notes in computer science*, vol. 3565:381-392, 2005.

[98] EE Greenblatt, JP Butler, JG Venegas, and T Winkler, "Pendelluft in the bronchial tree," *J Appl Physiol*, no. 117(9):979-88, 2014.

[99] KT Martin, "Resistance and compliance," RC eductional consulting services,.

[100] RE Amelon, K Cao, JM Reinhardt, GE Christensen, and ML Raghavan, "A measure for characterizing sliding on lung boundaries," *Ann Biomed Eng*, no. 42(3):642-50, 2014.

[101] PF Villard, M Beuve, B Shariat, and V Baudet, "Lung mesh generation to simulate breathing motion with a finite element method," , 2004, Eight International Conference on Information Visualisation.

[102] M Kindig, Z Li, R Kent, and D Subit, "Effects of intercostal muscles and costovertebral joint material properties on human ribcage stiffness and kinematics," *Comput Methods Biomech Biomed Engin.*, no. 18(5):556-70, 2015.

[103] D Chappelle and P Moireau, "General coupling of porous flows and hyperelastic formulations - from thermodynamics principles to energy balance and compatible time schemes," *European Journal of Biomechanics*, no. 46(2014) 82-96, 2014.

[104] B Suki, D Stamenovic, and R Hubmayr, "Lung Parenchymal Mechanics," *Compr Physiol*, vol. 1(3):1317-1351, 2011.

[105] I Frerichs et al., "Gravity effects on regional lung ventilation determined by functional EIT during parabolic flights," *J appl physiol*, no. 91(1):39-50, 2001.

[106] I Galvin, GB Drummond, and M Nirmalan, "Distribution of blood flow and ventilation in the lung: gravity is not the only factor," *Br J anaesth*, no. 98(4):420-8, 2007.

[107] D Garcia, "A fast all-in-one method for automated post-processing of PIV data," *Exp Fluids*, vol. 50:1247-1259, 2011.

[108] D Garcia, "Robust smoothing of gridded data in one and higher dimensions with missing values," *Compute stat Data Anal.*, vol. 54(4):1167-1178, 2010.

[109] AL Barach, "The use of helium as a new therapeutic gas," *Anesth Analg*, no. 14:210-213, 1935.

[110] P Jolliet et al., "A multicenter randomized trial assessing the efficacy of helium/oxygen in severe exacerbations of chronic obstructive pulmonary disease," *Am J Respir Crit Care Med*, no. 10.1164/rccm.201601-0083OC, 2016.

[111] S Häussermann et al., "Effects of a helium/oxygen mixture on individuals' lung function and metabolic cost during submaximal exercise for participants with obstructive lung diseases," *International Journal of COPD*, no. 2015: 10(1), 2015.

[112] M Montaudon et al., "Bronchial measurements in patients with asthma: comparison of quantitative thin-section CT findings with those in healthy subjects and correlation with pathologic findings," *Radiology*, vol. 253(3):844-53, 2009.

[113] C Kotaru et al., "Morphometric changes after thermal and methacholine bronchoprovocations," *J Appl Physiol*, no. 98(3):1028-36, 1985.

[114] PR Burgel, "The role of small airways in obstructive airway diseases," *Eur Respir Rev*, no. 20(119):23-33, 2011.

[115] DH Carr, S Hibon, M Rubens, and KF Chung, "Peripheral airways obstruction on high-resolution computed tomography in chronic severe asthma," *Respir Med*, no. 92(3):448-53, 1998.

[116] Y Hyung Kim, Y Kyung Lee, and JH Yoo, "Changes in CT scan-estimated airway dimensions during an acute exacerbation of asthma," *Intern Med*, no. 52(6):679-83, 2013.

[117] F Laurent, V Latrabe, C Raherison, R Marthan, and JM Tunon-de-Lara, "Functional significance

of air trapping detected in moderate asthma," *Eur Radiol*, no. 10(9):1404-10, 2000.

[118] J Sandeau et al., "CFD simulation of particle deposition in a reconstructed human oral extrathoracic airway for air and helium-oxygen mixtures," *Journal of aerosol science*, no. 41.3(2010):281-294, 2010.

[119] M Thomas and A Bruton, "Breathing exercises for asthma," *Breathe*, no. 10: 312-322, 2014.

[120] N Jahani et al., "A four-dimensional computed tomography comparison of healthy and asthmatic human lung," *J Biomech*, no. 3;56-102-110, 2017.

[121] PR Burgel, J de Blic, and P Chanez, "Update on the roles of distal airways in ashtma," *Eur Respir Rev*, no. 18:80-95, 2009.

[122] S Sankaran, L Gady, and CA Taylor, "Fast computation of hemodynamic sensitivity to lumen segmentation uncertainty," *IEEE trans med imaging*, no. 34(12):2562-71, 2015.

[123] A Lungu et al., "Diagnosis of pulmonary hypertension from magnetic resonance imaging-based computational models and decision tree analysis," *Plum circ*, no. 6(2):181-90, 2016.

[124] TT Soong, P Nicolaides, CP Yu, and SC Soong, "A statistical description of the human tracheobronchial tree geometry," *Respir physiol*, no. 37(2):161-72, 1979.

[125] YK Mariappan, KJ Glaser, and RL Ehman, "Helium-3 magnetic resonance elastography of the lung," *Clin anat*, no. 23(5):497-511, 2016.

[126] EE Greenblatt et al., "Analysis of three-dimensional aerosol deposition in pharmacologically relevant terms: beyound black or white ROIs," *J Aerosol Med Pulm Drig Deliv*, no. 28(2):116-29, 2014.

[127] F Pedregosa et al., "Scikit-learn: machine learning in python," *JMLR*, no. 12(2011):2825-2830, 2011.

[128] H Hoppe et al., "Grading airway stenosis down to the segmental level using virtual bronchoscopy," *Chest*, no. 125(2):704-11, 2004.

[129] L Yoshihara, CJ Roth, and WA Wall, "Fluid-structure interaction including volumetric coupling with homogenised subdomains for modeling respiratory mechanics," *Int J Numer Method Biomed Eng*, no. 10.1002/cnm.2812, 2016.

[130] MH Tawhai et al., "CT-based geometry analysis and finite element models of the human and ovine bronchial tree," *J Appl Physiol*, no. 97(6):2310-21, 2004.

[131] AD Freed and DR Einstein, "An implicit elastic theory for lung parenchyma," *Int J Eg Sci*, no. 2013 Hen;62:31-47, 2013.

[132] W De Wever, J Coolen, and JA Vershakelen, "Imaging techniques in lung cancer," *Breathe*, no. 7:338-346, 2011.

[133] M Zompatori, F Ciccarese, and L Fasano, "Overview of current lung imaging in acute respiratory distress syndrome," *European respiratory review*, no. 23:519-530, 2014.

[134] K Naberan et al., "Use of spirometry in the diagnosis and treatment of chronic obstructive pulmonary disease in primary care," *Arch bronconeumol*, no. 42(12):638-44, 2006.

[135] Chhabra, "Clinical application of spirometry in asthma: Why, when and how ofter?," *Lung india*, no. 32(6):635-637, 2015.

[136] MA Wall, PC LaGesse, and JA Istvan, "The "worth" of routine spirometry in a cystric fibrosis clinic," *Pediatr pulmonol*, no. 25(4):231-7, 1998.

[137] C Tantucci et al., "The best peak expiratory flow is flow-limited and effort-independent in normal subjects," *Am J respir crit care med*, no. 165(9):1304-8, 2002.

[138] PDJ Junwale, AW Bhade, and PN Chatur, "Statistical data classification on the basis of statistical data mining," *International journal of computer science and telecommunications*, vol. 3, no. 2, 2012.

[139] GL Ruppel, "What is the clinical value of lung volumes?," *Respir care*, no. 57(1):26-35, 2012.

[140] A Ohwada and K Takahashi, "Concave pattern of a maximal expiratory flow-volume curve: a sign of airflow limitation in adult bronchial asthma," *Pulm med*, no. 2012: 797495, 2012.

[141] D Bellamy, "spirometry in practise," The British Thoractic Society COPD consortium, 2005.

[142] MR Miller and et al, "Standardisation of spirometry," *Eur Respir J*, no. 26(2):319-38, 2005.

[143] M Beaumont et al., "Gravity effects on upper airway area and lung volumes during parabolic flight," *J appl physiol*, no. 84(5):1639-45, 1985.

[144] "Fluent 6.3: User's guide," Lebanin, 2501 p., 2006.

[145] JE Daugherty, *Assessment of chemical exposures: calculation methods for environmental professionals*. Boca Raton: Lewis publishers, 1997.

[146] MC Hart, MM Orzalesi, and CD Cook, "Relation between anatomic respiratory dead space and body size and lung volume," *Journal of applied physiology*, no. 18(3):519-522, 1963.

[147] MF Petrini, MS Phillips, and DA Walsh, "Pulmonary tissue volume and blood flow as functions of body surface area and age," *Lung*, no. 166(1):47-63, 1988.

[148] JD Hoisak, KE Sixel, R Tirona, PC Cheung, and JP Pignol, "Correlation of lung tumor motion with external surrogate indicators of respiration," *Int J radiat oncol biol phys*, no. 60(4):1298-306,

2004.

[149] S Hughes et al., "Assessment of two novel ventilatory surrogates for use in the delivery of gated/tracked radiotherapy for non-small cell lung cancer," *Radiother Oncol*, no. 91(3):336-41, 2009.

[150] AS Beddar et al., "Correlation between internal fiducial tumor motion and external marker motion for liver tumors imaged with 4D-CT," *Int J radiat oncol biol phys*, no. 67(2):630-8, 2007.

[151] PJ Besl and ND McKy, "A method for registration of 3-D shapes," in *IEEE Trans. on Pattern analysis and machine intelligence*, Los Alamitos, USA, 1992.

[152] F Chollet. https://github.com/fchollet/keras.

[153] The theano development team, "Theano: a python framework for fast computation of mathematical expressions," *arXiv*, no. 1605.02688v1, 2016.

[154] R Sinkus et al., "Imaging anisotropic and viscous properties of breast tissue by magnetic resonance-elastography," *Magn reson med*, no. 53(2):372-87, 2005.

[155] R Santarelli, *Helium-3 magnetic resonance elastogrpahy of the lung*., 2013.